Master's thesis

NTNU
Norwegian University of Science and Technology
Faculty of Engineering
Department of Structural Engineering

Elise Sophie Christensen and Sigrid Freihow Sande

Evaluation of Externally Reinforced Bridge Exposed to Alkali-Silica Reactions

Condition Assesment of Elgeseter Bridge

Master's thesis in Civil and Environmental Engineering
Supervisor: Terje Kanstad, NTNU

June 2020

NTNU
Norwegian University of
Science and Technology

Elise Sophie Christensen and Sigrid Freihow Sande

Evaluation of Externally Reinforced Bridge Exposed to Alkali-Silica Reactions

Condition Assesment of Elgeseter Bridge

Master's thesis in Civil and Environmental Engineering
Supervisor: Terje Kanstad, NTNU
June 2020

Norwegian University of Science and Technology
Faculty of Engineering
Department of Structural Engineering

NTNU

Kunnskap for en bedre verden

Department of Structural Engineering
Faculty of Engineering
NTNU – Norwegian University of Science and Technology

ACCESSIBILITY

Open

MASTER THESIS 2020

SUBJECT AREA:	DATE:	NO. OF PAGES:
Concrete Structures	June 7th 2020	162 + 81

TITLE:

Evaluation of Externally Reinforced Bridge Exposed to Alkali-Silica Reactions

Tilstandsvurdering av utvending forsterket bru utsatt for alkalireaksjoner

BY:

Elise Sophie Christensen
Sigrid Freihow Sande

SUMMARY:
This master thesis a thorough condition assessment of Elgeseter Bridge has been performed focusing on the effect external reinforcement has on ASR exposed concrete. Elgeseter bridge is a 200 m long beam bridge placed in Trondheim consisting of nine spans. Core samples have shown harmful alkali-silica reactions (ASR) in the bridge. Severe cracks are observed in critical sections and are strengthened with externally bonded fiber reinforcement.

ASR is a chemical reaction occurring in concrete made of alkali-reactive aggregates reacting together with alkali in the cement. This process forms a swelling gel which leads to an expansion of the concrete. Elgeseter Bridge is estimated to have elongated 200 mm since construction. This thesis contains an assessment of the additional imposed forces due to this elongation. The resulting forces are included in the original decisive load situation for Elgeseter bridge found by Stemland and Nordhaug (2018) in a previous master thesis.

Two linear elastic FE models were established to evaluate the additional forces in the bridge due to ASR expansion. Model 1 consists of beam and truss elements, whereas model 2 is a volume model of solid elements.

To evaluate the capacity in ULS of the strengthened parts of Elgeseter Bridge, design rules from Fib Bulletin 90 (2019) are considered. The material used is carbon fiber reinforcement (CFRP) which is a strong and light composite material. The purpose is to increase both moment and shear capacity.

The most utilized section is in an unstrengthened, originally zero moment section with a bending moment utilization of 2.91 in model 1 and 3.02 in model 2. CFRP strengthening reduced the utilization ratio with about 70\% in critical sections. Though, regarding debonding issues of the CFRP, all strengthened sections were found to be insufficient. Only the support sections have an acceptable utilization ratio when considering axial forces combined with bending moment.

RESPONSIBLE TEACHER: Professor Terje Kanstad, NTNU

SUPERVISOR(S): Terje Kanstad, NTNU, Håvard Johansen, The Norwegian Public Road Administration

CARRIED OUT AT: Department of Structural Engineering, NTNU Trondheim

Preface

This master thesis is the final work of our five years master's degree in Civil and Environmental Engineering at The Norwegian University of Science and Technology. This assignment is written in cooperation with The Department of Structural Engineering and The Norwegian Public Road Administration.

Our main motivation is to preserve existing concrete structures and to rehabilitate structures in a sustainable and economic way. An admiration of great structures has thrived with our increase in knowledge. Especially bridges have captured our interests and therefore it was very attractive to write an assignment regarding a damaged concrete bridge. Having Elgeseter Bridge as a case was therefore very appealing.

During the past 5 years of education, we have walked over Elgeseter Bridge in both good and bad days. Writing this thesis has also included both blessings and frustration. Looking back, this bridge has become a symbol of our journey in Trondheim. The bridge still stands and so do we.

Writing this thesis has led to many academic discussions and our insight in engineering and design of concrete structures has increased significantly. A deeper knowledge has been obtained regarding alkali-silica reactions in concrete and external fiber reinforcement.

We want to thank our supervisor, Professor Terje Kanstad for indispensable help and for guiding us to achieve a deeper understanding of the topic. Our co-supervisor in The Public Road Administration, Håvard Johansen also deserves our gratitude. Furthermore, Kathrine and Hans Stemland have contributed with valuable discussions and knowledge in addition to rest of the team presently working with Elgeseter Bridge.

Abstract

This master thesis a thorough condition assessment of Elgeseter Bridge has been performed focusing on the effect external reinforcement has on ASR exposed concrete. Elgeseter bridge is a 200 m long beam bridge placed in Trondheim consisting of nine spans. Core samples have shown harmful alkali-silica reactions (ASR) in the bridge. Severe cracks are observed in critical sections and are strengthened with externally bonded fiber reinforcement.

ASR is a chemical reaction occurring in concrete made of alkali-reactive aggregates reacting together with alkali in the cement. This process forms a swelling gel which leads to an expansion of the concrete. Elgeseter Bridge is estimated to have elongated 200 mm since construction. This thesis contains an assessment of the additional imposed forces due to this elongation. The resulting forces are included in the original decisive load situation for Elgeseter bridge found by Stemland and Nordhaug (2018) in a previous master thesis.

Two linear elastic FE models were established to evaluate the additional forces in the bridge due to ASR expansion. Model 1 consists of beam and truss elements, whereas model 2 is a volume model of solid elements.

To evaluate the capacity in ULS of the strengthened parts of Elgeseter Bridge, design rules from Fib Bulletin 90 (2019) are considered. The material used is carbon fiber reinforcement (CFRP) which is a strong and light composite material. The purpose is to increase both moment and shear capacity.

The most utilized section is in an unstrengthened, originally zero moment section with a bending moment utilization of 2.91 in model 1 and 3.02 in model 2. CFRP strengthening reduced the utilization ratio with about 70% in critical sections. Though, regarding debonding issues of the CFRP, all strengthened sections were found to be insufficient. Only the support sections have an acceptable utilization ratio when considering axial forces combined with bending moment.

Sammendrag

Det er i denne oppgaven utført en tilstandsvurdering av Elgeseter Bru med et fokus på lastvirkninger av alkalireaksjoner og utvendig fiberforsterkning av bruen. Elgeseter Bru er en 200 m bjelkebru i Trondheim som består av ni spenn. Kjerneprøver av betongen har vist at bruen er utsatt for ASR ekspansjon. Omfattende sprekker er observert i kritiske snitt. Disse er forsterket med utvendig fiberforsterkning (CFRP).

ASR er en kjemisk reaksjon i betongen som oppstår av at alkali-reaktivt aggregat reagerer med alkali i sementen. Denne prosessen danner en ekspanderende gel som leder til en ekspansjon i betongen. Det er estimert at Elgeseter Bru har forlenget seg med 200 mm siden den ble bygget. Denne oppgaven inneholder en gjennomgang av de ytterlige kreftene som oppstår i bruen på grunn av ekspansjonen. De originale lastvirkningene er inkludert i kapasitetsberegningen. Disse er funnet i Stemland og Nordhaug (2018) sin masteroppgave.

To lineær-elastiske FE modeller ble etablert for å evaluere tilleggskreftene fra ASR ekspansjonen. Modell 1 består av bjelkeelementer, mens modell 2 er bygd opp av volumelementer.

For å evaluere kapasiteten i bruddgrensetilstanden i de forsterkede delene på Elgeseter Bru, er det brukt dimensjoneringsregler fra Fib Bulletin 90 (2019). Materialet som er brukt er karbonfiberforsterkning som er et sterkt og lett kompositttmateriale. Hensikten er å øke både moment- og skjærkapasitet.

Det mest påkjente snittet opptrer i et av de originale momentnullpunktene i den uforsterkede delen av innerbjelken. Utnyttelsesgraden her er 2.91 i modell 1 og 3.02 i modell 2. CFRP forsterkningen bidrar til å redusere utnyttelsen av kritiske momentnullpunkt med nesten 70%. En vurdering av heftbrudd mellom CFRP og betongen viser derimot at alle forsterkede snitt i bruen er kritiske. Ved å inkludere de opptredende aksialkreftene sammen med bøyemomentet er det kun snittene over støttene som har en akseptabel utnyttelsesgrad.

Contents

Chapter 1

Introduction

During the past decades, the world has been exposed to a vast and rapid change seen from an environmental point of view. The population has increased enormously, leading to more consumption of our commodities, as well as an increased emission of greenhouse gases. This results in extreme weather and higher exposure to existing structures. Concrete is one of the most common building materials, and lately, it is observed that it is more subjected to deterioration than assumed in the first place.

The environmentally induced degradation of concrete structures is only one aspect. Many structures have been attributed to aging, micro-environmental issues, poor initial design or lack of maintenance. There is also the issue that the existing structures can not meet the new demands for extreme weather and earthquakes or an increase in traffic volume. To avoid more environmental emissions, it is convenient to strengthen the existing structures instead of building new ones.

Having considered the challenges above, carbon fiber reinforcement seems like a promising solution. It is a very strong and light composite material which with an adequate application can contribute significantly to the load bearing capacity.

Elgeseter Bridge is a representative example of a deteriorated concrete structure. A chemical reaction occurs due to the appearance of alkali reactive aggregates in the concrete, leading to an expansion of the concrete. This chemical reaction is referred to as alkali-silica reactions (ASR). It affects the bridge at a structural level, and relatively large cracks have occurred in several places. External carbon fiber reinforcement serves as an attempt to restore the capacity.

This study is a condition assessment of Elgeseter Bridge focusing on the effect external reinforcement has on ASR exposed concrete.

ASR reactions lead to an elongation of the bridge as well as imposing external loads on the concrete. Quantifying the loads is challenging due to many uncertainties in the extent of ASR. A considerable part of this assignment is to determine the effects imposed on the structure due to the ASR-exposure. This is performed by using an FEA software to create an idealized frame model and

a solid volume model. By using two approaches, weaknesses in the respective models will be visualized. This is an interesting aspect to study and is accounted for throughout the report when comparing and evaluating the results. The analyses are linear elastic, but with the implementation of non-linearity in the cracked areas. This can be challenging to include and the impact of this simulation must be thoroughly assessed.

The utilization of sections in the bridge is evaluated including the ASR-loads in addition to the decisive acting loads. The original acting load situation for Elgeseter Bridge has been studied in 2018 by Norhaug and Stemland and their results have been used for further calculations in this investigation. Capacity calculations have been performed by using the outdated guideline NS 3473 edition from 2003.

Calculations of the fiber reinforcement capacities in ULS are executed following the guidelines in Fib Bulletin 90 (2019). The effects of carbon fiber reinforcement are assumed to contribute differently to a local and global scale. By studying the external reinforcement locally in sections, an increase in shear and moment capacity can be determined. While studying the whole bridge, the impact on the expansion and possible redistribution of forces can be observed.

Furthermore, this report demonstrates the fundamental aspects regarding both alkali-silica reactions and carbon fiber reinforcement. A review of the conditions in the Bridge is also presented. The two FE models are thoroughly compared to isolate deviations. The effects of different modeling of non-linearity and external reinforcement are analyzed and determined. Hence, the utilization ratio and the general assessment of the bridge's condition at the current state are concluded. A brief review of the effects occurring in the future has similarly been examined.

Chapter 2

Alkali Silica Reactions

Alkali-silica reaction (ASR) is a chemical reaction occurring in concrete made of alkali-reactive aggregates reacting together with alkali in the cement. This process forms a swelling gel, which leads to an expansion of the concrete. The expansion induces tensile stresses in the concrete and leads to a formation of cracks in the structure. Further damage and decomposition of the concrete can occur in combination with chloride- or carbonation-induced corrosion or freeze-thaw cycles. This is resulting in a reduction of the structure's capacity. A thorough damage assessment must, therefore, be performed on all structures affected by ASR [1].

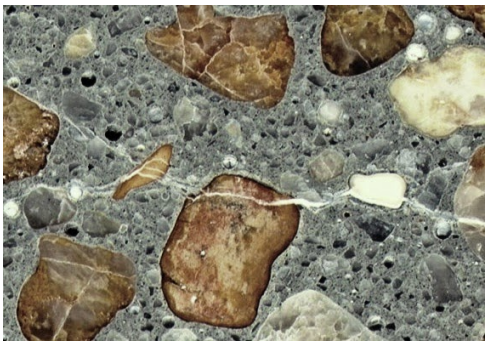

Figure 2.1: Concrete with ASR-gel [2]

Concrete exposed to ASR-damage gets a multi-directional pressure that causes a characteristic intensive map cracking at the surface. It imposes a compression on the concrete near the steel reinforcement and creates additional stress in the steel. The extent of the ASR-damage can be classified by the crack width, patterns and intensity, expansion history and splitting strength [3].

A large number of structures in Norway are exposed to ASR. A common assumption was that ASR had an insignificant influence on the structures in Norway due to a low mean temperature and a slow-reacting pace of the most common aggregates. Nowadays, many structures have reached the point of fifty years in

service life and the visible damage is more severe than first assumed [4].

The chemical reaction happens at a small scale but gives reaction products at a long term perspective leading to consequences on a structural level. ASR gives implications for both the serviceability and the load bearing capacity [4]. The reaction mainly depends on three factors:

- At least 20% reactive aggregates (SiO_2)
- Sufficient alkalis in the cement (Na^+, K^+) and hydroxyl ions (OH^-)
- Moist environment with a relative humidity of at least 80-90%

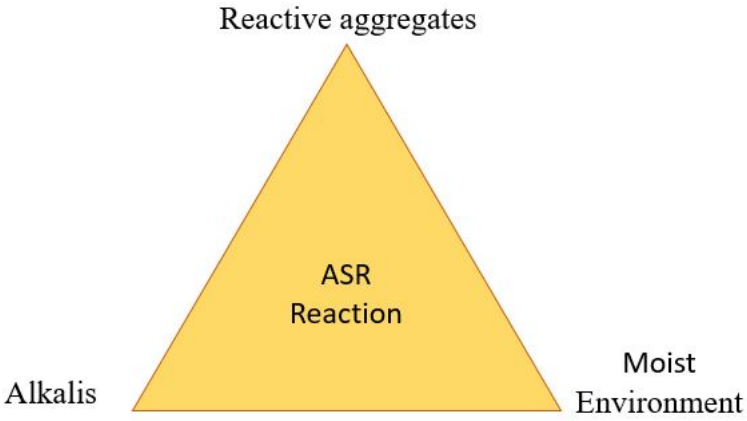

Figure 2.2: Necessary factors for ASR-reaction

With the presence of hydroxyl, alkali metal, calcium ions and water the reaction begins. The hydroxyl ions provoke the destruction of atomic bonds of the siliceous compounds, whereas the alkali ions react with $Si(OH)_4$ complexes which form a fluid $(Na, K) - Si - OH$ gel. This gel then substitutes Na and K with Ca and the gel solidifies. The solidified gel swells by water absorption leading to the mentioned expansion [6]. As the gel is swelling, pressure is obtained in the gel and this must be balanced by tensile stresses in the concrete. This happens locally so that micro-cracks appear both in the cement paste and the aggregate. The crack pattern will consist of diffuse micro-cracks but is easily recognized as the shapes are very typical for ASR and the gel can be visible as white spots or stripes. Consequently, the strength and stiffness of the concrete are reduced [5].

Due to the demand for high relative humidity, outdoor concrete structures are more often exposed to ASR such as dams, tunnels and bridges. The expansion may vary in size over the structure itself and locally in smaller parts. This is

due to different exposure of humidity or aggregates in the concrete. The variation in the expansion can also be visible over the cross-section and therefore it is important to notice that the measured exposure on the surface is just an average value [1].

The outer part of the exposed concrete will alternately be humidified and dried out depending on the weather conditions. Each time the concrete is drying, the water will take away some of the alkalies leading to that the outer layer (5-10 cm) has a lower ratio of alkali-ions. Consequently, the conditions for ASR reactions are favorable a few centimeters within the concrete and a greater expansion will occur here. A combination of this, as well as some shrinkage in the concrete, leads to macro-cracking of the outer layer where the tensile stress is exceeding the capacity of the concrete. Once the surface has cracked, these cracks will be filled with water when exposed to rain or splashes. The high humidity within the cracks gives a favorable environment for further ASR reaction leading to greater cracks. The cracks develop vertically down in the concrete until the reinforcement is reached, then they turn in direction growing parallel to the surface. As a consequence, the surface gets rotation and cracks will be wider at the surface. Damages on the concrete can also occur in the form of large single cracks and delamination of the concrete [4].

Figure 2.3: Characteristic map-cracking in concrete due to ASR [7]

The severity of the damages caused by ASR strongly depends on the design and geometry of the structure, the type of reinforcement (normal or prestressed) and the distribution of the expansion over the cross-section. Since the challenges related to ASR are quite new, limited research has been done regarding the effects on the capacity. For calculation of the effects due to ASR, one can assume there are many similarities to the calculation model for shrinkage in concrete. Yet the size of the expansion due to ASR compared to the shrinkage in concrete is a lot higher. Furthermore, the alkali-silica reaction is also affecting the strength and stiffness of the concrete.

2.1 Mechanical Aspect

ASR is leading to an internal micro-cracking of the concrete and the mechanical properties of the concrete are affected. This mainly influences the compressive strength, the tensile strength and Young's modulus of the material.

Even though the research regarding ASR mainly has focused on the internal chemical mechanisms it is important to know how the mechanical properties are affected by the expansion. The Institution of Structural Engineers came up with a relation between expansion, compressive and tensile strength and Young's modulus in the nineties and this is still used as guidance [4]. This is shown in table 2.1

Property	Exspansion [mm/m]				
	0.5	1.0	2.5	5.0	10.0
Cubic compression strength	100	85	80	75	70
Uniaxial compression strength	95	80	60	60	-
Tensile strength	85	75	55	40	-
Young's modulus	100	70	50	35	30

Table 2.1: Properties [%] with increasing expansion [‰]

Clearly, the tensile strength is most affected when the concrete develops micro-cracking. This is the only one that changes significantly when the expansion is below 0.5 ‰. The table shows that from this point the properties mentioned above are gradually more influenced as the expansion increases, but the reduction is not severe for the total capacity until the expansion has reached 2.5 ‰ [4]. This is a quite high expansion and this rarely occurs in structures. Often the expansion is somewhere between 1-1.5 ‰ and from research projects and master theses, it is shown that the effects can be significant in this area as well. Consequently, it is believed that the results from The Institution of Structural Engineers are somewhat imprecise.

An important aspect is that the impact on the properties depends on in which direction the strength is measured compared to the dominating micro-crack direction. Strains induced by the ASR will be reduced in the compressed direction compared to the tensioned part [8]. Meaning that the stress state in the concrete affects the expansion resulting in an anisotropic material behavior when it comes to stiffness and strengths. Several research projects have investigated this by testing strength and stiffness in different directions to get an overview of the correlations, but no clear relationship between compressive strength and stress state has been found. From a study made by Barbosa et al.[9] it was concluded that the compressive strength and stiffness became lower in the direction perpendicular to the cracks compared to the direction going parallel with the cracks. This statement was supported by a research project done by Giaccio et al.[10]. Their results showed that the compressive strength and stiffness was higher with cracks in the same direction as the loading. The theory that the

expansion, cracking and change in stiffness and strength were directional with the stress state was confirmed by Gautam et al. [11] who tested many drilled cubes with different stress states.

Regarding the influence of the load bearing capacity, the reduction in the compressive strength is not decisive until the expansion has reached a high value, about 2-3‰, according to The Norwegian Public Road Administration. Delamination of concrete can also impact the compressive strength negatively [1]. An investigation done by Kongshaug et al. states that the compressive strength is not suited as a damage indicator since it is not affected by ASR expansion at the same rate as the elastic modulus. The reduction in compressive strength can be correlated to other properties rather than longitudinal expansions [8].

The Norwegian Public Road Administration's report of ASR [1] states that with an expansion of 1 ‰, the tensile strength of the concrete is almost equal to zero in some directions due to the crack formations. The shear strength and bond strength depend on the tensile strength of the concrete which may not be sufficient when the tensile strength is lost. A critical place is in the anchorage zone where the reinforcement is limited. This can strongly affect the load carrying capacity of the structure.

From a stiffness damage tests (SDT) it is possible to assess the degree of damage in the concrete. The test is done by performing five loading cycles in compression on concrete specimens. By recording stresses and strains it is possible to calculate the damage parameters. Such parameters are the modulus of elasticity, stiffness damage index, plastic damage index, and non-linearity index. The damage is characterized as a function of the expansion level using a load equal to 40% of the compressive strength. From an investigation done with SDT testing performed by Kongshuag et al. it has been concluded that the relative modulus of elasticity decreases with increasing levels of expansion due to ASR[8].

The anisotropic behavior of ASR affected concrete was also investigated in the same research project by looking at the behavior with restrained samples. They observed that the ASR induced expansion was prevented in the restrained direction and the expansion did not get transferred between the directions. Consequently, uniaxial compressive stress on the concrete will reduce the overall damage caused by ASR. Since the restraint prevents the expansion it also prevents the reduction in the elastic modulus. Concrete subjected to compressive stresses about 3 MPa will not get a reduction in Young's modulus [1].

The magnitude of micro-cracking is correlated to the degree of expansion in a given direction, and the number of cracks and their orientation is generating the reduction of the anisotropic stiffness. The general conclusion from Kongshaug et al. was that all the damage indicators showed a reduction in damage in the restrained directions [8].

There are no researches in Norway stating that ASR expansion will wear out in time [1]. Nevertheless, this is if the structure is free to move. As earlier explained, structures with restraints will stop expanding in one direction when the compressive stresses in this direction are about 2-5 MPa.

2.2 Loads from ASR

The expansion from ASR does not solely affect the mechanical properties of the concrete, it may also impose additional forces in structures. For reinforced concrete, the expansion due to ASR is to be considered as a long term load.

A reinforced concrete structure exposed to ASR expansion gets an internal restraint from the reinforcement. If the structure is statically indeterminate it will also have an external restraint as deflection and displacement get prevented. In addition, if parts of the structure expand more than other parts, this will give imposed forces in the structure. Following, these three cases are explained in detail.

Internal Restraint from Reinforcement

Only the concrete will expand when exposed to ASR. Due to the bond between the concrete and the reinforcement, the steel bars will be strained as it is following the concrete. This results in stresses both in the reinforcement and the concrete. Internal equilibrium is obtained such that the force in the steel is equal to the force over the reinforced cross-section. This is shown in the form of an axial-load in the gravity center and an eccentric moment shown in figure 2.4. This is an internal rearrangement of the forces and for a situation with statically determined structure it will not give external loading [1].

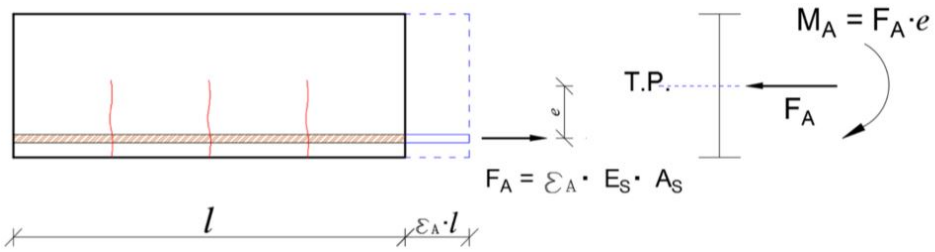

Figure 2.4: ASR-loads on reinforced concrete [1]

Internal stresses are developing as long as the material is linear elastic. Since the ultimate moment capacity is calculated when the steel is yielding the initial strain from ASR give little impact on the capacity of the cross-section. In this way, it is possible to look at these internal stresses as an inner pre-tension effect. Even though the internal stresses give a small impact, the stage of the cross-section has a significant impact. Whether it is in stage I or II is very important for how the cross-section is responding [1]. Usually a structure, during its service life, will be in stage II as it is exposed to dead load and live load. Being in stage II means that only the reinforcement is obtaining the tensile stresses. In some cases, structures may have parts in stage I and stage II at the same time, and this should be taken into account in capacity controls.

External Restraint

Once the structure is fixed for elongation or rotation, it gets an external restraint. The prevented expansion induced by ASR will lead to an external load contribution.

This can be understood by looking at a cross-section where the free expansion has a linear distribution over the height. Typically the upper part of a beam is more exposed to ASR than the lower part, which results in a higher expansion in the top giving a uniform gradient in the free expansion, ε_0. This induces a greater tensile force in the top, making the beam tend to curve upwards. If the beam is without external constraints, the beam would be subjected to such curvature and no external loads would appear.

In a statically indeterminate structure, the beam would be prevented to curve due to the external constraints. This is occurring in the form of a secondary moment giving compression in the upper part and tension in the lower part. This provides stress-contributing strains, ε_σ, in the cross section. To get the actual resulting strain in the beam, ε, the stress-contributing strains are added to the free expansion.

$\varepsilon = \varepsilon_0 + \varepsilon_\sigma$

This is illustrated in figure 2.5:

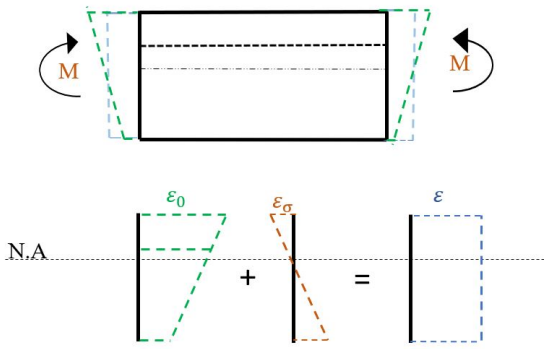

Figure 2.5: Effect of external constraints

The beam gets an expansion due to the ASR-loads, but since the curvature is prevented, the elongation is uniform and a secondary moment is present. This external moment imposes stresses on the concrete and is defined by equation (2.1).

$$M_y = \int_A z \cdot \varepsilon_\sigma \mathrm{E}\, dA \tag{2.1}$$

External Restraint from Adjoining Parts

The expansion of a structure due to ASR is often not uniform throughout the whole structure. Factors as more humidity and reactive aggregates locally in the structure could make some parts expand more than adjoining parts.

Figure 2.6 displays two connected beams, where beam 1 is subjected to an initial strain ε_0 from ASR and beam 2 is not. If both beams were subjected to the same ε_0, they would both expand equally and there would not be any forces in the beams due to the expansion of ε_0. When beam 1 expands more compared to beam 2 it will strain beam 2, since this beam is forced to follow, to maintain compatibility in the section. This strain will subject beam 2 to a tension force N_2 from the adjoining beam. Furthermore, beam 2 will resist the strain from beam 1, which will give a compression force in beam 1, N_1. The resulting strain of the beams ε is illustrated in figure 2.6 by the blue line.

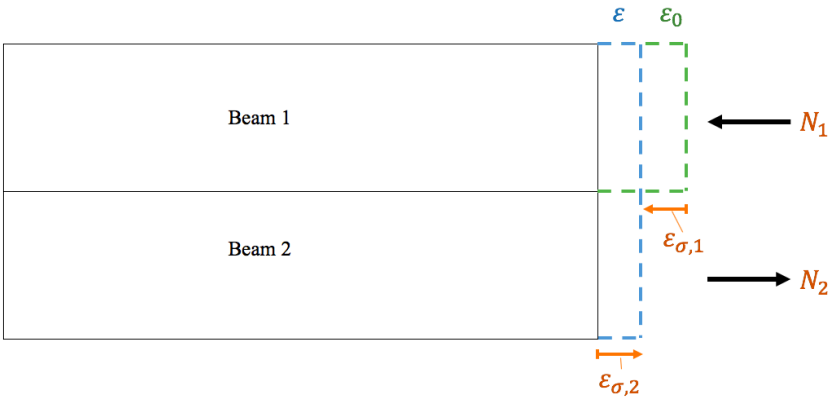

Figure 2.6: Effect of external restrain from adjoining parts

An important aspect of this situation is the difference in the resulting strain ε and the stress contributing strain ε_σ. The stress contributing strain is an imaginary strain state that represents the stresses in the cross section. The initial strain must be subtracted from the resulting strain to achieve the stress contributing strain. Such that:

$$\varepsilon_\sigma = \varepsilon - \varepsilon_0$$

The initial strain does not contribute to any stresses itself, as the expansion is due to ASR. It is the retaining forces from the section trying to be in compatibility that introduce these forces. Figure 2.7 illustrates the stress contributing strain of the sections.

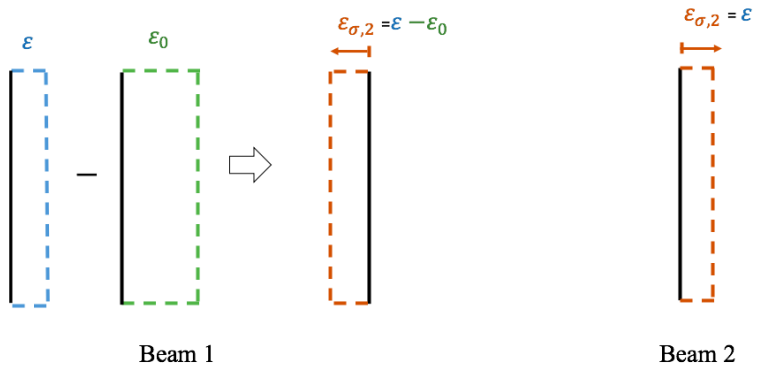

Figure 2.7: Strain of beam 1 and 2

The resulting axial forces in the section is found by the following equation:

$$N_x = \int_A \varepsilon_\sigma \mathrm{E}\ dA \tag{2.2}$$

Resulting Loads form ASR

Depending on the boundary conditions, different load effects can be obtained. The effects caused by the constraints also depend on the stress state in the concrete. In addition, the support system, the size of the affected parts, the reinforcement layout and the variation in expansion over the structure parts decide the resulting load effects from ASR.

The resulting moment coming from ASR includes the effects of both the internal and external constraints. These effects result in a positive moment, leading to an increase in field moments and a reduction over the supports. The shift in the moment may introduce significant moments in places originally designed with poor reinforcement such as zero moment sections illustrated in figure 2.8. Since such sections are not designed for high bending moments they are possibly very critical. At these places, the elastic moment capacity can be exceeded leading to the formation of plastic hinges. The static system changes and capacities may be exceeded elsewhere as well.

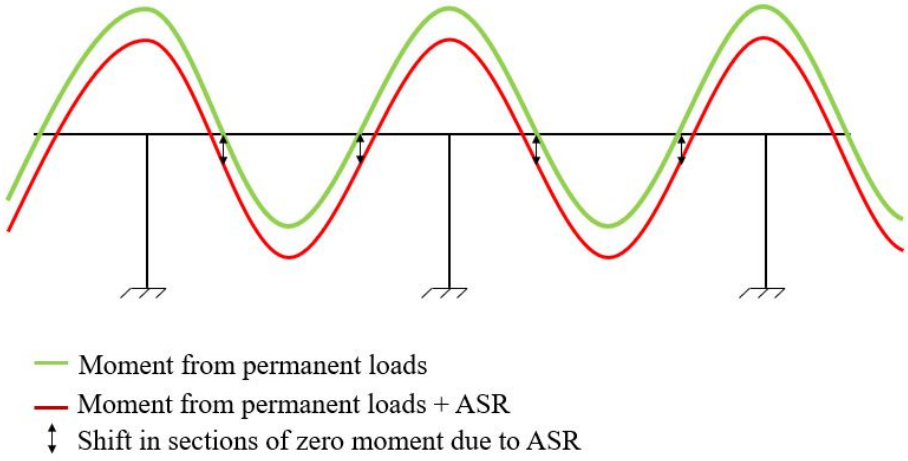

Figure 2.8: Shift in moment distribution due to ASR-loads

If a part within the structure is imposed to a higher ASR-expansion, the part will be compressed, whereas the less exposed parts are set in tension. This may occur locally in the beam or extend over the entire structure. The axial forces occurring due to different expansions can become very high and impact the load bearing capacity of the structure.

Chapter 3

Carbon Fiber Reinforced Polymers

The performance requirements for many existing civil engineering structures do not satisfy today's demands. The need for upgrading structures has become an arising issue that needs to be solved. This has led to an innovation in methods used for strengthening. During the last 20-30 years a new technique has become common for strengthening concrete structures. This method consists of using externally bonded fiber reinforced polymer composites, also known as FRP [12].

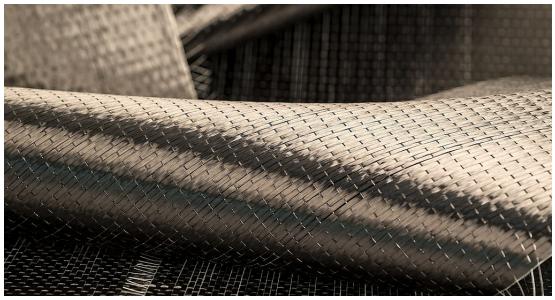

Figure 3.1: CFRP fabric [13]

3.1 Products and Application Techniques

The fibers can either be of glass, aramid, basalt or carbon and are combined with a polymer matrix. Together they make a strong composite material working with the original material. The matrix is typically a polymer of thermosetting and has the function to protect and bind the fibers and to distribute the loads. The fibers together with a matrix define the FRP material and its mechanical properties [14].

Fibers made of carbon is preferable when dealing with concrete structures and is featured as CFRP. The properties of the fibers depend on how they are made and the amount of carbon. All types of carbon fiber offer high yield strength- and modulus materials [12].

(a) FRP Sheets[15]

(b) FRP Strips [16]

(c) FRP Rods [17]

Figure 3.2: FRP Products

The Application of FRP can be divided into different categories in the field of civil engineering. Further in this report, only the strengthening of structures with externally bonded FRP will be treated. The FRPs are mainly used for strengthening structures and are available in the form of thin unidirectional strips, flexible sheets/fabrics or rods. The strips are approximately 1 mm thick and the rods have a diameter of a few millimeters. Both are made by pultrusion. The sheets have fibers in one or several directions [18].

There are different ways to apply the FRP strengthening and the type of method must be carefully chosen by evaluating the aspect of the situation. The structure part must be considered as well as the purpose of the strengthening. The different methods are mainly separated into two categories:

- Cured in-situ systems
- Pre-cured (prefabricated) systems

When providing flexural strength, the fibers must be placed in the longitudinal direction on the tensioned area, see figure 3.3. It is also beneficial to attach fibers at the sides of a beam. Flexural strengthening FRP is often in the form of long strips, fiber sheets or laminates.

For increasing the shear capacity, FRP shear-reinforcement is installed in three different configurations; side bonding covering two sides, U-wrapped and com-

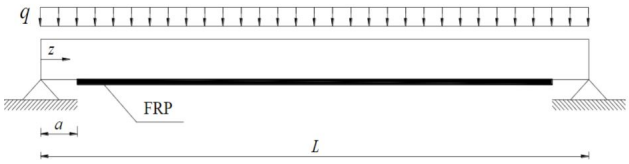

Figure 3.3: Flexural strengthening on the tension side [19]

pletely wrapped beams. Completely wrapped beams have the highest strengthening effect, but can be challenging to install due to availability. U-wrapping of a beam provides a certain possibility of debonding which reduces the effectiveness of the material. Even though, one can almost achieve the same strength as a complete wrap by sufficient anchoring which is preventing delamination of the U-wrap's ends. In the same way as for steel stirrups, the shear reinforcement can be laid orthogonal on the member's longitudinal axis or in an inclined position [19].

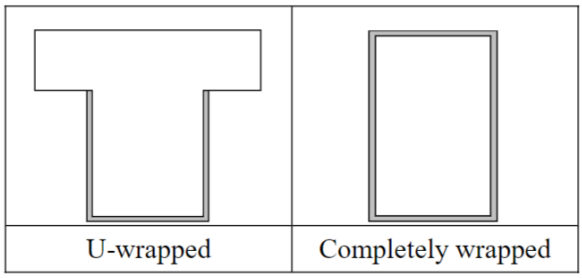

Figure 3.4: Configurations of shear reinforcement [19]

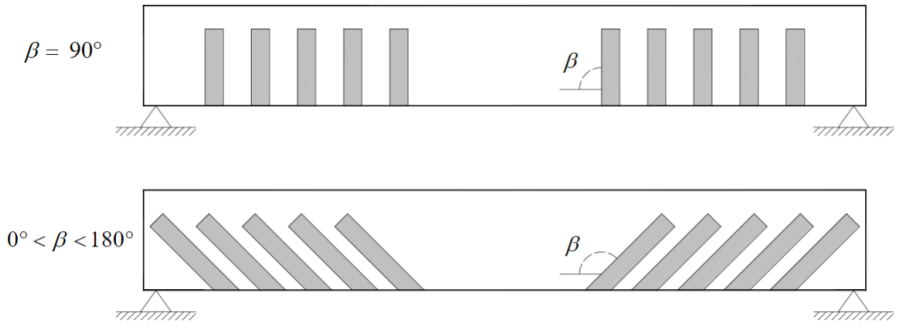

Figure 3.5: Lateral view of FRP strengthening [19]

The most common and basic technique of applying external bonded FRP is a manually bonding of the reinforcement onto the surface [18]. Three elements need to be evaluated; the substrate, the adhesive and the FRP reinforcement. The surface must be controlled for unevenness, cracks and imperfections. The

levels of humidity, chloride and sulphate must be considered, as well as the strength and carbonization of the existing parts.

The deteriorated concrete must be removed and restored with shrink-free cement and measures to prevent corrosion of existing steel must be done. If the surface is too rough it can be leveled by using epoxy paste. The next step is to sandblast the concrete surface to a suitable roughness degree. Furthermore, the surface must be cleaned to remove any dust, foreign particles, oil or other materials that could prevent the bonding. When treating a concrete member with sharp corners or edges, these have to be rounded to a radius of minimum 20 mm [19].

Afterwards a suitable bonding agent must be chosen. This can be a multiple-component system or a single bonding agent. Eventually the FRP reinforcement can be connected [18].

There are some general requirements for the conditions around the application of FRP concerning temperature and humidity. Even though FRP can be installed on structural elements in both dry and humid environments, a very moist environment can delay the curing of the resin [18]. In the case where fire can occur, protection for fire must also be provided. Fire insulation can be done by using protective plasters or panels [19].

When installing FRP outdoors it is necessary to prevent chemical-physical reactions in the matrix and the reinforcement must therefore be protected against sunlight. This can be done by using a protective acrylic paint [19].

The FRP material needs sufficient anchoring to maintain the desired capacity both for bending and shear. This can either be done by different applications of FRP-material, bolts or steel plates. Concerning flexural strengthening, the most common method is the use of U-shaped straps placed orthogonal to the flexural strengthening. This solution maintains the position of the longitudinal strip and prevents debonding [19].

3.1.1 Assumptions for Application and Design

The right application of the FRP materials is extremely important as it is the basis of the design rules. Some assumptions of the application and the properties of the composites are made to be able to design the strengthening and these must be fulfilled [18]:

- Steel stirrups have sufficient deformation capacity such that the FRP can reach its design strength
- Slip between FRP and the concrete is negligible. This is provided for as long as the adhesive used is of high quality and has at least a thickness of 1.0 mm. In this way it is justified that viscoelastic phenomena are negligible.
- Interlaminar shear strength of FRP is higher than the adhesive bond shear strength. To ensure this, it is important to choose a resin of high quality.

- Preparation done at the surface is good enough to achieve the required bond strength.
- An elastic analysis method of a cracked cross section can be used to determine the strain in the existing steel reinforcement at the time of FRP application.

3.2 Benefits and Challenges with FRP

3.2.1 Benefits

FRP is often used in cases where low weight combined with high strength and stiffness is needed. Also, it offers a lot of other advantages as a strengthening of reinforced concrete structures. Compared to steel, the same volume of FRP only weights one fourth, which makes it easier to work with and will reduce labour costs. It has a very high tensile strength and is immune to corrosion. This compensates the high costs of FRP compared to steel by providing the same strength with a smaller volume. In addition, the FRP strengthening solutions are flexible in size and geometry and even the stiffness can be tailored to suit the design requirements [18].

The most common use of FRP is to increase the flexural stiffness and the moment capacity [20]. By using FRP it is possible to increase the strength in reinforced concrete beams with up to 200% [21]. Furthermore, the composite material has very convenient properties for shear strengthening. According to a scientific research project the shear strength can be increased by 60 – 120% for reinforced concrete beams [21]. Columns in compression can also benefit from strengthening with FRP. Referring to a scientific research project by Jan Arve Øverli and Erik Thorenfeldt in 2001 [22] shows that one layer of fiber sheet on a column provided a 20% increase in the capacity and two layers increased it by 50%. Considering the torsion capacity of reinforced concrete beams, the use of FRP reinforcement increases the capacity significantly. A research project performed by Salom, Gergley and Young [23] shows the increase of torsion capacity by 70% with the use of laminates. As for seismic strengthening, FRP is a very beneficial method for both repair and retrofitting [18]. FRP strengthening can provide sufficient shear capacity when retrofitting columns and is a very effective method to prevent critical shear collapses [24].

3.2.2 Challenges

Aside from the increased capacity of reinforced concrete with the use of FRP, there are some challenges by using this method. FRP-materials are costly and there is often a demand for low investments and minimal assembling of cost during its service life. As previously mentioned, the application of the material requires thorough processing of the surface before installation and the surfaces must be available. Other parts of the structure may prevent the availability, and this can also make it hard to provide the necessary anchoring length. There is also a problem associated with temperature, fire, sunlight and other environmental degradation effects. The effects of the material can be challenging, especially in a composite material, such as shrinkage, creep and fatigue. It depends on

the adherence to the concrete and this must be thoroughly taken care of. It is essential to be aware that the FRP materials need to be protected from mechanical damage as it is exposed and vulnerable at the surface. In addition, the failure mode of an FRP strengthened element is brittle and often occurs with little or no indication of failure [24].

3.3 Materials and Mechanical Properties

3.3.1 Carbon fiber Reinforcement

Carbon Fiber-reinforced Polymers (CFRP) is a composite containing fibers of carbon, matrix and adhesive. The carbon fibers are a discontinuous material that gives the composite most of its strength and stiffness, while the matrix is a continual material that binds the fibers [12]. In this way, the CFRP is similar to concrete composites, with reinforcement made of fibers and the matrix having the same purpose as the concrete. The resin is used as the bonding adhesive between the CFRP plate and the concrete. Hence, the resin can be used as the matrix in the CFRP.

Carbon Fibers

Carbon fiber composites have a higher strength, stiffness and a lower density than steel [12]. It is five times lighter and can be ten times stronger than steel [24]. The fibers' geometric properties, such as the ratio between the fiber length and its diameter, makes it possible to transfer the tension from the fibers to the matrix. Carbon fibers have a high resistance to corrosion, and is favorable in many chemical environments.

Material	Elastic modulus	Tensile Strength	Ultimate tensile strain
High Strength Carbon	215-235 GPa	3500-4800 MPa	1.4-2.0 %
Ultra High Strength Carbon	500-700 GPa	2100-2400 MPa	0.2-0.4 %
Steel	185 GPa	3070 MPa	1.5-2.0 %

Table 3.1: Properties of carbon fibers compared to steel [18].

Compared to steel, carbon fibers have different tensile properties such as a much lower ductility and a more brittle behavior. Carbon fibers are linear elastic until their final rupture.

Matrix

The matrix in a composite has multiple purposes, such as binding the fibers, distribute the load between the fibers and protect the fibers from external environmental impacts [12]. Furthermore, the matrix has mechanical properties in the composite such as transverse modulus and strength, shear capacity and compression capacity [18]. The matrices normally have low yield stress and stiffness and are sensitive to high temperatures. The advantages of the matrix material are their chemical resistance, low price, low density and that they are easy to facilitate [12].

Polymers are sensitive for temperature changes and as a result, the mechanical and bonding properties of the matrix can be affected by this. There are two types of polymers, thermoset and thermoplastic. The most significant difference between the two polymers is their behavior when subjected to high temperatures. The glass transition temperature T_g is defined as the temperature where a polymer transfers from a stiff to a more rubbery state and the mechanical properties of the polymer changes. See figure 3.6 illustrating the behavior of the thermoset and thermoplastic exposed to temperatures above T_g. This has to be considered while designing, in case of high temperatures such as a fire situation [18].

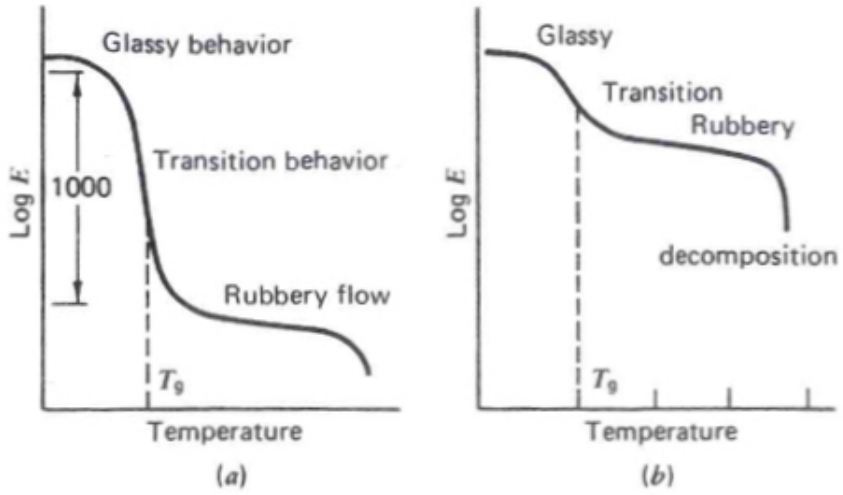

Figure 3.6: Transition behavior of thermosets and thermoplastic [12].

The thermosets epoxy, polyester and vinyl ester are the most common polymeric matrix materials used in structures and detailing in the construction industry. This is because of their good mechanical properties, high chemical resistance and processability [18]. Epoxy resins are favorable due to their good mechanical properties, durability and low weight. Epoxies will also bind to several types of fibers, resist humidity and chemical degradation, and shrink less during the hardening process [12]. Compared to epoxy, polyester and vinyl ester are cheaper [18]. See table 3.2 for characteristic properties of polyester and epoxy.

Property	Polyester	Epoxy
Density [kg/m^3]	1100-1400	1200-1300
Tensile strength [MPa]	35.5-103.5	55.0-130.0
Young's modulus (tension) [GPa]	0.5-4.4	0.5-10
Young's modulus (comp) [GPa]	0.5-6.0	0.5-12.0

Table 3.2: Properties polyester and epoxy [12].

The matrix must have a good bond strength with the fibers. To achieve this, one can modify the chemical structure of the matrix.

Adhesives

The adhesive is the bonding agent between the concrete surface and the FRP composite. It provides shear load distribution between the two composites and prevents interfacial failures. Since the concrete is weak in comparison to the adhesive, the interfacial failures most commonly occur in the concrete itself and not in the adhesive. Debonding in the adhesive is only realistic if the strength of the concrete is very high, or the temperatures are higher than the glass transition temperature T_g [18]. The most commonly used adhesive is epoxy which consists of epoxy resin and hardeners.

3.3.2 Mechanical Properties

Figure 3.7 and table 3.3 shows typical tensile stress-strain behavior of the fiber, matrix and FRP composite. Comparatively, one can see that the fibers have a higher stiffness and a lower ultimate strain than the matrix, and as a consequence of this, the matrix has a stiffness in between. The FRP fails at the same ultimate strain as the fibers.

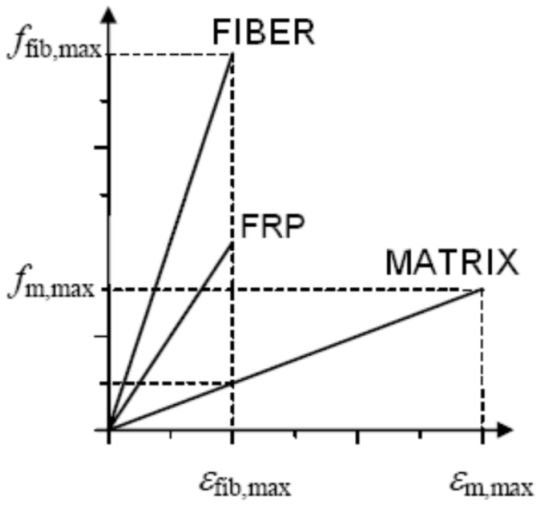

Figure 3.7: Tensile stress-strain behavior of fiber, FRP and matrix [19].

Estimation of some mechanical properties in a composite such as a CFRP plate can be found by using the *rule of mixtures* [18]. This rule states that:

$$E_f = E_{fib} \cdot V_{fib} + E_m \cdot V_m \tag{3.1}$$

$$f_f = f_{fib} \cdot V_{fib} + f_m \cdot V_m \tag{3.2}$$

		CFRP low modulus	CFRP high modulus
Modulus of elasticity	E_f E_{fib}	160 GPa 210-230 GPa	300 GPa 350-500 GPa
Ultimate strength	f_f f_{fib}	2800 MPa 3500-4800 MPa	1500 MPa 2500-3100 MPa
Ultimate strain	ε_{fu} $\varepsilon_{fib,u}$	1.6 % 1.4-2.0 %	0.5 % 0.4-0.9 %

Table 3.3: Properties of fibers (fib) and FRP (f) [19].

Where E is the elastic modulus, f is the tensile strength, V is the volume fraction. The sub notes f, fib and m are "FRP", "fiber" and "matrix", respectively.

The equations are based on the hypothesis of a perfect bond between the fibers and matrix [19]. Thus this rule can give a quite accurate modulus of elasticity for unidirectional composites, the rule of mixtures can be unconservative, especially for obtaining the ultimate strength [18]. For such predictions, one should test the material. For FRP composites impregnated in-situ, one shall use the direction perpendicular to the direction the impregnation is applied for computations of V_{fib} [19]. This is because of the volumetric fraction of the fibers may vary in this direction. Fib Bulletin 90 [18] recommends calculating the mechanical properties of the FRP composite by only using the fiber fraction and a reduction factor, r, such that:

$$r \cdot E_{fib} \cdot t_{fib} = E_f \cdot t_f \tag{3.3}$$

A CFRP plate is linear elastic until its final rupture, and do not have the same ductile behavior as steel have. This must be accounted for when designing carbon-fiber reinforced concrete [24]. See figure 3.8 below that illustrates the stress-strain curve for both CFRP and steel.

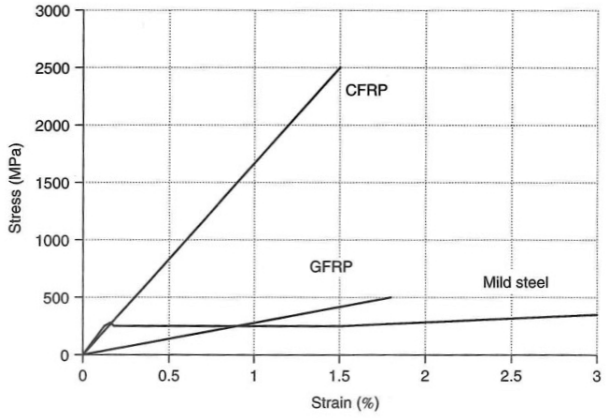

Figure 3.8: Tensile stress-strain behavior of CFRP compared to mild steel [24].

To understand the mechanical properties of a fiber-reinforced concrete beam, it is essential to comprehend the bond behavior between the FRP composite and concrete beam. The term *debonding* describes failure occurring due to loss of shear strength between the concrete and FRP composite. This failure can occur inside the concrete, in the adhesive-concrete or adhesive-FRP interfaces, and in the adhesive or FRP itself. See figure 3.9 for different locations of debonding. The most common, which is concrete failure, happens often a few millimeters within the concrete as a result of the adhesive's penetration in a thin layer of the concrete which then attains a higher strength [18]. This creates an interface in the concrete with different mechanical properties and a critical zone. Another failure mode in the concrete is along the steel reinforcement line which is a weakened layer.

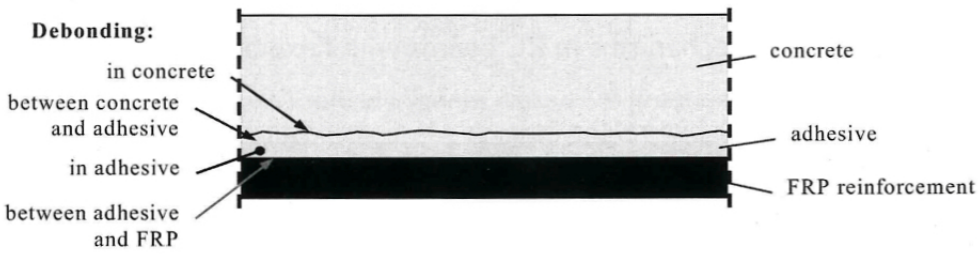

Figure 3.9: Typical locations of debonding for a FRP strengthened concrete member [18].

The bond behavior can be described by the differential equation:

$$\frac{ds^2}{dx^2} - p_f\left(\frac{1}{E_f \cdot A_f} + \frac{1}{E_c \cdot A_c}\right)\tau_b(s) = 0 \tag{3.4}$$

Where s is the slippage, E, A is the elastic modulus and cross-section, respectively. Sub notes f and c is the FRP reinforcement and the concrete, respectively. $\tau_b(s)$ is the local bond stress-slip law. ρ_f describes the bonded perimeter, and varies for different types of FRP reinforcement.

The concrete deformation $\frac{1}{E_c \cdot A_c}$ can most commonly be neglected, which gives a simpler differential equation:

$$\frac{ds^2}{dx^2} - \frac{p_f}{E_f \cdot A_f}\tau_b(s) = 0 \tag{3.5}$$

Typically, the bond behavior can be explained by the relationship between the shear stress at interface τ_b and the corresponding slip s. This relationship describes the shear stress transfer behavior and the debonding process and can be found by using experimental results and mode 2 fracture energy [18]. The relation $\tau_b - s$ depends on the geometry of the components and the mechanical

properties of the materials.

Recommended by Fib bulletin 90 [18], the bond behavior for a surface bonded FRP can be expressed by figure 3.10. The figure shows a linear increasing curve until reaching its maximum shear stress τ_{b1}, followed by a decreasing curve as a result of the damage that occurs in the materials. The maximum shear bond stress τ_{b1} and the ultimate slip s_0 depends on the properties of the concrete, the strengthening system and other geometric properties. Also, the maximum shear bond strength correlates with the concrete tensile strength. The slope of the increasing curve k_1 depends on both the thickness and shear modulus of the adhesive layer and the concrete.

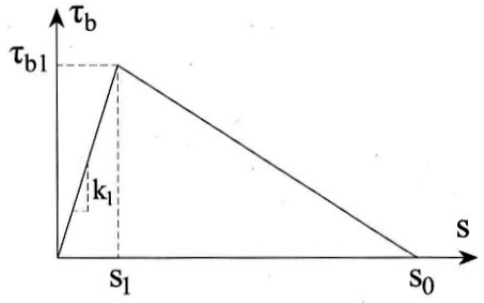

Figure 3.10: Bilinear bond-slip consitutive law [18].

3.3.3 Debonding Mechanisms

Debonding initiates with a localized debonding, which happens at a limited area often close to a formation of a shear or flexural crack. This localized debonding does not necessarily affect the capacity of the strengthened element. But if the crack propagates along the length of the beam and composite action between the FRP and the beam is lost, bond failure is a fact. This failure often happens in an abrupt and brittle matter. There are essentially two types of debonding in flexural strengthened concrete structures; *end debonding* and *intermediate crack debonding*.

As the name suggests, end debonding initiates at the end of the FRP plate, caused by high interfacial shear and normal stresses due to the abrupt termination of the FRP reinforcement [24]. Interfacial debonding at the anchorage zone has a strong correlation with the bond stresses such as the shear and normal stresses in the FRP-concrete interface near the end of the FRP plate. These stresses establish tensile stresses, and usually the debonding process happens at a very thin layer of the concrete adjacent to the adhesive illustrated in figure 3.11. This crack will further propagate along the beam, often from the end of the FRP soffit. Other times, the crack can be induced by the first crack closest to the beam support and propagate towards the end [18].

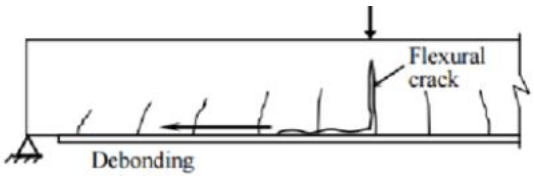

Figure 3.11: Debonding due to flexural cracks [26]

Concrete cover separation is another type of end debonding where the concrete cover is torn off, with a critical inclined crack at the level of the steel reinforcement illustrated in figure 3.12. This failure is often caused by high shear forces and negligible bending moment [18]. A study from Smith and Teng [25] showed that when the plate end was closer to the support, the crack at the end became more critical inclined. This shows the importance of shear force in such failures since the shear force is increasing while the bending moment decreases closer to the supports. This type of failure can be understood by two different approaches. The first analogy is to have a critical inclined crack at the unstrengthened part of the beam, and the concrete cover behaving like a composite with the FRP attached to the rebars. The curvature of the beam will create high interfacial stresses between the concrete cover and the rebars, resulting in horizontal debonding along with the steel reinforcement. The other analogy is to consider the shift in tensile forces between the FRP and the rebars and the missing shear ties between the two of them. If the tie becomes too large to be carried by the concrete this induces the concrete cover to fail, and the crack will propagate along the rebars.

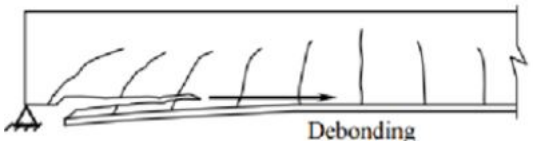

Figure 3.12: Debonding due to concrete cover separation [26]

Debonding can appear at intermediate flexural or shear-flexural cracks, which is a case of intermediate crack debonding. This often occurs in sections with high moments and shear forces which leads to a crack and creates high shear interfacial stresses between the FRP and concrete. This again leads to detachment of a thin layer in the concrete, and the cracks propagate towards the end of the beam.

Unevenness in the concrete surface can cause debonding, especially localized debonding. This can be prevented by proper concrete surface preparation, as explained in 3.1.

Chapter 4

Elgeseter Bridge

Elgeseter bridge is a concrete bridge located in Trondheim, opened in 1951 after two years of construction. With its slender columns and simple design, the bridge has a high architectural value and is an important landmark in the city of Trondheim. As a part of the European highway E6, it crosses the river Nidelva from Elgeseter street in the south to the city center in the north. The bridge was constructed by dr. ing. A. Aas-Jakobsen, designed by the architects G. Blakstad and H. Munthe-Kaas and built by Ingeniør F. Selmer AS [27].

Figure 4.1: Overview of Elgeseter bridge seen from the west [28]

Throughout the history, there have existed several bridges at the same location as Elgeseter bridge. The earliest documentation of a bridge is in 1178, which probably was a footbridge of wood. This bridge was the only connection crossing Nidelva until 1683 when The Old Town Bridge was built on the east side of the river. After this, the bridge decayed quickly. About 200 years later, a new bridge was built at this location as a part of the new railroad Størensbanen in 1864. This was a railway bridge made of wood called Kongsgaard Bridge and was later used as a tram and road bridge until the opening of Elgeseter Bridge [29].

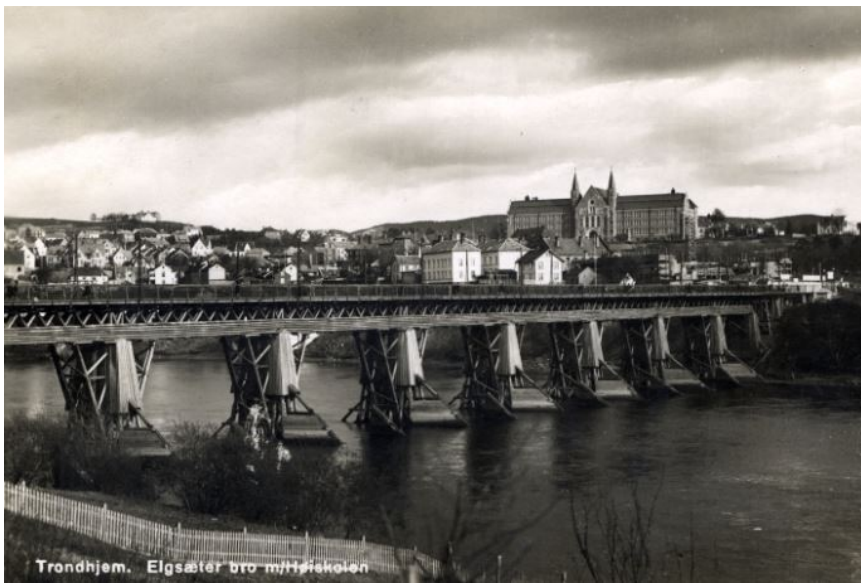

Figure 4.2: Kongsaard Bridge [30]

In 2004 Elgeseter Bride received the award "Betongtavlen" justified by the fact that the bridge is an outstanding, forward-looking and beautiful structure [31]. Since 2008 the bridge has been protected as an industrial heritage by the Norwegian Directorate for Cultural Heritage [27].

4.1 Properties of the Bridge

Elgeseter bridge has a total length of 200 meters and its girder is ranging 15 meters above the river. It consists of 9 spans with a length varying from 21.25 m at the end spans to 22.5 m in the remaining spans. The bridge has a width of 23.4 meters which accommodates four vehicle lanes, two pedestrian lanes at each side and two bike trails. On the south side of the bridge, there are 5 vehicle lanes and smaller pedestrian lanes.

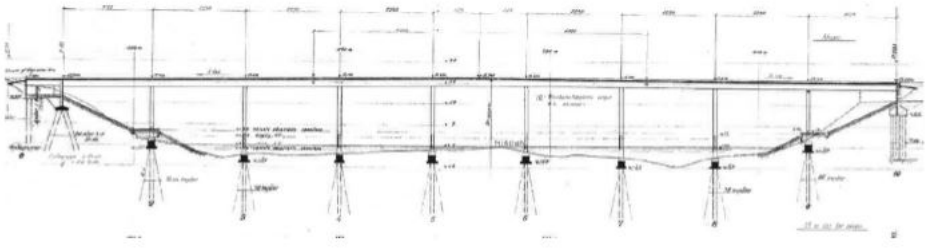

Figure 4.3: Elevation view of Elgeseter brigde [32]

The girder consists of four continuous beams cast in the bridge deck. The beams have cross sections of 800x1430 mm and a distance between each other of 5.5 m from the center of the cross sections. The thickness of the bridge deck is varying from 230-380 mm. The beams are supported by 8 column rows that are monolithically connected to the beams in column row nr. 1-7, where column row nr. 1 is at the south side of the bridge. At column row 9, at the north side, the beams have a pinned connection to the columns. The columns have a diameter of 800 mm and a length of 15 m in column row 2-7 whereas they are 10 m at each end. The columns are fixed at the bottom by approximately 80 friction piles made of wood [32].

Figure 4.4: Cross section of the bridge [4]

The abutment in the south is fixed, whereas the abutment in north is roller supported with a CIPEC extension joint. The static system of the bridge is presented in figure 4.5

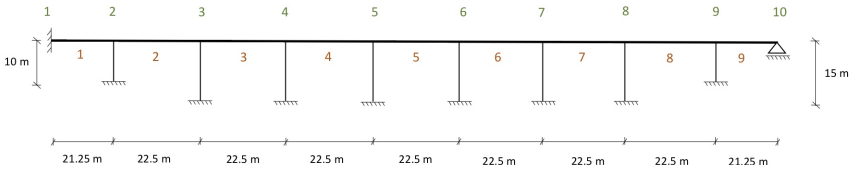

Figure 4.5: Static system of Elgesterer Bridge [4]

4.2 Alkali-silica Reaction in Elgeseter Bridge

In 1990, concrete core samples of Elgeseter Bridge showed harmful alkali-silica reactions. The structure has shown signs of the expansion in the bridge by vertical cracks in the columns, horizontal displacement of columns and reoccurring closing of the extension joint. In 1995, the extension joint needed rehabilitation because the joint was closed, 10 years after the last replacement. In 2000 it was estimated an extension of 20 mm since 1992 based on measurements of the opening in the joint. In 2013, the gap in the expansion joint was measured to be about 10 mm shorter compared to 2004. There are several uncertainties in these measurements, such as expansion due to temperature, temperature coefficient and movement in the abutments [32].

Based on the measurements of the gap in the extension joint, Dr. Ing. Aas-Jakobsen estimated a chart describing the extension of the bridge deck in the

longitudinal direction, see figure 4.6. Point 1-4 describes measured points in the transverse direction of the bridge in the northern abutment. All values are corrected for expansion due to temperature. By this chart, the bridge has had an estimated extension of 3.2 mm per year, and in total about 140-180 mm.

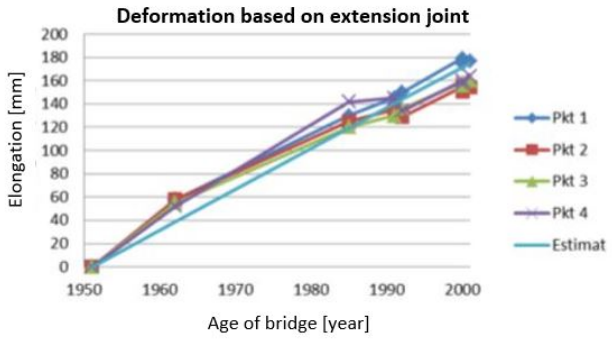

Figure 4.6: Deformation based on gap in extension joint [32]

Measurements of horizontal displacement at the column tops were done in 1991. These results show a total average displacement of 100 mm, which gives an average expansion of 2.5 mm each year. See figure 4.7. These measurements may be more accurate, as they don't have the same uncertainties such as expansion due to temperature and movements in the abutments [32].

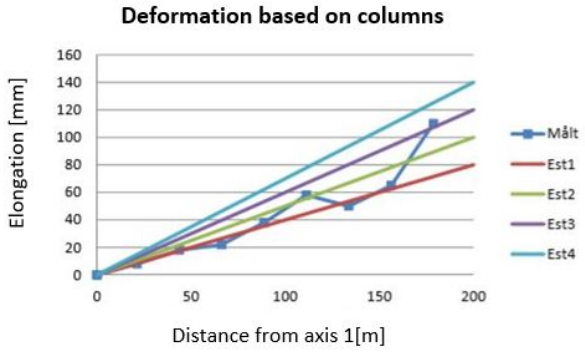

Figure 4.7: Deformation based on measurement from columns [32]

Aas-Jakobsen has estimated that in the worst case, the total extension of the bridge deck might be as large as 200 mm if the bridge has continued expanding since the last inspection. This will give a total strain of 1 ‰ in the longitudinal direction.

Results from concrete core samples in 1991 showed that there were severe alkali-silica reactions in the bridge deck, columns and the outer beams. In the inner

beams, there was no sign of ASR [32]. This can be explained due to the fact that the ASR-damaged parts of the bridge are exposed to humidity in a much higher degree than the inner beams. This was also visible during an inspection in 2012, where it was significant signs of water exposure in the outer beams, see figure 4.8. Due to earlier rehabilitation of pavements, it is reasonable to believe that membranes in these areas may be impaired which may lead to more humidity around the pavements [32].

Figure 4.8: Observation of water exposure on outer beam [32]

These observations and core samples have led to an assumption of the variations in expansion at the bridge made by H. Johansen [33]. The suggestion assumes that the bridge has a gradient from top to bottom where the upper face has a higher expansion compared to the lower face. In addition, it assumes that the outer beam expands more than the inner beam. The expansion in the longitudinal direction of the bridge is assumed to be constant. Further in this report, it is assumed that the bridge has this strain field with $a = 0.5$. See figure 4.9 illustrating the suggestion from H. Johansen.

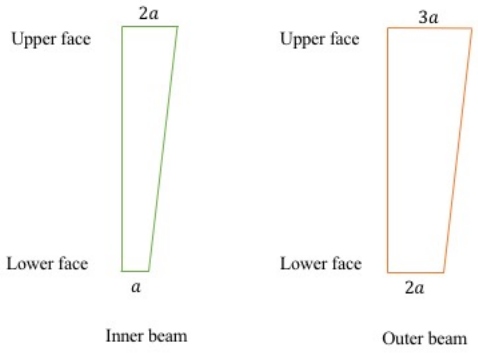

Figure 4.9: Suggestion of strain field in beams, with respect to the central axis of beams

This variation in expansion leads to the occurrence of additional moments and axial forces. The inner beams are subjected to a tensile force whereas the outer beams obtain a compression force as explained in section 2.2.

4.2.1 Condition of the Columns

The columns have shown severe damages due to ASR. Expansion in the columns was measured to be up to 2-3‰ in some parts and it was discovered cracks up to 7 mm [1],[4]. Columns in axis 9 were measured to have a horizontal displacement of 150 mm, which can lead to significant moment forces in the columns.

In 2003 it was decided to move the columns in axis 7-9. The columns in axis 9 had their foundation moved, while the columns in axis 7-8 were blasted in the top and re-casted. Furthermore, the columns were wrapped in CFRP at several places in two of the columns. Over a period of 8 years, the humidity and development of cracks were investigated in the columns. The results showed that the CFRP wrap might reduce the rapidity of the crack propagation and prevent further cracking in existing cracks. In addition, it was found that the transverse compressive forces due to ASR were not extensive enough to reduce the expansion in the columns, which needs compressive stresses at 3-5 MPa. This led to the conclusion that it is not necessary to provide additional CFRP on the columns unless there are significant signs of further expansion of crack widths [35].

The condition of the columns is not treated further in this study.

4.2.2 Condition of the Bridge Deck

Core samples have shown that the bridge deck is subjected to severe ASR damage. Both STD tests and microscopy studies show that the bridge deck is more exposed to ASR than the beams. It is found horizontal cracks in core samples and newly casted concrete has needed replacement [36].

An intact and adequate condition of the bridge deck is necessary to transfer horizontal moments and in-plane stresses. Though, this assignment mainly focuses on the beams and the load bearing capacity in the longitudinal direction where the condition of the deck probably has a modest influence [33].

4.2.3 Condition of the Beams

During an inspection done by Aas-Jakobsen in 2012 [32], it was discovered large cracks up to 6 mm in the inner beams about 4.5 m from the columns. The largest cracks were found in the western beam between axis 3-4 towards axis 4, and the eastern beam between axis 6-7 towards axis 7. See figure 4.10 for locations of critical cracks. At these mentioned parts, it was typically only one extensive crack which was propagating continuously throughout the cross section.

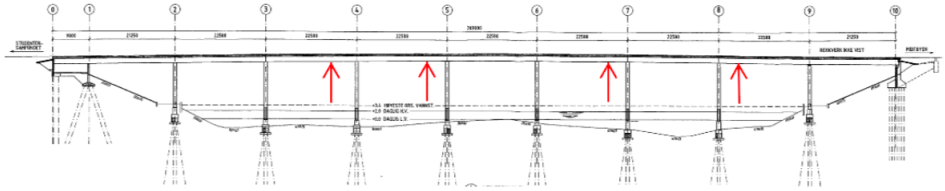

Figure 4.10: Locations of severe cracks in Elgeseter Bridge [32]

At sections 4.5 m from the columns, the moment due to self weight is zero. As a consequence of this, the amount of reinforcement in these sections is as modest as only 3Ø32 in the bottom of the beams. As explained earlier, the inner beams are subjected to a tension force due to the ASR expansion in the outer beams and bridge deck. At these originally zero moment sections, the amount of reinforcement is not sufficient to handle neither the additional tensile forces nor the acting moment, which leads to extensive cracks in these sections.

Figure 4.11: Severe cracks found in zero moment section north of axis 8 [32]

Smaller cracks were found in the middle of the spans, with a magnitude of about 2 mm. These cracks were typically closed at the top and bottom of the beams with its largest width in the middle, which is not typical for a flexural crack. The shape of these cracks is a result of the effect ASR has on the reinforcement. When the concrete expands due to ASR, the reinforcement will be strained, causing an effect similar to pre-tensioned reinforcement. This will cause the crack to close at the height of the rebars [32].

4.2.4 External Carbon Fiber-Reinforcement at Beams

As the cracks detected in the inner beams had a magnitude that might have been crucial for the capacity of the beams, it was decided to reinforce the most critical cracks with CFRP. The beams are strengthened with externally bonded carbon fiber reinforced polymers (CFRP). The fiber-reinforcement chosen for

flexural capacity was Sika CarboDur M, placed in the beams longitudinal direction at the soffit. SIKA Wrap Hex-230C was used as shear reinforcement, placed at the sides of the beams with an angle of 45 degrees. The CFRP was bonded with epoxy. Figures 4.12, 4.13 and 4.2.4 shows the details of the chosen CFRP reinforcement [34]. The flexural reinforcement is anchored 200 mm from both columns, while the shear reinforcement was placed only at the areas with severe cracks.

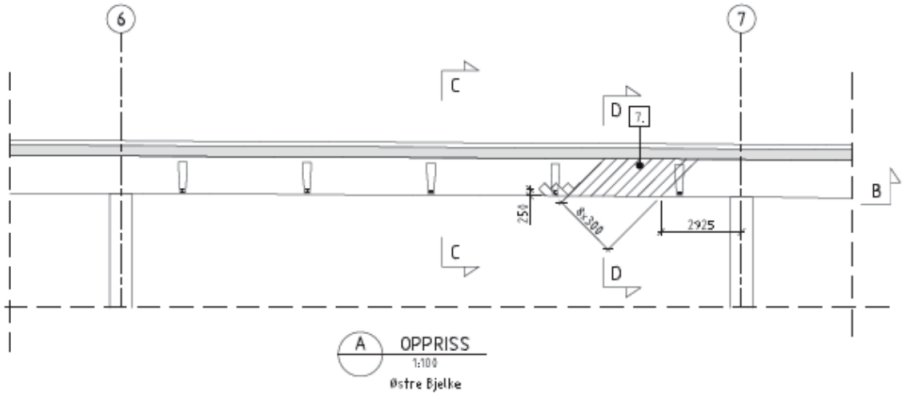

Figure 4.12: Details of CFRP reinforcement from the side of the beam [34]

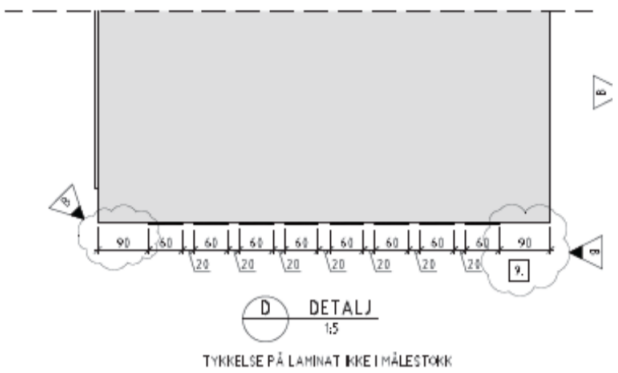

Figure 4.13: Details of CFRP reinforcement at cross section of beam [34]

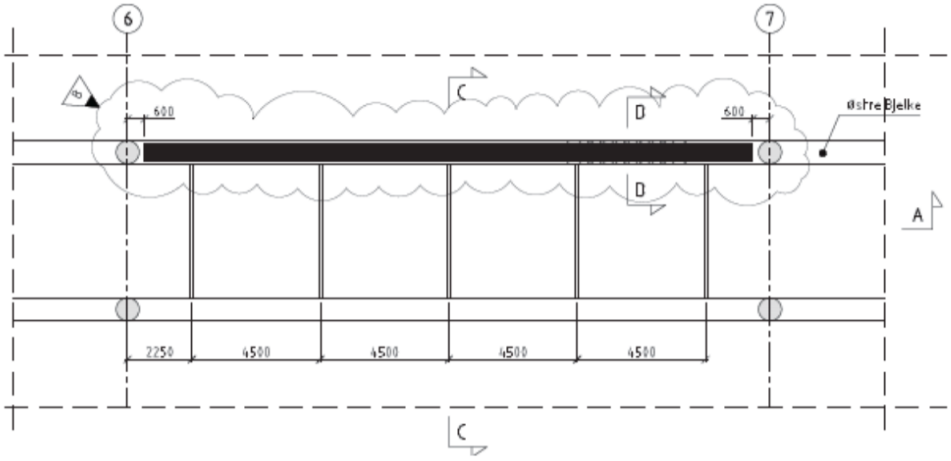

Figure 4.14: Details of CFRP reinforcement at the beam seen from underneath [34]

The fiber reinforcements are placed differently in the east-facing and west-facing beam. On the east-facing beam both flexural and shear reinforcement are placed in span 3, span 6 and span 8. Whereas for the west-facing beam is strengthened in span 3, span 4 and span 6, but in span 3 there is only the externally bonded shear reinforcement.

Different rehabilitation measures of the beams were considered prior to the application of the CFRP, such as external post-tensioning. This was considered to be an uncertain solution due to the alkali-silica reactions in the bridge. By post-tensioning the bridge at confined areas, the effects from expansions due to ASR might contribute to higher stresses at other locations of the bridge [34]. It was also considered to mechanically anchor the CFRP, but problems such as limited cover for the reinforcement and a considerable amount of reinforcement made solutions with anchoring unfavorable. The chosen solution was considered to be sufficient due to its anchoring of the CFRP in the beam's compression zone and CFRPs favorable effects on ASR such as possible restraining of additional expansion.

4.2.5 Development of ASR in Elgeseter Bridge in the Future

There are not documented any instances where alkali-silica reactions cease in Norway. For a structure that is not restrained, the expansion is assumed to continue unlimited. Otherwise, it is presumed to stop if the compressive stresses are about 3-5 MPa in a given direction [32]. Further expansion can also be prevented if the humidity and/or the alkalinity is reduced in the concrete. Unless measures are taken to reduce the ASR expansion in the bridge, one should assume that expansion continues.

Results from a report of The Norwegian Public Road Administration shows that the expansion joint only had a reduction of 3 mm in 2012 compared to

2004, compared to Aas-Jakobsen's measurements that showed a 10 mm reduction from 2003 to 2013 [32], [35]. The Norwegian Public Road Administration concluded that their measurements indicated that the expansion of the bridge deck has stopped [35]. This illustrates the difficulties of measuring the expansion joints due to many uncertain factors, and as well as the difficulties of concluding further expansion of the bridge based on measurements, especially when only looking at a short period of the bridge's lifetime.

The consequences of further expansion of the bridge might be continuous cracking due to ASR which can lead to frost damage and corrosion of the concrete [35]. As well, the alkali-silica reactions may reduce the strength of the concrete. The zero-moment areas are especially prone to further axial forces which may lead to rearrangement of forces in the bridge. These possible outcomes present a great uncertainty of the future capacity of Elgeseter Bridge. The consequences may be on a scale that it is sensible to consider that the expansion of the bridge due to ASR continues in its service life.

Trøndelag County Council has evaluated the expansion with bolt measuring equipment that was installed in the bridge deck in 1991. It was found that the average expansion in the longitudinal direction was 1.2 mm each year by these measurements. Also, the average reduction in the opening of the expansion joint was 2.1 mm each year, based on collected measurements since 1951. In light of these results, it was concluded that one should expect additional expansion of 50 mm during the bridge's lifetime, and that possible expansion as of today is 200 mm. This would mean a total expansion of 250 mm is predicted [37].

Chapter 5

Load Situation for Elgeseter Bridge

Load calculations and capacity control of Elgeseter Bridge is thoroughly done in the previous master thesis of Stemland and Nordhaug [4] as well as Myklebust [5]. The background for these calculations will be given in this section and the results will be evaluated and used later in this report.

5.1 Guidelines

During the construction of Elgeseter Bridge in 1951, the guideline NS 427 was used. In 1973 this was replaced by the guideline NS 3473 [38] which was used until the Eurocode was introduced in 2010. NS 3473 has been renewed several times in its service life and the last edition was published in 2003. There are some differences in these regulations and it is recommended to use the current building code of the time the bridge was made when performing a bridge classification.

Since Elgeseter Bridge was build before NS 3473 was published, the first edition should be used for the bridge classification. Despite this, the evaluation done by Stemland and Nordhaug [4] is performed after the newest version of NS 3473. In addition, they have supplemented their calculations with today's rules in the Eurocode. Handbooks published by The Norwegian Public Road Administration are also used in the study. These are Handbook N400 [39] regarding bridge design and Handbook R412 [40] regarding bridge classification.

5.2 Materials

5.2.1 Concrete

The Norwegian Public Road Administration has provided guidelines for existing bridges [40]. According to this, Elgeseter Bridge has concrete of class A with reference to NS 427. Transferred to the classifications in NS 3473 of concrete quality, this is a C25 concrete, which provides a characteristic cubic strength of

25 MPa.

However, it is expected that the ASR-damage has reduced the strength. During the rehabilitation of the bridge in 2014-2015, core samples were drilled out and tested. This was done during a special investigation in 2019 as well.

The results from the inspection in 2014 gave a mean value of 36.8 MPa and a standard deviation of 9.1 MPa. By following the NS 3473, 11.1.3, the most important resulting strengths were calculated and they were a little higher compared to the strength of a C25 concrete, but not of a significant magnitude. As the test-results and the computed ones correspond quite well, it seems safe to use a C25 concrete in the calculations.

One interesting aspect to consider, is the high deviation in the test samples. It is almost twice as big as in other general cases. The high variation can indicate that the effects of ASR are different over the bridge due to locally varying amounts of reactive aggregates. Based on the tests from 2014-2015, this could mean that the strength is reduced by 60% at the most exposed areas.

For the plate and the beam it is assumed a C25 concrete with the following properties:

Compressive cylinder strength	f_{ck}	20.0 MPa
Compressive cubic strength	f_{cck}	25.0 MPa
Structural strength	f_{cn}	16.8 MPa
Tensile strength of concrete	f_{ctk}	2.10 MPa
Structural tensile strength	f_{tn}	1.40 MPa
Material factor for concrete	γ_c	1.4
Design compressive strength	$f_{cd} = f_{cn}/\gamma_c$	12 MPa
Design tensile strength	$f_{td} = f_{tn}/\gamma_c$	1.0 MPa

Table 5.1: Properties of concrete C25

The short-term Young's modulus of the concrete is calculated by point 9.2.1 in NS 3472. This is found to be:

$E_c = 23300MPa$

Since ASR-loading is a long-term load, it is necessary to calculate the reactions with the long term Young's modulus, which is found by equation (5.1)

$$E_{c,longterm} = \frac{E_{c,shortterm}}{1+\phi} \tag{5.1}$$

With creep number $\phi = 2$. This is based on an estimation of the concrete quality and the degree of damage. The long term modulus becomes:

$E_{c,longterm} = 7766$ MPa

5.2.2 Reinforcement

In the bridge, it is used smooth steel bars with two different steel strengths, St. 52 and St.32. Since the main longitudinal reinforcement, as well as the transverse reinforcement, is made of St. 52, this quality is used for the entire reinforcement.

Referring to Lyse and Wige's book [41] typical work diagrams for different steel qualities are shown in figure 5.1.

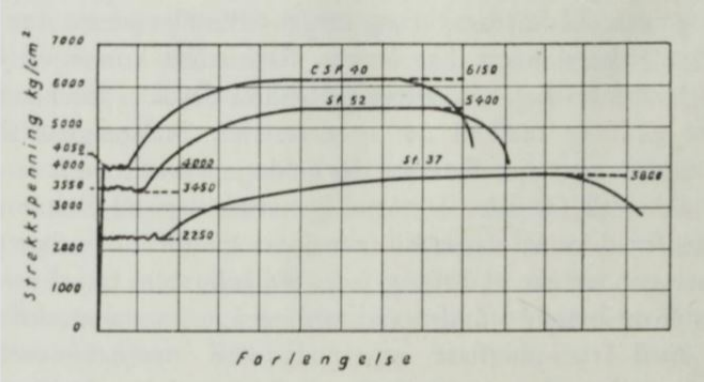

Figure 5.1: Work diagrams for steel strengths [41]

The yield strength of St. 52 is set to 340 MPa. The fracture strain is estimated to 1‰, which also is the limit defined by NS 3473 [38]. The steel's Young's modulus is 200 000 MPa with characteristic yield strain of 1.0‰.

f_{sk}	340 MPa
γ_s	1.25
$f_{sd} = f_{sk}/\gamma_c$	272 MPa

Table 5.2: Steel St.52 properties

Elgeseter Bridge is exposed to splashes and the exposure class is determined to be XD3 in NS 3473. This class of exposure is recommended to have a cover of 50 mm. Aas-Jakobsen suggests a cover of 55 mm for the beam [34] and this is used further in the calculations.

5.3 Cross-section

Over the beams there is a variation in thickness of the bridge deck. At both ends the thickness is 150 mm, while in the middle the thickness is 380 mm. This is simplified to a uniform thickness of 280 mm.

The cross-section of the bridge is consisting of four T-beams. The web has a width equal to 800 mm. The flange in each T-cross-section has a length of 5500

mm, which also is the center distance between the beams. The total height of the cross-section is 1710 mm, where the web is 1430 mm and the plate is 280 mm. The mass center is placed 1206 mm from the lower face of the cross-section.

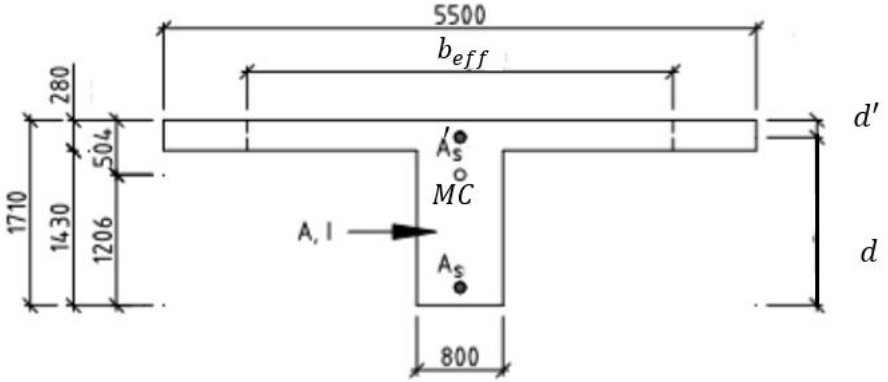

Figure 5.2: Simplified cross-section

These simplifications of the cross-section are counting for all the beams and are also used by Aas-Jakobsen [34] in their calculations.

5.4 Loads

The handbook N400 [39] gives a categorization of different load types depending on their variation over time. It is four main classifications separating the loads into permanent loads, variable loads, deformation loads and accidental loads.

This has been used in the previous investigation done by Stemland and Nordhaug [4]. The different loads have been analyzed in a Robot model to find the acting moments. The bridge was analyzed with its total length and width, including columns. The cross-section of the bridge in the model is corresponding to the cross-section shown in figure 5.2. Columns were fixed at the bottom and monolithically cast to the beams. Furthermore, the bridge was fixed at axis 1 and had roller supports at axis 10. To simulate the different stiffnesses in the bridge due to the altering amount of reinforcement along the bridge, the stiffness was modified in different sections [4].

The highest moment occurring in different sections for different loads are reported below. Only the temperature load will have an impact on the section of zero moment.

5.4.1 Permanent Loads

The permanent loads include the self-weight and the super-self-weight. The super-self-weight consists of weight due to permanent elements such as the coating on the road, crash barriers and banisters. According to the computational models done by The Norwegian Public Road Administration, the self-weight for one beam with a concrete-density of 25 kN/m^3 is modeled as 70 kN/m [33]. The super self-weight depends on whether it is the inner or outer beam that is considered. The inner beams have a super self-weight of 20 kN/m whereas the outer beams have a super self-weight of 28 kN/m.

The resulting moments and shear forces due to permanent loads are reported in table 5.3 and 5.4.

Section	Moment [kNm]
Support 1	-2995
Support 2-8	-3480
Support 9	-4086
Field 1	1497
Field 2-8	1740
Field 9	2827

Table 5.3: Design moments, permanent loads

Section	Shear force [kN]
Support 2-8	935
Support 9	961
Zero moment section, field 6	606
Zero moment section, field 8	631

Table 5.4: Design shear forces, permanent loads

5.4.2 Traffic Loads

For calculation of the traffic load on existing bridges, the Handbook R412 chapter 3 is used [40]. Traffic loads arise from vehicles, cyclists and pedestrians placed in the driving lane, hard shoulder, cycle track and sidewalk. Since the load can be at several places, the worst placement for the inner and outer beam must be investigated. The bridge must be classified in a way that reflects the amount of traffic load allowed. This is done by calculation controls after the partial factor method and assures that the decisive load effects do not exceed the resistance capacity. Elgeseter Bridge is characterized as class Bk 10/50 and this is used to find the suited load situation.

The traffic load must be defined for both the longitudinal and the transverse direction. R412 gives six different load models which is listed below:

- Wheel load model
- Axle load model

- Bogie load model
- Triple bogie load model
- Vehicle load model
- Lorry load model

Commonly, in long-spanning structures it is the vehicle load model or the lorry load model which is decisive. For Elgeseter Bridge the lorry load model is the most critical one. This load consists of distributed loads as well as an axle load found for bk 10. The dynamic impact is included in all the loads given in the handbook R412.

According to the handbook, R412 [40], maximally two lanes can be loaded with traffic load form a vehicle. There is no other specification about the placement and according to the research done by Stemland and Nordhaug [4], two trucks being placed in different lanes at each side of a support creates a critical situation.

Both breaking and acceleration over the road will induce horizontal traffic loads on the bridge. Furthermore, there are centrifugal and transverse forces. As Elgeseter Bridge is simply supported in one end, Myklebust states that the effects due to horizontal traffic loads in the longitudinal direction can be neglected [5].

Due to a recommendation in N400, it is not necessary to calculate snow together with traffic and since this is a highly trafficked bridge, there is no need to calculate the snow load at all.
This acting moments and shear forces due to traffic are found in table 5.5 and table 5.6.

Section	Moment [kNm]
Support 1	-2895
Support 2-8	-1805
Support 9	-1884
Field 1	1587
Field 2-8	2257
Field 9	2618

Table 5.5: Design moments, traffic load

Section	Shear force [kN]
Support 2-8	661
Support 9	666
Zero moment section, field 6	456
Zero moment section, field 8	460

Table 5.6: Design shear forces, traffic load

5.4.3 Wind Loads

Depending on if there is traffic or not, the load on the sidewalk and the wind load will vary in magnitude. The wind load will affect the bridge both in the vertical and horizontal directions. Since this load situation will most likely not be decisive, only the vertical load effects are studied.

The calculations are based on NS-EN 1991-1-4 [42] in combination with Handbook N400 [39]. Elgeseter Bridge is classified as bridge type 1 which neglects the dynamic response. Properties have been estimated based on the location of the bridge, wind direction, terrain and environment.

For the calculations, a reference area of the bridge has been used. This is defined by the area in the relevant direction of the wind over a reference length of 1 m. The area will depend on if there is traffic load working simultaneously.

The resulting moments and shear forces are reported in the tables below depending on whether it is traffic or not:

Without traffic

Section	Moment [kNm]
Support 1	-518
Support 2-8	-333
Support 9	-386
Field 1	326
Field 2-8	483
Field 9	464

Table 5.7: Design moments, wind load without traffic

Section	Shear force [kN]
Support 2-8	90
Support 9	58
Zero moment section, field 6	92
Zero moment section, field 8	60

Table 5.8: Design shear forces, wind load without traffic

With traffic

Section	Moment [kNm]
Support 1	-307
Support 2-8	-198
Support 9	-229
Field 1	193
Field 2-8	287
Field 9	275

Table 5.9: Design moments, wind load with traffic

Section	Shear force [kN]
Support 2-8	90
Support 9	58
Zero moment section, field 6	92
Zero moment section, field 8	60

Table 5.10: Design shear forces, wind load with traffic

5.4.4 Thermal Loads

Thermal loading occurs in the structure since the concrete will expand when heated and shrink with decreasing temperatures. A free structure will elongate as a result of high temperatures. The thermal loads are divided into different impacts:

- Evenly distributed temperature
- Vertically varying temperature
- Horizontal varying temperature
- Difference in evenly distributed temperature over different structure parts
- Difference in temperature over wall thickness between inner and outer walls

Since temperature loads are assumed not to be decisive for Elgester Bridge, it seems sufficient to control only evenly and vertical varying temperatures. The loads are obtained from Stemland and Nordhaug [4] and calculated after NS-EN-1991-1-5 [43].

To find the thermal effects due to an evenly distributed load, the values for the highest and lowest temperatures are defined. This is done by following point 6.1 where Elgeseter Bridge is categorized as type 3 as it is a beam-bridge in concrete.

Vertical variation of temperature gives a variation in expansion and contraction as well. Forces will be induced if the cross-section is retained for curving or friction in the rotation supports.

With both the thermal effects considered together, different combinations occur:

Section	Moment [kNm]
Support 1	-1037
Support 2-8	-1087
Support 9	-1296
Field 1	-1926
Field 2-8	-1922
Field 9	1254
Zero moment	1922

Table 5.11: Design moments, temperature load

Section	Shear force [kN]
Support 2-8	30
Support 9	20
Zero moment section, field 6	30
Zero moment section, field 8	20

Table 5.12: Design shear forces, temperature load

5.4.5 Deformation Loads

The deformation loads consist of creep and shrinkage. The effects due to creep are maintained by using the long-term E-modulus in the calculations based on an estimated creep number. The shrinkage of the concrete is not calculated in specific because Elgeseter is an outdoor bridge in a moist climate. Despite this, the shrinkage will work opposite of the expansion due to ASR, so that when measuring the expansion, a contribution may be missing and ASR effects are higher than assumed.

5.5 Load-combinations in ULS

Rules for load-combinations are found in Handbook R412 [40]. Decisive load-combinations of characteristic loads are used in dimension calculations. The goal is to find the worst case scenario for the structure by combing different loads with load factors. Stemland and Nordhaug performed the control only in the ultimate limit state [4].

Two sets of load-combinations were controlled, a and b. The differences between the two combinations are the load factors for self-weight and for variable loads. The loads were combined with different load factors and with different unfavorable main loads.

Combination	SW	DEF	TR	TEMP	W	W-TR
ULSa-TR	1,15/1,0	1,0	1,3	-	-	-
ULSa-TEMP	1,15/1,0	1,0	-	1,0	-	-
ULSa-W	1,15/1,0	1,0 -	-	1,6	-	
ULSb-TR	1,0	1,0	1,2	0.8	-	0,8
ULSb-W	1,0	1,0	-	0,8	1,3	-
ULSb-W-TR	1,0	1,0	0,8	0,8	-	1,3

Table 5.13: Load factors for different combinations

By controlling the different load-combinations, the worst combination is found for each section. Regarding the decisive moments, the ULSb-TR combination is the worst for all the section, except the section of zero moment. ULSb-TR is the combination with dominating traffic load. In the section of zero moment, the ULSa-TE is the worst, where the temperature load is dominating.

Section	Moment [kNm]	Load Combination
Support 1	-7544	ULSb-TR
Support 2-8	-6674	ULSb-TR
Support 9	-7567	ULSb-TR
Field 1	5097	ULSb-TR
Field 2-8	6216	ULSb-TR
Field 9	7192	ULSb-TR
Zero moment	1922	ULSa-TE

Table 5.14: Decisive load combination, moment

For the decisive shear force, the ULSa-TR gave the worst scenarios.

Section	Shear force [kN]	Load combination
Support 2-8	1935	ULSa-TR
Support 9	1971	ULSa-TR
Zero moment section, field 6	1290	ULSa-TR
Zero moment section, field 8	1324	ULSa-TR

Table 5.15: Decisive load combination, shear forces

In addition to the acting loads considered in this chapter, the effects of ASR must be quantified.

Chapter 6

Design of External Fiber Reinforcement

As for today, there are no official standards for design rules for externally bonded carbon fiber reinforcement in Norway. A new annex for EC 1992-1-1 is under development and is based on the technical report Fib Bulletin 90 (2019) [18]. To evaluate the capacity in ULS of the strengthened parts of Elgeseter Bridge, design rules from Fib Bulletin 90 is considered with a focus on the draft of the new annex in EC 1992-1-1. These design rules are presented in the following chapter.

6.1 Anchorage Capacity

To prevent debonding of the externally bonded reinforcement the FPR material must be properly anchored by introducing a bond length. This must be able to transfer the maximum force between the FRP reinforcement and the concrete. The effective bond length gives a minimum demand to ensure this and must therefore be verified.

The maximum force taken by the external FRP depends on the stress in the FRP, the cross-sectional area and the bond length. The attained force can increase up to a certain value proportional to the extended bonded length. Up to one point, the force will remain approximately constant as the bonded length still increases. The length at this certain point is referred to as the effective bond length l_e.

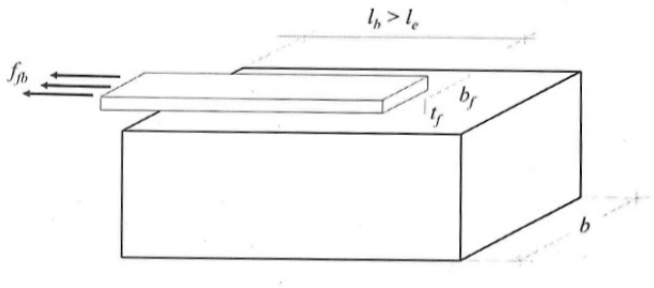

Figure 6.1: Maximum stress transmitted by FRP strengthening in the case of $l_b > l_e$ [18].

The effective bond length can also be defined from the $\tau - s$ constitutive law of bonding. By this law, the length must be able to take the ultimate slip s_0 in a bond-slip test. The other parameter is the shear stress, which gives a perspective of the bond strength. These characteristics together with the FRP stiffness define the effective length. In addition to the relations in the constitutive law of bonding, it is derived from the boundary conditions and by using the assumption of a rigid-softening bi-linear law.

$$l_e = \frac{\pi}{2} \cdot \sqrt{\frac{E_f \cdot t_f \cdot s_0}{\tau_{b1}}} \tag{6.1}$$

Since the relation between deformation capacity and strength of the system gives the fracture energy, one can also define the effective length from this value.

$$l_e = \pi \cdot s_0 \cdot \sqrt{\frac{E_f \cdot t_f}{8 \cdot G_f}} \tag{6.2}$$

The fracture energy can also be written directly as a function of the mean compressive- or tensile strength of the concrete. This is due to the bond strength itself, τ_{b1}, which depends on the concrete strength and the fracture energy which correlates only with the strength of the adhesives and the concrete. This is regardless of the relationship between slip and strength, assuming a proper application of the external FRP. The fracture energy can now be written as:

$$G_f = k_b^2 \cdot k^2 \cdot f_{cm}^{\frac{2}{3}} \tag{6.3}$$

Where k_b is a shape factor

$$k_b = \sqrt{\frac{2 - \frac{b_f}{b}}{1 + \frac{b_f}{b}}} \tag{6.4}$$

b_f and b is the width of the FRP plate and the width of the concrete, respectively. k is a coefficient accounting for the assumed value of the ultimate slip, $s_0 = 0.025$, and varies for mean and characteristic values. Combining 6.2 and 6.3 the effective length can be written as:

$$l_e = \frac{\pi}{k_b} \cdot \sqrt{\frac{E_f \cdot t_f}{8 \cdot f_{cm}^{\frac{2}{3}}}} \tag{6.5}$$

For mean value with $k = k_m = 0.25$

$$l_e = 1.5 \cdot \frac{\pi}{k_b} \cdot \sqrt{\frac{E_f \cdot t_f}{8 \cdot f_{cm}^{\frac{2}{3}}}} \tag{6.6}$$

For characteristic value (5%) with $k = k_k = 0.17$

6.1.1 Debonding at End Anchorage Zone

The definitions in the previous section lay the basis for the simplified method in Eurocode 1992 1-1 for calculation of the anchorage capacity [18]. Verifications must be done by evaluating issues related to peeling-off and cover separation. Peeling-off can be controlled by checking the reinforcement's ends as in a bond-test. This will ensure that the capacity in the anchorage is sufficient depending on the bond length. The cover-separation is treated in section 6.3.3 [18]. To be able to verify the issues the ultimate strength of the bond must be known.

The maximum tensile stress f_{fb} and the maximum tensile force F_{fb} obtained in the fiber defines the capacity of the anchorage and is given as:

$$f_{fb}(l_b) = \beta_l(l_b) \cdot \sqrt{\frac{2E_f \cdot G_f}{t_f}} \tag{6.7}$$

$$F_{fb}(l_b) = \beta_l(l_b) \cdot b_f \cdot \sqrt{2E_f \cdot t_f \cdot G_f} \tag{6.8}$$

The beta factor depends on the bonded length.

$$\beta_1 = \begin{cases} \frac{l_b}{l_e} \cdot (2 - \frac{l_b}{l_e}) < 1 & \text{for } l_b < l_e \\ 1 & \text{for } l_b > l_e \end{cases} \tag{6.9}$$

Rewritten with the earlier definition of fracture energy eq.(6.3), the mean debonding strength and the characteristic debonding strength is given respectively:

$$f_{fbm} = k_m \cdot k_b \cdot \beta_l \sqrt{\frac{2E_f}{t_f} f_{cm}^{\frac{2}{3}}} \tag{6.10}$$

$$f_{fbk} = \frac{k_k}{\gamma_{fb}} \cdot k_b \cdot \beta_l \sqrt{\frac{2E_f}{t_f} f_{cm}^{\frac{2}{3}}} \tag{6.11}$$

The design bonding strength can be achieved by dividing k_k with the safety factor γ_{fb}.

6.1.2 Debonding at Intermediate Cracks

Intermediate debonding is the same process as end debonding, just located another place. Therefore, the maximum strain in the fiber can be used to control this failure as well in a simplified approach. The strain in the FRP can become larger at the intermediate part of the beam compared to the end. This is due to the unfavorable local mechanism at the end of the bond. The maximum strength found in section 6.1.1 for end debonding must therefore be corrected by a factor, k_{cr}. The requirement for the ultimate strength is now given as:

$$f_{fbm,IC} = k_{cr,m} \cdot f_{fbm} \tag{6.12}$$

$$f_{fbk,IC} = k_{cr,k} \cdot f_{fbk} \tag{6.13}$$

$$f_{fbd,IC} = \frac{k_{cr,k}}{\gamma_{fb}} \cdot f_{fbk} \tag{6.14}$$

Where $k_{cr,m} = 2.1$ and $k_{cr,k} = 1.8$. The subnote IC refers to intermediate cracks. By using the safety-factor we obtain the design value of the bond strength. This value limits the ultimate bending moment.

6.2 Moment Capacity in ULS

Concrete beams subjected to bending can be strengthened by FRP reinforcement at the tension zone with fibers in the direction of the tension force resultant. This increases its flexural capacity, but the increase in stiffness may reduce the deflection of the beam. The FRP reinforcement may therefore reduce the ductility of the concrete beam and lead to a brittle failure mode. Furthermore, the beam commonly achieves more but smaller cracks. Typically the failure mode due to bending moment emerges as debonding of the FRP reinforcement occurring after steel yielding. Debonding modes that happen in beams subjected to bending are intermediate crack debonding and end debonding. Other flexural failure modes that may occur are steel yielding followed by either concrete crushing or FRP rupture and concrete crushing before steel yielding [18]. Such failure modes need to be controlled according to Eurocode 1992-1-1 [44].

To analyze the ultimate limit state of beams under these conditions, it is required that the issue of debonding is given particular attention and that the contribution of the FRP reinforcement is properly considered. Besides, several assumptions need to be taken into account, mentioned in section 3.1.1.

The analysis is based on the assumption that plane sections remain plane and strain compatibility with full composite action, requiring that at each cross-section of the beam the applied load is lower than the designed resistance. Furthermore, the analysis is based on horizontal and flexural equilibrium. For a full analysis of the ultimate limit state of the beam, shear resistance should also be considered, further discussed in section 6.3.

6.2.1 Intermediate Crack Debonding

The concept of intermediate crack debonding was discussed in section 3.3.3. The bond behavior is based on the theory of shear-stress slip relation. Fib Bulletin 90 [18] discusses two different methods for ULS calculations of intermediate crack debonding; simplified and accurate. The simplified method is conservative and based on ultimate strain state, while the accurate method is based on force differences at intermediate crack elements.

Simplified method

This method is more conservative since strains are typically lower than assumed by this method. It assumes that end debonding failure is designed to not occur. It is based on the stress of the FRP, eq. 6.12, 6.13 and 6.14 found in chapter 6.1.2, simplifying the analysis to a flexural load-bearing capacity.

Applying the simplified method, the stress capacity of the FRP at ULS is the minimum of the bond strength in intermediate crack debonding $f_{fbd,IC}$ found in section 6.1.2 and the design tensile strength f_{fd}.

More accurate method

This method is based on the change of the tensile force between cracks, which must be lower than the bond resistance. Each concrete element between cracks in the structure should be considered, and the transmission of bond stress should be used to estimate the ultimate limit state values. In this way, the necessary shear force the FRP needs to transfer to the concrete element can be obtained. The resistance of stress change in the FRP between two cracks is correlated to the bond-slip law, the distance between cracks and the stress level of the FRP.

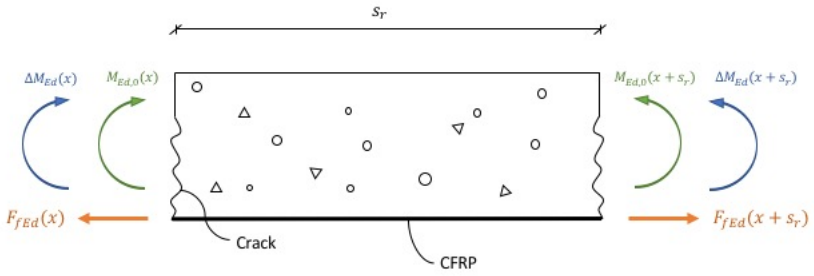

Figure 6.2: Illustration of tensile force F_{fEd} in the CFRP

The change in the design FRP bond force over a element between two cracks is predicted by:

$$\Delta F_{fEd} = F_{fEd}(x + s_r) - F_{fEd}(x) \tag{6.15}$$

Where s_r is the average crack spacing, which could be found by a detailed analysis, or with the simpler estimation; $s_r = 1,5 \cdot l_{e,0}$. $l_{e,0}$ is the transfer length of

the reinforcing steel, which can be found by the following analysis.

$$l_{e,0} = \frac{M_{cr}}{z_s \cdot F_{bsm}} \tag{6.16}$$

Where M_{cr} is the cracking moment, z_s= 0,85h and F_{bsm} is the bond force per length.

$$M_{cr} = \kappa_{fl} \cdot f_{ctm} \cdot W_{c,0} \tag{6.17}$$

The factor κ_{fl} is a constant depending on the bond conditions of the longitudinal rebars. F_{bsm} can be obtained by:

$$F_{bsm} = \sum_{i=1}^{n} n_{s,i} \pi \phi_{s,i} \cdot f_{bsm} \tag{6.18}$$

Where $n_{s,i}$ is the number of steel rebars, $\phi_{s,i}$ is the bar-diameter and f_{bsm} is the mean bond stress of the reinforcing steel, depending on compressive strength and bond conditions.

The FRP force, $F_{fEd}(x)$, can be found by the acting bending moment and geometry of the structure and depends on the tensile strength of the reinforcing steel.

$$F_{fEd}(x) = \begin{cases} \frac{\Delta M_{Ed}(x)}{z_m} \cdot \frac{d_f E_f A_f}{d_f E_f A_f + d_s E_s A_s} & \text{for } \sigma_s(x) < f_{yd} \\ \frac{M_{Ed}(x)}{z_m} - A_s \cdot f_{yd} & \text{for } \sigma_s(x) = f_{yd} \end{cases} \tag{6.19}$$

ΔM_{Ed} is defined as the additional bending moment after application of CFRP, such that $\Delta M_{Ed} = M_{Ed} - M_{Ed,0}$.

The resistance of change in tensile forces in the FRP is given as:

$$\Delta F_{fRd} = \frac{\Delta F_{fk,B} + \Delta F_{fk,F} + \Delta F_{fk,C}}{\gamma_{fb}} \tag{6.20}$$

$\Delta F_{fk,B}$ represents the transmission bond strength due to the adhesive of the FRP. $\Delta F_{fk,F}$ is the bond strength due to the friction in the intermediate layer, while $\Delta F_{fk,C}$ is the bond strength due to the curvature of the element between intermediate cracks.

Assuming the resistance is a sum of these three components, one can estimate the design bond resistance force which may limit the moment capacity. The verification of the bond transmission strength can be obtained by two different

approaches.

The most accurate method applies detailed calculation methods to obtain $\Delta F_{fk,B}$, $\Delta F_{fk,F}$ and $\Delta F_{fk,C}$. Change in bond strength due to the adhesive can be found by using a bilinear approach of the bond law, and depends on the width and thickness of FRP, tensile load at the lower stressed crack, ultimate strength of FRP strip, maximum shear bond stress and ultimate slip. $\Delta F_{fk,F}$ depends on bond friction strength, stiffness of the FRP, ultimate slip, thickness and width of the FRP, crack spacing and tensile force of the FRP. Change in bond strength due to member curvature is correlated to characteristics such as crack spacing, the strain of concrete, width and thickness of FRP and strain of FRP at the lower stressed crack. The weakness with this method is its dependence on the tensile load of the FRP at the stressed crack, and as a consequence the superposition principle is invalid. This method will not be further discussed in this assignment.

As an alternative to the detailed method, one can use a more simple and conservative method. In this analysis, it is assumed that the strain of steel reinforcement is evaluated and that the strain of the FRP is not larger than 0.01 or f_{bd}/E_f at any point in the structure. Elements between cracks start at the crack at the location of the maximum moment and end at the crack closest to the position of the zero moment. The simplified method states that:

$$\Delta F_{fk,B} = 2.3 \cdot \tau_{b1k}\sqrt{s_r} \cdot b_f \tag{6.21}$$

$$\Delta F_{fk,F} = 0.1 \cdot \tau_{bFk} \cdot s_r^{4/3} \cdot b_f \tag{6.22}$$

$$\Delta F_{fk,C} = \frac{\kappa_h}{h} \cdot s_r^{1/3} \cdot b_f \tag{6.23}$$

Whereas τ_{b1k} is the characteristic maximum shear bond stress and τ_{bFk} is the characteristic bond friction strength. The values 1.3 and 0.1 can be replaced with 1.85 and 0.095 to achieve mean values, respectively. $\kappa_h = 2000$ for reinforced concrete and $\kappa_h = 0$ for prestressed reinforced concrete since the curvature is assumed to be small.

6.3 Shear Capacity in ULS

6.3.1 General Procedure

Shear strengthening is achieved by applying FRP systems externally to the member as mentioned briefly in section 3.1. Eurocode 1992-1-1 [44] is still used for calculations regarding shear resistance of FRP strengthened reinforced concrete beams. This also includes all practical detailing rules. Additional requirements are needed if the members also have adhesively bonded longitudinal reinforcement as shown later.

When applying FRP, the members are often reinforced concrete members meaning that all the internal steel is already placed in the member. The strengths must be verified due to new loads or detoration and eventual deviations from the capacity must be covered by additional external reinforcement. It is also important to do a shear resistance analysis after attachment of flexural bonding. This is to prevent that shear failure is the dominant failure mode and if so, this must be avoided by applying additional shear reinforcement. If it is a need for external reinforcement, the contribution of shear strength from the fibers is added to the strength of the steel shear-reinforcement:

$$V_{Rd} = V_{Rd,s} + V_{Rd,f} \tag{6.24}$$

Following the procedure in Eurocode 1992-1-1 [44], the first calculation should be regarding the requirement of design shear reinforcement. As long as the acting shear force V_{Ed} is lower than the shear resistance $V_{Rd,c}$ after strengthening there is no need for design shear reinforcement in addition to the minimum demand.

In the case of calculating $V_{Rd,c}$ for a member with FRP strengthening in the longitudinal direction, the area of FRP shall not be included in the area of tensile reinforcement A_{sl}.

Cases where the internal shear steel reinforcement is not enough to cover the minimum demand, FRP material must be applied to achieve adequate shear reinforcement. Besides, there is a requirement given in Eurocode 1992-1-1 [44] that states that half the minimum reinforcement should be internal stirrups and not other rebars. If this does not apply for the member, FRP must be applied to fulfill the demand.

If the concrete member needs externally bonded FRP, controls must be done concerning insufficient shear capacity and in regards to flexural debonding. The latter only applies for members having flexural FRP strengthening while verification in relation to insufficient shear capacity regards all cases [18]. Insufficient shear capacity indicates that shear cracks are appearing in the member and can lead to brittle failure.

6.3.2 Shear Strengthening in Relation to Insufficient Capacity

The contribution from the FRP systems to the total shear strength is treated similarly as the steel reinforcement. $V_{Rd,f}$ is the design shear force taken by FRP and gives a contribution to the total V_{Rd} for the member. The shear force taken by the FRP is given as:

$$V_{Rd,f} = \frac{A_{fw}}{s_f} h_f \cdot f_{fwd} \cdot (\cot\theta + \cot\alpha)\sin\alpha \tag{6.25}$$

Where

- A_{fw} is the area of the externally bonded reinforcement measured perpendicular to the direction of the fibers.
- s_f is the spacing of strips parallel to the member's length axis
- h_f is the height of FRP crossing the shear crack
- α is the angle between fibers and the member's axis perpendicular to the shear force
- f_{fwd} is the design value of the average stress on the FRP intersected by the shear crack.
- θ is the inclination of the strut in the truss model.

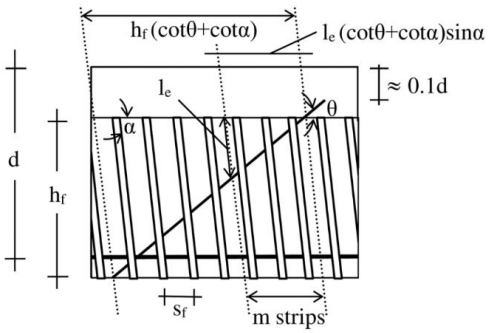

Figure 6.3: FRP shear reinforcement [18]

The values of the parameters strongly depend on the details of the FRP system. Important factors are the degree of bonded area, the number of FRP layers (as many layers will reduce the effective thickness) and the configuration of the system. In section 3.1, three configurations of shear reinforcement were introduced; complete wrap, U-wrap and side-wrap. The choice of configuration has a huge impact on the design value of the average stress.

For a closed FRP configuration, the design value of the stress becomes the highest, hence this is the most favorable. Calculations of the system's strength f_{fwd} is taking into account the non-uniform stress distribution in the FRP over a shear crack as well as bending of fibers around the corners of the cross-section by introducing the factor k_r. A long-term factor, a_t, is also accounted for.

$$f_{fwd} = f_{fwd,c} = k_r \cdot a_t \cdot f_{fd} \tag{6.26}$$

The U-wrap configuration covers three sides and will not provide the same strength as the closed system, $f_{wd,c}$. This is due to that the bond strength, f_{fbwb}, is often lower and thus will be the design strength for the fiber. The bond strength will strongly vary with the bond length. To verify that the bond length is $\geq l_e$ the conditions in equation (6.27) must be satisfied.

$$h_f / \sin\alpha \geq l_e \text{ and } l_e \geq s_f / (\cot\theta + \cot\alpha) \sin\alpha < h_f / \sin\alpha \tag{6.27}$$

If all the external shear reinforcements have $l_b \geq l_e$, the bond strength is equal to f_{fwd} determined by the bond-slip law, where the characteristic bond strength

is obtained by equation (6.11).

$$f_{fbwd} = \frac{f_{fbk}}{\gamma_{fb}} \tag{6.28}$$

If the bond length in some or all of the fibers is below the effective bond length the strength is reduced. How much the strength is reduced depends on the spacing (s_f), the inclination of the crack (θ) and fibers (α), number of strips in total covering the crack (n) and number of strips with a low bond length (m).

If just some of the strips have a smaller length than l_e, the second condition in equation (6.27) will not be satisfied and the bond strength is obtained by equation (6.29).

$$f_{fbwd} = [1 - (1 - \frac{2ms_f}{3l_e})\frac{m}{n}]\frac{f_{fbk}}{\gamma_f} \tag{6.29}$$

Further, if all of the strips have a smaller length than l_e, none of the conditions in equation (6.27) will be satisfied and the bond strength is obtained by equation (6.30).

$$f_{fbwd} = \frac{2}{3}\frac{(ns_f)/(\cot\theta + \cot\alpha)\sin\alpha}{l_e}\frac{f_{fbk}}{\gamma_f} \tag{6.30}$$

Though, with the right anchorage in the compression zone, a three-sided configuration can reach the strength of a closed system. The anchoring system is given an effectiveness factor through testing, k_a, and can provide up to 90% of the strength of a closed system.

$$f_{fwd} = k_a \cdot f_{fwd,c} \tag{6.31}$$

6.3.3 Shear Strengthening in Relation to Flexural Debonding

For concrete members where shear reinforcement is not required based on shear capacity, shear control must still be performed. The flexural FRP might fail due to high shear forces providing cracks in the concrete near the end or in the intermediate part leading to debonding, see section 3.3.3. These problems can be solved by attaching external shear reinforcement and therefore some additional requirements must be controlled.

A problem that may occur is a detachment of the concrete cover near the supports when using flexural FRP strengthening as explained in 3.3.3. To avoid a failure in the concrete due to tensile stresses, one can attach transverse shear strips at the end of the flexural FRP. This must be done if the acting shear force, V_{Ed}, is higher than the modified shear strength, $V_{Rd,c,fe}$.

$$V_{Rs,c,fe} = 0,75[1 + 19,6 \cdot \frac{(100\rho_s)^{0.15}}{a_f}]V_{Rd,c} \tag{6.32}$$

This strength gives an adjusted shear capacity accounting for the distance of the longitudinal strip from the support and the amount of steel reinforcement.

A simple method to design the strap conservatively is to require that it sustains the maximum anchorage force possible in the longitudinal strip:

$$F_{fwEd} = f_{fbd} \cdot b_f \cdot t_f \cdot \tan\theta \tag{6.33}$$

Another method is to design it by taking the difference between the acting shear force V_{Ed} and $V_{Rd,c,fe}$. When applying external strips for this case it will count as shear reinforcement when calculating shear capacity by equation (6.25) [18].

External straps along the member are also needed to prevent intermediate debonding due to offset crack edges. If the shear force provides high stresses in the ties and struts these cracks may occur. A limit is made based on a ratio of the acting shear, the shear resistance and the tension stress in the existing links.

$$\frac{V_{Ed} \cdot \sigma_{sw}}{V_{rd,max}} \leq \begin{cases} 75 \text{ MPa} & \text{for ribbed links} \\ 25 \text{ MPa} & \text{for smooth links} \end{cases} \tag{6.34}$$

Where the stress in the stirrups is given as:

$$\sigma_{sw} = \sqrt{\frac{V_{Ed}}{\frac{A_{sw}}{s} z \cdot (cot\theta + cot\alpha) sin\alpha}} \tag{6.35}$$

Additional shear straps will ensure the tensile resistance of the longitudinal reinforcement if the limit is exceeded. These are designed for the value:

$$V_{fEd} = max \begin{cases} \frac{E_f \cdot A_f}{E_f \cdot A_f + E_s \cdot A_s} V_{Ed} \\ V_{Ed} - V_{Rd,max} \end{cases} \tag{6.36}$$

Regardless of the problems above, all members strengthened with adhesively bonded longitudinal reinforcement need to have shear straps if the concrete shear-compression capacity is critical. It occurs when the acting shear force exceeds the given limit:

$$V_{Ed} \leq 0,33 \cdot f_{ck}^{\frac{2}{3}} \cdot b_w \cdot d_s \tag{6.37}$$

If needed, the shear reinforcement is designed in the same way as above (6.36).

6.4 CFRP Strengthening on ASR Damaged Concrete

Strengthening structures with fiber reinforcement seem like a promising solution for ASR-damaged concrete. An external composite material would suppress the stresses and might be able to limit the damage. CFRP, with its great properties and the strength-weight ratio, seems like a good choice for strengthening and extending the service life for ASR-damaged concrete. Some researches report a high capability to do so, but contradicting results have also been reported. What can be a challenge is a need for a good adherent with the concrete.

The existing design rules discussed earlier do not apply for concrete with severe large cracks and damage. This is due to the fact that the theory is based on an assumption of no severe damage and only small cracks in the structure. In circumstances with lager cracks, one must execute extraordinary design calculations. Regarding the alkali-silica reaction, a lot of stresses are induced and cracks will occur. The effect of an open crack due to further ASR reaction is hard to characterize and the influence on the fiber's strength capacity is difficult to determine. Besides, the question arises of whether FRP strengthening can prevent the expansion by inducing a contradicting pressure on the concrete [45].

Externally Bonded CFRP at Damaged RC Beams

Elgeseter Bridge is externally reinforced with CFRP at areas with cracks up to 6 mm. As the beams are u-wrapped with CFRP, the condition of the beams underneath are unknown. This might be a factor of uncertainty regarding the beams' capacity in these sections. Considering the typically brittle failure mode of beams with externally bonded CFRP, it is crucial to know that the applied CFRP prevents failure and if so, how the structure responds. Large cracks contribute to high local stresses in the carbon fibers and high shear stresses in the adhesive interface. This may lead to local debonding and following, a propagation of the crack leading to failure.

An experimental and theoretical analysis conducted by M. I. Kabir et al. [46] studied three different beams that were loaded up to its ultimate strength and then repaired using CFRP. The results showed that two of the beams exceeded its original capacity, while the third only gained 54% of original capacity after strengthening. All of the beams' ductility was found to be less than the control beams and had brittle failure modes. The poor performance of the third beam was believed to be a consequence of its pre-existing large deformation and severely large tension cracks. Another discussed aspect is the possibility of existing yielding in the rebars that led to no contribution in resistance and higher forces in the CFRP. It was discussed if a greater amount of CFRP would contribute to a higher capacity. The results from this analysis show that the severity of the damage is crucial to determine the capacity of the structure. The reduction in capacity could be catastrophic and the applied CFRP would only contribute to false security.

Experimental analysis on shear strengthened pre-cracked beams by F. Yu et al. [47] studied the effects of pre-cracked degree. The study included 18 shear strengthened beams with different shear span and degree of damage. It was con-

cluded that the debonding area decreased with decreasing pre-cracked degrees. In addition, it was found that beams with a high pre-cracked degree (80%) had a lower increase of capacity than specimens with a low (40%) or no pre-cracked degree. Following, the beams with a low pre-cracked degree (40%) had a comparable increase in capacity compared to the non-cracked specimens. This led to the conclusion that especially in high pre-cracked beams, the degree of pre-cracking had a great effect on the shear capacity of the strengthened beams.

A third study by O. Bjenddou et al. analyzed strengthened beams with damage level from 0% to 100% found that all beams exceeded original capacity after strengthening. Whereas the beam with no initial damage increased its capacity with 87% and the beam with 100% initial damage increased its capacity with 44%. It was also noticed that the mechanical behavior of all repaired beams changed from elastoplastic to elastic, and all failures were brittle and sudden. The conclusion from this study was that beams in all degrees of damage increased its moment capacity when strengthened with CFRP [48].

The conflicting results from the presented analyses demonstrate the uncertainties with this subject. They all indicate that the capacity of the repaired beams decreases when the damage level is high compared to undamaged beams, but the results vary. An aspect of this might be a variation of deflection in the original beam, yielding in reinforcement and sizes of cracks.

Externally Bonded CFRP at RC Beams Subjected to ASR

There are mainly two favorable effects on the ASR damage concrete that is introduced by CFRP. The external material will isolate the concrete and prevents a moist environment which is necessary for developing ASR. Also, it will reduce the active stresses caused by ASR by creating a confinement action.

In addition to the formation of cracks, the concrete will continue to expand. A study done by Diab et al. shows that the degree of expansion in the concrete has a high impact on the resulting strengthening effect [45]. The magnitude of the expansion at the time of application is more important than the mechanical properties of the composite material. At the early stages of the expansion, the effect of CFRP gives a considerable impact on the expansion. The same research project was done by Diab et. Al shows that concrete cores in an ASR-friendly environment expanded 0.282% between the first and second month, while a core with CFRP only expanded in the range of one-tenth of the original one, approximately 0.024% under the same conditions. Regarding the specimen strengthened at later ages, the CFRP was considerably less effective since at a late age the concrete seems to have reached a stable maximum in expansion. The study shows that applying the CFRP after one month reduces the expansion with 31.4% while applying it after two months it is only reduced with 4.1% [45].

An investigation on the bond behavior done by Haddad and Al-Sayed [3] supports the theory that ASR-damage reduces the strength of CFRP strengthening. Concrete blocks with ASR-damage were tested with CFRP and compared to non-reactive blocks with the same CFRP solution. The research project re-

ported that the ultimate bond force of the CFRP was limited to almost 69% as ASR propagated. They also found clear connections between the reduction in the ultimate bond force and the bond width, bond length, and ASR-treatment level.

It is therefore claimed to be a high level of risk connected to the external reinforcement of ASR-damaged concrete. The main reason to believe that this is somewhat dangerous is the lack of data regarding the effects on the bond behavior to ASR-damaged concrete.

The conclusions made by Haddad and Al-Sayed is stating that the use of CFRP on ASR-damaged concrete loses its potential when applied on severely damaged concrete.

This is not enough investigation to place any conclusion about whether CFRP is a suitable reinforcement method or not. On the other hand, it enlightens the issues regarding the subject. This will be relevant further in the report regarding the use of CFRP on an ASR-damaged concrete bridge.

The applied CFRP on Elgeseter Bridge is not designed by the proposed new annex in Eurocode as it was applied in 2014 and the calculations were based on publication 36 by The Norwegian Concrete Association from 2006. Since then, the design rules have evolved. Thus, existing design rules are not recommended to use when the structure is severely damaged. The severity of damage in the reinforced beams at Elgeseter Bridge is today uncertain. It may be more or bigger cracks beneath the CFRP compared to when it was applied, and it is unknown if there is yielding in the reinforcement and if it is contributing to the load distribution. A method to examine the condition of the beams may be to use infrared thermography to detect cracks under the CFRP [49]. It is necessary to investigate the capacity of the beams when including all new information of the forces acting on the bridge, especially considering the forces due to ASR. Furthermore, it is important to consider the possible effects due to the large cracks and the ASR effects on the beams.

Chapter 7

Models in Abaqus/CEA

Abaqus/CAE, "Complete Abaqus Environment", is a finite element analysis software suited for modeling, analyzing, and visualizing complex simulations. Abaqus/CAE is a user-friendly software with many possibilities to design properties of features such as geometry and material, as well as defining the desired analysis of the structure. The software consists of different modules where each module represents a logical aspect of the modeling process, such as defining material, geometry, mesh, and assembling of different parts. Abaqus/CAE is considered to be well suited for this problem, considering its ability to create materials, assemblies and constraints with desired behaviors.

The scope of using Abaqus/CEA is to simulate the behavior of the alkali-silica reactions in Elgeseter Bridge and its corresponding forces. Self-weight, live load, and other variable loads are not included in this analysis. The initial analysis consists of two different models where only expansion from the ASR is considered to evaluate the reactions in the bridge. The first model is a 3D frame model of the whole bridge consisting of beam and truss elements. The second is a 3D solid model of four spans from axis 6-10. The second model is established to compare the results to the idealized frame model.

When using FEA software, it is important to be aware of the simplifications that are made and its possible effects. Also, it is important to verify the results with other calculations. Abaqus/CEA is an FEA software with many possible approaches to a problem, which requires a high awareness of the choices that are made and its potential outcome.

To find the effects of ASR expansion on the bridge, there are some important aspects to be considered to simulate the true reactions. The models are applied to a variable temperature field to resemble the variations of expansions in the different parts of the bridge according to figure 4.9. The reinforcement is designed without an expansion coefficient, which will simulate the contribution in the concrete from the strain of the reinforcement. To achieve realistic effects, the reinforcement must be modeled as accurately as possible.

There are some limitations in the two different models which makes it difficult to design all properties and aspects similar. The differences are assumed to

have a minimal effect on the results and might explain deviations in results. All material properties and dimensions of the concrete are similar in both models. Furthermore, only a linear elastic analysis is evaluated in this case.

7.1 Model 1: Frame model

The frame model is based on a suggestion from The Norwegian Public Road Administration by H. Johansen to be used in further calculations of the bridge [33]. To take care of the crucial effects of ASR induced expansion, the whole bridge is modeled with all nine spans and four beams. Due to the complexity and size of the model, it is beneficial to make it as a simple frame model. In this way, the running time is less, and it is easier to interpret the results in the post-processing.

The model is built up by 3D beam- and 3D truss-elements representing the concrete and reinforcement, respectively. Using beam elements for the concrete section, the analysis will preserve the classical beam theory in every element. By using a shear flexible element, the Timoshenko Beam Theory is used and not Euler Bernoulli's. This retains Navier's hypothesis claiming that all plane sections remain plane, but not necessarily perpendicular to the neutral axis. This is due to that the shear deformations are accounted for in the Timoshenko Theory and make the beam lesser stiff compared to Euler Bernoulli Theory. The effect is important when the beam elements are defined as thick beams.

The beams and their respective part of the plate are formed as longitudinal elements illustrated in figure 7.1 (a). These are modeled and placed in the T-cross section's center of mass. The elements are given the dimension of the cross-section as shown in figure 7.1 (b).

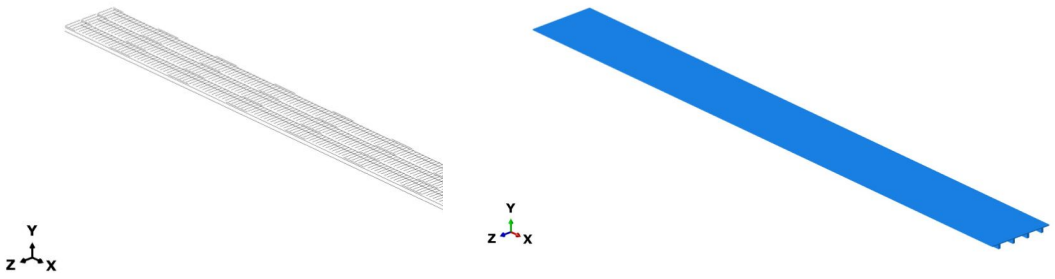

(a) Frame model with elements (b) Frame model with rendered elements

Figure 7.1: Frame model in Abaqus

To make sure that the beams act in a compatible system, transverse beam elements are connecting the longitudinal beams. The marked lines in figure 7.2 shows how the transverse elements lie between the beams and are placed within the plate's thickness. This figure also shows the placement of the reinforcement as dark circles above and below the mass center. The mass center is indicated

with a hollow circle below the flange.

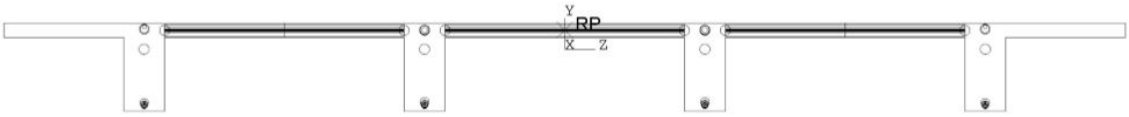

Figure 7.2: Placement of transverse elements and reinforcement

The transverse elements will transfer loads between the beams and are supposed to preserve the effect of the stiff and continuous plate in the bridge. If the inner beam is loaded, the transverse elements will get vertical moments and shear forces, and the vertical load effects are transferred to the adjoined beams as presented in figure 7.3. To have good compliance between the longitudinal elements, as it occurs in reality, the low vertical bending stiffness is preserved by giving the elements a low height equal to the thickness of the plate.

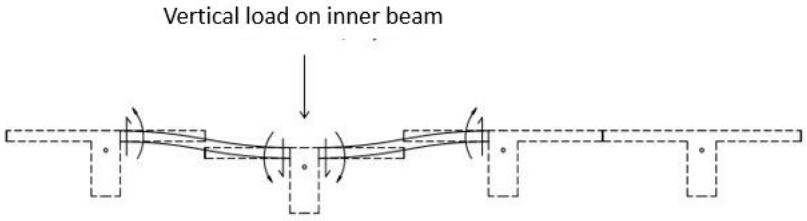

Figure 7.3: Transfer of vertical loads on the inner beam [33]

If the outer beams are given a higher expansion than the inner beams the transverse elements will get horizontal shear forces illustrated in figure 7.3. This will preserve the effect that the inner beams are set in tension trying to follow the outer beams. Providing the transverse elements a considerably great width, a large horizontal flexural- and shear stiffness is preserved. In this way, the longitudinal deformations are modeled realistically.

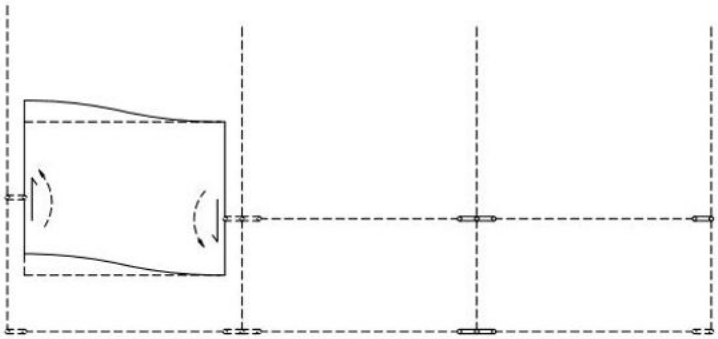

Figure 7.4: Load effects on transverse element when different expansion occur in the beams [33]

7.1.1 Elements and Mesh

The 3D-frame model is made in Abaqus, where the beams are made as a longitudinal beam element in the form of wire elements. In each span, the beam consists of 1.25 meter long elements, such that span 1 and 9 consists of 17 elements with a total length of 21.25 m, and the rest of the spans have 18 elements providing a length of 22.5 m. Some of the elements are divided into smaller parts to preserve some important effects. This occurs in the area of zero moment sections, which is placed four meters on each side of the supports and spans over 0.5 m. These elements have a size of 0.1 m. Also, it is chosen to separate the beam into support areas and span areas. The support areas are set to 4 meters on each side of the support, such that the point of zero moments is in the transition between a positive and a negative moment.

The mesh must coincide with the drawn elements and is set to 1.25 meters and is adapting to the places where the elements are smaller. The elements used in the mesh are beam elements B31 which is a 2-node linear beam in space with shear flexibility.

Initially, the transverse elements are given rectangular cross-sections with a thickness of 280 mm and a width of 1.25 m, such that the entire surface of the bridge is covered by these elements. Since the transverse elements need to preserve the bridge's bending stiffness and the shear stiffness some adjustment may be done to the cross-section. This can be calibrated with the solid model which has modeled the continuous plate directly. The transverse elements are connected in the mass center of each longitudinal beam and have a length of 4.7 meters.

The reinforcement is included in the analysis and is modeled as wire elements. These wire elements are drawn and meshed as truss elements. Compared to beam elements, they transmit only axial force. The element type is called T32D and is a 2-node linear 3D truss. The total reinforcement in different sections is calculated as one area for the upper reinforcement and one area for the lower

reinforcement. These properties are given to their representative truss elements.

7.1.2 Constraints

To ensure adequate behavior between the transverse and longitudinal elements, the choice of connection is important. A general multi-point constraint (MPC) is chosen. This is a constraint that allows the motion of the slave node, or a region of slave nodes, to be connected to the motion of a single point being a master node. The master node is in the center of mass in the longitudinal beam and the slave node(s) is at the end of the transverse beam elements as shown in figure 7.5. This constraint will preserve the important effects of the transverse elements and represent the connection between the beams with approximately the right stiffness.

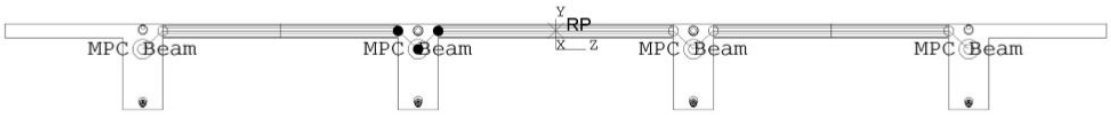

Figure 7.5: MPC-constraint between beam elements

The bridge is fully constrained on the south end and simply supported in the north end, allowing the bridge to move in the longitudinal direction. Also, a boundary condition is set at the point of each support. Even though the columns in axis 2-8 are monolithically connected to the beams, it is shown that they deform as the bridge is expanding due to ASR-loading. The column rows are therefore modeled as roller supports, illustrated in figure 7.6.

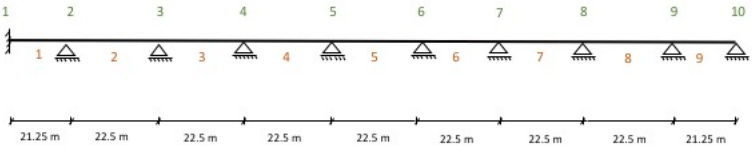

Figure 7.6: Bondary conditions in Abaqus

The boundary conditions are defined in the initial step in the model. This means that the conditions are set before any loading is applied.

To maintain a compatible relationship between the concrete and the steel, a multi-point connection is used. Instead of using a beam type connection as between the longitudinal and transverse beam elements, a tie connection is applied. This ensures that all active degrees of freedom are equal at each slave node and the control point. The control point is the master node in the beam's mass center. In this way, the beam elements contain the master nodes for both the reinforcement and transverse elements. The multi-point constraint is attached in the nodes of each element and it is therefore crucial that the steel and the

concrete elements are meshed equally. The connection is illustrated in figure 7.7.

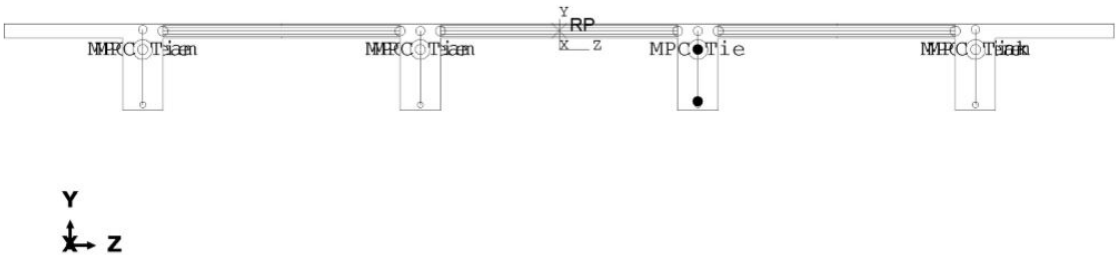

Figure 7.7: MPC-constraint between concrete and steel

7.1.3 Material Properties

Different types of material are defined and assigned to the different parts of the model. The longitudinal beam elements are assigned to a concrete material with the properties in table 7.1. Since ASR- expansion is a long term effect the long term E-modulus is used.

For the transverse elements, the concrete has initially the same properties as in the longitudinal ones, but with a density equal to zero.

The material properties of the reinforcement are presented in table 7.1.

	Concrete	Steel
Young's modulus [MPa]	7766	200 000
Poisson's ratio	0.3	0.3
Density [g/mm^3]	2400	7830
Yield stress [MPa]	12	272
Expansion coefficient	$1 \cdot 10^{-5}$	0

Table 7.1: Material properties in model 1

The yield limit for the steel is defined. This is done in the perfect plastic module in Abaqus. The steel's design yield limit is correlated to a plastic strain of 0.0 ‰. This means that the steel cannot get any higher stress than 272 MPa, and the forces will be rearranged. It is important to notice that even though the stresses are limited to the yielding stress, the strain will continue to increase. To ensure that this is happening, a non-linear geometry is activated in the analysis.

7.1.4 Reinforcement

The amount of reinforcement varies in different parts of the bridge and is, in this case, simplified in a total of twelve different sections in the inner and outer beams:

- Support 1, upper face and lower face
- Support 2-8, upper face and lower face
- Support 9, upper face and lower face
- Support 10, upper face and lower face
- Field 1
- Field 2-8
- Field 9
- Zero moment

The amount of reinforcement is shown in the drawings made by Aas-Jakobsen. Certain modification is done when choosing the active bars:

- The shear reinforcement is not accounted for
- The inclined bars are not included
- Only the reinforcement in the effective flange width has been included when calculating the amount in the upper face
- The anchoring bars of the shear reinforcement is not counted as longitudinal reinforcement
- The distribution reinforcement in the plate is not included

The main reinforcement is listed next to the cross-sectional drawings from Aas-Jakobsen. These amounts are included in the model. The total area has been summed up and is applied as the section area of their respective reinforcement in the model.

The center of mass has been calculated from the placement of the reinforcement in the drawings. Aas-Jakobsen has assumed a cover equal to 55 mm and the shear reinforcement in the beam is mostly ø13. With a longitudinal reinforcement of ø32, the effective depth will be:

$c = 55 + 13 + 32/2 = 84$ mm for the lower and upper reinforcement

Further, a spacing of 67 mm between each bar row is assumed. In Annex B the number of bars, steel area, and eccentricity from the mass center is given for each section.

7.1.5 Loading and Temperature Field

To simulate the ASR loading in Abaqus, predefined temperature fields are used. In the initial step, all four beams are given a temperature field of 0 degrees. Further, a new step is defined where temperature equal to the ASR expansion is set.

The temperature field used is recommended by H. Johansen [33] which is showed in figure 4.9 with a = 0.5 ‰. In Abaqus, the temperature in the mass center is defined in addition to a gradient over the cross-section. This gives the right variation of temperature over the height. Due to limitations in Abaqus regarding beam elements, it is not possible to model linear variations in the transverse directions. Therefore, the temperature is equal over the top flange in each beam. The mistake done is considered to be small since the temperature is right in the

center axis of the beams. A jump in the stresses between the beams is expected as the variation is not linear.

The predefined temperature module is following the relationship between the change in temperature and the expansion coefficient together with the free expansion given as strain.

$\Delta T = \frac{\varepsilon_0}{\alpha_T}$

This results in the following temperatures equal to the assumed linear expansion:

Point	α_T	ε_0	ΔT
Inner beam, top flange	10^{-5}	0.001	$100°C$
Inner beam, bottom	10^{-5}	0.0005	$50°C$
Outer beam, top flange	10^{-5}	0.0015	$150°C$
Outer beam, bottom	10^{-5}	0.001	$100°C$

Table 7.2: Temperatures equal to free expansion

In the beam's mass center the temperature magnitude is imposed. The gradient over the cross-section is $29.2°C$/m and gives the following magnitudes:

Part	Temperature in mass center
Inner beams	$85.28°C$
Outer beams	$135.28°C$

Table 7.3: Temperature in mass center

7.1.6 Modeling of Crack

Large cracks have been observed in the sections of zero moments to the left of support four and the left of support 7 in both of the inner beams and four meters to the right of support 8 on the inner beam facing east. To evaluate the current condition of the bridge, it is desirable to analyze the effects of the existing cracks and to implement this in the model. To do so, locations where the cracks appear is given a modified Young's modulus. In reality, the cracked section behaves differently with no tensile strength in the concrete. This is not possible to model in the frame model since using beam elements limits the possibilities of changing material properties within a section. The modification of the stiffness in these areas is considered as a sufficient approach. The crack areas have a size of 0.5 m, and is located 4.0-4.5 m to the left from support 4 and support 7 and similarly 4.0-4.5 m to the right from support 8.

The modification of Young's modulus must represent the reduction in bending stiffness equivalent to a cracked section. In Appendix D.A the equivalent bending stiffness for the area with reinforcement in stage I and stage II is found. The calculations gave a reduction in the bending stiffness with approximately 75% from stage I to stage II. The same reduction is implemented in Young's modulus going from 7766 MPa to 1941 MPa. This will also affect the axial stiffness, EA,

in the model.

In the cracked section the mass center of the concrete will change due to the stage II assumption. Despite this, the beam elements are still placed in the stage I mass center. This will not be entirely correct since the stress distribution will be different in the stage II section where a non-linear behavior is simulated.

7.1.7 Derivation of Results

Results are obtained by using Probe Values in Abaqus. Probe Values displays the desired results at chosen elements and nodes. When post-processing the model with free expansion, the forces can be obtained directly in each beam. When reinforcement is present in the analysis, the forces from the concrete section and reinforcement needs to be summarized to obtain the total forces and moments in the section, this is visualized in figure 7.8.

$$N = N_c + N_s' + N_s \tag{7.1}$$

Where N_c is the axial force in the concrete and N_s is the lower face reinforcement and N_s' is the upper face reinforcement.

$$V = V_c \tag{7.2}$$

To obtain the total bending moment, the reinforcement forces in the upper and lower face is multiplied with its respective lever arm. If in tension, the lower reinforcement contributes to a positive moment while the upper reinforcement contributes to a negative moment, such that:

$$M = M_c + N_s \cdot e_s - N_s' \cdot e_s' \tag{7.3}$$

Where e_s' and e_s is the eccentricity from the mass center of the concrete for the upper and lower reinforcement, respectively.

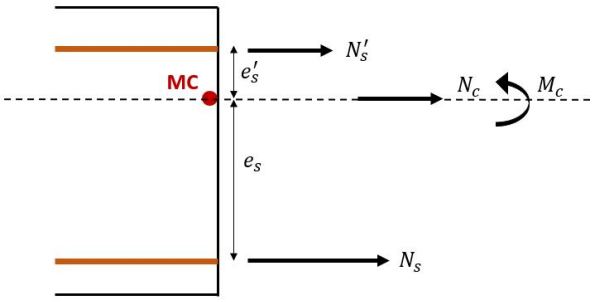

Figure 7.8: Forces obtained in the inner beam

7.2 Model 2: 3D Solid Model

The 3D solid model is designed to be as equivalent as possible to the properties of Elgeseter Bridge in reality. Considering the much higher computational processing with solid elements, it includes only 4 spans with two of the four bridge beams. This simplification is justified by the fact that the third span is representative for the rest of the bridge from axis 7-1, which was also verified in the frame model. Due to the bridge's symmetrical behavior, it is found sufficient to only model two of the beams, due to its symmetrical behavior.

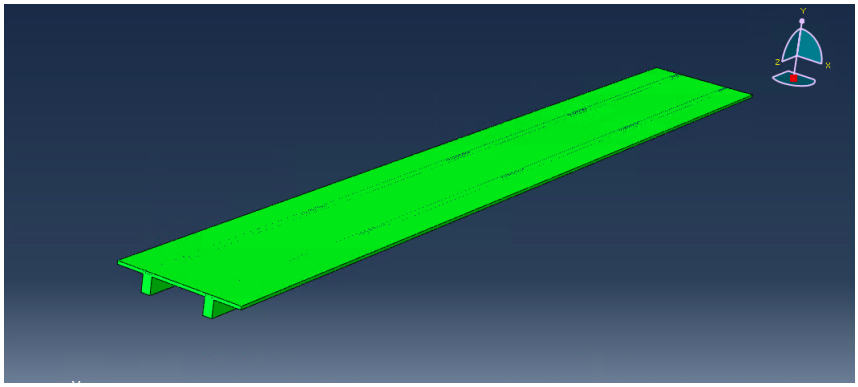

Figure 7.9: Solid model in Abaqus/CEA

Model 2 is modeled with solid elements. Following, Classical Beam Theory is not applied in this model and there is no assumption of plane sections remaining plane. Solid elements maintain local effects and variations in the section. Using solid elements is beneficial when analyzing beams with a high height to length ratio and when properties in the cross-section vary. Solid elements require a much higher computational effort and are often not necessary in large structures with a low height to length ratio. Though, solid elements are favorable when local effects are relevant. When modeling ASR expansion in Elgeseter Bridge, solid elements have benefits such as greater possibilities in the modeling and the opportunity to consider local effects.

The purpose of this second model is to validate the frame model, to see if it is suitable to use in similar situations. To achieve a satisfactory reference model, the model must be as true to reality as possible. Also, it is crucial to understand the differences in the models and which effects this might lead to.

7.2.1 Elements and Mesh

Concrete and steel reinforcements are meshed individually, which makes the mesh finer and the processing of the analysis run faster.

The concrete consists of cubic elements C3D8R, an 8-node linear brick with reduced integration and hourglass control. This is the standard element type in solid 3D computations and is considered to be adequate for this analysis. To

make the transitions of the elements sufficient, the mesh transition is minimized to reduce the mesh distortions. The size of each element is about 150 mm. This is a small element size compared to the dimensions of the bridge but is considered necessary to perceive the axial stresses in the cross-section of the bridge as the bridge deck is thin compared to the beam length.

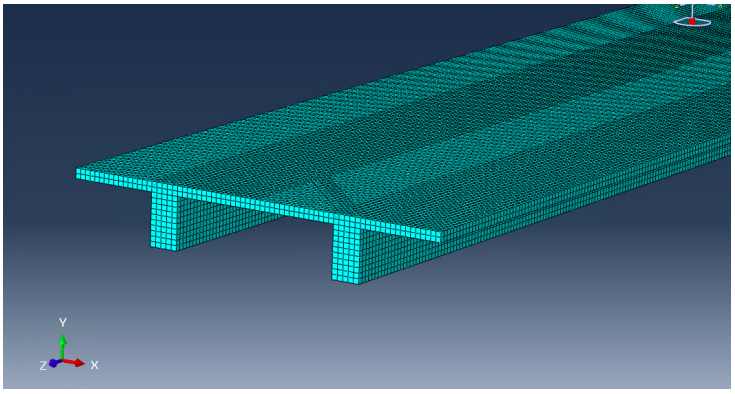

Figure 7.10: Mesh of Solid model

The reinforcement is modeled as wire elements, which is common when modeling reinforcement in Abaqus. Wire elements are idealizing solid 3D elements where the depth and height of the element are considerably small compared to the length. The sections of the reinforcements are chosen to be trusses, which will describe its behavior adequately. The reinforcement is meshed in T3D2, a 2-node linear 3D truss. The approximate size of these elements is 250 mm.

7.2.2 Constraints

Conservative simplifications were made to the boundary conditions that were evaluated to be the most reasonable conditions of the bridge. At the column rows in axis 7-10, the bridge is only restrained in the vertical direction, while at column row 6 the cross-section is restrained in all directions which is equivalent to a fully constrained boundary condition. At the symmetry axis of the bridge, the cross-section is restrained in Ux, Ry and Rz when referring to the axis' in figure 7.9. The columns are evaluated to have low stiffness, which justifies the boundary conditions in axis 7-10 to be reasonable.

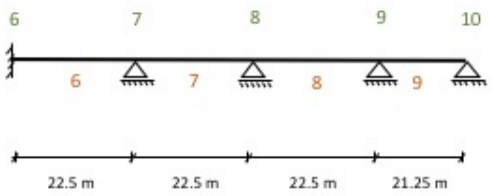

Figure 7.11: Static system in Abaqus, solid model

Embedded region is used to maintain the constraints between the reinforcement and the concrete, where the concrete is the host region.

7.2.3 Materials

The material properties in the solid model are equal to the ones in the frame model, presented in table 7.1. Young's modulus is not reduced due to ASR effects, because there are uncertainties about how much this affects the modulus. Non-linear effects are included in the analysis to take the yield stress into account.

7.2.4 Reinforcement

The reinforcement is modeled as accurately as possible according to the original drawings of Elgeseter Bridge presented in annex A. This is easier to achieve in a solid model compared to the frame model, though it increases the workload. The benefit of modeling the reinforcement as exactly as possible is to achieve a sufficient reference model to compare with the frame model.

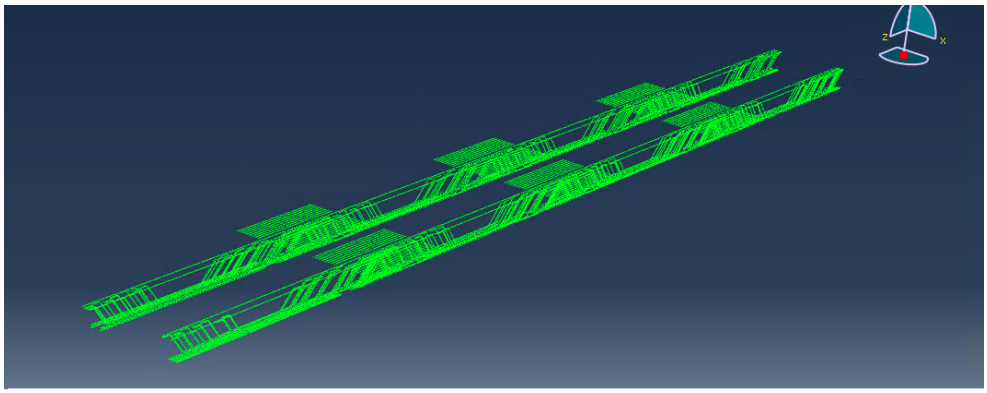

Figure 7.12: Reinforcement in Solid model

The concrete cover is assumed to be 55 mm which places the center of bars 84 mm from the bottom and top when including stirrups. The center distance between each bar is assumed to be 67 mm. All longitudinal bars are included in the analysis to retain the effects of ASR expansion. The distribution reinforcement in the plate and stirrups is not included. In certain sections, there are no section drawings available, and deviations are expected. The length of bars is found by scaling analysis and this might lead to some deviations as well. The deviations are small and the most critical sections have nearly exact positions of the bars.

7.2.5 Loading and Temperature Field

Two temperature fields are used in the solid model to simulate the strain field in the cross-sections due to ASR. The advantages of modeling two scenarios are the fact that there are uncertainties about how the ASR expansion behaves. Examining the bridge's response to different strain models gives a better picture of how the chosen model affects the results. In addition, analyzing one model that is equal to the frame model is important to verify results.

Temperature field 1 is modeled equivalent to the temperature field in the frame model. The outer beam is subjected to a vertically linear varying temperature, whereas the top has a temperature of 150 °C, which will give a strain at 1.5‰ and 100 °C at the bottom. The inner beam varies from 1‰ in the top to 0.5‰ in the bottom. See figure 7.13.

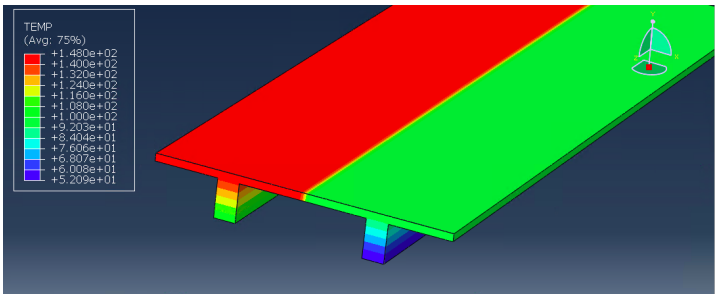

Figure 7.13: Temperature field 1 in Solid model

Temperature field 2 is modeled with a horizontal linear varying field in addition to the vertical one. The strain in the center axis of the beams is equal to the ones in temperature field 1. As a consequence, the top of the beam has a field varying from 1.75‰ to 1.25‰. See figure 7.14 illustrating temperature field 2. Creating this strain field in the frame model is not possible in Abaqus, due to limits using beam elements.

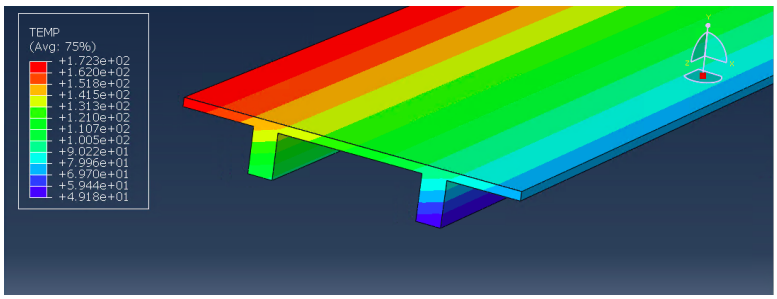

Figure 7.14: Temperature field 2 in Solid model

The temperature fields are defined with Analytical Fields in Abaqus, and the desired parts are subjected to the fields in Predefined Fields at a step. Temperature field 1 is modeled by two analytical fields depending on the vertical axis,

whereas each beam is subjected to one field. Temperature field 2 is modeled with one analytical field depending on the vertical and horizontal axis.

Temperature Field 1 - Outer Beam

$$T = 150 - (50/1710) \cdot y \tag{7.4}$$

Temperature Field 1 - Inner Beam

$$T = 100 - (50/1710) \cdot y \tag{7.5}$$

Temperature Field 2

$$T = 175 - (50/5500) \cdot x - (50/1710) \cdot y \tag{7.6}$$

Where the origin of the function (where x=y=0) is at the top of the outer beam and z is the longitudinal axis of the beam.

To evaluate the effects of the temperature change, the temperature in the initial step is 0°C, and increases over time to the final result as described. As the reinforcement does not have an expansion coefficient, only the concrete will expand and all effects from the reinforcement are retained.

7.2.6 Modeling of Crack

To simulate the condition of the bridge as of today, a field of 0.5 meters have a reduced Young's Modulus in the web. Young's modulus in the web is 78 MPa, whereas the flanges have its original long-term modulus of 7766 MPa. Other than the reduced Young's modulus, the properties of the cracked section are identical to the rest of the bridge, see table 7.1. The field is placed at the location of a large crack in span 8, 4-4.5 meters from column row 8 at the inner beam. Compared to the frame model, the crack is modeled differently due to the higher possibilities by using solid 3D-elements. It is believed that reducing Young's modulus in only the crack zone of the section would give more accurate results and would be a good approach to the non-linearity of the problem.

7.2.7 Derivation of Results

Results of stresses and displacement are derived by Field and History Outputs. Field Output Requests visualize expansion and stress by field maps.

To obtain forces and bending moments in the bridge, Free Body Cut (FBC) has been used. FBC can derive resultants and components of forces and moments in chosen sections. Sections are accessed by View Cut throughout the model. As FBC only shows components of the total section in its respective concrete mass center, the forces are required to be decomposed to obtain the forces in each of the two bridge beams. Axial forces are decomposed in two equal axial forces at each beam's mass center (N). Similarly, the bending moments about the transverse horizontal axis (M_y) and vertical shear forces (V_z) are decomposed into equal components. The bending moment about the vertical axis (M_z) is decomposed in two force resultants at each beam's mass center which contributes

to the axial forces.

As a consequence of not being able to obtain resulting forces in each beam directly by FBC, the model is not suitable to analyze the different bending moment and vertical shear forces in each beam. Some deviations may occur when they are decomposed equally. By treating this at the start of the modeling, obtaining forces in each beam separately would be possible. This should be considered earlier in the process for similar cases. Although, deviations are expected to be small when both beams have approximately the same stiffness and are only subjected to ASR loads. In analyses where the inner beam has a simulated crack, it might be larger deviations and results need to be verified with the frame model.

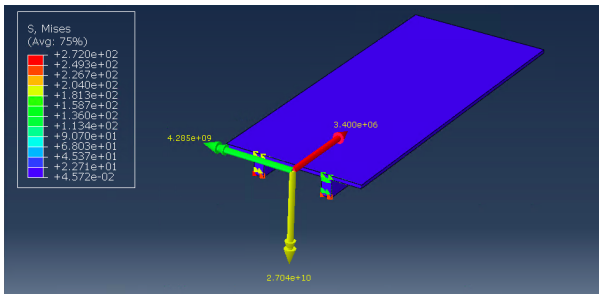

Figure 7.15: Illustration of Free Body Cut in Solid model

Free Body Cut does not include the forces in the reinforcements, these need to be obtained individually by using Probe Values. In each section, reinforcement stresses in each element are summarized by Probe Values, and forces are found by an equivalent section area. Total reinforcement forces at each beam (N_s) in different sections are afterward added to their respective resultants obtained by Free Body Cut. To find the total bending moment, reinforcement forces are multiplied with their respective arm to the concrete mass center. This leads to the correct results in each section.

The total forces at each beam section in the bridge is found by:

$$N = \frac{F_x}{2} + \frac{M_z}{5.5\text{ m}} + N_s \tag{7.7}$$

Where $N_s = \sigma_{s,tot} \cdot A_{eq}$

$$V_z = \frac{F_z}{2} \tag{7.8}$$

$$M_y = \frac{M_y}{2} + N_s \cdot e \tag{7.9}$$

$$V_y = F_y \tag{7.10}$$

7.3 Verification of the Models

Simple analyses have been performed to compare and verify the two models. The source of the deviations and the impacts must be found and quantified. To examine the deviations between the two models, it is necessary to isolate the effects of each change in the model step by step. To do so, results have been compared in the following situations:

- Free expansion with temperature field 1 & 2
- Restrained expansion with a constant temperature field of 1‰ throughout the bridge
- Restrained expansion with both temperature fields.
- Restrained expansion with cracked sections and both temperature fields.

The models are based on different theories due to the elements used in the analyses. This will affect the results and some deviations are expected already at this point in the analysis.

The reinforcement will not expand when the temperature field is imposed. Due to the connection between steel and concrete, the steel will restrain the expansion of the concrete. This provides an internal constraint and the total elongation of the bridge will become smaller. Further, this will strain the reinforcement and create additional compression in the concrete, as well as supplementary moments due to the tensioned wires. This restraining effect is explained thoroughly in section 2.2.

In the solid model, the reinforcement is placed accurately in the entire length and span. On the contrary, the frame model only accounts for the main upper and lower face reinforcement. The main difference will show in the resulting forces in the beam as the volume model activates more reinforcement when looking at different sections.

This difference in modeling will especially apply in the sections of zero moment. The frame model simplifies the section of zero moment by placing it over a length of 0.5 m with only 3ø32. When including all reinforcement from the original drawings, the solid model has more reinforcement in this section, see figure 7.16. This might lead to greater deviation in the forces in these areas. The cracked sections are imposed over the point of zero moment and spans over the same 0.5 m.

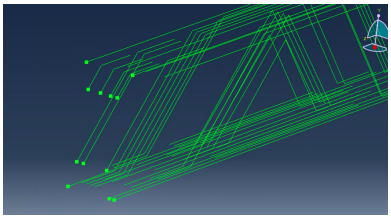

(a) Illustration of modelled reinforcement in Solid model

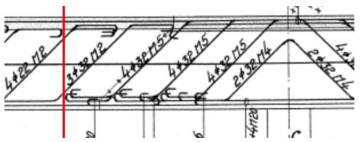

(b) Drawing of reinforcement

Figure 7.16: Reinforcement in zero moment section

Another important aspect is the behavior of the two models regarding the restraining effect by the reinforcement. The reinforcement will strain the solid model locally in the cross section. On the contrary, the frame model will attain restraining from the reinforcement more evenly over the cross section. This is due to the preconditions of the models.

Both of the models are subjected to temperature field 1. It is assumed that this temperature field will not cause deviations due to the similarities in the modeling. The differences in temperature field 1 and 2 are expected to give deviations in the axial forces in the solid model.

What first arose as a problem with the frame model, was the axial forces dropping in magnitude further away from the end compared to the solid model. This was expected to be a problem as the transverse elements behave separately and not as a continuous plate. The solid model has a much stiffer plate and the frame model gets a shear stiffness and bending stiffness in plane that is too low. On the other hand, the vertical bending moments occurring in both the models were quite similar. This shows that the vertical bending stiffness induced by the transverse beam elements is adequate. The transverse elements are therefore adjusted in the cross-sectional area to impose a higher bending stiffness in plane, but retain the original vertical bending stiffness. By optimizing the cross-section calibrated with the solid model, the height becomes 230 mm and the width becomes 2.26 m. This is done before comparing the two models further.

7.3.1 Free Expansion

Running the analysis without reinforcement will simulate the free expansion of the bridge. By not including the self-weight, the external forces caused by ASR will be isolated.

External forces appear when imposing a temperature field with a gradient over the height and a different expansion in the inner and outer beams. This can be explained by the different stress-contributing strains occurring as explained in section 2.2. This results in a tensile force in the inner beams, compression force in the outer beams, and an almost constant positive moment over the entire

bridge.

The models are exposed to temperature fields with gradients. Three cases were investigated:

1. Frame model with temperature field 1
2. Solid model with temperature field 1
3. Solid model with temperature field 2

Axial forces and moments for the three cases are shown in figure 7.17, 7.18 and 7.19, respectively. The graphs are starting at support section 7, which is 133.75 m from support 1.

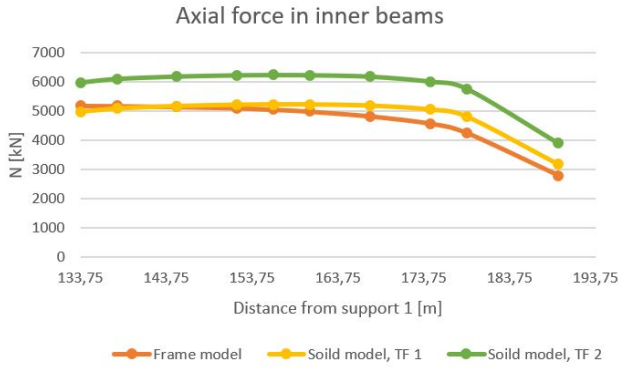

Figure 7.17: Axial forces in inner beam

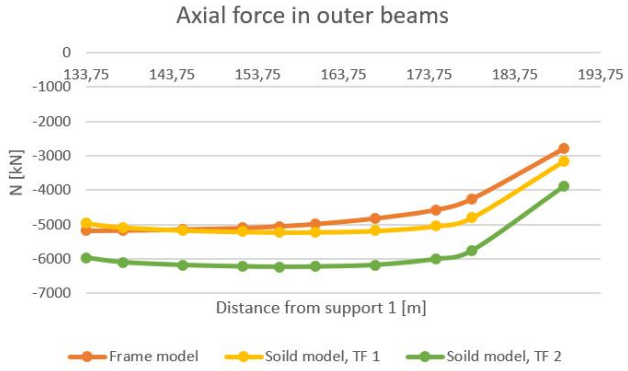

Figure 7.18: Axial forces in outer beam

As the figures illustrate, there is small deviations between the frame model and the solid model subjected to temperature field 1 whereas greater deviations occur for temperature field 2.

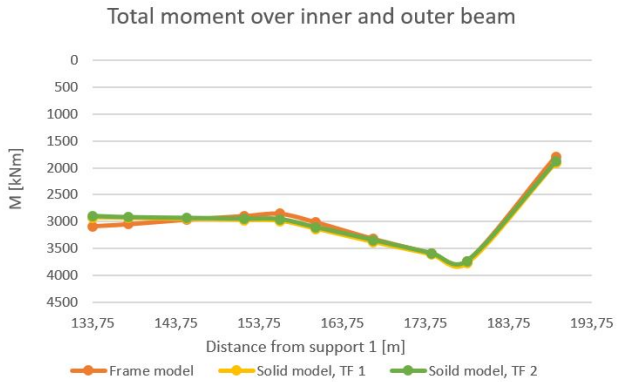

Figure 7.19: Total moment over inner and outer beam

Case 1 vs Case 2

The percentage difference is listed for the inner beam in table 7.4. The frame model deviates with 4.1% to -13.6% compared to the solid model. The variation becomes higher closer to the end of the bridge. This might be a result of the bending stiffness in plane still is somewhat insufficient in the frame model. Better optimization of the cross-sectional area of the transverse elements would maybe improve the accuracy between the two models regarding axial forces.

Section	S7	ZM 7-8	F7	ZM 7-8	S8	ZM 8-9	F8	ZM 9-8	S9	F9
Deviation	4.1	1.8	-0.4	-2.1	-3.4	-4.7	-7.5	- 10.4	-13.0	-13.6

Table 7.4: Deviations [%] in the frame model compared to the solid model
Axial force inner beam, temperature field 1

Figure 7.19 shows small variations in the total moment over one inner and outer beam. The moments in the frame model have a variation of 5.3% to -6.3% compared to the solid model. This is a good result considering the differences in the models. Table 7.5 presents the deviations in the total bending moment between the two models.

Section	S7	ZM 7-8	F7	ZM 7-8	S8	ZM 8-9	F8	ZM 9-8	S9	F9
Deviation	5.3	3.8	0.4	-2.6	-4.6	-4.1	-1.9	-0.8	-1.3	-6.3

Table 7.5: Deviations [%] in the frame model compared to the solid model
Total moment, temperature field 1

Regarding the total strain, case 1 and case 2 only differs with 0.7%.

Case 2 vs Case 3

The deviations presented in table 7.6 shows that temperature field 2 results in forces that are about 20% higher compared to temperature field 1. This is a

result of the strain gradient in the horizontal direction. It is varying between 1.75-1.25‰ in the top of the beam in TF 2, whereas it is only 1.5 and 1‰ in TF 1. This shows the effects of the chosen temperature gradient, although their respective mass center has the same gradient in both cases. This is important to bear in mind while using the different models. The flexural bending only deviates with about 1 % between the two models. This is since the vertical gradient is equal in both situations.

Section	S7	ZM 7-8	F7	ZM 7-8	S8	ZM 8-9	F8	ZM 9-8	S9	F9
Deviation	-20	-20	-20	-19	-19	-19	-19	-19	-20	-23

Table 7.6: Deviations [%] in the solid model with TF1 compared to solid model with TF2
Axial force in inner beam

Case 1 vs Case 3

The deviations between the frame model with temperature field 1 and the solid model with temperature field 2 is similar to the ones in table 7.6, as expected. The deviations are higher at the end spans due to the lower transverse shear stiffness and bending stiffness in plane as explained earlier. The deviations in flexural bending are similar to the ones in table 7.5.

Section	S7	ZM 7-8	F7	ZM 7-8	S8	ZM 8-9	F8	ZM 9-8	S9	F9
Deviation	-15	-18	-20	-22	-23	-25	-28	-31	-36	-40

Table 7.7: Deviations [%] in the frame model compared to the solid model
Axial force inner beam, temperature field 2

Considering the total strain in the model, case 1 and case 3 get a deviation of 1.7%

7.3.2 Restrained with Constant Temperature Fields

To control the post-processing of the model in Abaqus, an analysis with constant temperature and reinforcement is submitted. The temperature field is constant at 100° C, which will give a strain of 1‰ in the concrete.

The forces in the concrete elements added to the force in the steel elements should become zero as there are no external axial forces. To obtain the correct result, the axial forces in the concrete and steel, as well as the moment in the concrete must be gathered as output data from Abaqus. The moment caused by the reinforcement must be added manually by multiplying the axial forces and their respective arms. The results are verified, and the method is used for the further gathering of outputs in the models with reinforcement.

Section	Frame model [kN]	Solid model [kN]
Support 7	104	53
Zero moment	107	200
Field 7	111	300
Zero moment	110	3.5
Support 8	107	45
Zero moment	110	41
Field 8	116	365
Zero moment	111	204
Support 9	112	133
Field 9	91	83

Table 7.8: Axial forces in inner beams
Temperature field 1
Restrained

The total force in the sections is close to zero. The frame model has an average deviation of 100 kN, whereas the solid model varies more in its deviation.

As earlier mentioned, the reinforcement forces in the solid model are found by summarizing the stresses at each element in the desired section. Forces are found by multiplying stresses with an average equivalent reinforcement section area. As different reinforcement sections also have different stresses, the equivalent area is weighted by stresses and area. This is done approximately and only by one representing section, as performing this at each section would be unnecessarily time-consuming. Results show that the more accurate the equivalent reinforcement section area is, the total forces in the beam becomes close to zero, such that $N_{concrete} = N_{steel}$. Accordingly, it is reasonable to believe that total forces in each section would become closer zero if the equivalent area were more precisely calculated at each section in the solid model.

When evaluating the total moment in the beams, there are some deviations seemingly with a pattern. The supports obtain a higher moment in the solid model, about 60% while deviations in the zero moment sections lie about 130%. Generally, the deviations are increasing towards the end of the bridge, as reported in table 7.9. In the fields the frame model gives higher moments. These deviations are a consequence of the different modeling. The amount of reinforcement differs in the models which give different tension forces from the reinforcement. This again gives deviations in the moment. The most important aspect is the preconditions of the two models. The transverse elements in the frame model adequately transfer the axial forces but do not distribute the bending moment satisfactorily. This is handled more sufficiently in the solid model. In addition, the frame model transfers forces point-wise and not continuously as the solid model.

Section	S7	ZM 7-8	F7	ZM 7-8	S8	ZM 8-9	F8	ZM 9-8	S9	F9
Deviation	-63.4	-126.9	47.3	-139	-66.9	-161	32	-283	-86.5	61.3

Table 7.9: Deviations [%] in the frame model compared to the solid model
Total moment, constant temperature

7.3.3 Restrained with Temperature field 1 & 2

As performed for the free expansion analysis, three cases are investigated to evaluate the effect of the restraints:

1. Frame model with temperature field 1
2. Solid model with temperature field 1
3. Solid model with temperature field 2

The earlier deviations reported between the models are expected to still occur. Axial forces and moments obtained from the three cases are shown in figure **??** and 7.22.

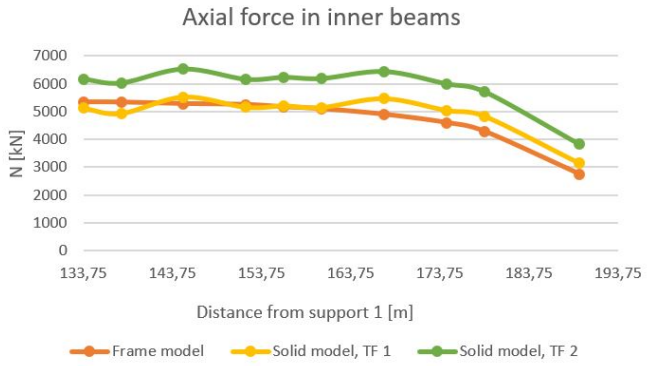

Figure 7.20: Axial forces in inner beam

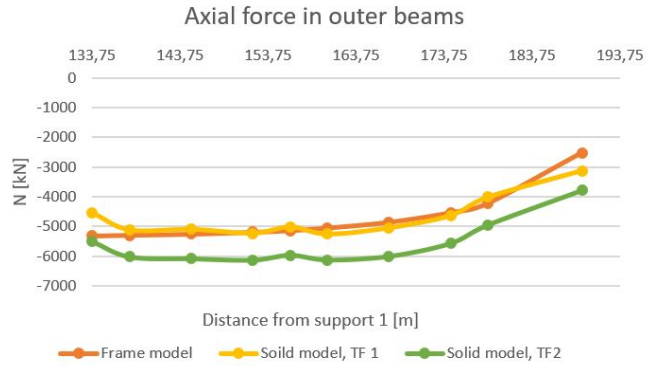

Figure 7.21: Axial forces in outer beam

The axial forces show low deviations between case 1 and case 2. Solely looking at the solid model, the axial forces variate more over the sections compared to the frame model. This is assumed to be a result of the more varying amount of reinforcement in addition to the local effects of the reinforcement in the solid model.

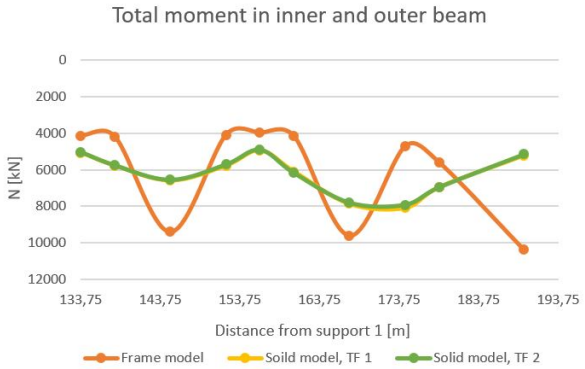

Figure 7.22: Total moment

The moments are very similar for case 2 and case 3 as seen in the free expansion analysis. A relatively high deviation occurs between case 1 and case 2.

Case 1 vs Case 2

Section	S7	ZM 7-8	F7	ZM 7-8	S8	ZM 8-9	F8	ZM 9-8	S9	F9
Deviation	0.8	7.6	-4.5	1.8	-0.5	-1.1	-11.7	-9.6	-12.8	-14.4

Table 7.10: Deviations [%] in the frame model compared to the solid model
Axial forces inner beam, temperature field 1

The deviations in axial forces are modest. This indicates that the different modeling of reinforcement does not impact the resulting axial forces in a severe way.

Section	S7	ZM 7-8	F7	ZM 7-8	S8	ZM 8-9	F8	ZM 9-8	S9	F9
Deviation	-22.3	-37.5	29.8	-41	-23.9	-46.3	18	-71.2	-24.1	49.6

Table 7.11: Deviations [%] in the frame model compared to the solid model
Total moment, temperature field 1

Table 7.11 shows high deviations in total bending moment. This is a consequence of the preconditions of the models as explained earlier. As the frame model consists of beams, the assumption of plane sections remaining plane by

Navier's hypothesis applies to the model. This leads to constant strains throughout the transverse direction in the beam and no local effects due to the locations of reinforcement. Since the solid model is not confined by this assumption, local effects in the transverse direction due to the reinforcement occurs. This is shown by figure 7.23 which shows the longitudinal strains in the model. Especially in the bridge deck where a lot of reinforcement is placed in the top of the beam, these local effects occur when the reinforcement restrains to a greater extent in the area of the beam web compared to the flanges. This might influence the resulting moment in the solid model compared to the frame model.

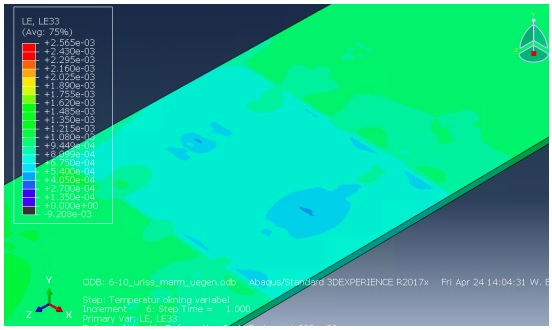

Figure 7.23: Strains in longitudinal direction of the beams

This different behaviour in the two models leads to higher deviations in the longitudinal strain, where the frame model differs with -2.8% in total strain compared to the solid model. This is reasonable as the solid model is expected to have a greater elongation due to the local effects of the reinforcement.

Another aspect to the deviations in the total bending moment is the difference in the modeling of the reinforcement, such as more varying amount and positioning in the solid model, as explained earlier.

Results from case 2 and case 3 show the same deviations as earlier without the reinforcement. This is expected and shows that adding reinforcement in the model does not influence this. This also applies to case 1 compared to case 3. Therefore, only the results from comparing case 1 and case 2 are reported.

7.3.4 Cracked Sections

The cracked sections are implemented in the model. The goal is to model non-linearity in a linear model, which can be problematic. The cracked sections are in stage II and will not have the same bending stiffness as the uncracked concrete in stage I. To preserve this effect, the sections must be modified.

As explained in the previous sections in this chapter, the non-linearity approach is executed differently in the two models. The solution in the solid model might be more true to the expected behavior of the beam section, where the crack creates an almost not-existing concrete stiffness in the tension zone.

Two situations are analyzed to understand the effect of the non-linearity:

- Free expansion, temperature field 1, and cracked sections
- Restrained expansion, temperature 1 and cracked section

Free Expansion

Figure 7.24, 7.25 and figure 7.26 shows the axial force and moments obtained in the frame and solid model.

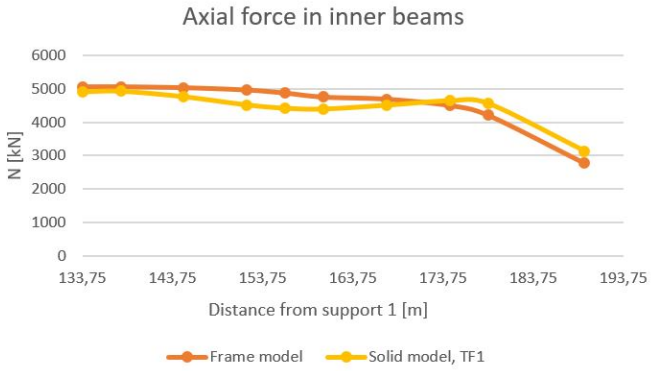

Figure 7.24: Axial forces in inner beam
Free expansion with crack

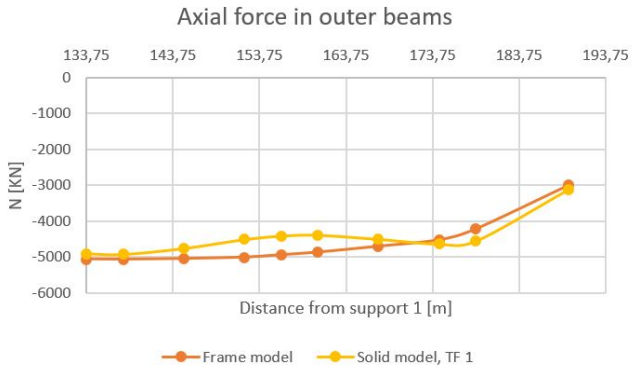

Figure 7.25: Axial forces in outer beam
Free expansion situation with cracks

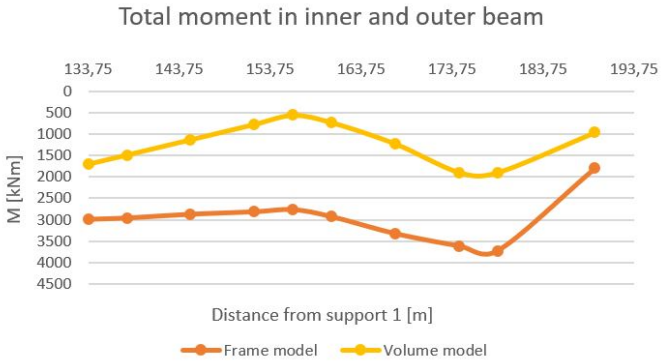

Figure 7.26: Total moments
Free expansion situation with cracks

The percentage difference in axial force in the inner beams between the frame model the solid model is shown in table 7.12.

Section	S7	ZM 7-8	F7	ZM 7-8	S8	ZM 8-9	F8	ZM 9-8	S9	F9
Deviation	3.1	2.7	5.4	9.1	15	7.6	3.9	-3.1	-8.4	-12.7

Table 7.12: Deviations [%] in the frame model compared to the solid model
Axial force in inner beam, temperature field 1

The deviations in the axial forces are within a range of approximately 10%, which can be expected due to the many differences. What is interesting is that the frame model now provides higher forces and moments in multiple sections compared to the solid model. The free expansion analysis without cracks has a majority of higher forces in the solid model. This implies that the axial forces are reduced in a higher degree in the solid model compared to the frame model.

Section	S7	ZM 7-8	F7	ZM 7-8	S8	ZM 8-9	F8	ZM 9-8	S9	F9
Deviation	-13.7	-0.4	21.5	45.5	41	50.5	26.4	-4.9	-1.8	-7.3

Table 7.13: Deviations [%] in the frame model compared to the solid model
Total moment, temperature field 1

Table 7.13 presents the deviation in the total moment between the two models.

In areas close to the simulated crack, moment deviations between the two models are increasing in a greater magnitude than the axial forces. This is a result of the differences in simulation in the two models and can be explained by idealizing the cross-section to a square cross-section. The axial stiffness is defined by $EA = E \cdot bh$, whereas bending stiffness depends on $EI = E \cdot \frac{bh^3}{12}$. If one reduces the total stiffness by reducing E, which is done in the frame model, the reduced stiffness will affect both axial and bending stiffness the same way. On the contrary, if the height is reduced as done in the solid model, the bending

stiffness will be reduced by a third exponent compared to the axial stiffness.

Restrained Expansion

The same simulation of cracks is implemented in the analysis with reinforcement giving the resulting axial forces and moments as illustrated in figure 7.27, 7.28 and 7.29.

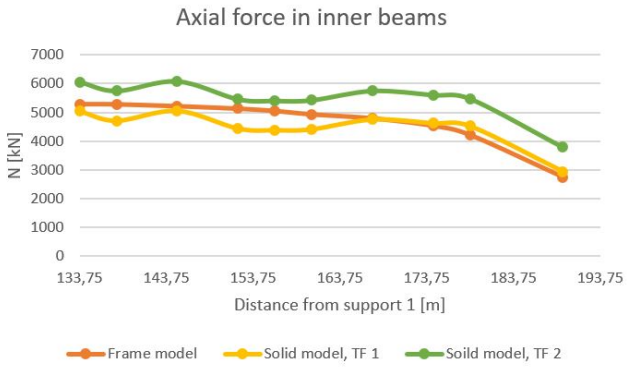

Figure 7.27: Axial forces in inner beams
Restrained expansion with cracks

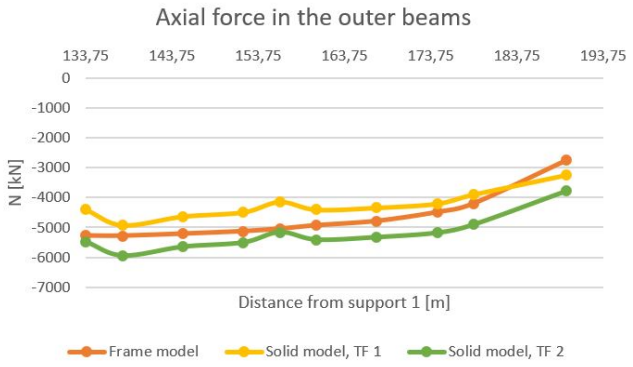

Figure 7.28: Axial forces in outer beams
Restrained expansion with cracks

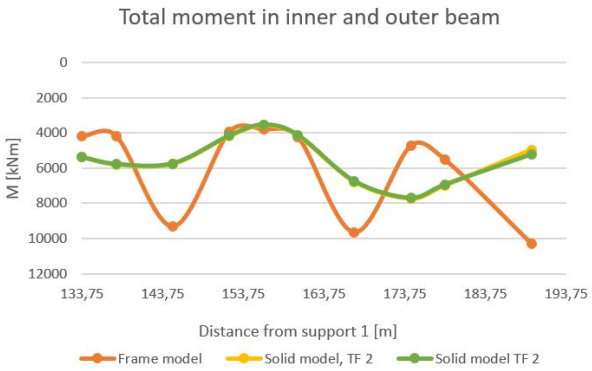

Figure 7.29: Total moments
Restrained expansion with cracks

The percentage deviations between the axial force in the inner beam exposed to temperature field 1 are reported in table 7.14.

Section	S7	ZM 7-8	F7	ZM 7-8	S8	ZM 8-9	F8	ZM 9-8	S9	F9
Deviation	3.5	9.6	2.2	12.9	12.3	4.7	0.3	-2.2	-6.6	-5.9

Table 7.14: Deviations [%] in the frame model compared to the solid model
Axial force inner beam, temperature field 1

When reinforcement is included in the analysis, the deviations between the models are in the same range as without reinforcement. These deviations are small but are increasing around the area of the crack.

Section	S7	ZM 7-8	F7	ZM 7-8	S8	ZM 8-9	F8	ZM 9-8	S9	F9
Deviation	-28.7	38.4	38.2	-5.9	6.6	2.2	29.7	-63.9	-26.4	51.8

Table 7.15: Deviations [%] in the frame model compared to the solid model
Total moment, temperature field 1

When the analysis includes reinforcement, the deviation between the two models is smaller compared to the ones reported in table 7.13, especially in the area close to the simulated crack. This is a result of two different types of deviation canceling each other out. The deviations in moment between the two models when reinforced and uncracked show that the frame model obtains about 20-40% lower forces compared to the solid model. When the analysis includes a cracked section, the frame model obtains about 40-50% higher forces.

As the cracks are modeled differently in the models, expected deviations occur as was seen in the free expansion situation. The solid model is modeled with almost zero stiffness in the tension zone, which in a section with small amounts of reinforcement reduces the capacity significantly. Earlier analyses show that

the reinforcement is already yielding without the simulation of the crack. When the section is modeled with no tension capacity, the moment is reduced considerably since the reinforcement is not able to incorporate additional tension forces. A rearrangement of moment occurs in a much higher degree compared to the frame model, since this model still has a concrete tension capacity. This leads to smaller deviations between the two models compared to the uncracked analysis. The assumption of a crack in the whole web of the beam is conservative and might result in a larger rearrangement in forces compared to the reality.

The deviations in the solid model between temperature field 1 and 2, is corresponding with earlier deviations. This implies that the chosen temperature field does not affect the results from the simulation of crack. This also implies that the different temperature fields in the solid model and the frame model should not affect the deviations in the simulation of crack.

7.4 Carbon Fiber Reinforcement in Abaqus

To comprehend the effects of the applied external fiber reinforcement in Elgeseter Bridge, both models in Abaqus are implemented with CFRP. The application of CFRP in the models differs from each other due to limitations in the frame model. The most important aspect of this simulation is to see the global effects in the model such as the redistribution of forces. By applying fiber reinforcement in the bridge, the stiffness in the beam with a crack has increased. This might affect the global arrangement of forces, especially in further expansion of the bridge.

Concerning global behavior, it is a possibility that the increase in stiffness due to CFRP can attract more forces and moments. This leads to a rearrangement of the forces and may cause a higher utilization in some sections compared to an unstrengthened situation. This can contradict the intention of adding the extra reinforcement and is therefore an interesting aspect to investigate.

In reality, the bridge is assumed to have a longitudinal extension of about 200 mm before the fiber reinforcement was applied. As explained earlier, reports suggest that the bridge will additionally elongate about 50 mm during its estimated lifetime [37]. As the fiber reinforcement was applied in 2014, it is assumed that its stiffness does not contribute to the capacity until additional forces or expansion is applied. Accordingly, an analysis including CFRP and a strain field equivalent to the additional extension of 50 mm is submitted in Abaqus. This would indicate the distribution of the forces in the bridge due to further ASR expansion.

When total forces in the estimated lifetime of the bridge are calculated, the steel is assumed to yield. To implement that the steel is ineffective in the areas with CFRP, the analysis is run without any steel reinforcement in this section. In this way, one can sum the resulting forces from the analysis with 200 mm expansion without CFRP and the analysis with an expansion of 50 mm with CFRP, without obtaining higher forces in the steel reinforcement than in reality.

7.4.1 Modeling of CFRP in Frame model

The frame model is limited to the use of wire elements only. It is evaluated that the best way to include the carbon fiber reinforcement is to increase the stiffness in Young's modulus rather than adding an extra wire element.

The mistakes made by only including the CFRP in the form of stiffness are expected to be small when investigation the global effects of local strengthening. A more detailed analysis of the fiber's behavior can be seen in the solid model.

The external shear reinforcement is neglected in this approach. The flexural FRP is applied to both the inner beams in span 3 and span 6, whereas in field 8 only one of the beams is strengthened. This is to see how the unsymmetrical behaviour impacts the results. The important properties are listed in table 7.16

A_f	672 mm^2
y_f	-0.7 mm
E_f	210 000 MPa

Table 7.16: Properties of flexural reinforcement

The strips cover almost the entire span except from 200 mm on each end, but in the Abaqus model, it is simplified to cover the entire span between two axes completely. The contribution to the stiffness in the cracked parts and the uncracked parts are calculated separately.

The increase in stiffness is found by comparing the equivalent bending stiffness with and without the fiber reinforcement. For the cracked parts this is done in stage II and for the rest of the field, it is done in stage I. The calculations are shown in appendix D.B.

For the cracked section, the bending stiffness is increased with 23%. This is implied as a 23% increase in Young's modulus going from 1941 MPa to 2387 MPa.

Concerning the uncracked section, the increase in bending stiffness is only 3.1%. The concrete contributes to most of the stiffness, so the additional carbon fibers do not give the same impact on the total stiffness. Young's modulus increases from 7766 MPa to 7999 MPa.

The elements in the frame model are now separated into three different sets which get different section assignments. One set representing the uncracked part of the bridge, another representing the reinforced cracked sections and the last set representing the uncracked, externally reinforced part of the beam. The concrete material assigned to the sets is equal except the stiffness.

Set	Young's modulus [MPa]
Strengthened cracked parts	2387
Strengthened fields	7999
Unstrengthened fields	7766

Table 7.17: Modified Young's modulus

7.4.2 Modeling of CFRP in Solid model

Carbon fiber reinforcement was applied to the model in Abaqus according to drawings from Aas-Jakobsen [34]. The fiber strips and sheets are modeled as shells with their corresponding thickness. Mechanical properties of the CFRP in the model is listed in table 7.18.

	$E_{f,1}[MPa]$	$E_{f,2}[MPa]$	$f_{fd}[MPa]$	Plastic Strain	Exp. coeff.$[\Delta T^{-1}]$
Sika CarboDur M16	210000	500	2307	0.0	0
SikaWrap 231C	210000	500	2750	0.0	0

Table 7.18: Mechanical properties of CFRP in Abaqus

The CFRP is assigned lamina material and composite sections, whereas the wrap is a composite of 5 layers and the strips of 4. According to product brochures, both have fibers oriented in the longitudinal direction of the strips and sheets [53]. This is implemented in the composite layers.

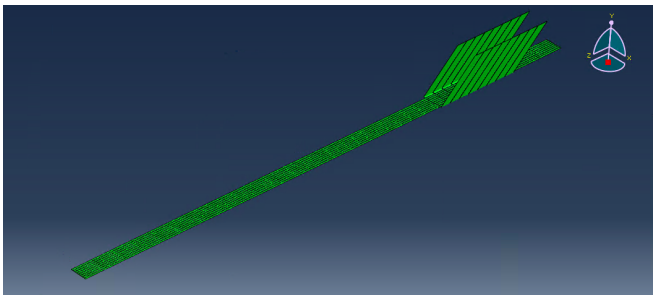

Figure 7.30: CFRP in the Solid model

When creating a lamina material in Abaqus, Young's modulus parallel ($E_{f,1}$) and perpendicular ($E_{f,2}$) to the fiber direction must be defined. As there is no information about this in product brochures, all other directions are assumed to have the same stiffness as epoxy. Young's modulus of 500 MPa is chosen according to table 3.2, which is considered to be conservative.

Modeling the CFRP wrap exactly according to drawings is difficult due to its geometry. As an approximation, the wrap is modeled as in figure 7.31. This is considered to retain its most important properties, such as its tension stiffness in the inclined direction at the web to contribute to the shear capacity.

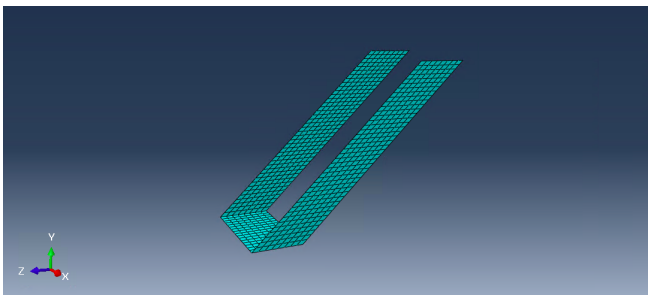

Figure 7.31: U-wrap in the Solid model

Both strips and wrap are constrained to the concrete by tie constraint, without rotational DOFs to resemble the behavior of the adhesive between the concrete and CFRP. Still, Abaqus can not account for debonding issues and this must be considered by calculation according to design rules.

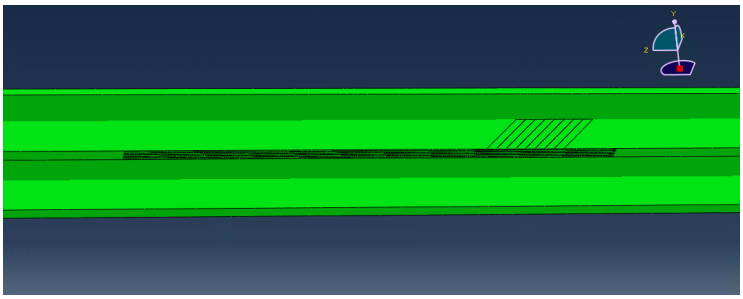

Figure 7.32: CFRP connected to the beam in Solid model

Chapter 8

Influence of Modifications in Abaqus

Modifying the models in Abaqus to reflect on the impacts cracked sections and strengthened parts have on the structure is an interesting issue to exploit. How the bridge reacts and redistributes forces due to changes of stiffness in certain areas, can be simulated in Abaqus to obtain a greater insight into this matter. Further in this chapter, this is investigated by looking at the results in each model.

8.1 Influence of Simulation of Crack in Abaqus

A situation with reinforcement, ASR-load, and cracked sections is submitted. The contribution from the reinforcement will be affected due to the stage II condition in the concrete. When only some sections have a stage II condition, a redistribution of the ASR-load is expected.

The procedure of calculating ASR effects from The Norwegian Public Roads Administration [1] shows that the retaining due to the reinforcement is reduced in a cracked section. In a cracked section, the steel is yielding and can not obtain higher stresses, but will continue to be strained. At this point, the initial strain will not be significant for the capacity in ULS. This means that less of the free expansion is restrained and therefore a greater effect from the ASR is achieved resulting in higher strains. The higher strains make the structure less stiff and an increase in total elongation is assumed. Also, the increase in ductility will theoretically result in lower axial forces and moments.

An overview of how the forces and moment decrease in both the models are shown in figure 8.1 and figure 8.2. An interesting aspect is how the crack in a section of zero moment affects the area around. This is observed mostly in the result from the solid model, but also in the moment distribution from the frame model. The closest support and the adjacent section of zero moment on the other side get a lesser magnitude in forces. This makes the sections less utilized and it can be discussed if this is why there are no cases of cracks on both sides of a support.

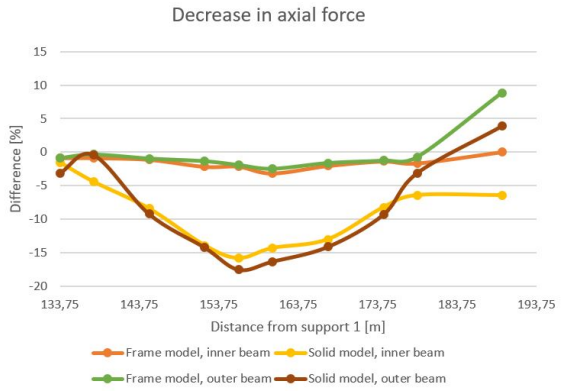

Figure 8.1: Decrease in axial forces

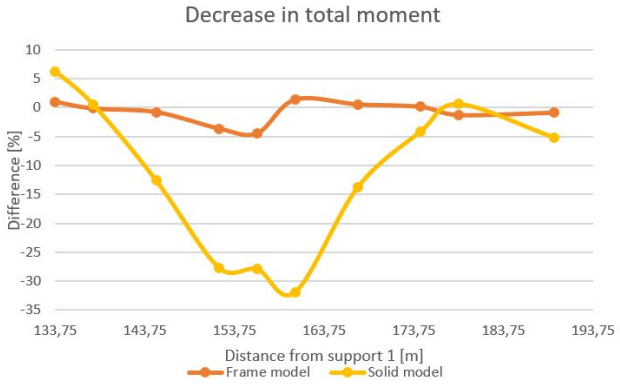

Figure 8.2: Decrease in total moment

Looking at the models separately, the decrease in forces due to cracks can be visualized better.

8.1.1 Influence of Cracks in the Frame Model

The frame model is studied and the results are visualised in the following graphs:

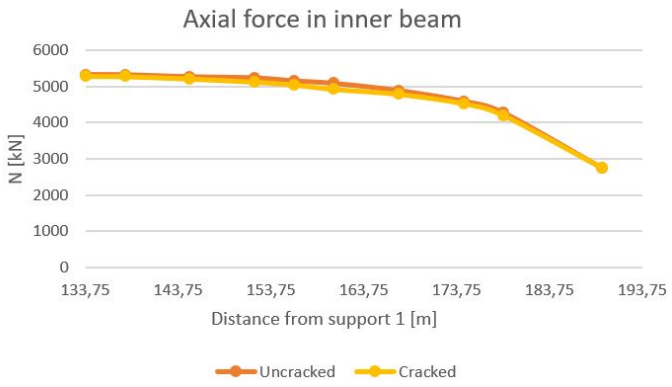

Figure 8.3: Axial forces in inner beam
Frame model

The axial force in the frame model is approximately reduced with 2 % evenly over the beams, except in the cracked section in the inner beam where it is reduced with approximately 3.2%. The impact on the concrete is reduced with about 7%, but since the steel compensates by obtaining higher forces, the overall axial force does not decrease significantly.

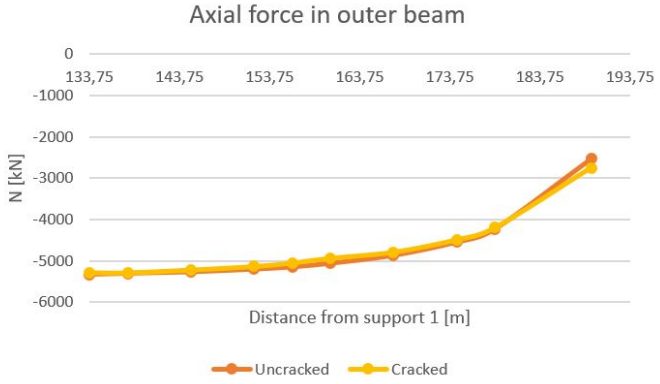

Figure 8.4: Axial forces in outer beam
Frame model

The outer beams have an even reduction of about 2% with a little higher reduction of 2.4% in the cracked section. The overall reduction is due to the general lower stiffness of the structure.

Figure 8.5: Moment distribution between the beams
Frame model

The change in the total moment over the inner and the outer beam is not very significant, and the impact of the crack is rather small in the frame model considering the moments. The crack occurs in the section of zero moment to the right of support 8 and makes the steel in the section yield which therefore increases the steel's contribution to the total moment. However, the crack affects an area around the closest support. In support 8 and section of zero moment 8-7, there is a reduction of 3-4.5%. To get a deeper understanding of the crack's influence, it is beneficial to see how the moment is distributed over the inner and outer beam, illustrated in figure 8.6.

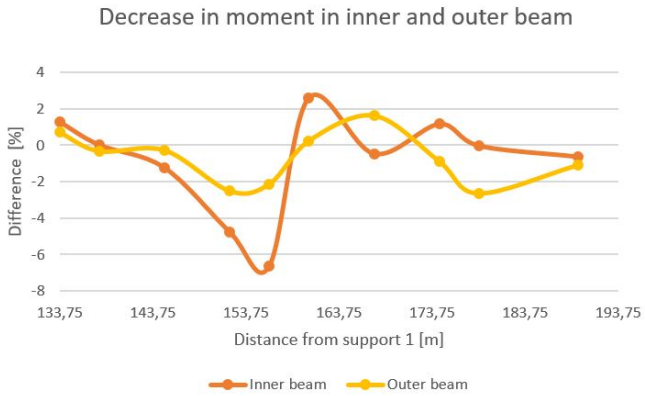

Figure 8.6: Moment distribution between the beams
Frame model

The moment in the inner beam has a reduction of 4.7-6.7% in the area around the cracked section. Considering the cracked section itself, the reduction in stiffness gives a decrease in the concrete's moment of about 6.9%. Still, the compensating forces in the reinforcement increase the total moment of 2.6%. This can be seen as the peek in figure 8.6.

The weakness in the concrete due to the crack results in a rearrangement of the bending moment, this is seen as a less significant change of moments in field 8 and 9. Due to the reduced stiffness in the bridge, the outer beams generally have a small decrease in bending moment. The highest reduction is also seen around support 8. This indicates that the crack impacts the outer beam as well. There is a small increase in the moment after the cracked section and this occurs because the outer beams need to assist the inner beams by taking more forces.

8.1.2 Influence of Cracks in the Solid Model

The solid model gets a much higher reduction in both the axial forces and bending moments in the entire model compared to the frame model. The results from the solid model are reported in the following graphs.

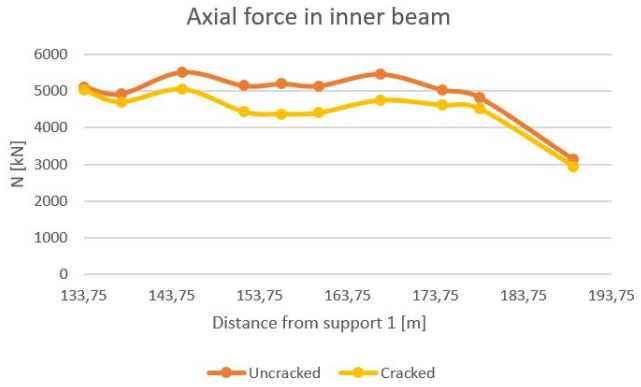

Figure 8.7: Axial force in inner beam
Solid model

Figure 8.7 illustrates a relatively high drop in the axial force around support 8 in the inner beams. The reduction in axial force is about 13-15% between the section of zero moment to the left of support 8 extending through field 8. Further away from the crack, the deviation becomes smaller as the graph in figure 8.7 clearly shows.

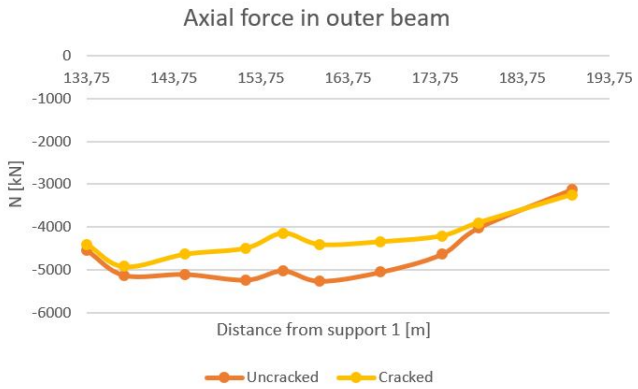

Figure 8.8: Axial force in outer beam
Solid model

The same trend as in the inner beam occurs for the outer beam as seen in figure 8.8. The reduction in axial force is greater in the same area surrounding the crack, and the reduction decreases towards support 7 and support 9.

Figure 8.9: Total moment in outer beam
Solid model

The variation in the moment is presented in figure 8.9. The total moment over the inner and outer beam gets a reduction of 33% in the cracked section. The area around support 8 obtains a high impact of the crack, leading to a reduction of about 28% in the same area the frame model showed a reduction. Also, a reduction of about 13% is seen in both the fields close to the crack. Otherwise, the reduction in the bending moment is quite small and fading out away from the cracked section.

Generally, the solid model gets a greater impact of the crack. The reason for this is probably the different ways the crack is modeled and how it is affecting the global system as explained in section 7.3.

8.2 Influence of Simulation of CFRP in Abaqus

The simulation of CFRP in the models will increase the stiffness locally in the bridge. As seen previously, the reduction of stiffness due to cracks had a significant impact on the structure. The scope of implementing CFRP in the models is to observe the possible effects on the bridge globally and locally.

8.2.1 Influence of CFRP in Frame Model

The adjustment in the stiffness is imposed in the Abaqus model and compared to the situation without the fiber reinforcement. Both models are subjected to a temperature field equivalent to an expansion of about 200 mm. This is a fictitious situation since the externally bonded fiber reinforcement is applied after the expansion. Even though this is a wrong assumption, it can give a picture of how an increase in stiffness can give an impact on ASR expansion.

In this case, there is only made a cracked section on the east-facing beam in field 8 and not on both of the inner beams as the other cracked sections. This reflects a realistic simulation of the situation and can indicate if the symmetry assumptions made previously are reliable.

The change in moment given in percentage after application of CFRP is shown in figure 8.10. As expected, it is some increase in the moment over the inner beam where the carbon fiber reinforcement is applied. This is shown with different colors for span 3, span 6 and span 8. The non-strengthen span 1, 2, 4 and 5 gets a reduction, while span 7 in between two strengthened spans obtains a small increase.

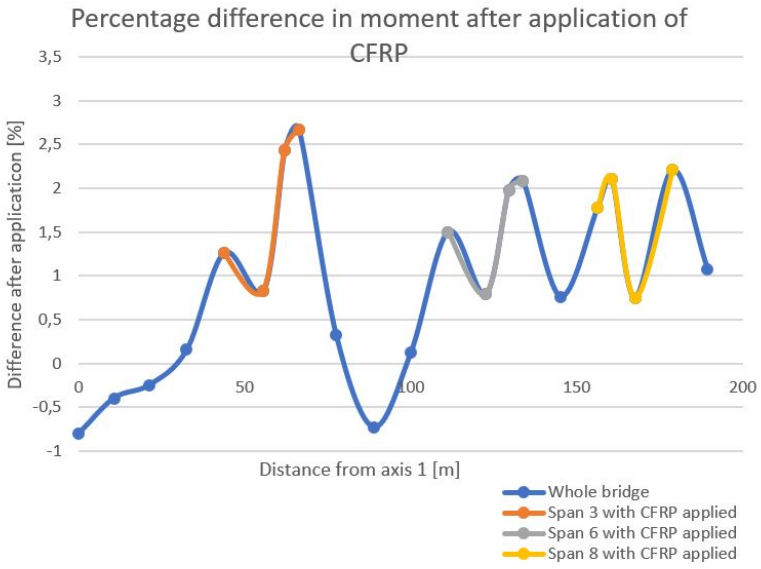

Figure 8.10: Impact on moment after application of CFRP on inner beams

The alteration in the axial force shows similar behavior. Though, a small increase can be seen in span 4 as well. The increased stiffness seems to have a higher impact on the axial forces.

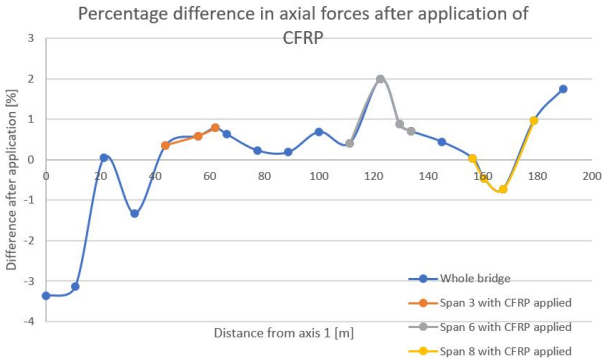

Figure 8.11: Impact on axial forces after application of CFRP

In span 8, a decrease in axial forces is observed. This could be explained by the asymmetrical crack and strengthening imposed in this span. This can be understood by comparing the inner beams to each other. Table 8.1 compares the forces in the inner beams and gives an impression of the force distribution.

Section	$M_{east}[kNm]$	$M_{west}[kNm]$	$N_{east}[kN]$	$N_{west}[kN]$
Support 8	1966	1966	5052	5122
ZM 8-9	2183	2085	4921	5097
Field 8	4902	4945	4808	4833
Support 9	2977	2863	4278	4141

Table 8.1: M and N for both of the inner beams

The west faced beam is not cracked and even though the crack in the east-facing beam is strengthened, it is not adequate to increase the stiffness to an uncracked state. Therefore, the moments and axial forces are expected to be reduced in the cracked area compared to the same section in the other inner beam.

A decrease of about 170 kN in the axial force is seen in the actual cracked part and some effects are imposed to support 8 and field 8, but with less impact. Regarding the moment it is necessary to study the forces separately in the concrete and the steel. In the cracked section the steel obtains higher stresses which makes the contribution from the reinforcement greater. This increase is greater than the observed decrease in the concrete and therefore the total moment is greater. Regarding the other sections where the steel is not yielding, the axial forces are reduced in both the steel and the concrete. The impact on the moment is therefore rather small because the negative contribution coming from the upper reinforcement is reduced as well. All in all, the effect of having one cracked inner beam is not very significant. This can justify the simplification of symmetry done previously.

8.2.2 Influence of CFRP in Solid Model

To understand the influence of CFRP in Elgeseter bridge, a comparison with and without CFRP is done. Both models are subjected to a temperature field equivalent to an expansion of about 50 mm and have the simulation of a crack at zero moment section 8-9. All reinforcement is active in this analysis. Results are presented in figure 8.12, 8.13 and 8.14.

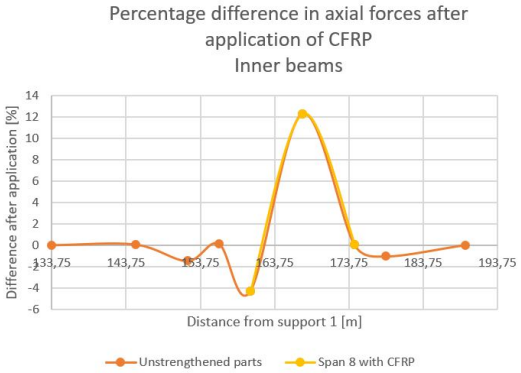

Figure 8.12: Impact on axial forces in inner beams after application of CFRP

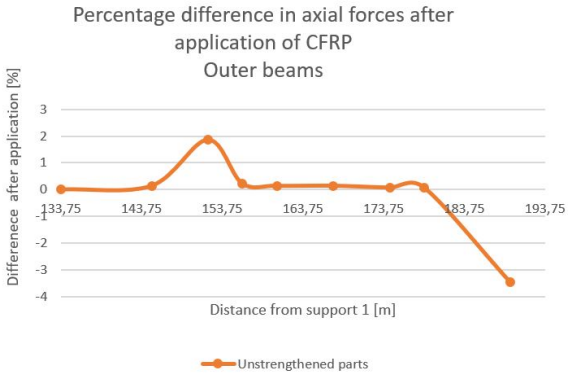

Figure 8.13: Impact on axial forces in outer beams after application of CFRP

The deviations in axial forces are small. Some deviations can be explained by errors when obtaining the stresses from reinforcement in Abaqus. This shows that the application of CFRP in the model mainly does not affect the acting axial forces in the bridge globally. The exceptions occur in ZM 8-9 and field 8, where a local effect of the stiffness of the CFRP appears. An interesting aspect is that the CFRP does not affect the axial forces in the outer beam. The increased stiffness of the inner beams does not contribute to additional restraining forces imposed by the ASR expansion.

Until the span between axis 8 and 9, where the CFRP is placed, the moment distribution is quite similar in both models. However, in field 8 there is an increase in the acting moment. This is expected since the moment capacity and

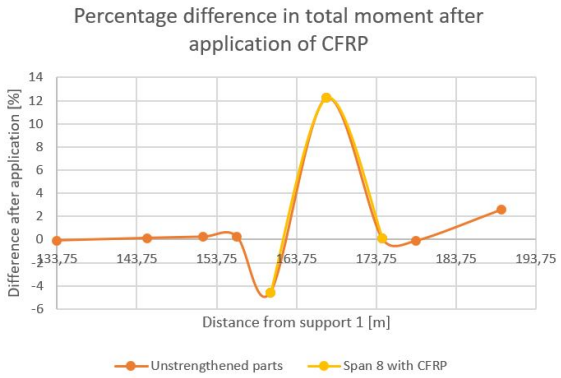

Figure 8.14: Impact on total moment after application of CFRP

stiffness is increased when applying CFRP. In a statically indefinite structure where parts of the structure become stiffer, a higher moment will occur in these parts.

8.3 Evaluation of Global Behaviour

The simplicity in making a model of beam elements, such as in the frame model, makes it possible to get a good overview of the global behavior in the bridge. The assumed expansion field is evaluated for an uncracked, cracked and CFRP-strengthened situation.

The model was verified in alignment with the solid model but is still a significantly simplified version of the reality. Despite this, the principles occurring in the global model is evaluated to be representative of the bridge. The main focus is to see how the crack and CFRP is changing the global behavior and the total elongation.

The behavior of the bridge is very constant in field 1-6 in the uncracked simulation. The change towards the end of the bridge is due to an extra amount of reinforcement and the impact of the expansion near the hinged end. For a situation where the whole bridge is in stage I, the total elongation is 185.369 mm when reinforcement is included.

A symmetrical cracked situation is simulated. Here, both the inner beams are cracked to the left of support 4, to the left of support 7 and the right of support 8. Since the sections gets a lower stiffness, less forces are imposed. This is seen as the lighter fields in figure 8.15b. The cracks making the structure less stiff, increase the bridge's total strain with 0.354 mm, giving an elongation of 185.723 mm.

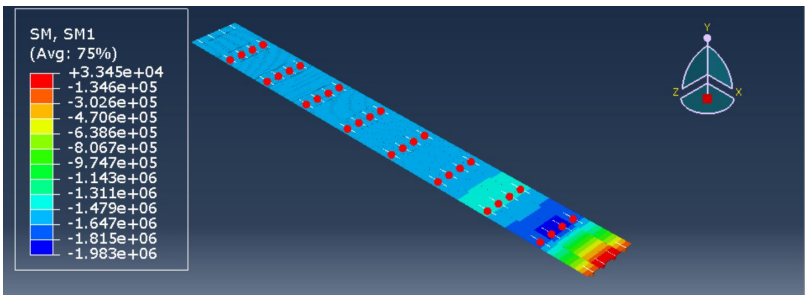

(a) Moments for the uncracked bridge

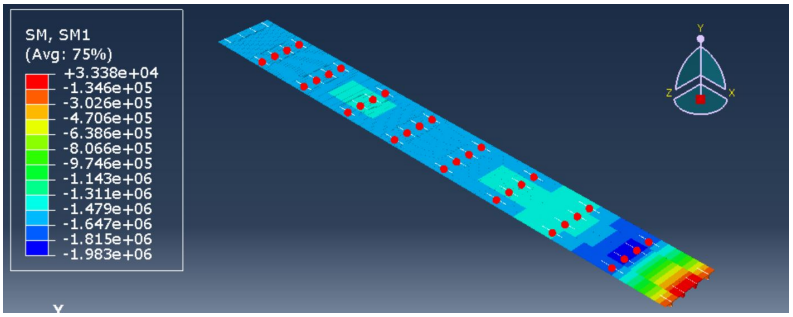

(b) Moments for the cracked bridge

The output from Abaqus is visualized in the figures above. It is important to be aware that these numbers only show the impact on the concrete as the contributions from the steel are added manually. The moment is therefore just the global secondary moment coming from the gradient in the expansion field. However, the elongation of the bridge will be affected directly by the steel retaining the concrete's expansion.

Carbon fiber reinforcement is then evaluated as a strengthening for ASR-damaged concrete. The fictitious situation where the fiber was applied form the start of the ASR-development, as explained in section 8.2.1, is submitted.

The elongation is reduced solely with 0.038mm. The effect of the crack has a larger impact on the structure than the strengthening has. This is due to that the stiffness is much more affected by cracks than it is from the increase due to what the CFRP provides.

The observed effects of the CFRP strengthening do not have a significant impact on preventing the ASR-expansion, nor reducing the load coming from it. In reality, the CFRP at Elgeseter Bridge was applied after it was exposed to the majority of the ASR expansion. Therefore, the CFRP has not yet really been subjected to any significant expansion. Further expansion is still expected, but interpreting the result from this model, the CFRP will most likely give no preventing effect towards this.

Chapter 9

Capacity Control in ULS

Capacity control for selected sections have been performed in the ultimate state and only for the inner beams. The inner beam will be more utilized compared to the outer beam. This is because the inner beam is subjected to higher traffic loads and the restraint forces imposed by ASR expansion sets the inner beams in tension. The tension force has a significantly negative impact on the moment capacity, whereas the outer beam is exposed to a compression force which will increase the moment capacity. Later in the report, the effect of carbon fiber reinforcement will be evaluated and this only applies to the inner beam. Limiting the capacity control to the inner beam is therefore concluded to be adequate.

Representative sections for support 2-8 and field 2-8 as well as for support 1 and 9 and field 1 and 9, have been controlled in regards to moment capacity.

The shear forces are higher towards the end of the bridge and therefore the shear capacity will be the most critical in this part. According to Nordhaug and Stemland, not any section of the bridge has a critical shear capacity utilization [4]. As carbon fiber strengthening only has been performed at the sections of zero moments, the calculated shear capacity is limited to these sections.

9.1 Moment Capacity in ULS

Elgeseter bridge is a beam bridge with beams carrying the bridge deck. The beam and the plates are monolithically cast as one. This means that the plate and the beam will act in a fully compatible way. Therefore, it is defined as a T-cross section. When calculating the capacity of this section, the size of the active part of the plate has a width limitation. This dimension must be found to calculate the moment capacity.

Due to the variation in reinforcement throughout the bridge, the moment capacity will change within the beams. The reinforcement is shown in the original drawings in appendix A. For the capacity control, the amount of active reinforcement has been chosen to represent the real situation. In addition to the main reinforcement, the contribution from inclined bars and stirrup anchoring bars is included.

The inclined bars are most likely activated as tension reinforcement in the bridge. Due to their inclination at 45°, the total area will not be effective. Therefore it is decided to include 70 % of the inclined bars in the lower face. In addition, 70% of the inclined bars in the upper face are included, assuming that these also contribute as tension reinforcement due to the small compression zone.

According to NS 3473, the strain in the reinforcement can not exceed 1 ‰. The sections' total capacity is decided from the capacity of the compression zone. This is not valid if the strain of the steel exceeds 1‰. If this occurs, it is required to do another evaluation of the strain in the concrete. The strain control of the steel must include the initial strain in the reinforcement coming from imposed ASR deformation.

Under-reinforced cross sections are assumed which indicates that the reinforcement will yield before the concrete crushes. The amount of reinforcement is relatively low and ε_s is assumed to be larger than ε_{cu} for M_{Rd}. This assumption must be verified.

9.1.1 Effective Flange Width

The effective flange width defines the part of the flange that is activated in the ultimate state. This is only relevant when the flange is set in compression, where the capacity is calculated for a T-cross section with the effective flange width. On the contrary, when the flange is in tension, the capacity will be calculated for a rectangular section with a width equal to the web, b_w [50].

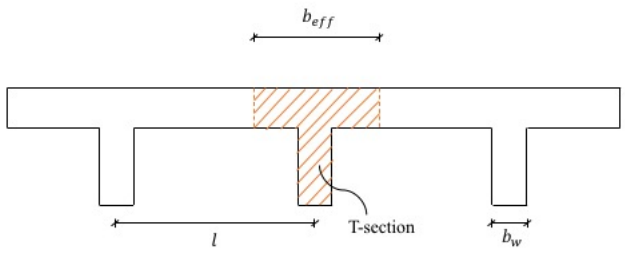

Figure 9.1: Illustration of b$_e ff$

In accordance with NS 3473, $b_{eff} = b_{eff,1} \cdot 2 + b_w$.
Where b_w is the width of the web and $b_{eff,1}$ is the effective distance on one side of the web. The distance is given by:

$$b_{eff,1} = min \begin{cases} b_1 \\ 0.1 \cdot l_0 \\ 8 \cdot t_f \end{cases} \tag{9.1}$$

Where b is the original width, l_0 is the distance between the zero moment sections and t_f is the thickness of the flange. l_0 is set to $0.7 \cdot l$ following NS EN

1993, where l is the span length.

The size of the effective flange width is depending on the actual flange width, the static system and the thickness of the flange. In this case, only the static system varies for the sections giving different values of l_0. Since all the fields 1-8 have identical boundary conditions, the effective flange width is calculated equally even though field 1 is somewhat shorter. In field 9 there is a roller support at the end and this changes the static system leading to a different effective flange. The calculations are performed after NS 3473, section 9.5, and is shown thoroughly in appendix C.A. This is resulting in the effective widths reported in table 9.1

	Effective flange width [mm]
Field 1-8	3950
Field 9	4412

Table 9.1: Effective flange widths

The sections over the supports will have tension in the flange and are therefore calculated differently. However, an important aspect is that all the reinforcement within the effective flange width shall be included in the capacity control even though the width is set to the web's dimension.

9.1.2 Sections over Supports

The sections over the supports are equally reinforced in support 2-8 and therefore obtains the same capacity. Support 1 and support 9 differs and are calculated separately.

The support sections are calculated as a rectangular cross-section with the width b_w and including all the tension reinforcement within b_{eff}. With the permanent loads, a negative moment will be imposed with tension in the upper part, illustrated in figure 9.2.

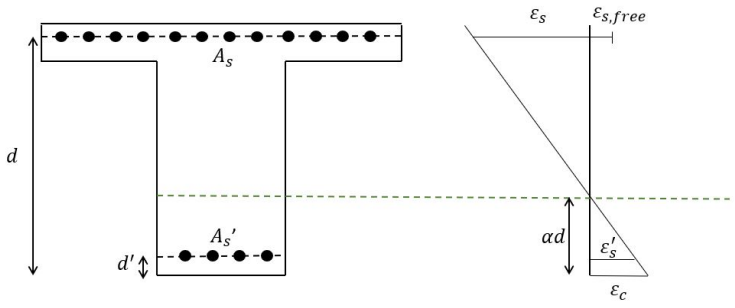

Figure 9.2: Strain in support sections

The height of the compression zone, αd, is obtained by defining α from equation (9.2).

$$\alpha = \frac{f_{yd}A_s - f_{yd}A'_s}{0.8 f_{cd} b d} \tag{9.2}$$

Where A_s is the tension reinforcement and A'_s is the compression reinforcement. It is assumed that all the reinforcement is yielding, and this must be verified. Besides, the total strain can not exceed 10 ‰ and verification including the initial strain due to ASR must be performed.

The latter is controlled for the tensile reinforcement using the following equation:

$$\varepsilon_s = \frac{\varepsilon_{cu} \cdot (1 - \alpha)}{\alpha} + \varepsilon_{s,free} \leq 0.01 \tag{9.3}$$

In addition, yielding in the compression reinforcement must be controlled also including the initial strain:

$$\varepsilon'_s = \frac{\alpha d - d'}{\alpha d} \cdot \varepsilon_{cu} - \varepsilon'_{free} \geq 0.00136 \tag{9.4}$$

Finally, the moment capacities for the support sections are obtained by taking equilibrium of the cross section:

$$M_{Rd} = 0.8\alpha \cdot (1 - 0.4\alpha) \cdot f_{cd} \cdot b \cdot d^2 + f_{yd} \cdot A'_s \cdot h' \tag{9.5}$$

The results are reported in table 9.2 and a thorough calculation is given in appendix C.C.1.

	Inner beam [kNm]	Outer beam [kNm]
Support 1	-9 557	-8 029
Support 2-8	-9 947	-9 654
Support 9	-12 302	-11 140

Table 9.2: Moment capacity over supports

9.1.3 Sections in Fields

Likewise, for the field sections, the amount of reinforcement is equal for field 2-8 and changes in field 1 and field 9.

In the field sections, the compression zone is in the upper part of the section, illustrated in figure 9.3. Usually, in cases where it is a large T-cross section, the compression zone is very small. The neutral axis is likely to lie within the flange area. If the flange has a relatively large height, the section can be calculated as a rectangular cross-section with the width b_{eff}. The demand for a thick flange

for concrete B20-B45 is that $t/d > 0.33$ [50].

If the flange is rather thin, a small compression zone results in the strain of the reinforcement becoming significantly large before the ultimate strain is achieved in the concrete. If $\varepsilon_s < \varepsilon_{cu}$ the neutral axis might be in the flange. To simplify this, it can be assumed that there is constant compression in the flange with a resulting compression force acting in the middle of the flange. This method is applied if the strain of the steel exceeds 1‰[50].

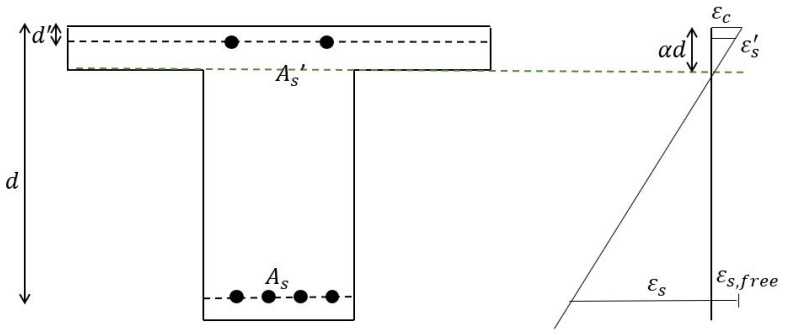

Figure 9.3: Strain in field sections

The compression zone is found by equilibrium:

$$\alpha = \frac{f_{yd}A_s - f_{yd}A'_s}{0.8 f_{cd} b d} \tag{9.6}$$

The strain in the reinforcement is controlled by:

$$\varepsilon_s = \frac{\varepsilon_{cu} \cdot (1-\alpha)}{\alpha} + \varepsilon_{s,0} \leq 0.01 \tag{9.7}$$

In Elgeseter Bridge, all field sections have $\varepsilon_s \geq 1‰$, which indicates a thin flange. The moment capacity in ULS is found by assuming constant compression in the flange:

$$M_{Rd} = f_{yd}A_s(d - \frac{t}{2}) + f_{yd}A'_s(\frac{t}{2} - d') \tag{9.8}$$

An additional control of the stress in the concrete is performed, assuring that $\sigma_c \leq_{cd}$:

$$\sigma_c = \frac{M_{Rd}}{t \cdot b_{eff}(d - t/2)} \tag{9.9}$$

Results are presented in table 9.3. Calculations are shown in appendix C.C.2.

	Inner beam [kNm]	Outer beam [kNm]
Span 1	5980	5682.7
Span 2-8	6400	5832
Span 9	9128.8	8300

Table 9.3: Moment capacity in fields

9.1.4 Zero Moment Sections

The zero moment section lies in the transition between the field area and the support area. Ideally, the moment would be zero. Despite this, the reaction from the ASR-load will set the lower part in tension and the upper part in compression. Accordingly, the zero moment sections will be calculated by the same procedure as the field sections.

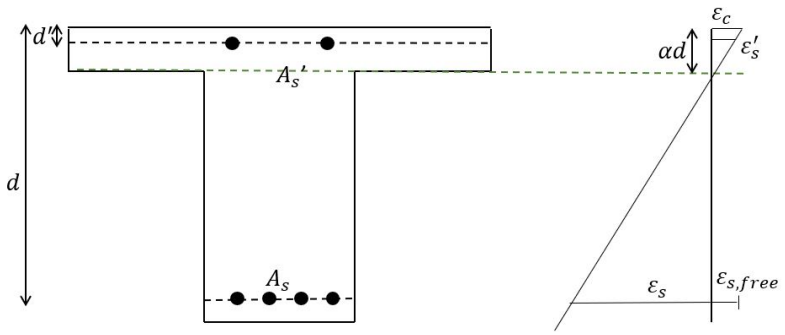

Figure 9.4: Strain in zero moment sections

The zero moment section stands out as a section with a poor amount of reinforcement compared with the rest of the bridge. The demand for minimum reinforcement was not a requirement at the time the structure was built and the capacity is significantly lower than other sections.

The compression zone is found by equilibrium:

$$\alpha = \frac{f_{yd}A_s - f_{yd}A_s'}{0.8 f_{cd} b d} \tag{9.10}$$

The strain in the reinforcement is controlled by:

$$\varepsilon_s = \frac{\varepsilon_{cu} \cdot (1-\alpha)}{\alpha} + \varepsilon_{s,0} \leq 0.01 \tag{9.11}$$

All zero moment sections have $\varepsilon_s \geq 1‰$, which indicates a thin flange. The moment capacity in ULS is found by assuming constant compression in the flange, as explained earlier:

$$M_{Rd} = f_{yd}A_s(d - \frac{t}{2}) + f_{yd}A'_s(\frac{t}{2} - d') \tag{9.12}$$

An additional control of the stress in the concrete must be performed, assuring that $\sigma_c \leq_{cd}$:

$$\sigma_c = \frac{M_{Rd}}{t \cdot b_{eff}(d - t/2)} \tag{9.13}$$

Annex **??** shows thorough calculations. Results are presented in table 9.4.

	Inner beam [kNm]	Outer beam [kNm]
Zero moment section	1332	1377

Table 9.4: Moment capacity in zero moment sections

9.2 Capacity of Moment and Axial Force Combined in ULS

As the inner beams are subjected to an axial tension force, it is essential to find the capacity of both combined. The method is obtained by S.Sørensen [50].

The procedure involves using different strain failure criteria and finding the equivalent moment and axial force that gives these strains. This results in a diagram that presents different combinations of M and N at maximum capacity. By drawing a line between the different combinations, one can obtain an estimate of combinations that would give a failure. This diagram is called an M-N diagram.

There are four main ultimate states which are controlled:

1. $\varepsilon_c = \varepsilon_{cu} = 0.0035$ and $\varepsilon_s = \varepsilon_{yd} = 0.00136$

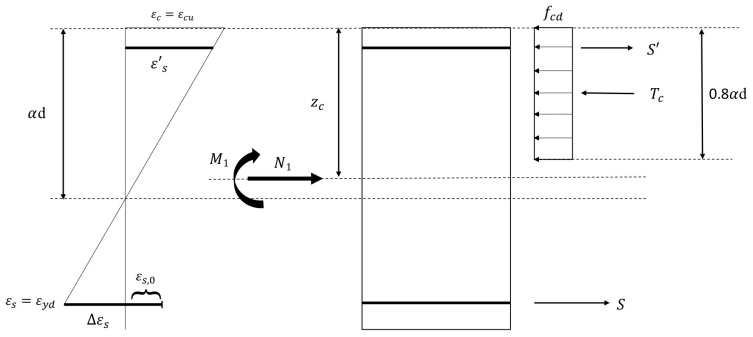

Figure 9.5: Strain Failure 1

2. $\varepsilon_c = \varepsilon_{cu} = 0.0035$ and $\varepsilon_s = 0.01$

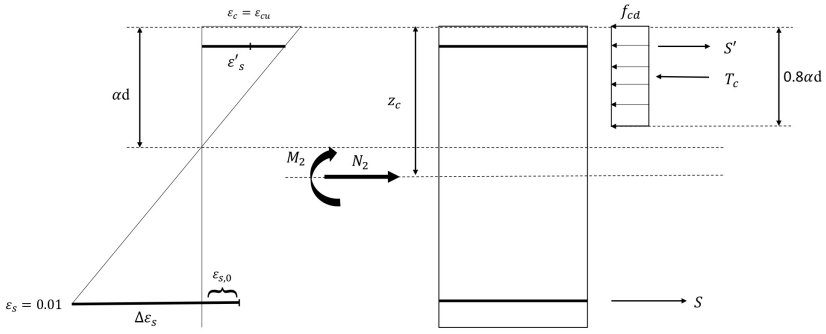

Figure 9.6: Strain Failure 2

3. $\varepsilon_c = 0$ and $\varepsilon_s = 0.01$

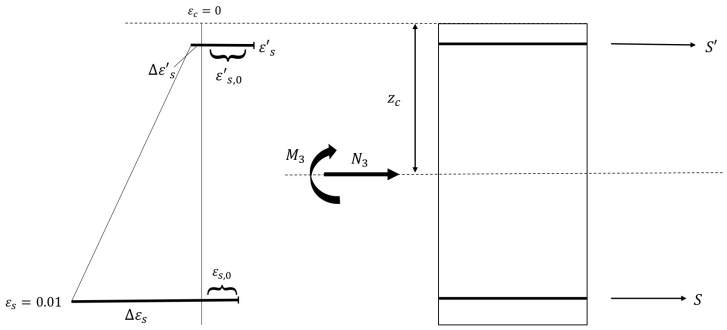

Figure 9.7: Strain Failure 3

4. $\varepsilon'_s = \varepsilon_{yd} = 0.00136$ and $\varepsilon_s = 0.01$

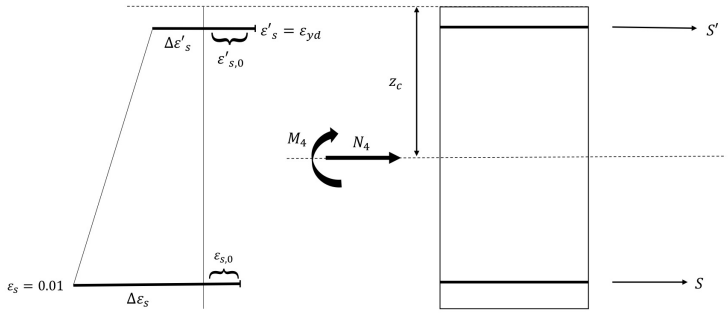

Figure 9.8: Strain Failure 4

To preserve the effects due to ASR-loading, the capacity control is calculated as a pre-stressed beam. The initial strain in the reinforcement is the strain from free expansion caused by ASR-load. This is accounted for in the total strain in the steel, but is not providing stress directly to the concrete.

By investigating relevant sections such as the field-section, support-section, and section of zero moments, one can see how the axial force is influencing the moment capacity. A compression force is increasing the moment capacity for all sections. The outer beams are subjected to such a compression force and this will be beneficial for the entire beam. A tensile force will significantly decrease the moment capacity. Consequently, the capacities found in section 9.1 are changing due to the axial force.

The same amount of reinforcement is used as in section 9.1. The initial strain in the steel depends on the steel's location. The expansion decreases with 0.5 ‰ over the cross-section in the inner beam, giving a gradient of $2.92 \cdot 10^{-4}$‰ pr mm.

The calculations done for each point are found in appendix C.C.4. This results in the following MN-capacities for field sections 2-8, support sections 2-8 and the zero moment sections. In these tables, a positive N indicates a tensile force and a positive M gives tension at the lower face

Field sections		
Point	N	M
1	-16 057	8 663
2	-9 557	9 7867
3	4 689	4673
4	4 689	4673

Table 9.5: Combined moment and axial force
Field sections

Support sections		
Point	N [kN]	M [kNm]
1	-7 288	-13 188
2	261	9 729
3	9 813	479
4	10 224	928

Table 9.6: Combined moment and axial force
Support sections

Support sections		
Point	N [kN]	M [kNm]
1	-19 5886	5 265
2	-12 349	5 973
3	1 934	959
4	1 934	959

Table 9.7: Combined moment and axial force
Zero moment sections

Figure 9.9 shows clearly how the moment capacity is influenced as the axial force is changing.

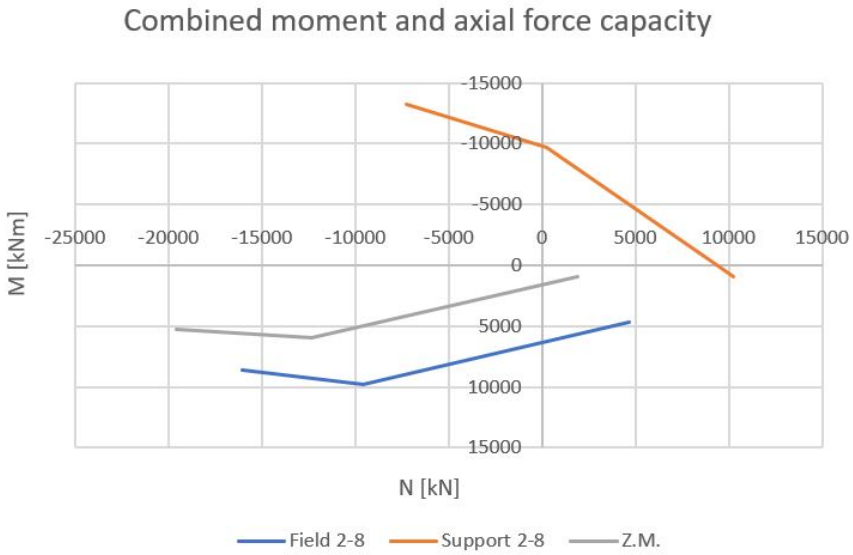

Figure 9.9: Capacity with combined moment and axial force

A high additional tension force is crucial for the sections. The moment capacity is strongly reduced with high axial forces. The sections of zero moments are the most critical section. It only allows a tension force of 1 934 kN to still be in equilibrium. With this force, the moment capacity is reduced to 960 kNm.

Looking at the field section, the maximum axial tension force is 4 968 kN with the respective moment capacity of 4 673 kNm. Regarding the support sections, a maximum tension force of about 9000 kN can be applied to section, but then the moment capacity for negative moments (tension in the upper part) is approximately zero.

9.3 Shear Capacity in ULS

9.3.1 Shear Capacity in ULS without Axial Forces

The shear capacity is only calculated for the critical sections. Some of the zero moment sections have been strengthened with shear carbon fiber reinforcement. To understand the effect of this, the original shear-capacity must be investigated. Shear capacity is only calculated for the inner beams, as they are strengthened.

Shear capacity is calculated by the design rules in NS 3473. Shear-tension capacity V_{sd} is obtained by three different contributions.

V_{co} is the contribution from the concrete and is calculated by:

$$V_{co} = 0.3 \cdot (f_{td} + \frac{k_A \cdot A_s}{\gamma_c \cdot b_w \cdot d}) b_w \cdot d \leq 0.6 \cdot f_{td} \cdot b_w \cdot d \cdot k_V \tag{9.14}$$

Shear capacity contribution from stirrups $V_{sd,s}$ is calculated by the following:

$$V_{sd,s} = \frac{f_{yd} \cdot A_{s,s}}{S_s} z \cdot (1 + \cot\,\alpha)\sin\,\alpha \tag{9.15}$$

α is defined as the inclination of the stirrups. In this case, $\alpha = 90°$.

Contribution from the inclined longitudinal reinforcement $V_{sd,i}$ is found by eq. (9.16). Inclined longitudinal reinforcement is defined as the reinforcement in a section at 45°, at a point $z = 0.9 \cdot d$ from the bottom of the beam, see figure 9.10. θ is assumed to be 90°.

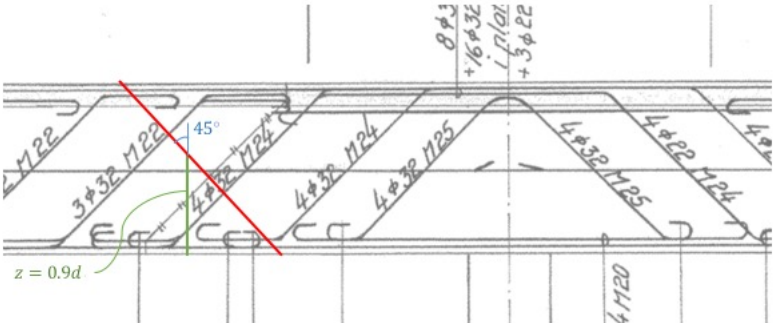

Figure 9.10: Section to find the contribution from inclined reinforcement

$$V_{sd,i} = \sum f_{yd} \cdot A_{s,i} \cdot \sin\,\theta \tag{9.16}$$

Shear-compression capacity is calculated by:

$$V_{ccd} = 0.3 \cdot f_{cd} \cdot b_w \cdot (1 + \cot\,\alpha) \tag{9.17}$$

With the following condition:

$$V_{ccd} \leq 0.45 \cdot f_{cd} \cdot b_w \cdot z \tag{9.18}$$

Detailed calculations are found in appendix C.D. Calculations give the following results:

$V_{co} = 441.9$ kN
$V_{sd,s} = 603$ kN
$V_{sd,i} = 1082.5$ kN

Such that:

$V_{sd} = V_{co} + V_{sd,s} + V_{sd,i} = 2127.4$ kN

Shear-compression capacity:
$V_{ccd} = 2880$ kN

9.3.2 Combined Shear and Axial Force Capacity in ULS

According to NS 3473 section 12.3.2.3, a beam subjected to both shear and tensile axial force should have the contribution from the concrete in shear-tension capacity as the largest of the following:

$$V_{cd,0} = V_{co} \cdot (1 - \frac{N_f}{1.5 \cdot f_{td} \cdot A_c}) \geq 0 \tag{9.19}$$

$$V_{cd,0} = V_{co} \cdot (1 - \frac{\varepsilon_s}{\varepsilon_{yd}}) \tag{9.20}$$

Where ε_s is the strain of the longitudinal reinforcement when the beam is subjected to all acting forces and $\varepsilon_s \leq \varepsilon_{yd}$.

The beams subjected to axial compression will increase its capacity in ULS. Since the capacity without axial force is assumed to be adequate, this is not calculated for the outer beam. If the capacity of the outer beam is found to be insufficient, this will be included.

There is assumed an axial tension force found in the results from the solid model. By these calculations, it is found that $V_{cd,0} = 0$. Detailed calculations can be found in appendix C.D.1. This results in following shear capacity in ULS when the section is subjected to both shear and axial tension force:

$V_{sd} = V_{sd,s} + V_{sd,i} = 1685.5$ kN

Chapter 10

Capacity of CFRP in ULS

The carbon fiber reinforcement will contribute to additional strength. The capacity of the strengthening is calculated by using fib bulletin 90 [18]. The methods are explained in chapter 6.

10.1 Moment Capacity

Moment capacity of strengthened beams is obtained according to 6.2. All failure modes must be considered as discussed earlier. With externally bonded CFRP the stiffness of the section increases, which leads to an increase in the design bending moment capacity for the cross-sections. Still, the aspects of debonding due to cracks and end-debonding are important to be considered. These failures modes are brittle and rapid which is undesirable.

The capacity is obtained for field sections and zero moment sections. This is due to the fact that these sections are critical and strengthened. To obtain the moment capacity, only longitudinal reinforcement strips are included. The mechanical properties of the CFRP strips can be found in table E.1.

10.1.1 Design Bending Moment Capacity in ULS

The method of finding moment capacity is obtained from fib bulletin [18] appendix 6.1. The method finds flexural resistance by taking moment equilibrium about the attack point of the compression force. The compression zone is evaluated by force equilibrium and considers the compression distribution in the concrete by the strain in the concrete.

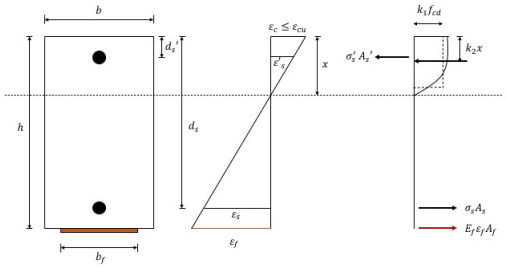

Figure 10.1: Section capacity in ULS

To find the flexural resistance of the cross-section, moment equilibrium is taken about the attack point of the compression force.

$$M_{Rd} = A_s \cdot \sigma_s \cdot (d_s - k_2 \cdot x) + A_f \cdot E_f \cdot \varepsilon_f \cdot (h - k_2 \cdot x) \tag{10.1}$$

By taking equilibrium of the internal forces in the cross section, an expression for the compression zone is found:

$$x = \frac{A_s \cdot \sigma_s + A_f \cdot f_{td}}{k_1 \cdot f_{cd} \cdot b} \tag{10.2}$$

Using the formulas below the factors k_1 and k_2 is obtained based on the concrete's strain:

$$k_1 = \begin{cases} 1000\varepsilon_c \cdot (0.5 - \frac{1000}{12}\varepsilon_c) & \text{for } \varepsilon_c \leq 0.002 \\ 1 - \frac{2}{3000\varepsilon_c} & \text{for } 0.002 \leq \varepsilon_c \leq 0.0035 \end{cases} \tag{10.3}$$

$$k_2 = \begin{cases} \frac{8-1000\varepsilon_c}{4\cdot(6-1000\varepsilon_c)} & \text{for } \varepsilon_c \leq 0.002 \\ \frac{1000\varepsilon_c(3000\varepsilon_c-4)+2}{2000\varepsilon_c(3000\varepsilon_c-2)} & \text{for } 0.002 \leq \varepsilon_c \leq 0.0035 \end{cases} \tag{10.4}$$

Detailed calculations is found in appendix E.A.1. The moment capacity of the cross sections is presented in the table below:

Section	Moment capacity
Field sections	9048 kNm
Zero moment sections	4323 kNm

Table 10.1: Bending moment capacity of cross sections

10.1.2 Combined Moment and Axial Force Capacity

The same procedure as used in section 9.2 is executed to obtain the limitation of the combined moment and axial force allowed in the sections with FRP.

The estimated strain failures are:

1. $\varepsilon_c = \varepsilon_{cu} = 0.0035$ and $\varepsilon_s = \varepsilon_{yd} = 0.00136$

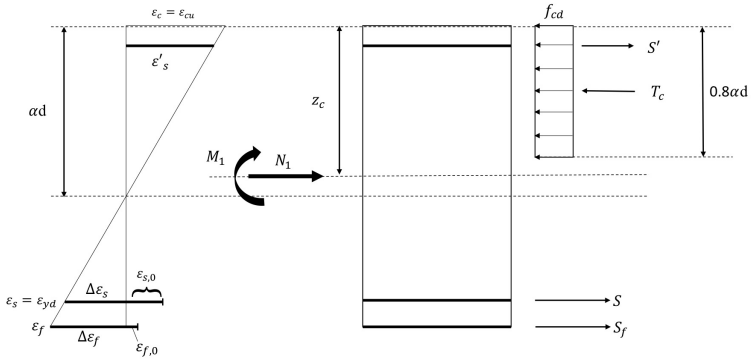

Figure 10.2: Strain Failure 1

2. $\varepsilon_c = \varepsilon_{cu} = 0.0035$ and $\varepsilon_f = \varepsilon_{fu} = 0.01038$

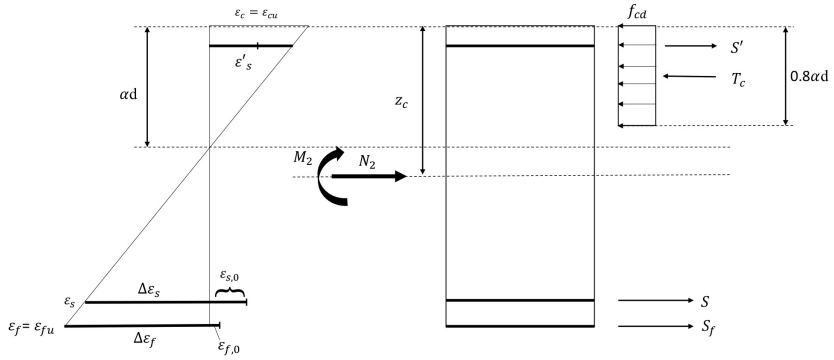

Figure 10.3: Strain Failure 2

3. $\varepsilon_c = 0$ and $\varepsilon_f = \varepsilon_{fu} = 0.01038$

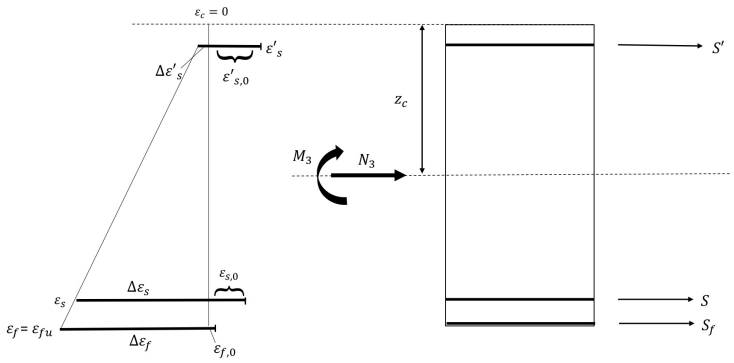

Figure 10.4: Strain Failure 3

4. $\varepsilon'_s = \varepsilon'_{yd} = 0.00136$ and $\varepsilon_f = \varepsilon_{fu} = 0.01038$

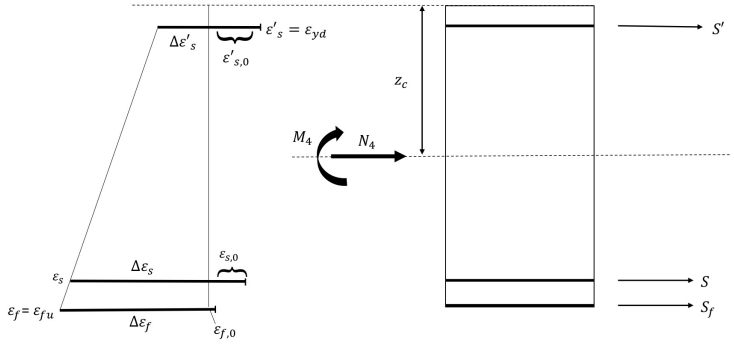

Figure 10.5: Strain Failure 4

Detailed calculations can be found in E.A.2. Results are presented below:

	M [kNm]	N [kN]
Strain failure 1	8705	-1620
Strain failure 2	11 569	-8178
Strain failure 3	6436	6154
Strain failure 4	6436	6154

Table 10.2: Combined moment and axial force capacity
Field sections

	M [kNm]	N [kN]
Strain failure 1	5537	-1935.6
Strain failure 2	7802	-1124
Strain failure 3	2726	3399
Strain failure 4	2726	3399

Table 10.3: Combined moment and axial force capacity
Zero Moment Sections

The sections can sustain all combinations of M and N within the lines presented in figure 10.6.

Figure 10.6: Combined moment and axial force capacity with CFRP

10.1.3 Intermediate Crack Debonding

The capacity of intermediate crack debonding is found by the design rules given in 6.2.1. Detailed calculations can be found in appendix E.A.2.3.

To prevent intermediate crack debonding, the change of tensile force in FRP, ΔF_{fEd}, must be lower than the change in resistance, ΔF_{fRd}, at an element between cracks as explained in section 6.2.1.

The acting bending moment due to live loads and self-weight between the axis and zero moment section is negative and will therefore not be critical. As a consequence, only an area between zero moment sections and field sections is evaluated.

Calculations in appendix E.A.2.3 gives the following properties:

b_f	60 mm
n_f	8
s_r	400 mm
k_b	1

Table 10.4: Properties in calculation of ΔF_{fd}

τ_{b1d} and τ_{bFd} is obtrained by eq. (10.5) and (10.6)

$$\tau_{b1d} = 0.23 \cdot k_b^2 \cdot f_{cm}^{2/3} / \gamma_{BA} \tag{10.5}$$

$$\tau_{bFk} = 10.8 \cdot \alpha_{cc} \cdot f_{cm}^{-0.89} / \gamma_{BA} \tag{10.6}$$

The intermediate crack debonding capacity is found to be:

$\Delta F_{fd,B} = 36$ kN

$\Delta F_{fd,F} = 60.56$ kN

$\Delta F_{fd,C} = 4.14$ kN

Summarizing all of the contributions, the resistance of change in tensile forces at each element is:

$\Delta F_{fRd} = 100.7$ kN

10.2 Shear capacity

10.2.1 Shear Strengthening due to Insufficient Shear Capacity

The contribution from the fiber reinforcement to the shear capacity is calculated by following section 6.3.

As described in section 4.2.4 the carbon reinforcement used for shear strengthening is SIKA Wrap Hex-230C. It is applied with 5 layers and laid in eight strips with $b_f = 300$ mm. These are placed with an angle $\alpha = 45°$. Only four of the strips are active over the existing crack and contribute to the shear capacity in the cracked section [51].

The general increase in shear capacity is calculated for a hypothetical shear crack and it is assumed to have an angle of $\theta = 45$ to obtain the lowest shear tension capacity the reinforcement can give. The situation is illustrated in figure 10.7

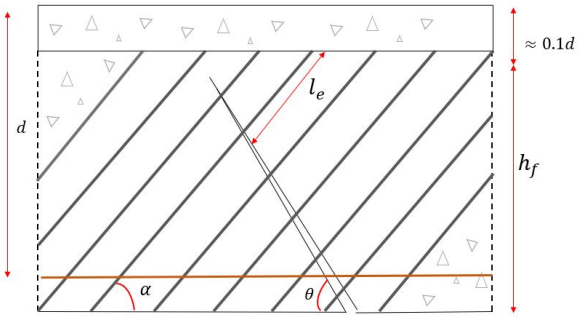

Figure 10.7: Shear FRP over a 45° crack

The capacity is obtained by using equation (6.25) and is thoroughly shown in appendix E.A.3.1. The following properties are defined:

A_{fw}	301.6 mm
s_f	0.503 mm
h_f	1309.6 mm
θ	45 °
α	45 °
f_{fbwd}	508.5 MPa

Table 10.5: Properties of shear CFRP

The effectiveness of each layer is reduced when multiple layers are applied. In this case, there are five layers with a thickness of $t_0 = 0.128$ mm. The total thickness is reduced to an effective thickness of $t_f = 0.502$. The total area contributing to the shear capacity is given as $A_f = 2 \cdot b_f \cdot t_f$ since it is symmetrically placed on both sides of the beam.

The application of the CFRP covers the entire web and is defined as a full-depth FRP. The shear crack is assumed to extend over a height equal to $h_w - 0.1d_s$. Due to the full-depth application, the height of the FRP strengthening crossed by the shear crack is equal to the crack-height itself. Since there is no spacing between the strips, it is considered to be a full area bond with spacing $s_f = b_f / sin\alpha$.

The application is not entirely closed and it is placed like an u-wrap. To find the design strength of the fiber reinforcement f_{fwd}, the bond strength f_{fbwd} must be controlled and compared to the strength of a closed system $f_{fwd,c}$ as explained in section 6.3.2. The bond strength is found to be the decisive design strength.

The bond strength is found by using equation (6.28). This assumes that all the strips intersected by the shear crack have a bond length greater than the

effective bond length l_e. This must be verified by calculating l_e.

Given the following properties in table 10.5 the shear capacity is found.

$$V_{Rdf} = 670 \text{ kN} \tag{10.7}$$

Exisiting crack

In the existing crack, it can be assumed that all the steel is ineffective, though x-ray photos may indicate otherwise [51]. This means that only the shear reinforcement can carry the shear forces over the crack. It is assumed that the structure is carrying the self-weight as this force is already exposed to the structure at the time of application. Thus, the fiber reinforcement in the cracked section must carry all the other live loads.

This crack is most likely not caused by insufficient shear capacity as crack shows more characteristics to a bending crack rather than a shear crack. Despite this, the same method has been used to find the shear capacity as above, with some modifications shown in appendix E.A.3.1. The shear force can only be transmitted by the fiber reinforcement. Knowing that four of the strips is contributing to the shear capacity, the total capacity in the cracked section can be found.

The same conditions for $l_b > l_e$ are controlled, resulting in that some of the strips have a less bond length than the effective length. This is due that when such a large vertical crack is spanning over the web, the upper strip most likely has a $l_b < l_e$ in accordance to figure 10.8. The four activated straps are indicated with a grey color. The lower strip is anchored further under the web and this will have an adequate bond length. As the extent of the crack is uncertain, it is on the safe side it is assumed that one strip has a bond length less than the effective length. The strength of the fiber reinforcement is therefore reduced.

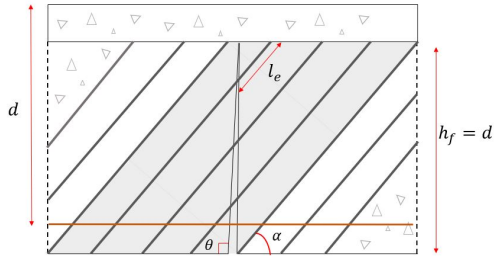

Figure 10.8: Shear FRP over the existing crack

The highest vertical shear force possible that can be sustained by one strip is found to be $V_{Rd,s} = 125.1$ kN. Since the crack activates four of the strips, the total shear capacity will be:

$$V_{Rdf,zm} = 500.4kN \tag{10.8}$$

10.2.2 Shear strengthening due to Flexural Debonding

The fiber shear reinforcement is placed locally at the beam over the cracked sections. Thus, most parts of the regarded beam are without shear fiber reinforcement but still have flexural reinforcement. This can lead to the failures described in section 6.3.3. A control for concrete cover separation and shear-induced intermediate crack debonding must be performed.

If the shear capacity concerning concrete cover separation is exceeded there should be transverse strips at the end of the flexural fiber reinforcement. While, if the shear resistance against shear-induced intermediate debonding is exceeded, transverse strips should be distributed over the entire span. This is to optimize the flexural fiber reinforcement's strength and prevent local failures.

The limit for the acting shear force preventing concrete cover debonding is found by using equation (6.32), which is a reduced shear resistance $V_{Rd,c,fe}$. The critical section is close to the column and properties for a support section are used. The amount of tension reinforcement and the geometrical placement is important. Table 10.6 shows the properties used for the calculations and the steps are shown in Annex E.A.3.2.

a_f	200 m
ρ_s	$1.9 \cdot 10^{-2}$
V_{co}	441.9 kN

Table 10.6: Properties for concrete cover control

This leads to the acting shear force being limited to:

$$V_{Rd,c,fe} = 351.2 \text{ kN} \tag{10.9}$$

Intermediate debonding due to shear cracks may also occur when subjected to a high shear force. Most likely it will occur in the field area. The limit preventing shear induced flexural debonding is found by rearranging equation (6.35) to get the highest allowed acting shear force. The calculations are reported in Annex E.A.3.2 and important properties are listed in table 10.7.

A_{sw}	265
s	175
z	1413
θ	45 °
α	45 °
$V_{Rd,max}$	288 kN

Table 10.7: Properties for shear induced intermeidate debonding

This gives an acting shear force restricted by the value of $V_{Ed,max}$:

$$V_{Ed,max} = 468kN \tag{10.10}$$

Chapter 11

Results

11.1 Resulting ASR-Loads

Both the frame model and the solid model have been evaluated thoroughly. The models are considered to be representative of the acting forces in the bridge, especially the axial forces. It is important to bear in mind that the assumptions made in both models contribute to differences. This is discussed thoroughly in section 7.3.

The areas of the bridge which are not modeled in the solid model are represented by the results from the frame model. The solid model is inadequate to obtain the difference in resulting moments in the inner and outer beam, whereas these dissimilarities are easy to derive in the frame model.

Analyses including cracked sections are used when deriving forces in the models. This results in lower acting forces in some sections. Nevertheless, it is considered to be preferable since it takes into account the redistribution of forces, which is reasonable to believe occurs in the bridge.

Temperature field 2 has a linear strain gradient in both directions and is considered to be the most accurate. In light of this, temperature field 2 is submitted in the solid model to obtain the acting forces in the bridge. Since these results give axial forces 20% higher compared to temperature field 1, it is considered conservative to evaluate temperature field 2.

11.1.1 Elongation of Models

Simulation	Frame Model TF 1	Solid Model TF 1	Solid Model TF 2
Free exp.	1.12‰	1.112‰	1.101‰
Free exp. w/crack	1.1225‰	1.124‰	not analyzed
Restrained exp.	0.9268 ‰	0.9547‰	0.9526‰
Restrained exp. w/crack	0.9286‰	0.9675‰	0.965‰

Table 11.1: Strain from different simulations in Abaqus

The strain obtained in a cracked and restrained situation gives an elongation of 185.72 mm in the frame model. Implying the strain in the solid model to the whole bridge gives a total elongation of 193.5 mm for the same temperature field.

An interesting observation is the difference in strain between the two models exposed to the same temperature field. If the two models were to have the same elongation, different temperature fields must have been made for each model.

As previously mentioned, today's elongation is measured to be 200 mm. That is not achieved by the expansion field given above. To obtain this elongation, the strain factor a must be calibrated and imposed in the model. By iterating and using the same distribution as shown in figure 4.9, a is found to be 0.5385‰ for the frame model. The following temperature field should have been used:

Part	ΔT	ε_0
Inner beam, top	107.7 °C	0.001077
Inner beam, mass center	91.83 °C	0.0009183
Inner beam, bottom	53.85 °C	0.0005385
Outer beam, top	161.55 °C	0.0016155
Outer beam, mass center	145.68 °C	0.0014568
Outer beam, bottom	107.7 °C	0.0010707
Gradient	$31.49°C/m$	0.0003149/m

Table 11.2: Temperature and strain providing $u_1 = 200mm$

This is not been used further for modeling in the frame model. Still, just by observing the impact on the concrete in a situation with symmetrical cracks, it is clear that this affects the result. The maximum global imposed bending moment occurring in the concrete has increased by 7.8 % and the maximum tension force in the concrete has an increase of 7.7 %.

The solid model has greater expansion when modeled with reinforcement due to the preconditions of the model. A solution for a temperature field that causes an elongation of 200 mm and a strain of 0.001 is iterated in temperature field 2. Resulting temperature field to accommodate this condition is:

$$T = [175 - (50/5500) \cdot x - (50/1710) \cdot y] \cdot 1.0375 \tag{11.1}$$

This results in a strain factor $a = 0.51875$‰ which gives a total elongation of 200.3 mm.

11.1.2 Acting Axial Forces due to ASR

Frame model

Section	Inner beam [kN]	Outer beam [kN]
Support 1	5530	-5663
Support 2-7	5354	-5302
Support 8	5050	-5048
Support 9	4210	-4197
Field 1	5518	-5622
Field 2-7	5210	-5245
Field 8	4792	-4787
Field 9	2745	-2755
ZM 8-7	5130	-5131
ZM 8-9	4931	- 4933
ZM 9-8	4532	-4488

Table 11.3: Resulting ASR axial force
Frame model

Solid model

Section	Inner beam [kN]	Outer beam [kN]
Support 2-7	6058	-5487
Support 8	5398	-5158
Support 9	5468	-4905
Field 2-7	6077	-5652
Field 8	5744	-5331
Field 9	3793	-3788
ZM 8-7	5455	-5508
ZM 8-9	5421	-5414
ZM 9-8	5600	-5183

Table 11.4: Resulting ASR axial force
Solid model

11.1.3 Acting Bending Moments Due to ASR

Frame model

Section	Inner beam [kNm]	Outer beam [kNm]
Support 1	1909	2176
Support 2-7	2111	1986
Support 8	1908	1905
Support 9	2913	2618
Field 1	4700	4466
Field 2-7	4808	4598
Field 8	4865	4783
Field 9	4740	5536
ZM 8-7	1931	2011
ZM 8-9	2122	2105
ZM 9-8	2404	2321

Table 11.5: Resulting ASR bending moment
Frame model

Solid model

Section	Inner beam [kNm]	Outer beam [kNm]
Support 7	2693	2693
Support 8	1770	1770
Support 9	3468	3468
Field 7	2870	2870
Field 8	3373	3373
Field 9	3468	3468
ZM 8-7	2076	2076
ZM 8-9	3373	3373
ZM 9-8	3848	3483

Table 11.6: Resulting ASR bending moment
Solid model

The total moment is divided equally over the two beams in the solid model.

11.1.4 Acting Shear Forces Due to ASR

The shear forces are only reported between support 8 and 9 in the inner beam. This is because only this area is externally strengthened with CFRP.

Section	Inner beam [kN]
Support 8	19.5
Support 9	38
Field 8	115.4
ZM 8-9	605
ZM 9-8	761
CFRP edge 8	333
CFRP edge 9	547

Table 11.7: Resulting ASR shear force

11.2 Resulting ASR-Loads in the Future

To simulate the additional 50 mm expansion expected in the future, a modified version of the frame model is used. Since it is known from the previous analysis that the steel is yielding in the cracked sections, it can not contribute to the additional expansion. The reinforcement is therefore removed in these parts. The stiffness is increased in the parts with CFRP as previously explained. The analysis is then submitted with a temperature field giving an elongation of 50 mm.

The forces from this analysis are superimposed to the analysis with the original temperature field. The total results of the inner beam are reported in this section.

The analysis of the solid model with no reinforcement in cracked sections was unable to be solved in Abaqus. This might be due to insufficient capacity in the structure. As a consequence, only results from the frame model are used.

11.2.1 Acting Axial Forces with Additional Expansion

Section	Inner beam [kN]
Support 1	6 969
Support 2-7	6 790
Support 8	6 384
Support 9	5 350
Field 1	6 954
Field 2-7	6 631
Field 8	6 074
Field 9	3 491
ZM 8-7	6 496
ZM 8-9	6 243
ZM 9-8	5 740

Table 11.8: Resulting axial force with additional expansion

According to this analysis, the forces will increase by 27% in the future. This is considered with the stiffness contribution from CFRP.

11.2.2 Acting Moment with Additional Expansion

Section	Inner beam [kN]
Support 1	1 999
Support 2-7	2 573
Support 8	2 494
Support 9	3 582
Field 1	5 760
Field 2-7	6 147
Field 8	6 149
Field 9	6 229
ZM 8-7	2 458
ZM 8-9	2 529
ZM 9-8	3 059

Table 11.9: Resulting moments with additional expansion

The moments will increase by approximately the same 27% in the future, except for the cracked section which will only increase by about 18%.

11.3 Utilization of Elgeseter Bridge in ULS

The utilization is calculated for the inner beam.

The resulting ASR bending moments listed in section 11.1.3 are added to the design moments reported in table 5.14 in section 5.5. This results in new design moments. The ASR-moments gathered from Abaqus gives a positive moment in all the sections. This leads to the ASR expansion having a positive impact on the sections over the support and a negative impact on the zero moments sections and the field sections.

As previously discussed, the inner beam obtains a reduction in moment capacity in ULS due to the axial tensile forces. Due to the uncertainties regarding the magnitude of the actual tensile force, it is interesting to evaluate the utilization of the beam without being subjected to an axial force. The utilizations of the sections are calculated with respect to the moment capacities found in sections 9.1. Besides, the highest axial force allowed acting together with M_{Ed} is reported in additional tables.

The shear utilization of the zero moment section is also determined with and without the effect of the axial force. The decisive load comes from the load combination where traffic is dominating found in table 5.15. Furthermore, the shear loads coming from ASR are added, which is shown in table 11.7.

11.3.1 Without CFRP

Moment Capacity Utilization in ULS

Section	$M_{Ed}[kNm]$	$M_{Rd}[kNm]$	UR
Support 1	-5 635	-9 557	0.59
Support 2-7	-4 563	-9 947	0.46
Support 8	-4 766	-9 547	0.50
Support 9	-4 654	-12 302	0.38
Field 1	9 797	5 980	1.64
Field 2-7	11 024	6 400	1.72
Field 8	11 081	6 400	1.73
Field 9	11 932	9 129	1.31
ZM 8-7	3 853	1 322	2.91
ZM 8-9	4 044	1 322	3.06
ZM 9-8	4 326	1 322	3.27

Table 11.10: Utilization of sections
Moments from Frame model

Section	$M_{Ed}[kNm]$	$M_{Rd}[kNm]$	UR
Support 7	- 3 981	-9 947	0.40
Support 8	-4 904	-9 547	0.51
Support 9	-4 099	-12 302	0.33
Field 7	9 086	6 400	1.42
Field 8	9 589	6 400	1.50
Field 9	10 660	9 129	1.17
ZM 8-7	3 998	1 322	3.02
ZM 8-9	5 295	1 322	4.00
ZM 9-8	5 770	1 322	4.36

Table 11.11: Utilization of sections
Moments from Solid model

The sections of zero moment get a very high utilization, which shows the critical situations in these sections. Only considering the acting moment from the temperature load, the capacity of the zero moment sections are utilized with a ratio of 1.45.

However, it is important to evaluate the probability of the temperature load acting with such a high magnitude. The large cracks appearing in the sections of zero moments will most likely be from ASR-loads and not temperature loads, due to the cracks local extent. The temperature loads may give moments in both directions and is a short-term load that can contradict the negative ASR-impact in the sections of zero moments. With this in mind, the case where only ASR-loads work in the sections of zero moments is evaluated as well. This argumentation was also made in the earlier investigation done by Stemland and Nordhaug [4].

Considering only the ASR-load, the zero moment sections still exceeds their capacity, but the utilizations are reduced.

Section	$M_{ASR}[kNm]$	$M_{Rd}[kNm]$	UR
ZM 8-7	1 921	1 322	1.45
ZM 8-9	2 122	1 322	1.61
ZM 9-8	2 404	1 322	1.82

Table 11.12: Utilization of sections only with ASR-load
Frame model

Section	$M_{ASR}[kNm]$	$M_{Rd}[kNm]$	UR
ZM 8-7	2 076	1 322	1.57
ZM 8-9	3 373	1 322	2.55
ZM 9-8	3 848	1 322	2.91

Table 11.13: Utilization of sections only with ASR-load
Solid model

Combined Moment and Axial Force Utilization in ULS

The capacity of every section in the inner beam is reduced with a present axial force. To be able to withstand the acting moments presented in this report, the highest possible tensile force are presented below:

	Frame model		Solid model	
Sections	M_{Ed}	N_{Rd}	M_{Ed}	N_{Rd}
Support 7	-4 563	5 500	- 3 981	6000
Support 8	-4 766	5 300	-4 904	5 000
Field 7	11 024	0	9 086	0
Field 8	11 081	0	9 589	0
ZM 8-7	3 853	0	3 998	0
ZM 8-9	4 044	0	5 295	0

Table 11.14: Maximum axial force combined with moment

As seen in section 11.1.2, the axial forces appearing in the beams are greater than the ones shown here. In figure 11.1, sections with the obtained acting loads are shown. Only the support sections can withstand both the bending moment and the axial force.

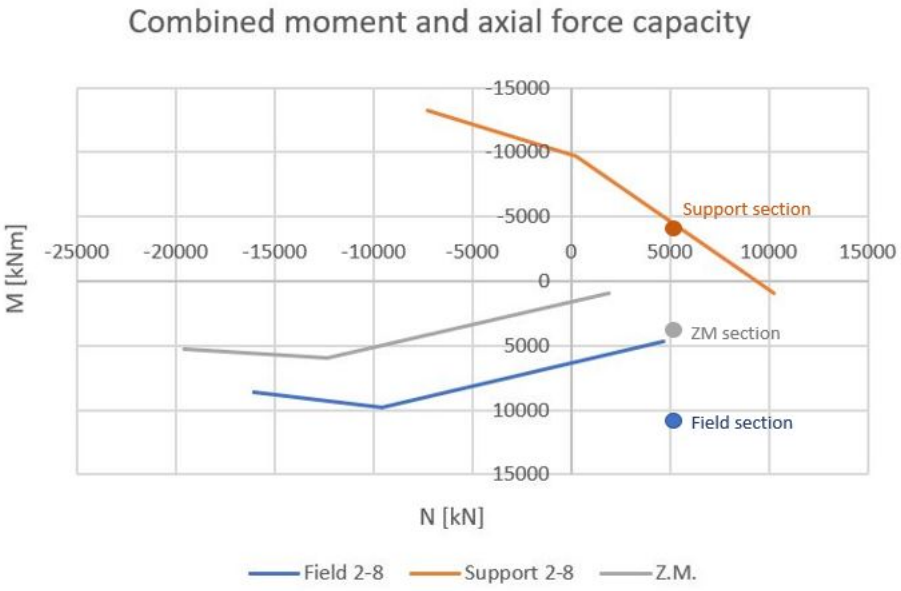

Figure 11.1: Utilization of representative sections

From the Abaqus modeling, both the frame model and the solid model provides a tension force of approximately 5000 kN in the inner beam. The support sections moment capacity will be reduced from $M_{Rd} = -9547$ kNm to $M_{Rd,N} = -4500$ kNm with a tension force of $N = 5000$ kN found in figure 11.1. Regarding the other sections, the situations are more critical as the maximum axial force is exceeded. If the beam in Elgeseter bridge is exposed to an axial force of this magnitude, the field sections and the sections of zero moments have lost their equilibrium, and failure will occur.

There are a lot of uncertainties connected to the magnitude of the expansions and the distribution between the beams. The ASR effects can be very local and have high divergence in reality compared to the linear expansion field assumed in this report. The axial force obtained in the Abaqus analysis will most likely not occur in every section in the entire bridge. The assumption that most parts of the bridge are in a stage I condition, might be too conservative. Still, it is realistic that some sections are exposed to high axial forces and this is a critical aspect to take into consideration.

Shear Capacity Utilization without Axial Force

Section	$V_{Ed}[kN]$	$V_{Rd}[kN]$	UR
ZM 8-9	1929	2127	0.91

Table 11.15: Utilization of sections
Solid model

The utilization is below 1 and the section is considered to be safe.

Shear Capacity Utilization with Axial Force

Section	$V_{Ed}[kN]$	$V_{Rd}[kN]$	UR
ZM 8-9	1929	1685.1	1.15

Table 11.16: Utilization of sections
Solid model

The utilization when considering the axial forces in the section exceeds 1. The uncertainties regarding the axial forces in the bridge as discussed previously applies to this utilization as well.

11.3.2 Including CFRP

Moment Capacity Utilization in ULS

By adding carbon fiber reinforcement, the moment capacity increases in field 3, field 6, and field 8 including the section of zero moments. A new utilization ratio has been calculated to accommodate for this. It is only the field- and zero moment section that will get an advantage with additional CFRP.

Section	$M_{Ed}[kNm]$	$M_{Rd}[kNm]$	UR
Support 1	-5 635	-9 557	0.59
Support 2-7	-4 563	-9 947	0.46
Support 8	-4 766	-9 547	0.50
Support 9	-4 654	-12 302	0.38
Field 1	9 797	5 980	1.64
Field 3 and 6	11 024	9 048	1.22
Field 2, 4, 5 and 7	11 024	6 400	1.72
Field 8	11 081	9 048	1.22
Field 9	11 932	9 129	1.31
ZM 8-7	3 853	1 322	2.91
ZM 8-9	4 044	4 323	0.94
ZM 9-8	4 326	4 323	1.00

Table 11.17: Utilization of sections and CFRP
Moments from Frame model

Section	$M_{Ed}[kNm]$	$M_{Rd}[kNm]$	UR
Support 7	-3 981	-9 947	0.40
Support 8	-4 904	-9 547	0.51
Support 9	-4 099	-12 302	0.33
Field 3 and 6	9 086	9 048	1.00
Field 2, 4, 5 and 7	9 086	6 400	1.42
Field 8	9 589	9 048	1.06
Field 9	10 660	9 129	1.17
ZM 8-7	3 998	1 322	3.02
ZM 8-9	5 295	4 323	1.22
ZM 9-8	5770	4323	1.33

Table 11.18: Utilization of sections with CFRP
Moments from Solid model

Looking only at the ASR-load, the contribution from CFRP makes the utilization less than 1 in the considered sections of zero moments.

Section	$M_{ASR}[kNm]$	$M_{Rd}[kNm]$	UR
ZM 8-7	1 921	4 323	0.44
ZM 8-9	2 122	4 323	0.49
ZM 9-8	2 404	4 323	0.56

Table 11.19: Utilization of sections
Frame model

Section	$M_{ASR}[kNm]$	$M_{Rd}[kNm]$	UR
ZM 8-7	2 076	4 323	0.48
ZM 8-9	3 373	4 323	0.78
ZM 9-8	3 848	4 323	0.89

Table 11.20: Utilization of sections with ASR-load
Solid model

Combined Moment and Axial Force Utilization in ULS

Considering the increased bending moment capacity, a larger axial force can be sustained together with the moment. For the acting moments obtained, table 11.21 shows the maximum tensile force the section can sustain.

	Frame model		Solid model	
Sections	M_{Ed}	N_{Rd}	M_{Ed}	N_{Rd}
Field 8	11 081	0	9 589	0
ZM 8-7	3 853	1 000	3 998	1 000
ZM 8-9	4 044	0	5 295	0

Table 11.21: Maximum Axial Force with Respective Moment

Even when including CFRP, the sections can still not carry the acting moment together with the acting load. This is clearly demonstrated in figure 11.2. Despite this, the capacity has increased and a higher axial force can be obtained by both sections while still being in equilibrium. The section of zero moment to the left of support 8 gets a tensile force resistance of about 1000 kN. If only the ASR loads were considered for the sections of zero moments, a tensile force of approximately 3000 kN could be subjected. In addition, the field sections do have a tensile resistance enough to carry a force of 5-6000 kN, but only with an acting moment of approximately 7000 kNm.

Figure 11.2: Utilization of representative sections with CFRP

Shear Capacity Utilization without Axial Force in ULS

The effect of CFRP in shear capacity is evaluated in the strengthened sections.

The contribution of the fiber shear reinforcement is found to be

$V_{Rd,f} = 670$ kN

This gives a total shear resistance of 2797 kN which is a significant increase.

Section	$V_{Ed}[kN]$	$V_{Rd}[kN]$	UR
ZM 8-9	1929	2797	0.69

Table 11.22: Utilization of section with CFRP

Shear Capacity Utilization with Axial Force

Section	$V_{Ed}[kN]$	$V_{Rd}[kN]$	UR
ZM 8-9	1929	2351	0.82

Table 11.23: Utilization of section with CFRP and axial force

By including the additional capacity, the section can withstand the tensile force in addition to a shear crack of 45 °.

Shear Capacity Utilization in Existing Crack

If the existing crack of 90 ° is evaluated, it is assumed that only the live loads are carried by the fiber reinforcement. This is due to the self-weight and the ASR-loads being imposed on the bridge at the time of the crack. Also, it is assumed that the steel is inactive so that the only way the forces are transferred is through the fiber.

The shear force coming solely from the self-weight is 631 kN, and gives a net acting shear force of:

$V_{Ed} = 1324 - 631 = 693kN$

The fiber reinforcement working over the existing crack has a capacity of:

$V_{Rd,frp} = 520kN$

Section	$V_{Ed}[kN]$	$V_{Rd}[kN]$	UR
ZM 8-9	693	520	1.33

Table 11.24: Utilization of section with the existing crack

This is not sufficient to transfer the shear force. Despite this, some assumptions have been made which could have increased the capacity if evaluated differently.

11.4 Utilization of Elgeseter Bridge in the Future

The ASR-loads are expected to increase. This is very critical as many sections already have insufficient capacity. With these additional loads, a new consideration of the moment utilization is performed. The evaluation has been made with the increase in stiffness for field 3,6 and 8 due to CFRP.

Moment capacity utilization

Section	$M_{Ed}[kNm]$	$M_{Rd}[kNm]$	UR
Support 1	-5 545	-9 557	0.58
Support 2-7	-4 101	-9 947	0.41
Support 8	-5 073	-9 547	0.53
Support 9	-3 985	-12 302	0.32
Field 1	12 051	5 980	2.02
Field 2,4,5,7	12 847	6 400	2.00
Field 3,6	12 051	9 048	1.33
Field 8	12 365	9 048	1.37
Field 9	13 421	9 129	1.47
ZM 8-7	4 380	1 322	3.31
ZM 8-9	4 451	4 323	1.03
ZM 9-8	4 981	4 323	1.15

Table 11.25: Utilization of sections with ASR-load Moments from Frame model

If the temperature loads are neglected in the sections of zero moments:

Section	$M_{ASR}[kNm]$	$M_{Rd}[kNm]$	UR
ZM 8-7	2 458	1 322	1.86
ZM 8-9	2 529	4 323	0.59
ZM 9-8	3 059	4 323	0.71

11.5 Evaluation of Intermediate Crack Debonding

11.5.1 Moment Induced

The acting forces that cause moment induced intermediate crack debonding are the shift in tensile forces at an element between two cracks. To estimate this, the theoretical crack spacing is found and the tensile forces in the CFRP at each crack are found depending on an estimated moment distribution. The method of finding tensile forces in the CFRP is explained in section 6.2.1.

The moment distribution is estimated by results derived from the report of Nordhaug and Stemland [4] and resulting ASR moment distribution.

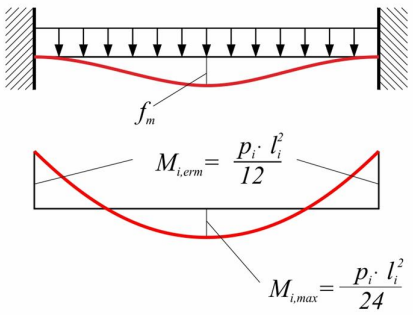

Figure 11.3: Moment distribution in a beam restrained in both ends [52]

Moment distribution from an evenly distributed load q in a beam with a length L fixed in both ends is given as:

$$M(x) = -\frac{qx^2}{2} + \frac{qL \cdot x}{12} - \frac{qL^2}{12} \tag{11.2}$$

As the distribution from ASR moment is more complex and difficult to obtain, a linear approach between the axis and field section is assumed. This might contribute to conservative results in some areas, especially around the field sections. In other sections, such as closer to the zero moment sections, the estimated moment distribution might be unconservative. This can lead to yielding in the steel reinforcement further away from the axis than in reality.

By eq. (6.19), F_{fEd} depends on whether it is yielding or not, which is determined by:

$$\sigma_s(x) = \sigma_{s,0}(x) + \frac{\Delta M_{Ed}(x)}{z_m} \cdot \frac{d_s \cdot E_s}{E_f A_f + E_s A_s} \tag{11.3}$$

Where

$$\sigma_{s,0}(x) = \frac{M_{Ed,0}(x)}{0.85 \cdot d_s \cdot A_s} \tag{11.4}$$

and

$$z_m \approx 0.8 \cdot \frac{d_f E_f A_f + d_s E_s A_s}{E_f A_f + E_s A_s} \tag{11.5}$$

Change in tensile force of the CFRP is found by eq. (6.15). The control is done in MATLAB, and detailed calculations are found in appendix F. Resulting ΔF_{fEd} is plotted from the zero moment section to the field section in figure 11.4.

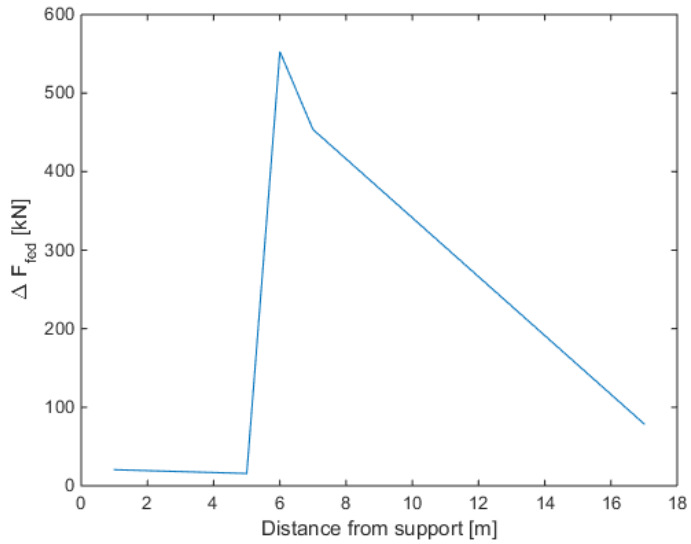

Figure 11.4: Shift in tension force including ASR-moment

Due to the uncertainties of the ASR moment distribution, an additional control is done without the ASR moment.

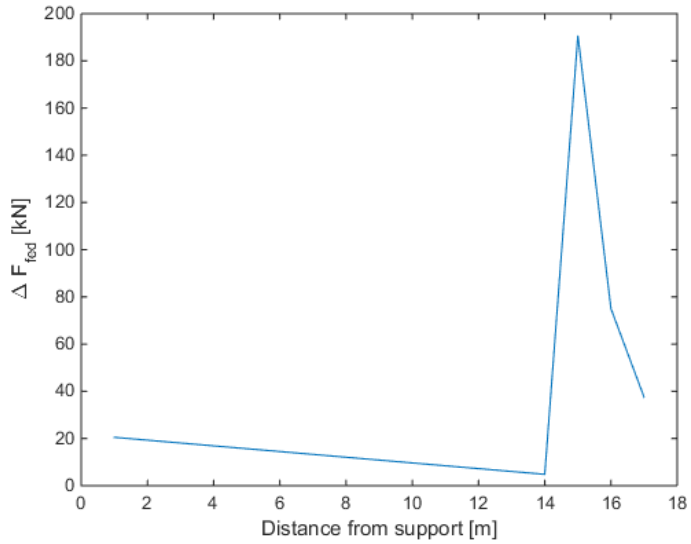

Figure 11.5: Shift in tension force without ASR-moment

The point of yielding is shown as a peak in the graph. This is due to the different approaches to obtain ΔF_{fEd} when the steel is yielding. The yield point is moved further towards the field when not including ASR-loads.

Both controls result in elements with a higher shift in tensile force than the

capacity, $\Delta F_{fRd} = 100.7$ kN. Due to the uncertainties of the ASR moment distribution, the location of which element that is retaining the highest shift in tensile forces is unknown. However, the control without ASR moment shows that the capacity is exceeded independently of the distribution of ASR moment. This moment will only increase the acting forces.

The control of moment induced crack debonding is important when designing externally bonded fiber reinforcement. It is to prevent that crack debonding is the determinate failure mode of the CFRP. This does not imply that the structure will fail at this load. As Elgeseter Bridge does not have cracks at each 400 mm as for today, the structure might not be in a critical stage considering intermediate crack debonding induced by moment. Still, debonding failure is undesirable and the analysis shows that if the CFRP fails it might be by intermediate crack debonding as the utilization is this high.

11.5.2 Shear Induced

The member is controlled for shear-induced flexural debonding of the CFRP strips and the support section is controlled for concrete cover separation. These controls are done to prevent the detrimental influence on flexural debonding [18].

Concrete cover separation in support section

Concrete cover separation is a crucial control done at the edge of the CFRP. In this case, it is critical near support 9. Here the acting shear force is

$V_{Ed} = 1971 + 547 = 2518$ kN

The concrete cover has no steel and solely the concrete contributes to the shear resistance. The capacity to prevent separation is found to be

$V_{Rd,c,fe} = 367.2$ kN

This is a very small capacity compared to the acting force, and concrete cover separation is likely to occur. Transverse strips should be designed to take the shear force and applied at the end section of the flexural FRP reinforcement. The strips are recommended to be designed after equation (6.33). Adding such strips will generally increase the shear capacity as well.

Shear induced intermediate debonding

The possibility of shear-induced intermediate crack debonding is evaluated for the whole beam with flexural reinforcement. Here the acting force can not exceed;

$V_{Ed,max} = 466$ kN

Looking at the shear forces from the decisive load combination and the additional ASR-load it is clear that this limit will be exceeded several places. The

safest solution is to attach transverse FRP wrapping to ensure the tensile resistance of the longitudinal reinforcement. The strips should be designed after equation (6.36).

Chapter 12

Discussion

12.1 General Aspects

12.1.1 Models

Several assumptions need to be made when modeling in FEM software, as there are many unknown properties of the real structure and the software often limits the possibilities in modeling.

The frame model is based on a suggestion from The Norwegian Public Road Administration [33]. This model consists of beam elements with transverse elements that preserve compatibility between the four beams. The transverse elements are constrained to the beam elements every 1.25 m. These elements contribute to a discontinuous transverse force distribution between the beams. The bridge is modeled as fully restrained in axis 1 and simply supported in axis 2-10. In reality, the bridge is somewhat constrained against elongation in axis 2-9 and rotation in axis 2-8 by the columns. Due to the observed total elongation of the bridge and the geometry of the columns, this effect is neglected in the analyses.

The solid model includes two of the beams between axis 6-10 in solid elements. This model preserves the effects of transverse stiffness and the behavior of the continuous plate between the beams. The solid model is fixed in axis 6, which is a simplification. In reality, the constraint of this axis is softer as the bridge is continuous before support 6 and the analysis might obtain higher forces in this section compared to reality. This effect is assumed to languish in span 6-7, such that axis 7 is expected to be representative. In addition, it is assumed that the bridge will have a repeating response to the ASR expansion after span 7-8, which is confirmed by the frame model. This leads to an assumption that this span is representative of the behavior of the rest of the bridge and it is not necessary to model more spans. The bridge is constrained with a symmetry constraint longitudinal to the inner beam. This results in a symmetric behavior of the bridge. In span 8-9 the bridge is cracked and externally reinforced in only one beam, and this will not be preserved in the model due to its symmetry condition. This might affect the results in the analyses. The solid model was not able to obtain the resulting forces of each beam, which is undesirable when modeling the non-linearity of the problem.

The frame model seems to describe the axial forces satisfactorily after adjusting the transverse elements' shear stiffness and bending stiffness in plane to retain the behavior of a continuous plate between the beam elements. The resulting bending moments and total strain in the two models have small deviations in analyses without reinforcement. Consequently, the two models are evaluated to be satisfactory equivalent to each other in analyses without reinforcement and non-linear modeling.

The reinforcement in the frame model was simplified by assembling it in a representing upper and lower reinforcement, which was connected to the beam at each element every 1.25 m. The solid model was modeled with each rebar positioned approximately according to the original drawings and connected continuously to the concrete. The detailed placement preserves the local effects of the positioning of the reinforcement and its continuous restrain on the concrete. When applying reinforcement in the analyses, relatively large deviations in longitudinal strain and bending moment arose between the two models. The deviations are assumed to be an effect of the preconditions of the beam elements and the modeling of the reinforcement. This leads to the discussion about the level of satisfaction the implementation of reinforcement has in the frame model, and if it represents the real impact the reinforcement has on the concrete section.

When modeling non-linearity such as cracks in the bridge, different approaches were made in the two models. The frame model was modeled with an adjusted stiffness of the cross-section, whereas the solid model reduced the stiffness significantly in only the web of the beam in the cracked area. The solution made in the frame model might be un-conservative as the cross-section still attains tensile strength, which the concrete does not have in a cracked state. On the contrary, the assumptions made in the solid model might be too conservative. With reducing the stiffness in the whole web, one assumes that the crack has propagated to the bridge deck. In reality, some parts of the web might be active and uncracked.

The frame model gets a much lower effect from the crack. This can be seen by comparing the elongation, axial forces and moments in the two models before and after the non-linearity is imposed. Although the impact of the crack is greater in magnitude for the solid model, the general effect can be seen in both the models. The forces decrease not only in the crack itself but also in the area around the crack. The effects extend to the section of zero moment on the other side of the support. The steel in the cracked sections gets more exposed as the concrete is weaker and will yield in both of the models.

The fact that the frame model does not obtain the same magnitude in the decrease of forces, shows a severe weakness in the approach. It is recommended to evaluate another way of modeling the non-linearity if a frame model is to be used in further analysis.

To test different effects of implementing non-linearity, Young's modulus has been further reduced in the frame model. When imposing Young's modulus equal to 5% of the original stiffness in the cracked section, the reduction in forces is

about 27%. This is similar to the results obtained in the solid model analysis. In addition, the solid model was submitted to an analysis with a 75% reduction in Young's modulus for the cracked section, as performed in the frame model. The impact of the crack became significantly more modest and closer to what was observed in the frame model. These investigations support the theory that the different non-linearity approaches have a severe impact on the results.

In both analyses, this study assumed that the concrete is in stage II in the cracked section and all other sections of the bridge are assumed to be in stage I. Conducting an analysis assuming the majority of the bridge is in an uncracked stage, is an important initial step. In reality, a more significant part of the bridge may be in a stage II condition. As seen by the analyses, the ASR expansion establishes severe forces in the bridge. This might lead to the conclusion that these assumptions of the bridge's condition are inadequate. Implementing this effect in the analysis is a thorough process, and one could attempt to model this non-linear situation by a linear elastic approach. Consequences of this would be a varying stiffness in the whole bridge and a varying neutral axis in the cross-sections. The solid model will sustain this effect, but it would have to be implemented in the frame model and considered. Though, including this in a linear elastic analysis with beam elements could create discontinuities in the model, which do not occur in reality. Aas-Jakobsen has started a project to evaluate the capacity of the bridge and is performing an ongoing investigation about these circumstances. Optimally, a condition between stage I and stage II would be ideal to model for global analyses. This is due to tension stiffening between the cracks, where the concrete still can sustain tension stresses.

12.1.2 ASR Effects

In this report, the effect of ASR has shown a significant impact on the structure. To determine the actual influence of the ASR, the total expansion of the structure must be known. The chosen expansion field is uniform over the entire bridge but with linearly variations over the height and width. A uniform expansion field is not necessarily the case as more variations are likely to occur in the expansion caused by ASR. This is due to local accumulations of reactive aggregates in the concrete.

From research projects, it is reported that the mechanical properties of the concrete get a significant impact form ASR, though it is hard to quantify. One of the most essential results is that the reduction in properties of the concrete depends on the crack's orientation. The directional dependency of the properties gives the concrete an anisotropic behaviour.

Generally, the tensile force gets considerably influenced, but this is also affected by the appearance of cracks. The compression strength is believed not to get significantly reduced before the expansion reaches a high value. Young's modulus is decreasing considerably with greater exposure of ASR. Measuring the reduction in stiffness is found to be the best way to evaluate the ASR-damage. The relation is obtained by running SDT test and gives a good indication of the severeness. Since the exposure from ASR can variate within the structure, so will Young's modulus. Neither this effect nor the general reduction in Young's

modulus is accounted for in this study. Including this effect, the forces obtained from ASR-loads would variate more within the structure.

The anisotropic behavior of ASR-damaged concrete has been neglected in the analysis. The occurrence of restrained parts within a structure provides local compression. If the compression is about 2-3 MPa it is high enough to retain the expansion in some directions. This can mean that the ASR-expansion is dependent on the stress in the concrete. If so, the stress state of the section from permanent loads must be evaluated and local expansions calculated. A stress-dependent expansion would most likely lead to less resulting loads form ASR than the ones reported in this study.

To find a representing expansion field accounting for the listed effects is very challenging. The only property that is sure for existing ASR-damaged structures is the total strain. The expansion field must be adjusted to this and modeled in the best way preserving the effects mentioned above.

12.1.3 CFRP Effects

International guidelines regarding the design of carbon fiber reinforcement have been insufficient in the past. As of today, a new annex to the Eurocode 2 is being developed based on design rules from Fib Bulletin 90. This provides methods to optimize the contribution of the fibers to the capacity when designing. When the current CFRP solution on Elgeseter bridge was designed, the Eurocode guidelines did not exist. The new information and aspects of the solution must be included when evaluating the strengthening.

A challenge with fiber reinforced polymers is to preserve the high strength in the fibers when working together with the concrete. The strength of the composite material is rarely able to reach its full potential before it reaches its bond strength or rupture. The design rules provide controls to avoid such failure modes and give a thorough demand for an application that takes advantage of the fiber's strength.

Debonding of FRP leads to a brittle failure mode, which is highly unwanted. This can be initiated by cracks and there is therefore a danger in not knowing the state of the concrete under the fiber material. The guidelines assume that the FRP is applied to concrete being in an adequate condition. Knowing that ASR leads to a formation of cracks in the concrete, it is discussed if FRP is a beneficial solution for strengthening of ASR-damaged concrete. Also, if the FRP is subjected to expansion, some researches show that it will harm the bond strength, which would decrease the capacity significantly.

The effects on the properties of fiber reinforcement coming from cracks and ASR-expansion are very uncertain. The applications of the fiber reinforcement must be executed with high consideration. The bond length and the way the external reinforcement is anchored serves as important by preventing rupture and maintaining the strength.

From another view, it can be discussed how fiber reinforcement gives a positive effect. If applied in a way that gives a confinement pressure, the CFRP can retain the expansion and reduce the stresses. Furthermore, the FRP will cover the surface preventing a moist environment. To prevent the expansion, the fiber reinforcement must be applied in an early stage of the exposure. Still, it is hard to achieve the confinement pressure unless the FRP is fully wrapped. This means that FRP solutions might retain expansion in columns better than in a beam.

The analysis of the global behavior of Elgeseter bridge showed approximately no effect in the total strain when introducing CFRP locally on the bridge. The layout will most likely not provide the necessary pressure to retain the expansion. Another aspect regarding global behavior is the possibility of rearrangement of forces due to the local increases of stiffness. The modeling in Abaqus showed only a small increase of forces in the strengthened sections and it was not imposing higher forces on the areas around. If the stiffness was significantly increased over the whole bridge, it could be assumed a small decrease in expansion, but also a considerable increase in forces.

Many aspects influence the strength of the fiber reinforcement and uncertainties arise when designing an FRP solution. The new rules include conservative controls so that unwanted failure modes are prevented. Still, cracks and inaccurate applications may reduce the strength in ways that are not accounted for when evaluating the capacity of the CFRP solution in this report.

12.2 Evaluation of Results and Utilization in ULS

The resulting loads used to determine the utilization of the bridge is a summation of the original loads found by Stemland and Nordhaug [**?**] and the ASR-load obtained from the Abaqus analysis.

Regarding the original loads, they have been calculated by using The Norwegian Public road administration's guidelines for existing bridges. The loads occurring today are probably deviating from what was common at the time the bridge was designed and recalculating the capacities and utilization is interesting. These are calculated by using NS3473 published in 2003, while the additional capacities from the CFRP are calculated by using the guidelines in Fib bulletin 90 (2019).

12.2.1 Elongation due to ASR

The frame model and the solid model gives different elongations for the same temperature field. This is due to that the beam model has a stiffer behavior where the steel is retaining the whole cross-sections following Navier's hypothesis. The local variation in the reinforcement in the solid model gives a more ductile behavior allowing a greater strain in the structure.

The elongation in the bridge is very similar when comparing the two models in a situation with free expansion. When including the reinforcement the steel is

restraining the expansion with 17.3% and 14.1% in the solid model. The deviations show how the local reinforcement effect makes the solid model less stiff.

When imposing sections with non-linearity in the structure the elongation only increased with 0.19 % in the frame model, whereas it increased with 1.3% in the other model. The impact of the crack has almost 5 times more effect on the elongation in the solid model. This shows the unconservative way the crack is modeled in the frame model, but the generally stiffer behavior must also be taken into account.

The measurement of the expansion in Elgeseter bridge is set to be 200 mm in the year 2020. This was not verified at the beginning of the investigation leading to this report where the expansion was set to be between 180-200 mm. Therefore, the used temperature field does not give a correct elongation as it is reported in the newest studies. By implementing the correlated temperature field giving 200 mm expansion, the forces would have become greater than the ones that are found in this report.

In addition, it is assumed an extra expansion of 50mm during Elgester bridge's service life. As the expansion continues to increase, so will the resulting forces. As earlier discussed, the elongation is not affected by introducing the effects form CFRP.

12.2.2 Axial Forces

The axial forces reported in section 11.1.2 are in a severe magnitude, which might affect the capacity of especially the inner beams in an unfavorable way. The axial forces in the solid model are more varying compared to the frame model, which has a smoother behavior. This is due to the more varying amount of reinforcement in the solid model.

As seen from the results, the axial forces are built up during the first span of the bridge from axis 10. This behavior is typical, as the bridge is less restrained in this area and the reinforcement needs to accumulate the restraining forces gradually. This response can indicate how the bridge is handling the axial forces. As the axial forces accumulate relatively quickly, it might indicate that the structure's response to the axial force is quite good. Still, this part of the bridge is modeled by stage I concrete and a linear elastic analysis. It is uncertain if the results from this project represent the reality in this response.

An essential aspect of the simulation in this project is the uncertainties about the assumed variation and gradient along the width of the cross-section. The resulting axial forces in the bridge depends mainly on this variation. Other gradients could result in the same expansion as the bridge has experienced, which would give higher or lower resulting axial forces.

The axial forces in the bridge strongly depend on the axial stiffness of the beams, due to the relationship between strain and stiffness. When modeling the bridge in stage I, the bridge has a great stiffness to obtain the large axial forces. As

explained earlier, the bridge might be more damaged and have a lower axial stiffness in reality. Furthermore, when capacity is reached in a section, a re-arrangement of forces occurs. The results from modeling a crack in the solid model clearly show that the bridge is capable to redistribute forces when weak areas occur.

The effect of applying CFRP on the inner beams gives a modest influence in the axial force. The increase is less than 13% in the solid model and only 1% in frame model. The small effects can be because of the equivalent stiffness with CFRP is not significantly higher than the stage I stiffness. So even if the inner beam gets a small increase in stiffness compared to the outer beam, the axial force arising due to the different expansion in the beams remains approximately the same.

12.2.3 Bending Moments

The moments gathered from Abaqus show the secondary moments, including the effects of internal and external constraints. These are deviating between the two models in varying degrees. The highest deviation occurs in the last field with up to 70 %.

As for axial forces, this can be explained by the local effects the reinforcement imposes in the solid model. Besides, a greater amount of reinforcement is activated in multiple sections in the solid model. Considering the field sections, the two models have approximately the same amount of reinforcement. Here the frame model provides higher moments, which indicates stiffer behavior as explained before. In the support section and especially in the sections of zero moment the solid model has a greater amount of reinforcement on the tension side. This is activated by the imposed ASR-loads and the steel in tension will give a higher contribution to the ASR-moments in these sections.

Adding the bending moments from the original loads, the acting moment exceeds the moment capacities in both the field sections and the sections of zero moment. Only the support sections have sufficient capacity, due to the beneficial effects of the ASR moment, illustrated with the utilization ratios in figure 12.1. Considering the additional axial forces, the compression force in the outer beam is beneficial for the utilization, whereas the inner beam gets an unfavorable impact from the tensile force. As explained earlier, it is essential to remember that the magnitudes of these axial forces and moments are undetermined due to the uncertainties about the stage of the concrete. The scope of this capacity control is to highlight the possible impacts of the acting moment and axial force combined.

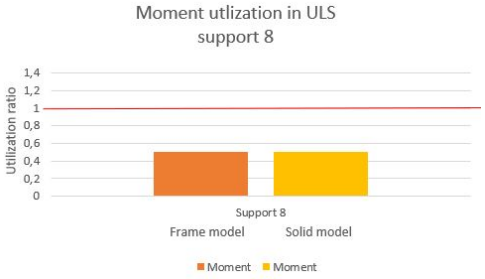

Figure 12.1: Bending moment utilization ratio for support section 8

When assuming that the strength of the CFRP can be fully utilized, the effect from the CFRP strengthening increases the moment capacity significantly. This occurs both for the field sections and the sections of zero moment. The moment capacity in the sections of zero moment has increased about 4 times, this is very beneficial for the general capacity of the bridge. The frame model which has higher field moments than the solid model still gets an over-utilized section in these places, while the section of zero moments gets a considerably lower utilization. Contrarily, in the solid model, the field section gets a utilization ratio below 1, while the section of zero moments still has a high utilization in some places. The utilization ratio is shown for field 8 and ZM 8-9 in figure 12.2 and figure 12.3 illustrating the effect of CFRP.

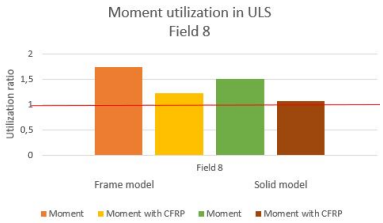

Figure 12.2: Bending moment utilization ratio for field 8

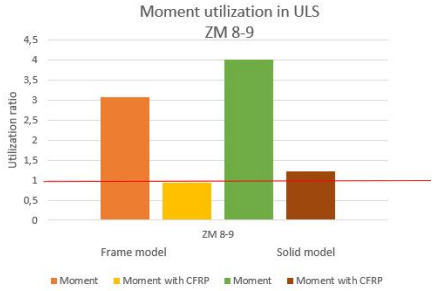

Figure 12.3: Bending moment utilization ratio for ZM 8-9

The question is whether it is safe to calculate with this increase in capacity due to the flexural reinforcement. The calculations reported shows that there is a

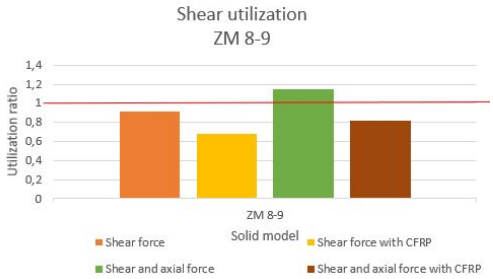

Figure 12.4: Shear utilization for ZM 8-9

risk of intermediate debonding due to both shear forces and moments. This would lead to a brittle failure mode for the CFRP and loss of the additional capacity.

A way to reduce the risk of moment induced debonding would be to apply a greater amount of flexural FRP. This can be executed at the sides of the web as the beam's width is already covered. To prevent the shear induced flexural debonding, transverse shear straps should be attached to the flexural FRP. Also, concrete cover separation is critical which is an unacceptable failure mode. Even though the strips are anchored in the compression zone of the beam, additional transverse strips can be necessary to optimize the end anchoring. This may prevent concrete cover separation.

12.2.4 Shear Forces

The shear force capacity is adequate in the beam with both the original shear force and the ASR-loads when not considering the axial forces. The CFRP increases the capacity further. When including axial forces in ULS capacity, the inner beams have exceeded their capacities. At strengthened sections, the utilization ratio is satisfying due to the contribution from the CFRP. The utilization ratio for the zero moment section with and without the axial force is presented in figure 12.4. The same figure also shows the impact of strengthening.

The fibers also ensure a way to transfer the shear forces over the existing cracks. Though, the shear force needed to be transferred over the crack is higher than the CFRP can sustain. This evaluation has been done taking into account many assumptions regarding the anchoring length and the bond strength utilized in the fibers. The bond strength of the fibers is reduced and might be higher. As well, some of the reinforcement may still be active and increase the capacity. However, the crack was assumed to only span over the web, but most likely it also extends over the deck. This would have a negative impact on the calculated capacity.

12.2.5 Additional Considerations

In this study, the main focus has been the acting axial forces, bending moment, and shear force in the strengthened parts. In addition to this, the expansion due to ASR contributes to other acting forces that should be evaluated. This is

not done in this report.

The opposing axial forces in the outer and inner beam creates large shear forces in the longitudinal direction of the bridge. These shear stresses need to be transferred by the flanges of the T-section. As the area of the intersection between the beams is significantly small, these stresses may be critically high. This might be a critical situation concerning the possibility of punching shear failure which is an undesirable failure mode. The possibility of this failure needs to be evaluated for Elgeseter Bridge.

Furthermore, the bridge will experience a torsional moment. This is a consequence of external restraining against the bending of the bridge in the transverse direction. The solid model obtains high torsional moments in some locations. By briefly analyzing the torsional resultants of the cross-section, it is obtained torsional forces as high as about 1000 kNm. This occurs in between supports sections and zero moment sections by the crack. The torsional moments drop to about 100 kNm around the support sections. In field sections, the torsional moment is relatively small, about 300 kNm. In the last span of the bridge, it increases towards the end, where it is found a torsional moment about 1600 kNm. On the contrary, the frame model obtains significantly smaller torsional forces, but the trend is similar to the solid model. Towards the end, the highest torsional moment occurs having a magnitude of 20 kNm. Evaluating the global response in the bridge, it seems that higher torsional moments occur around the cracked areas.

The difference of resulting torsional moment in the two models might be a result of the transverse beams in the frame model's capability to transfer the torsional forces adequately. This effect of the torsional moment needs to be evaluated and the calculation of capacity needs to consider this as well. Also, one should consider if the frame model is insufficient to obtain the acting torsional forces in the bridge. The frame model insufficiency to obtain the torsional effects in the bridge might also explain the high deviations in resulting bending moments between the two models. Further investigation of the response in the frame model is necessary to conclude the possible effect of these circumstances.

Chapter 13

Conclusion

Elgeseter Bridge is a concrete beam bridge located in Trondheim and is one of many structures exposed to alkali-silica reactions in Norway. The scope of this thesis has been to study the possible mechanical effects imposed on the structure. The implementation of externally bonded fiber reinforcement at the bridge is also thoroughly investigated. A condition assessment of the bridge is performed according to NS 3473 (2003) and Fib Bulletin 90 (2019).

A structure subjected to ASR expansion may attain additional imposed forces. The steel reinforcement will create an internal restraint and introduce axial forces and bending moments. External constraints may establish additional forces when a free expansion is prevented. If the magnitude of expansion varies in the structure, adjoining parts of the structure provide an external restraint. For Elgeseter Bridge, it is assumed that this effect creates compression forces in the outer beams and tensile forces in the inner beams. The imposed bending moment contributes to tensile stresses in the web of the beam and compression in the flanges. Regarding the capacity in ULS, this is beneficial for the support sections and detrimental for the field sections.

It was established two linear elastic FE models in Abaqus/CEA. Model 1 consists of beam and truss elements, whereas model 2 is a volume model of solid elements. Both models were imposed with a temperature field to simulate the ASR expansion in the structure. Resulting axial forces in the two models were coinciding. On the contrary, great deviations were found between the models in resulting bending moments when internal reinforcement was included in the analyses. These deviations are assumed to occur due to the preconditions of the models. The implementation of the non-linearity was performed using two different approaches, which resulted in deviating results.

To improve the load bearing capacity, Elgeseter Bridge is strengthened with externally bonded carbon fiber reinforcement in several spans. Six severe cracks are shear strengthened with CFRP wraps and five spans are flexurally strengthened with CFRP strips. The guidelines provided by Fib Bulletin 90 do not consider the potential negative impact damaged concrete may have on the bond strength. Consequently, the capacities derived in this study may be unconservative.

Considering the situation with cracked sections and external strengthening, the most utilized section in bending moment provides a limit for the load bearing capacity. In both models the critical section is the section of zero moment south of support 8 in the inner beam, being in an unstrengthened span. The utilization ratio obtained in the frame model was 2.91 in the frame model, whereas it was 3.02 in the solid model. Regarding the strengthened parts, the CFRP gave a favorable outcome, reducing the utilization significantly. Considering the section of zero moment south of support 9, the utilization ratio dropped from 3.27 to 0.94 in the frame model and 4.36 to 1.22 in the solid model. Though, the calculations assume full utilization of the strength in the CFRP, which is challenging to achieve in reality. When considering debonding issues, calculations revealed that this is critical and the capacity is over-exceeded by a ratio of approximately 5. Better optimization of the CFRP solution and additional transverse strips could be necessary to avoid this failure mode.

The tensile force obtained in the inner beam has a disadvantageous influence on the member's capacity. The magnitude of the force is uncertain and may vary locally in the beam. This study obtained a tensile force of approximately 5000 kN, which will reduce the moment capacity in ULS severely and the bending moment capacity in all the field sections and sections of zero moment are insufficient. When including the tensile force in ULS shear capacity calculations, the utilization ratio is 1.15. At strengthened sections, utilization ratio is 0.82.

Studies assume that Elgeseter bridge will get an additional expansion during the rest of its service life. The analyses performed indicated a higher utilization ratio as the forces will continue to increase.

The results obtained in this study indicate that the bridge in general has exceeded its load bearing capacity. Performing an analysis by assuming an uncracked stage in the majority of the bridge is an important initial evaluation. The results are in such a magnitude that it is reasonable to believe that the majority of the concrete is in a cracked stage. Conducting an analysis including this non-linearity might give more accurate and less detrimental results. Either way, Elgeseter Bridge is a massive concrete bridge with the opportunity of redistributing forces.

This study has not included the possible negative impact the alkali-silica reactions have on the concrete's properties, nor the possible reduction of expansion due to local compression stresses. Regarding the utilization of the bridge, torsional moment and shear stresses in the bridge deck is not evaluated. Despite this, the performed study is highlighting the important aspects of using carbon fiber reinforcement on structures exposed to alkali-silica reactions.

Bibliography

[1] Stemland H.,Rodum E.,Johansen H. *Alkalireaksjoner - Veiledning for konstruktiv analyse*
Etatsprogrammet Varige konstruksjoner 2012-2015.
Statens vegvesen (2016)

[2] civil-engg-world.blogspot.com:
`https://civil-engg-world.blogspot.com/2014/06/specification-alkali-silica-Reaction-Fine-Aggregate-Concrete.html`

[3] Haddad R.H., Al-Sayed A.
Bond behaviour between ASR-damaged concrete and CFRP sheets: Empirical modeling.
`(https://doi.org/10.1016/j.jobe.2019.101166)`
Journal of Building Engineering 20 (2020).

[4] Nordhaug, O.K., Stemland K.M.*Beregning av bru med alkalireaksjoner. Tilstandsvurdering og kapasitetskontroll av Elgester bru*
Master thesis, NTNU (2018)

[5] Myklebust, E.O. *Assessment of an existing bridge suffering from Alkali-Silica reaction*
Master thesis, NTNU (2018)

[6] Bertolini L, Elsener B., Pedeferri P.,Redaelli E.,Polder R: *Corrosion of Steel in Concrete: Prevntion, Diagnosis and Repair*
Wiley-VCH Verlag GmbH Co. KGaA, Weinheim, Germany. (2014)

[7] ConstructionEquipmentGuide.com
`https://www.constructionequipmentguide.com/asr-issues-cause-penndot-to-replace-miles-of-i-84/35933`

[8] Kongshaug, S.S., Oseland o., Kanstad T., Hendrix M.A.N., Rodum E., Markset G.: *Experimental investigation of ASR-affected concrete – the influence of uniaxial loading on the evolution of mechanical properties, expansion and damage indices*
Oslo Metropolitan University (2020).

[9] Barbosa R.A., Hansen S.G., Hansen K.K., Hoang L.C., Grelk B. *Influence of alkali-silica reaction and crack orientation on the uniaxial compressive strength of concrete cores from slab bridges*
Construction and Building Materials (2018).

[10] Giaccio G, Torrijos M.C., Tobes J.M., Batic O.R., Zerbino R: *Development of alkali-silica reaction under compressive loading and its effects on concrete behavior* ACI Materials Journal (2009).

[11] Gautam B.P., Panesar D.K., Sheikh S.A., Vecchio F.J. *Effect of Multiaxial Stresses on Alkali-Silica Reaction Damage of Concrete* ACI Materials Journal (2017).

[12] Thorenfeldt E., Täljsten B., Rødsætre J., Sandaker T.K.: *Forsterkning av betongkonstruksjoner*. Publikasjon nr. 36. Sandvika: Norsk Betongforening (2006).

[13] Arch Daily `https://www.archdaily.com/catalog/us/products/17406/structural-strengthening-with-cfrp-plates-and-frp-fabrics-sika/190191?ad_source=neufertad_medium=galleryad_name=open-gallery`

[14] Kvinge E.A.R., Randen E.: *ConLam - Et beregningsprogram for dimensjonering av betongbjelker med utenpåliggende, pålimt karbonfiberforsterkning*. Master thesis NTNU (2015).

[15] Rawlines Paints: `https://www.rawlinspaints.com/home/repair-materials/structural-repairs/2324-sikawrap-600-c.html`. Last visited 24.11.2019.

[16] Rawlines Paints: `https://www.rawlinspaints.com/home/repair-materials/structural-repairs/2311-sika-carbodur-m-type.html`. Last visited 24.11.2019.

[17] Global Sources: `https://www.globalsources.com/gsol/I/Carbon-fiber/p/sm/1163850949.htm1163850949`. Last visited 24.11.2019.

[18] Fédération internationale du béton (*fib*): *Bulletin 90: Externally applied FRP reinforcement for concrete structures.* Technical Report (2019).

[19] CNR - Advisory committee on technical recommendations for constructions: *Guide for design and constructions of externally bonded FRP systems for strengthening existing structures*. Roma: National Research Council (2013).

[20] Täljsten B., Blanksvärd T., Sas G.: *Handbok för dimensjonering och utförande i samband med försterkning av betongkonstruksjoner med pålimmade fiberkopositer*. Luleå Tekniske Universitet (2011).

[21] Pendhari S.S., Kant T., Desai Y.M.: *Application of polymer composites in civil construction: A general review.* (`https://doi.org/10.1016/j.compstruct.2007.06.007`) Composites structures volume 84; 114-128 (2008).

[22] Thorenfeldt E. Øverli J.A.: *Forsterkning av betong-søyler med karbonfiber*. SINTEF (2001).

[23] Salom P., Gergely J., Young D.: *Torsional Strengthening of Spandrel Beams with Fiber-Reinforced Polymer Laminates.* (https://doi.org/10.1061/(ASCE)1090-0268(2004)8:2(157) Journal of Composites for Constructions vol. 8 (2004).

[24] Teng J. G., Chen J. F., Smith S. T., Lam L.: *FRP Strengthened RC Structures.* John Wiley & Sons, Ltd (2001).

[25] Smith, S. T. and Teng, J. G.: Interfacial stresses in plated beams. *Engineering Structures, 23(7)*; 857-871 (2001).

[26] Cheng J.F. and Teng, J.G.: https://www.researchgate.net/figure/2-Debonding-failure-modes-of-an-FRP-plated-RC-beam-Source-Teng-Chen-2007$_f ig2_3$09351375 *Lastvisited*02.06.2020

[27] Kulturminnesøk: (https://kulturminnesok.no/minne/?queryString=https://data.kulturminne.no/askeladden/lokalitet/110549) Last visited 28.05.2020

[28] Filcker Lagrian: (https://www.flickr.com/photos/larigan/7306965198/in/photostream/) Last visited 28.05.2020

[29] Trondheim byleksikon (https://www.nb.no/items/URN:NBN:no-nb$_d igibok_2$008080104041?$page =$ 163) *Lastvisited*28.05.2020

[30] Oslo Byarkiv: (https://digitaltmuseum.no/011012629928/elgsaeter-bro-opprinnelig-bygget-som-jernbaneviadukt-av-tre-kongsgaard) Last visited 28.05.2020

[31] Bygg.no: (http://www.bygg.no/article/7556) Last visited 28.05.2020

[32] Statens Vegvesen and Aas-Jakobsen: *Rapport fra spesialinspeksjon 2012* 16-0406 Elgeseter bru (2013)

[33] H. Johansen *Klassifisering av Elgeseter Bru 2019-2020 Beregningsforutsetninger* (2019)

[34] Statens Vegvesen and Aas-Jakobsen: *Statiske kontrollberegninger og forsterkning Del 1 av 2* Bruer i Trondheim, inpseksjon og reprasjon. Oppgave 2 Elgeseter bru. (2014)

[35] E. V. Thorenfeldt
Alkali-silica reactions – Strengthening of bridge columns by use of CFRP Field testing on Elgeseter bridge, 2003-2011
Etatsprogrammet Varige konstruksjoner 2012-2015.
Statens vegvesen (2015)

[36] Private conversation with the ARKON Project Team.

[37] Trøndelag City Council
Oppsummerte Innmålinger Ekspansjon
(2020)

[38] *NS 3473: Prosjektering av betongkonstruksjoner*
Norsk Standard. 6th edition (2003)

[39] Statens vegvesen: *Håndbok N400 -Bruprosjektering, Prosjektering av bruer,ferjekaier og andre bærende konstruksjoner*
(2000)

[40] Statens vegvesen: *Håndbok R412 - Bruklassifisering*
(2014)

[41] Lyse I, Wiig, N.J: *Betong: uarmert og armert*
Bruns bokhandels forlag, Trondheim. (1957)

[42] *Eurokode 1: Laster på konstruksjoner. Del 1-4: Allmenne laster - Vind laster*
Norsk Standard (2008)

[43] *Eurokode 1: Laster på konstruksjoner. Del 1-5: Allmenne laster-Termiske påvirkninger*
Norsk Standard (2008)

[44] *Eurokode 2: Prosjektering av betongkonstruksjoner. Del 1-1: Almenne regler og regler for bygninger.*
Norsk Standard NS-EC 1992-1-1:2004+NA:2008. Standard Norge (2004).

[45] Diab S.H, Soliman A.M., Nokken M.: *Exterior Strengthening for ASR damaged concrete: A comparative study of carbon and basalt FRP*
`https://doi.org/10.1016/j.conbuildmat.2019.117435` Construction and Building Materials 235 (2020).

[46] Kabir M. I. et al.
Experimental and theoretical analysis of severely damaged concrete beams strengthened with CFRP
`https://www.sciencedirect.com/science/article/abs/pii/S0950061818311048`
Science Direct (2018).

[47] Yu F. et al.
textitExperimental study on high pre-cracked RC beams shear-strengthened with T CFRP strips
Composite Structures 225 (2019).

[48] Bjenddou O. et al.
Damaged RC beams repaired by bonding of CFRP laminates
`https://www.sciencedirect.com/science/article/abs/pii/S0950061806001036`
ScienceDirect (2007).

[49] Tashan J., Al-Mahaidi R.
Detection of cracks in concrete strengthened with CFRP systems using infra-red thermography.
`(https://www.sciencedirect.com/science/article/abs/pii/S135983681400167X)`
ScienceDirect (2014).

[50] Sørensen,S.I: *Betongkonstruksjoner - Beregninger og dimensjonering etter Eurocode 2.*
Fagbokforlaget, 2 opplag, 2015.

[51] Statens Vegvesen and Aas-Jakobsen:
Statiske kontrollberegninger og forsterkning
Del 2 av 2
Vedlegg D
Bruer i Trondheim, inpseksjon og reprasjon. Oppgave 2 Elgeseter bru.
(2014)

[52] Polar Fusion `http://www.polarfusion.org/wiring/l-moment-diagram.html`

[53] Sika Produktdatablad:*Sika CarboDur M*
(2017)

[54] Sika Produktdatablad:*SikaWrap 231 C*
(2017)

Appendix A

Original Drawings of Elgeseter Bridge

NYE ELGESETER BRU.

Lengdeprofiler. M. = 1/250.

Tegning 2038

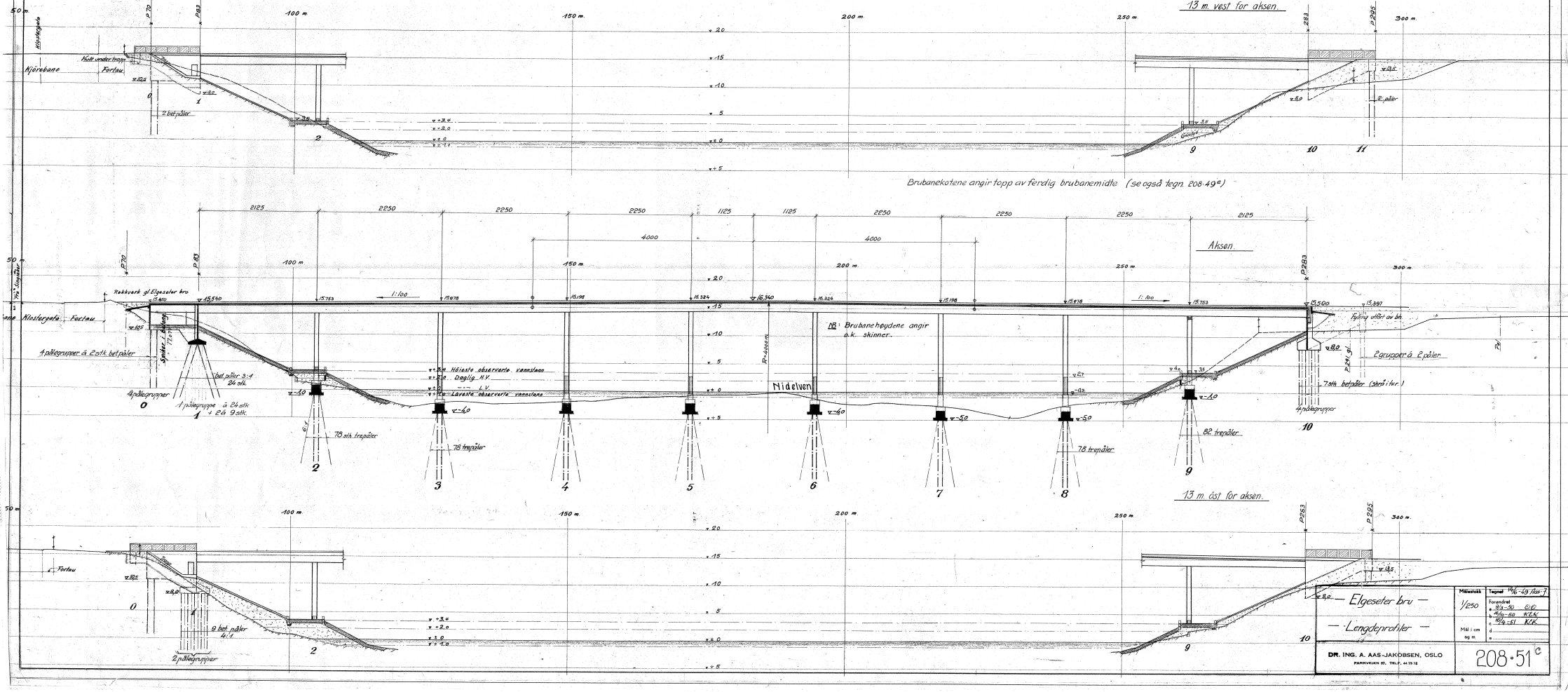

Brubanekotene angir topp av ferdig brubanemidte (se også tegn. 208.49ᵉ)

NB: Brubanehøydene angir o.k. skinner.

— Elgeseter bru —	Målestokk 1/250	Tegnet 14/6-49 Ihm-T	
— Lengdeprofiler —	Mål i cm og m	Forandret a 2/3-50 O.K. b 10/4-50 K.E.K. c 10/4-51 K.K. d e	
DR. ING. A. AAS-JAKOBSEN, OSLO PARKVEIEN 37. TELF. 44 23 72			208·51ᶜ

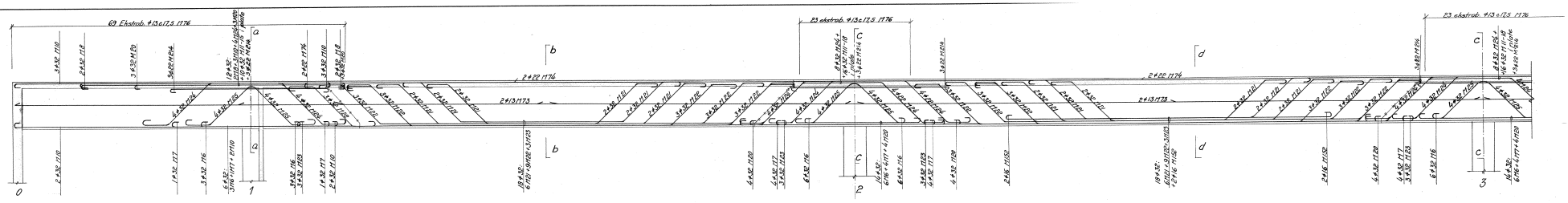

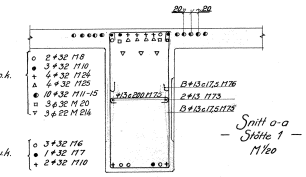

Snitt a-a
— Støtte 1 —
M 1:20

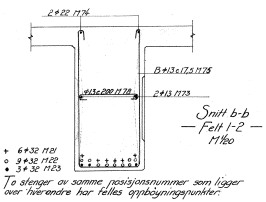

Snitt b-b
— Felt 1-2 —
M 1:20

To stenger av samme posisjonsnummer som ligger over hverandre har felles opnbøyningspunkter.

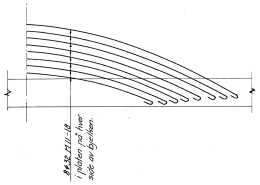

Bøyler i hele bjelkens lengde ϕ13 c 17,5 M 75. Ekstrabøyler som vist.
Armering over støtter 2 til 8 utføres ens. Snitt vist nedenfor.
Armering i felt 2-3 til 8-9 utføres ens. Snitt vist nedenfor.
Støpeskjøtene i bjelker fortannes. Ved hver skjøt innlegges 15 ϕ 22 M 218.
Støpeskjøt langs ak. bjelker som vist på tegn. 208.60 armeres med skråttstillede (45°)
B ϕ 16 St. 37 c 17,5 M 219 første 3 m fra søylesenter,
B ϕ 16 St. 37 c 35 M 219 neste 3 m.

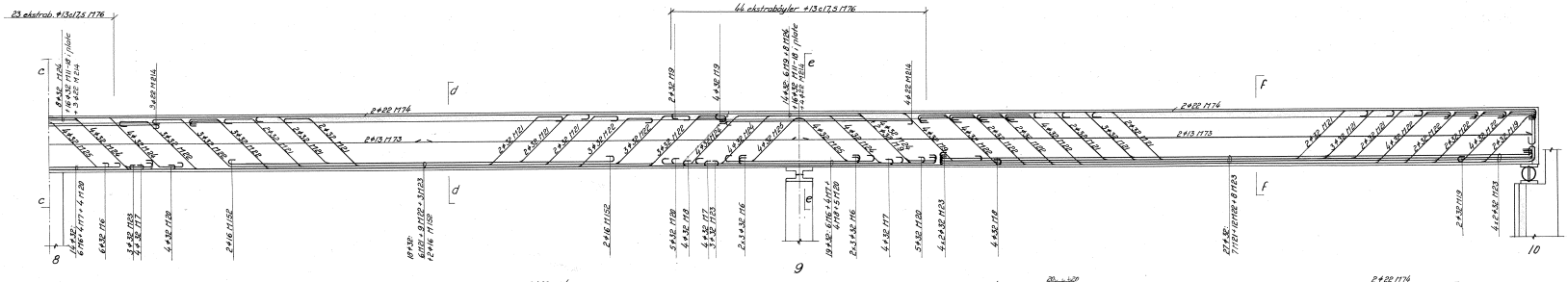

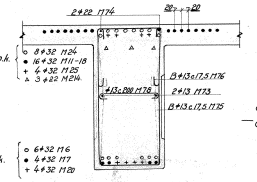

Snitt c-c
— Støtte 2-8 —
M 1:20

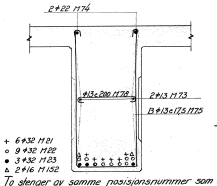

Snitt d-d
— Felt 2-3 til 8-9 —
M 1:20

To stenger av samme posisjonsnummer som ligger over hverandre har felles opnbøyningssted.

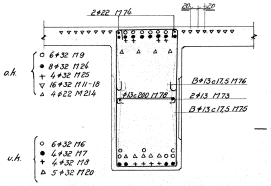

Snitt e-e
— Støtte 9 —
M 1:20

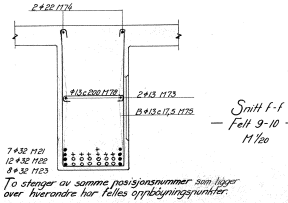

Snitt f-f
— Felt 9-10 —
M 1:20

To stenger av samme posisjonsnummer som ligger over hverandre har felles opnbøyningspunkter.

Betong med 350 kg sement pr. m³
Armering ϕ 32 mm av kvalitet St. 52.
Armering forøvrig av kvalitet St. 37.

— Elgeseter bru —	Målestokk	Tegnet	41.60 HCH
Armering i ytterbjelker A og D	1:50	Forandret	6/6 - 60 HCH
	1:20		31/8 - 60 KEK
	Mål i cm og m		14/10 - 60 KEK
		d	
		e	
DR. ING. A. AAS-JAKOBSEN, OSLO PARKVEIEN 57. TELF. 44 70 72			208·589

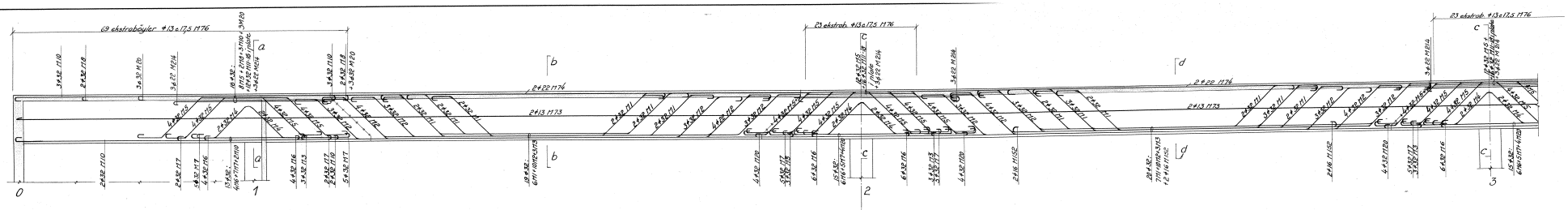

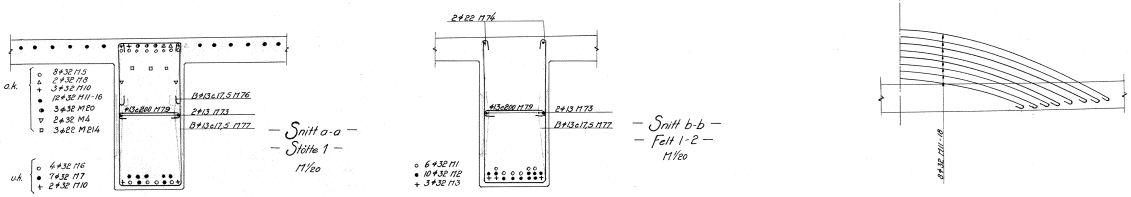

— Snitt a-a —
— Stötte 1 —
M 1/20

— Snitt b-b —
— Felt 1-2 —
M 1/20

Bøyler i hele bjelkens lengde Φ13 c 17.5 11777. Ekstrabøyler som vist.
Armering av stöttene 2 til 8 utføres ens. Se snitt c-c.
Armering i felt 2-3 til 8-9 utføres ens. Se snitt d-d.
Stöpeskjötene i bjelker fortannes. Ved hver skjöt innlegges 15 Φ 22 M 218
Stöpeskjöt langs ak bjelker som vist på tegn. 208 80 armeres med skrå Φ tillegg (45°)
B Φ 16 St 37 c 17,5 M 219 første 3 m fra søylesenter,
B Φ 16 St 37 c 35 M 219 neste 3 m.

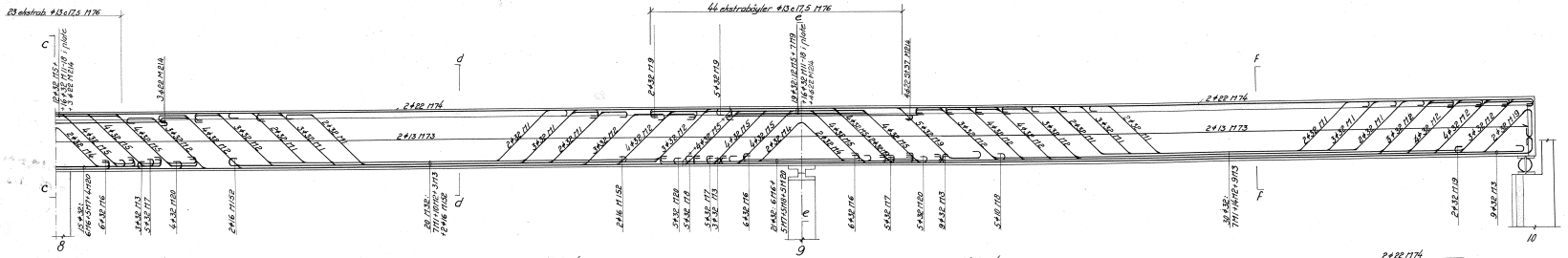

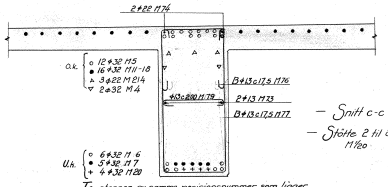

— Snitt c-c —
— Stötte 2 til 8 —
M 1/20

To stenger av samme posisjonsnummer som ligger over hverandre har felles opp bøyningspunkt

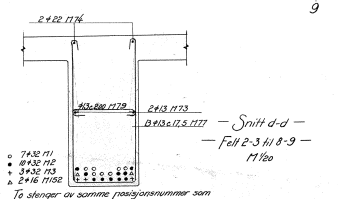

— Snitt d-d —
— Felt 2-3 til 8-9 —
M 1/20

To stenger av samme posisjonsnummer som ligger over hverandre har felles opp bøyningspunkt

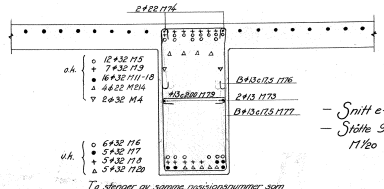

— Snitt e-e —
— Stötte 9 —
M 1/20

To stenger av samme posisjonsnummer som ligger over hverandre har felles opp bøyningspunkt

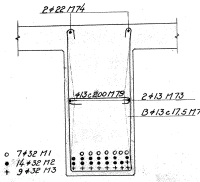

— Snitt f-f —
— Felt 9-10 —
M 1/20

Betong med 350 kg. sement pr. m³
Armering Φ 32 mm av kvalitet St. 52.
Armering forövrig av kvalitet St. 37.

— Elgeseter bru —	Målestokk 1/50, 1/20
Armering i midtbjelker B og C	Tegnet 18/1-50 NEN.
	Forandret 6/6-50 KCK.
	30/8-50 KCK.
	17/10-50 KCK.
	18/1-51 KCK.
DR. ING. A. AAS-JAKOBSEN, OSLO	208·59d

Appendix B

Reinforcement in Frame Model

The reinforcement used in the different sections in the frame model is given below in tables. The placement of the mass center of the steel is given as the eccentricity from the concrete section's mass center. The reinforcement is varying in the inner and outer beams and their reinforcement amounts are therefore given in different tables.

To find the eccentricities, the same process is used as for the more detailed reinforcement calculations in appendix C.B. The only difference is that the frame model only includes the main reinforcement for the upper and lower face.

2.1 Inner Beams

Support Sections

Support 1	Amount	Area [mm^2]	Mass center [mm]
Upper face	28ø32 + 3ø22	23647	353
Lower face	13ø32	10445	-1096

Table B.1: Reinforcement support 1

Support 2-8	Amount	Area [mm^2]	Mass center [mm]
Upper face	28ø32 + 3ø22	23647	366
Lower face	15ø32	12058	-1091

Table B.2: Reinforcement support 2-8

Support 9	Amount	Area [mm^2]	Mass center [mm]
Upper face	35ø32 + 4ø22	29654	354
Lower face	21ø32	16881	-1061

Table B.3: Reinforcement support 9

There is no cross-section drawing of support 10 and the reinforcement is taken from the longitudinal sections.

Support 10	Amount	Area [mm^2]	Mass center [mm]
Upper face	3ø32	2412	361
Lower face	11ø32	8842	-1104

Table B.4: Reinforcement support 10

Field Sections

Field 1	Amount	Area [mm^2]	Mass center [mm]
Lower face	19ø32	15273	-1073

Table B.5: Reinforcement field 1

Field 2-8	Amount	Area [mm^2]	Mass center [mm]
Lower face	20ø32 + 2ø16	16479	-1063

Table B.6: Reinforcement field 2-8

Field 9	Amount	Area [mm^2]	Mass center [mm]
Lower face	30ø32	24115	-1026

Table B.7: Reinforcement field 9

2.2 Outer Beams

Support Sections

Support 1	Amount	Area [mm^2]	Mass center [mm]
Upper face	26ø32 + 3ø22	22040	392
Lower face	13ø32	10450	1096

Table B.8: Reinforcement support 1

Support 2-8	Amount	Area [mm^2]	Mass center [mm]
Upper face	28ø32 + 3ø22	23647	399
Lower face	14ø32	11254	-1093

Table B.9: Reinforcement support 2-8

Support 9	Amount	Area [mm^2]	Mass center [mm]
Upper face	34ø32 + 4ø22	28850	382
Lower face	19ø32	15273	-1073

Table B.10: Reinforcement support 9

There is no cross-section drawing of support 10 and the reinforcement is taken from the longitudinal sections.

Support 10	Amount	Area [mm^2]	Mass center [mm]
Upper face	6ø32	4823	433
Lower face	10ø32	8038	-1109

Table B.11: Reinforcement support 10

Field Sections

Field 1	Amount	Area [mm^2]	Mass center [mm]
Lower face	18ø32	14469	-1077

Table B.12: Reinforcement field 1

Field 2-8	Amount	Area [mm^2]	Mass center [mm]
Lower face	18ø32 + 2ø16	14872	-1071

Table B.13: Reinforcement field 2-8

Field 9	Amount	Area [mm^2]	Mass center [mm]
Lower face	27ø32	21704	-1040

Table B.14: Reinforcement field 9

2.3 Zero moment section

In the zero moment sections, there is a small amount of reinforcement. These sections are in the transition between a positive and negative moment and therefore it is only 3ø32 in these spots. This is set as equal for every beam and is occurring 4 m from each side of the supports.

Zero moment sections	Amount	Area [mm^2]	Mass center [mm]
Lower face	3ø32	2412	-1122

Table B.15: Reinforcement zero moment sections

Appendix C

Section Capacities in ULS

C.A Effective Flange Width

Following NS 3473 point 9.5, the effective flange width of the T-section is defined. The guidelines state that if the flange is in the tension zone, the reinforcement, which is within a certain width given for the compression zone, must be counted as fully utilized. As of this, the effective flange width is equal for the support- and the field-sections.

The effective width depends on the boundary conditions and the length of the span. Span number 9 is the only one standing out as it is hinged. Even though field 1 varies in length, all the other spans (1-8) are assumed similar.

Span 1-8

$b_1 = \frac{b-b_w}{2} = \frac{5500\ \mathbf{mm} - 800\ \mathbf{mm}}{2} = 2350$ mm
$l = 22.5$ m
$l_0 = 0.7 \cdot l = 15.75$ m
$t_f = 280$ mm

$$b_{eff,1} = min \begin{cases} 2350 \text{ mm} \\ 1575 \text{ mm} \\ 2240 \text{ mm} \end{cases} \tag{C.1}$$

The minimum value gives $b_{eff,1} = 1575$ mm which result in $b_{eff} = 1575 \cdot 2 + 800 = 3950$ mm

Span 9

$b_1 = \frac{b-b_w}{2} = \frac{5500mm - 800mm}{2} = 2350$ mm
$l = 21.25$ m
$l_0 = 0.85 \cdot l = 18.06$ m
$t_f = 280$ mm

$$b_{eff,1} = min \begin{cases} 2350 \text{ mm} \\ 1806 \text{ mm} \\ 2240 \text{ mm} \end{cases} \tag{C.2}$$

The minimum value gives:
$b_{eff,1} = 1806$ mm

which result in:
$b_{eff} = 1806 \cdot 2 + 800 = 4412$ mm

C.B Reinforcement

C.B.1 Inner Beams

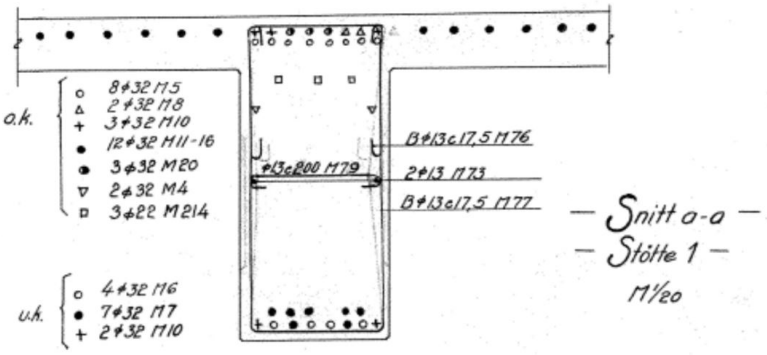

Figure C.1: Reinforcement in support 1

Support 1 Upper face
$n_{ø32} = 20 + 8 = 28$
$n_{ø22} = 3$
$n_{ø32,inclined} = 2$

$A_{s,ø32} = 803,84 \text{ mm}^2$
$A_{s,ø22} = 379,94 \text{ mm}^2$
$A_{s,ø32,inclined} = 563,7 \text{ mm}^2$
$A_s = n_{ø32} \cdot A_{s,ø32} + n_{ø22} \cdot A_{s,ø22} + n_{ø32,inclined} \cdot A_{s,ø32,inclined} = 24772,7 \text{ mm}^2$

$d_{0,1} = 84 \text{ mm}$
$d_{0,2} = 84 + 67 = 151 \text{ mm}$
$d_{0,3} = 291 \text{ mm}$
$d_{0,4} = 460 \text{ mm}$
$d_{eff} = \frac{\sum n_i \cdot A_{s,i} \cdot d_{0,i}}{\sum n_i \cdot A_{s,i}} = 128 \text{ mm}$ from the upper face

The cross section's mass center is 504 mm form the upper face, so with respect to the reference point, the reinforcement's mass center is:
$504 - 128 = 376 \text{ mm}$

Lower face
$n_{ø32} = 8 + 5 = 13$

$A_{s,ø32} = 803,84 \text{ mm}^2$
$A_s = n_{ø,32} \cdot A_{s,ø32} = 10450 \text{ mm}^2$

$d_{0,1} = 84 \text{ mm}$
$d_{0,2} = 84 + 67 = 151 \text{ mm}$
$d_{eff} = \frac{\sum n_i \cdot A_{s,i} \cdot d_{0,i}}{\sum n_i \cdot A_{s,i}} = 110 \text{ mm}$ from the lower face

The cross section's mass center is 1206 mm from the lower face, so with respect to the reference point, the reinforcement's mass center is:
$-(1206 - 110) = -1096$ mm
With a negative value as it is below the reference point.

Support 2-8

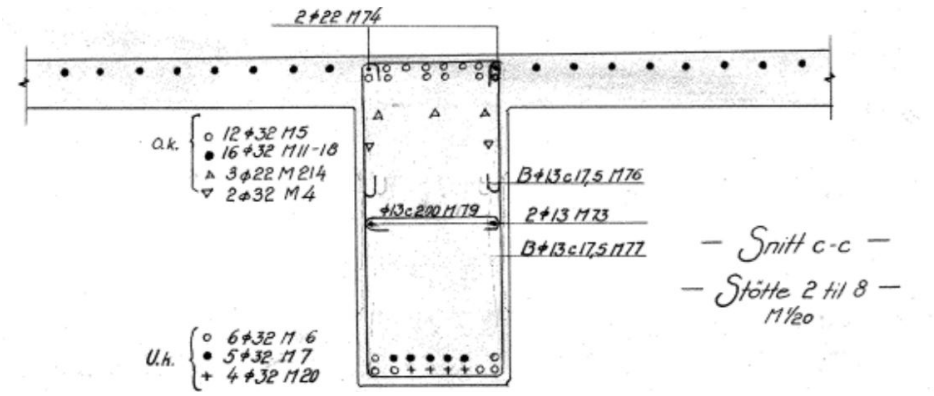

Figure C.2: Reinforcement in support 2-8

Upper face
$n_{ø32} = 22 + 6 = 28$
$n_{ø22} = 2 + 3$
$n_{ø32,inclined} = 2$

$A_{s,ø32} = 803,84$ mm^2
$A_{s,ø22} = 379,94$ mm^2
$A_{s,ø32,inclined} = 563,7$mm^2
$A_s = n_{ø32} \cdot A_{s,ø32} + n_{ø22} \cdot A_{s,ø22} + n_{ø32,inclined} \cdot A_{s,ø32,inclined} = 25532.6$ mm^2

$d_{0,1} = 84$ mm
$d_{0,2} = 84 + 67 = 151$ mm
$d_{0,3} = 291$ mm
$d_{0,4} = 460$ mm
$d_{eff} = \frac{\sum n_i \cdot A_{s,i} \cdot d_{0,i}}{\sum n_i \cdot A_{s,i}} = 122.5$ mm from the upper face

The cross section's mass center is 504 mm form the upper face, so with respect to the reference point, the reinforcement's mass center is:
$504 - 122.5 = 381.5$ mm

Lower face
$n_{ø32} = 8 + 7 = 15$

$A_{s,ø32} = 803,84$ mm^2
$A_s = n_{ø,32} \cdot A_{s,ø32} = 12058$ mm^2

$d_{0,1} = 84$ mm
$d_{0,2} = 84 + 67 = 151$ mm
$d_{eff} = \frac{\sum n_i \cdot A_{s,i} \cdot d_{0,i}}{\sum n_i \cdot A_{s,i}} = 124$ mm from the lower face

The cross section's mass center is 1206 mm form the lower face, so with respect to the reference point, the reinforcement's mass center is:
$-(1206 - 124) = -1082$ mm
With a negative value as it is below the reference point.

Support 9

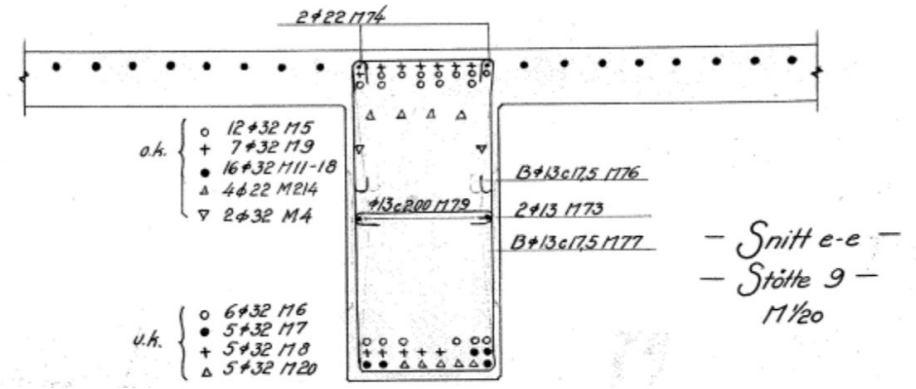

Figure C.3: Reinforcement in support 9

Upper face
$n_{ø32} = 22 + 8 + 5 = 35$
$n_{ø22} = 2 + 4 = 6$
$n_{ø32,inclined} = 2$

$A_{s,ø32} = 803,84$ mm^2
$A_{s,ø22} = 379,94$ mm^2
$A_{s,ø32,inclined} = 563,7$ mm^2
$A_s = n_{ø32} \cdot A_{s,ø32} + n_{ø22} \cdot A_{s,ø22} + n_{ø32,inclined} \cdot A_{s,ø32,inclined} = 31539.5$ mm^2

$d_{0,1} = 84$ mm
$d_{0,2} = 84 + 67 = 151$ mm
$d_{0,3} = 84 + 67 \cdot 2 = 218$ mm
$d_{0,4} = 291$ mm
$d_{0,5} = 460$ mm
$d_{eff} = \frac{\sum n_i \cdot A_{s,i} \cdot d_{0,i}}{\sum n_i \cdot A_{s,i}} = 138$ mm from the upper face

The cross section's mass center is 504 mm from the upper face, so with respect to the reference point, the reinforcement's mass center is:
$504 - 138 = 366$ mm

Lower face

$n_{ø32} = 8 + 7 + 6 = 21$

$A_{s,ø32} = 803,84 \text{ mm}^2$
$A_s = n_{ø,32} \cdot A_{s,ø32} = 16881 \text{ mm}^2$

$d_{0,1} = 84 \text{ mm}$
$d_{0,2} = 84 + 67 = 151 \text{ mm}$
$d_{0,2} = 84 + 67 \cdot 2 = 218 \text{ mm}$
$d_{eff} = \frac{\sum n_i \cdot A_{s,i} \cdot d_{0,i}}{\sum n_i \cdot A_{s,i}} = 145 \text{ mm}$ from the lower face

The cross section's mass center is 1206 mm form the lower face, so with respect to the reference point, the reinforcement's mass center is:
$-(1206 - 145) = -1061 \text{ mm}$
With a negative value as it is below the reference point.

Support 10

Upper face
$n_{ø32} = 5$

$A_{s,ø32} = 803,84 \text{ mm}^2$
$A_s = n_{ø,32} \cdot A_{s,ø32} = 4019 \text{mm}^2$

$d_{0,1} = 84 \text{ mm}$
$d_{0,2} = 375 \text{ mm}$
$d_{eff} = \frac{\sum n_i \cdot A_{s,i} \cdot d_{0,i}}{\sum n_i \cdot A_{s,i}} = 143 \text{ mm}$ from the upper face

The cross section's mass center is 504 mm form the upper face, so with respect to the reference point, the reinforcement's mass center is:
$504 - 143 = 361 \text{ mm}$

Lower face
$n_{ø32} = 8 + 3 = 11$

$A_{s,ø32} = 803,84 \text{ mm}^2$
$A_s = n_{ø,32} \cdot A_{s,ø32} = 8842 \text{ mm}^2$

$d_{0,1} = 84 \text{ mm}$
$d_{0,2} = 84 + 67 = 151 \text{ mm}$
$d_{eff} = \frac{\sum n_i \cdot A_{s,i} \cdot d_{0,i}}{\sum n_i \cdot A_{s,i}} = 102 \text{ mm}$ from the lower face

The cross section's mass center is 1206 mm form the lower face, so with respect to the reference point, the reinforcement's mass center is:
$-(1206 - 102) = -1104 \text{ mm}$
With a negative value as it is below the reference point.

Field 1

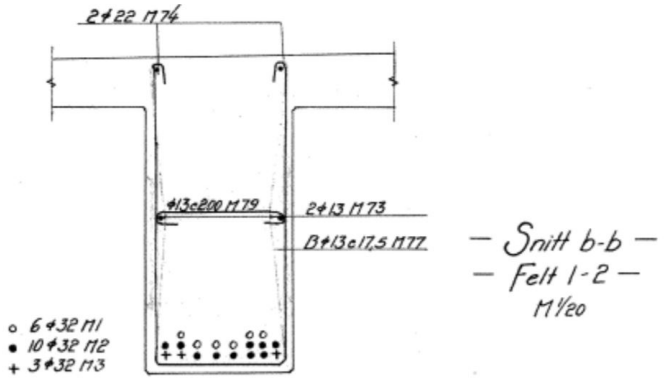

Figure C.4: Reinforcement in field 1

Upper face
$n_{ø22} = 2$

$A_{s,ø22} = 379.94 \text{ mm}^2$
$A_s = n_{ø,22} \cdot A_{s,ø22} = 760 \text{ mm}^2$

$d_{0,1} = 84 \text{ mm}$
$d_{eff} = \frac{\sum n_i \cdot A_{s,i} \cdot d_{0,i}}{\sum n_i \cdot A_{s,i}} = 84 \text{ mm}$ from the upper face

The cross section's mass center is 504 mm form the upper face, so with respect to the reference point, the reinforcement's mass center is:
$504 - 84 = 420 \text{ mm}$

Lower face
$n_{ø32} = 8 + 8 + 3 = 19$

$A_{s,ø32} = 803,84 \text{ mm}^2$
$A_s = n_{ø,32} \cdot A_{s,ø32} = 15273 \text{ mm}^2$

$d_{0,1} = 84 \text{ mm}$
$d_{0,2} = 84 + 67 = 151 \text{ mm}$
$d_{0,2} = 84 + 2 \cdot 67 = 218 \text{ mm}$
$d_{eff} = \frac{\sum n_i \cdot A_{s,i} \cdot d_{0,i}}{\sum n_i \cdot A_{s,i}} = 133 \text{ mm}$ from the lower face

The cross section's mass center is 1206 mm form the lower face, so with respect to the reference point, the reinforcement's mass center is:
$-(1206 - 133) = -1073 \text{ mm}$
With a negative value as it is below the reference point.

Field 2-8

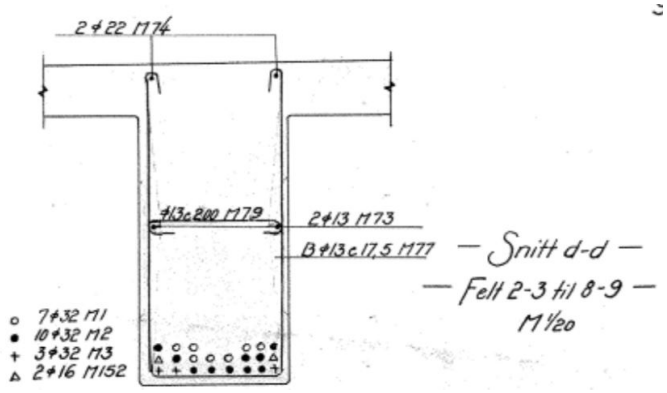

Figure C.5: Reinforcement in field 2-8

Upper face

$n_{ø22} = 2$

$A_{s,ø22} = 379.94 \text{ mm}^2$
$A_s = n_{ø,22} \cdot A_{s,ø22} = 760 \text{ mm}^2$

$d_{0,1} = 84 \text{ mm}$
$d_{eff} = \frac{\sum n_i \cdot A_{s,i} \cdot d_{0,i}}{\sum n_i \cdot A_{s,i}} = 84 \text{ mm}$ from the upper face

The cross section's mass center is 504 mm form the upper face, so with respect to the reference point, the reinforcement's mass center is:
$504 - 84 = 420 \text{ mm}$

Lower face
$n_{ø32} = 8 + 6 + 6 = 20$
$n_{ø16} = 2$

$A_{s,ø32} = 803,84 \text{ mm}^2$
$A_{s,ø16} = 200,96 \text{ mm}^2$
$A_s = n_{ø,32} \cdot A_{s,ø32} + n_{ø,16} \cdot A_{s,ø16} = 16479 \text{ mm}^2$

$d_{0,1} = 84 \text{ mm}$
$d_{0,2} = 84 + 67 = 151 \text{ mm}$
$d_{0,3} = 84 + 2 \cdot 67 = 218 \text{ mm}$
$d_{eff} = \frac{\sum n_i \cdot A_{s,i} \cdot d_{0,i}}{\sum n_i \cdot A_{s,i}} = 144.5 \text{ mm}$ from the lower face

The cross section's mass center is 1206 mm form the lower face, so with respect to the reference point, the reinforcement's mass center is:
$-(1206 - 144.5) = -1061.5 \text{ mm}$
With a negative value as it is below the reference point.

Field 9

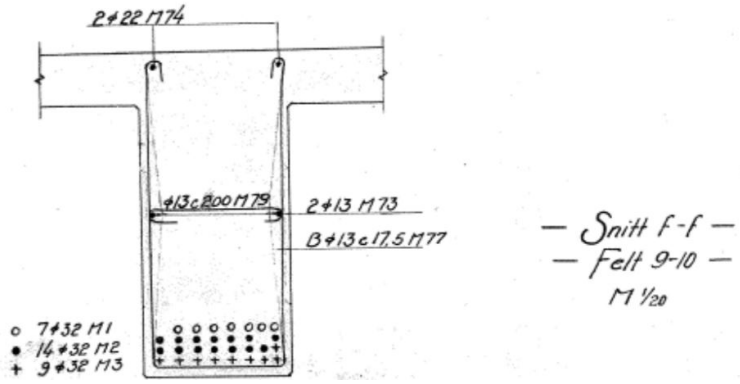

Figure C.6: Reinforcement in field9

Upper face

$n_{ø22} = 2$

$A_{s,ø22} = 379.94 \text{ mm}^2$
$A_s = n_{ø,22} \cdot A_{s,ø22} = 760 \text{ mm}^2$

$d_{0,1} = 84 \text{ mm}$
$d_{eff} = \frac{\sum n_i \cdot A_{s,i} \cdot d_{0,i}}{\sum n_i \cdot A_{s,i}} = 84 \text{ mm}$ from the upper face

The cross section's mass center is 504 mm form the upper face, so with respect to the reference point, the reinforcement's mass center is:
$504 - 84 = 420 \text{ mm}$

Lower face
$n_{ø32} = 8 + 8 + 7 + 7 = 30$

$A_{s,ø32} = 803,84 \text{ mm}^2$
$A_s = n_{ø,32} \cdot A_{s,ø32} = 24115 \text{ mm}^2$

$d_{0,1} = 84 \text{ mm}$
$d_{0,2} = 84 + 67 = 151 \text{ mm}$
$d_{0,3} = 84 + 2 \cdot 67 = 218 \text{ mm}$
$d_{0,4} = 84 + 3 \cdot 67 = 285 \text{ mm}$
$d_{eff} = \frac{\sum n_i \cdot A_{s,i} \cdot d_{0,i}}{\sum n_i \cdot A_{s,i}} = 180 \text{ mm}$ from the lower face

The cross section's mass center is 1206 mm form the lower face, so with respect to the reference point, the reinforcement's mass center is:
$-(1206 - 180) = -1026 \text{ mm}$
With a negative value as it is below the reference point.

Zero Moment Section

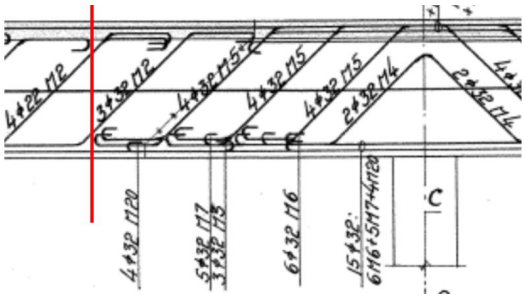

Figure C.7: Reinforcement in ZM indicated by red line

The sections occur both in the inner and outer beams. The placement is set to 4m to 4.5m form each side of every support.
Upper face

$n_{ø22} = 2$
$n_{ø32,inclined} = 4$

$A_{s,ø22} = 379,94 \text{ mm}^2$
$A_{s,ø32,inclined} = 563,7\text{mm}^2$
$A_s = n_{ø22} \cdot A_{s,ø22} + n_{ø32,inclined} \cdot A_{s,ø32,inclined} = 3010.6 \text{ mm}^2$

$d_{0,1} = 84 \text{ mm}$
$d_{0,2} = 430 \text{ mm}$
$d_{eff} = \frac{\sum n_i \cdot A_{s,i} \cdot d_{0,i}}{\sum n_i \cdot A_{s,i}} = 342.7 \text{ mm}$ from the upper face

The cross section's mass center is 504 mm form the upper face, so with respect to the reference point, the reinforcement's mass center is:
$504 - 342.7 = 161.3 \text{ mm}$

Lower face

$n_{ø32} = 3$
$n_{ø32,inclined} = 3$

$A_{s,ø32} = 803,84 \text{ mm}^2$
$A_{s,ø32,inclined} = 563,7 \text{ mm}^2$
$A_s = n_{ø32} \cdot A_{s,ø32} + n_{ø32,inclined} \cdot A_{s,ø32,inclined} = 4099.5 \text{ mm}^2$

$d_{0,1} = 84 \text{ mm}$
$d_{0,2} = 430 \text{ mm}$
$d_{eff} = \frac{\sum n_i \cdot A_{s,i} \cdot d_{0,i}}{\sum n_i \cdot A_{s,i}} = 226.5 \text{ mm}$ from the upper face

The cross section's mass center is 1206 mm form the lower face, so with respect to the reference point, the reinforcement's mass center is:

$-(1206 - 226.5) = -979.5$ mm
With a negative value as it is below the reference point.

C.B.2 Outer beams

Support 1

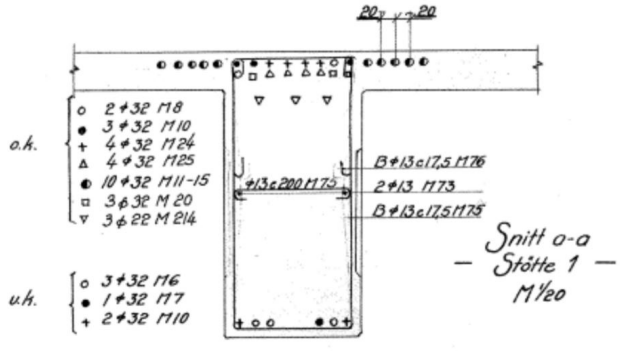

Figure C.8: Reinforcement in support 1

Upper face
$n_{ø32} = 18 + 4 = 22$
$n_{ø32,inclined} = 4$
$n_{ø22} = 3$

$A_{s,ø32} = 803,84$ mm^2
$A_{s,ø32,inclined} = 563,7$ mm^2
$A_{s,ø22} = 379,94$ mm^2
$A_s = n_{ø,32} \cdot A_{s,ø32} + n_{ø22} \cdot A_{s,ø22} + n_{ø32,inclined} \cdot A_{s,ø32,inclined} = 21075$ mm^2

$d_{0,1} = 84$ mm
$d_{0,2} = 84 + 67 = 151$ mm
$d_{0,3} = 291$ mm
$d_{eff} = \frac{\sum n_i \cdot A_{s,i} \cdot d_{0,i}}{\sum n_i \cdot A_{s,i}} = 112.6$ mm from the upper face

The cross section's mass center is 504 mm form the upper face, so with respect to the reference point, the reinforcement's mass center is:
$504 - 112.6 = 391.4$ mm

Lower face
$n_{ø32} = 6$

$A_{s,ø32} = 803,84$ mm^2
$A_s = n_{ø,32} \cdot A_{s,ø32} = 4823$ mm^2

$d_{0,1} = 84$ mm
$d_{eff} = \frac{6 \cdot 84}{6} = 84$ mm from the lower face

The cross section's mass center is 1206 mm form the lower face, so with respect to the reference point, the reinforcement's mass center is:
$-(1206 - 84) = -1122$ mm
With a negative value as it is below the reference point.

Support 2-8

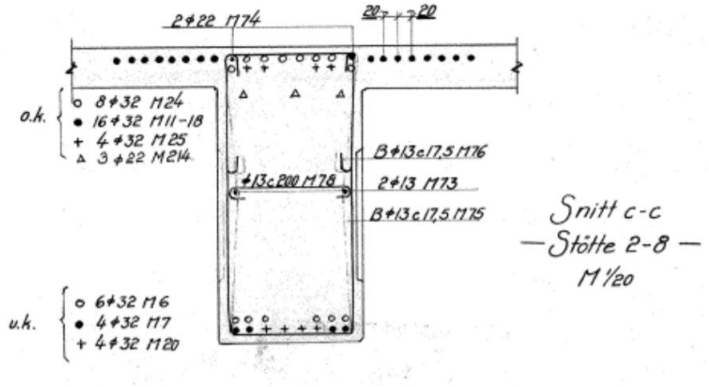

Figure C.9: Reinforcement in support 2-8

Upper face
$n_{ø32} = 22 + 2 = 24$
$n_{ø32,inclined} = 4$
$n_{ø22} = 3 + 2 = 5$

$A_{s,ø32} = 803,84$ mm^2
$A_{s,ø32,inclined} = 563,7$ mm^2
$A_{s,ø22} = 379,94$ mm^2
$A_s = n_{ø,32} \cdot A_{s,ø32} + n_{ø22} \cdot A_{s,ø22} + n_{ø32,inclined} \cdot A_{s,ø32,inclined} = 23442$ mm^2

$d_{0,1} = 84$ mm
$d_{0,2} = 84 + 67 = 151$ mm
$d_{0,3} = 291$ mm
$d_{eff} = \frac{\sum n_i \cdot A_{s,i} \cdot d_{0,i}}{\sum n_i \cdot A_{s,i}} = 105$ mm from the upper face

The cross section's mass center is 504 mm form the upper face, so with respect to the reference point, the reinforcement's mass center is:
$504 - 105 = 399$ mm

Lower face
$n_{ø32} = 8 + 6 = 14$

$A_{s,ø32} = 803,84$ mm^2
$A_s = n_{ø,32} \cdot A_{s,ø32} = 11254$ mm^2

$d_{0,1} = 84$ mm
$d_{0,2} = 84 + 67 = 151$ mm
$d_{eff} = \frac{\sum n_i \cdot A_{s,i} \cdot d_{0,i}}{\sum n_i \cdot A_{s,i}} = 113$ mm from the lower face

The cross section's mass center is 1206 mm form the lower face, so with respect to the reference point, the reinforcement's mass center is:
$-(1206 - 113) = -1093$ mm
With a negative value as it is below the reference point.

Support 9

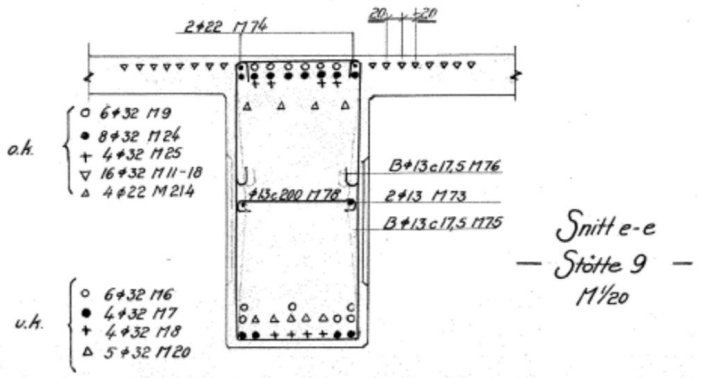

Figure C.10: Reinforcement in support 9

Upper face
$n_{ø32} = 22 + 8 = 30$
$n_{ø32,inclined} = 4$
$n_{ø22} = 4 + 2 = 6$

$A_{s,ø32} = 803,84$ mm^2
$A_{s,ø32,inclined} = 563,7$ mm^2
$A_{s,ø22} = 379,94$ mm^2
$A_s = n_{ø,32} \cdot A_{s,ø32} + n_{ø22} \cdot A_{s,ø22} + n_{ø32,inclined} \cdot A_{s,ø32,inclined} = 28645,6$ mm^2

$d_{0,1} = 84$ mm
$d_{0,2} = 84 + 67 = 151$ mm
$d_{0,3} = 84 + 67 \cdot 2 = 218$ mm
$d_{0,4} = 291$ mm
$d_{eff} = \frac{\sum n_i \cdot A_{s,i} \cdot d_{0,i}}{\sum n_i \cdot A_{s,i}} = 120.6$ mm from the upper face

The cross section's mass center is 504 mm form the upper face, so with respect to the reference point, the reinforcement's mass center is:
$504 - 120.6 = 383.4$mm

Lower face

$n_{ø32} = 8 + 8 + 3 = 19$

$A_{s,ø32} = 803,84 \text{ mm}^2$
$A_s = n_{ø,32} \cdot A_{s,ø32} = 15273 \text{ mm}^2$

$d_{0,1} = 84 \text{ mm}$
$d_{0,2} = 84 + 67 = 151 \text{ mm}$
$d_{0,2} = 84 + 67 \cdot 2 = 218 \text{ mm}$
$d_{eff} = \frac{8 \cdot 84 + 8 \cdot 151 + 3 \cdot 218}{19} = 133 \text{ mm}$ from the lower face

The cross section's mass center is 1206 mm form the lower face, so with respect to the reference point, the reinforcement's mass center is:
$-(1206 - 133) = -1073\text{mm}$
With a negative value as it is below the reference point.

Support 10

Upper face
$n_{ø32} = 6$

$A_{s,ø32} = 803.84 \text{ mm}^2$
$A_s = n_{ø,32} \cdot A_{s,ø32} = 4823 \text{ mm}^2$

$d_{0,1} = 84 \text{ mm}$
$d_{eff} = 84 \text{ mm}$ from the upper face

The cross section's mass center is 504 mm form the upper face, so with respect to the reference point, the reinforcement's mass center is:
$504 - 84 = 420\text{mm}$

Lower face
$n_{ø32} = 8 + 2 = 10$

$A_{s,ø32} = 803,84 \text{ mm}^2$
$A_s = n_{ø,32} \cdot A_{s,ø32} = 8038 \text{ mm}^2$

$d_{0,1} = 84 \text{ mm}$
$d_{0,2} = 84 + 67 = 151 \text{ mm}$
$d_{eff} = \frac{8 \cdot 84 + 2 \cdot 151}{10} = 97 \text{ mm}$ from the lower face

The cross section's mass center is 1206 mm form the lower face, so with respect to the reference point, the reinforcement's mass center is:
$-(1206 - 97) = -1109\text{mm}$
With a negative value as it is below the reference point.

Field 1

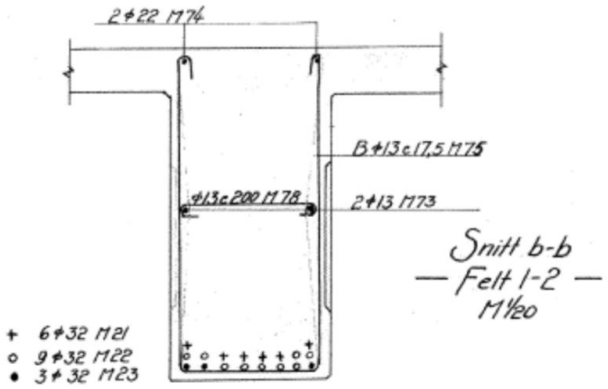

Figure C.11: Reinforcement in field 1

Upper face

$n_{ø22} = 2$

$A_{s,ø22} = 379.94 \text{ mm}^2$
$A_s = n_{ø,22} \cdot A_{s,ø22} = 760 \text{ mm}^2$

$d_{0,1} = 84 \text{ mm}$
$d_{eff} = \frac{\sum n_i \cdot A_{s,i} \cdot d_{0,i}}{\sum n_i \cdot A_{s,i}} = 84 \text{ mm}$ from the upper face

The cross section's mass center is 504 mm form the upper face, so with respect to the reference point, the reinforcement's mass center is:
$504 - 84 = 420 \text{ mm}$

Lower face

$n_{ø32} = 8 + 8 + 2 = 18$

$A_{s,ø32} = 803,84 \text{ mm}^2$
$A_s = n_{ø,32} \cdot A_{s,ø32} = 14469 \text{ mm}^2$

$d_{0,1} = 84 \text{ mm}$
$d_{0,2} = 84 + 67 = 151 \text{ mm}$
$d_{0,2} = 84 + 2 \cdot 67 = 218 \text{ mm}$
$d_{eff} = \frac{\sum n_i \cdot A_{s,i} \cdot d_{0,i}}{\sum n_i \cdot A_{s,i}} = 129 \text{ mm}$ from the lower face

The cross section's mass center is 1206 mm form the lower face, so with respect to the reference point, the reinforcement's mass center is:
$-(1206 - 129) = -1077 \text{mm}$
With a negative value as it is below the reference point.

Field 2-8

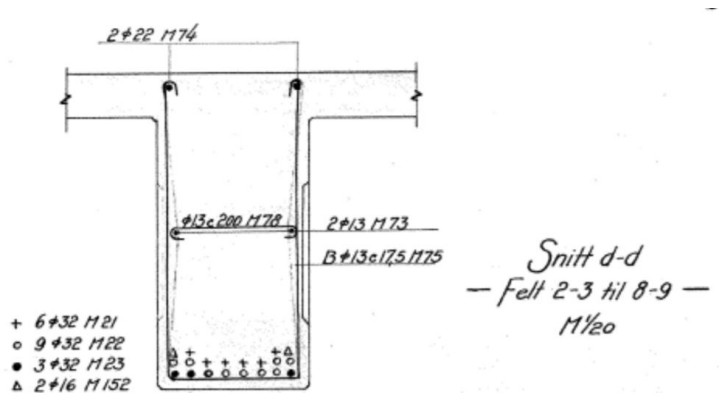

Figure C.12: Reinforcement in field 2-8

Upper face

$n_{ø22} = 2$

$A_{s,ø22} = 379.94 \text{ mm}^2$
$A_s = n_{ø,22} \cdot A_{s,ø22} = 760 \text{ mm}^2$

$d_{0,1} = 84 \text{ mm}$
$d_{eff} = \frac{\sum n_i \cdot A_{s,i} \cdot d_{0,i}}{\sum n_i \cdot A_{s,i}} = 84 \text{ mm}$ from the upper face

The cross section's mass center is 504 mm form the upper face, so with respect to the reference point, the reinforcement's mass center is:
$504 - 84 = 420 \text{ mm}$

Lower face
$n_{ø32} = 8 + 8 + 2 = 18$
$n_{ø16} = 2$

$A_{s,ø32} = 803,84 \text{ mm}^2$
$A_{s,ø16} = 200,96 \text{ mm}^2$
$A_s = n_{ø,32} \cdot A_{s,ø32} + n_{ø,16} \cdot A_{s,ø16} = 14871 \text{ mm}^2$

$d_{0,1} = 84 \text{ mm}$
$d_{0,2} = 84 + 67 = 151 \text{ mm}$
$d_{0,3} = 84 + 2 \cdot 67 = 218 \text{ mm}$
$d_{eff} = \frac{\sum n_i \cdot A_{s,i} \cdot d_{0,i}}{\sum n_i \cdot A_{s,i}} = 131 \text{ mm}$ from the lower face

The cross section's mass center is 1206 mm form the lower face, so with respect to the reference point, the reinforcement's mass center is:
$-(1206 - 131) = -1075 \text{ mm}$
With a negative value as it is below the reference point.

Field 9

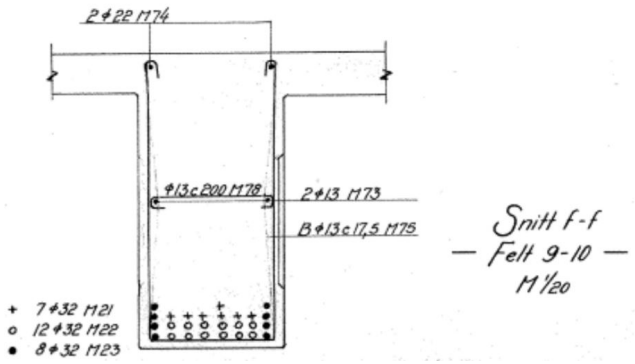

Figure C.13: 9

Upper face

$n_{ø22} = 2$

$A_{s,ø22} = 379.94 \text{ mm}^2$
$A_s = n_{ø,22} \cdot A_{s,ø22} = 760 \text{ mm}^2$

$d_{0,1} = 84 \text{ mm}$
$d_{eff} = \frac{\sum n_i \cdot A_{s,i} \cdot d_{0,i}}{\sum n_i \cdot A_{s,i}} = 84 \text{ mm}$ from the upper face

The cross section's mass center is 504 mm form the upper face, so with respect to the reference point, the reinforcement's mass center is:
$504 - 84 = 420 \text{ mm}$

Lower face
$n_{ø32} = 8 + 8 + 8 + 3 = 27$

$A_{s,ø32} = 803,84 \text{ mm}^2$
$A_s = n_{ø,32} \cdot A_{s,ø32} = 24115 \text{ mm}^2$

$d_{0,1} = 84 \text{ mm}$
$d_{0,2} = 84 + 67 = 151 \text{ mm}$
$d_{0,3} = 84 + 2 \cdot 67 = 218 \text{ mm}$
$d_{0,4} = 84 + 3 \cdot 67 = 285 \text{ mm}$
$d_{eff} = \frac{\sum n_i \cdot A_{s,i} \cdot d_{0,i}}{\sum n_i \cdot A_{s,i}} = 166 \text{ mm}$ from the lower face

The cross section's mass center is 1206 mm form the lower face, so with respect to the reference point, the reinforcement's mass center is:
$-(1206 - 166) = -1040 \text{ mm}$
With a negative value as it is below the reference point.

C.B.2.1 Zero Moment Sections

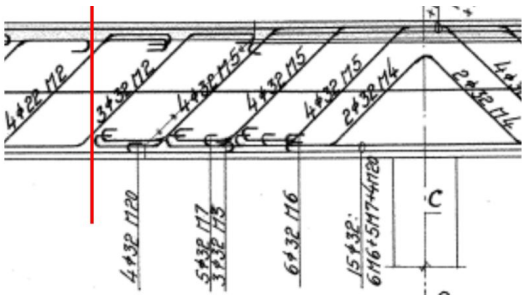

Figure C.14: Reinforcement in ZM indicated by red line

The sections occur both in the inner and outer beams. The placement is set to 4m to 4.5m form each side of every support.
Upper face

$n_{ø22} = 2$
$n_{ø32,inclined} = 3$

$A_{s,ø22} = 379,94 \text{ mm}^2$
$A_{s,ø32,inclined} = 563,7\text{mm}^2$
$A_s = n_{ø22} \cdot A_{s,ø22} + n_{ø32,inclined} \cdot A_{s,ø32,inclined} = 2448 \text{ mm}^2$

$d_{0,1} = 84 \text{ mm}$
$d_{0,2} = 430 \text{ mm}$
$d_{eff} = \frac{\sum n_i \cdot A_{s,i} \cdot d_{0,i}}{\sum n_i \cdot A_{s,i}} = 342.6 \text{ mm}$ from the upper face

The cross section's mass center is 504 mm form the upper face, so with respect to the reference point, the reinforcement's mass center is:
$504 - 342.6 = 161.3 \text{ mm}$

Lower face

$n_{ø32} = 3$
$n_{ø32,inclined} = 3$

$A_{s,ø32} = 803,84 \text{ mm}^2$
$A_{s,ø32,inclined} = 563,7 \text{ mm}^2$
$A_s = n_{ø32} \cdot A_{s,ø32} + n_{ø32,inclined} \cdot A_{s,ø32,inclined} = 4099.5 \text{ mm}^2$

$d_{0,1} = 84 \text{ mm}$
$d_{0,2} = 430 \text{ mm}$
$d_{eff} = \frac{\sum n_i \cdot A_{s,i} \cdot d_{0,i}}{\sum n_i \cdot A_{s,i}} = 226.5 \text{ mm}$ from the upper face

The cross section's mass center is 1206 mm form the lower face, so with respect to the reference point, the reinforcement's mass center is:
$-(1206 - 226.5) = -979.5 \text{ mm}$

With a negative value as it is below the reference point.

C.C Moment Capacity in ULS

The moment capacity is found for selected section being representative for the bridge in the inner and outer beam.

- Support 1
- Support 5
- Support 9
- Field 1
- Field 5
- Field 9
- Section of zero moments

The properties listed in table C.1 will be used in the following calculations

E_c	23 300 MPa
E_s	200 000 MPa
f_{cd}	12 MPa
f_{yd}	272 MPa
ε_{cu}	$3.5 \cdot 10^{-3}$
ε_{yd}	$1.36 \cdot 10^{-3}$

Table C.1: Properties in section

The controls are performed for an assumed situation with self-weight and other live loads including ASR-loads causing the sections over the supports to have tension at the upper face and sections in the fields to have tension at the lower sides.

C.C.1 Sections over the Supports

Over the supports, the flange lies in the tension zone. Therefore the section is calculated as a rectangular cross-section with the width b_w and the height h. All reinforcement placed within the effective flange width is counted as active tension reinforcement in the upper face. The upper reinforcement is referred to as A_s while the lower reinforcement being in the compression zone is referred to as A'_s.

C.C.1.1 Support 1

Inner Beam

$b_w = 800$ mm
$A_s = 24772.7\text{mm}^2$
$d = 1582$ mm
$A'_s = 10449.9$ mm^2

$d' = 110\text{mm}$
$h' = d - d' = 1472$ mm
$\varepsilon_{s,free} = 0.0009626$
$\varepsilon'_{s,free} = 0.0005321$

The compression zone height αd is found by taking equilibrium of the cross section and solving for α.

$\alpha = \frac{f_{yd}A_s - f_{yd}A'_s}{0.8 f_{cd} bd} = 0.321$

Controlling the that the strain in the steel is less than 0.01:

$\varepsilon_s = \frac{\varepsilon_{cu} \cdot (1-\alpha)}{\alpha} + \varepsilon_{s,free} = 0.00741 + 0.0009626 = 0.008373 < 0.01$

Then the moment capacity is found:

$M_{Rd} = 0.8\alpha \cdot (1 - 0.4\alpha) \cdot f_{cd} \cdot b \cdot d^2 + f_{yd} \cdot A'_s \cdot h' = 9556.6$ kNm

The compression reinforcement is assumed to yield. This must be verified such that $\varepsilon'_s > \varepsilon_{yd}$:

$\varepsilon'_s = \frac{\alpha d - d'}{\alpha d} \cdot \varepsilon_{cu} - \varepsilon'_{free} = 0.00274 - 0.0005321 = 0.00221 > 0.00136$

Outer Beam

$b_w = 800$ mm
$A_s = 21075$ mm^2
$d = 1597.4$ mm
$A'_s = 4823$ mm^2
$d' = 84$ mm
$h' = d - d' = 1513.4$ mm
$\varepsilon_{s,free} = 0.001467$
$\varepsilon'_{s,free} = 0.001025$

The compression zone height αd is found by taking equilibrium of the cross section and solving for α.

$\alpha = \frac{f_{yd}A_s - f_{yd}A'_s}{0.8 f_{cd} bd} = 0.360$

Controlling the that the strain in the steel is less than 0.01:

$\varepsilon_s = \frac{\varepsilon_{cu} \cdot (1-\alpha)}{\alpha} + \varepsilon_{s,free} = 0.00621 + 0.001467 = 0.007677 < 0.01$

Then the moment capacity is found:

$M_{Rd} = 0.8\alpha \cdot (1 - 0.4\alpha) \cdot f_{cd} \cdot b \cdot d^2 + f_{yd} \cdot A'_s \cdot h' = 8028.9$ kNm

The compression reinforcement is assumed to yield. This must be verified such that $\varepsilon'_s > \varepsilon_{yd}$:

$\varepsilon'_s = \frac{\alpha d - d'}{\alpha d} \cdot \varepsilon_{cu} - \varepsilon'_{s,free} = 0.00299 - 0.001467 = 0.00152 > 0.00136$

C.C.1.2 Support 2-8

Inner Beam
$b_w = 800$ mm
$A_s = 25532.6$ mm^2
$d = 1587.5$ mm
$A'_s = 12057.6$ mm^2
$d' = 115.3$ mm
$h' = d - d' = 1472.2$ mm
$\varepsilon_{s,free} = 0.0009642$
$\varepsilon'_{s,free} = 0.0005337$

The compression zone height αd is found by taking equilibrium of the cross section and solving for α.

$\alpha = \frac{f_{yd}A_s - f_{yd}A'_s}{0.8 f_{cd} b d} = 0.3$

Controlling the that the strain in the steel is less than 0.01:

$\varepsilon_s = \frac{\varepsilon_{cu} \cdot (1-\alpha)}{\alpha} + \varepsilon_{s,free} = 0.00814 + 0.0009642 = 0.00910 < 0.01$

Then the moment capacity is found:

$M_{Rd} = 0.8\alpha \cdot (1 - 0.4\alpha) \cdot f_{cd} \cdot b \cdot d^2 + f_{yd} \cdot A'_s \cdot h' = 9947.1$ kNm

The compression reinforcement is assumed to yield. This must be verified such that $\varepsilon'_s > \varepsilon_{yd}$:

$\varepsilon'_s = \frac{\alpha d - d'}{\alpha d} \cdot \varepsilon_{cu} - \varepsilon_{s,free} = 0.00265 - 0.0005337 = 0.00212 > 0.00136$

Outer Beam

$b_w = 800$ mm
$A_s = 24442.6$ mm^2
$d = 1605$ mm
$A'_s = 11253.8$ mm^2
$d' = 113$ mm
$h' = d - d' = 1132.6$ mm
$\varepsilon_{s,free} = 0.00147$
$\varepsilon'_{s,free} = 0.001033$

The compression zone height αd is found by taking equilibrium of the cross section and solving for α.

$\alpha = \frac{f_{yd}A_s - f_{yd}A'_s}{0.8 f_{cd} b d} = 0.291$

Controlling the that the strain in the steel is less than 0.01:

$\varepsilon_s = \frac{\varepsilon_{cu} \cdot (1-\alpha)}{\alpha} + \varepsilon_{s,free} = 0.00852 + 0.00147 = 0.00999 < 0.01$

Then the moment capacity is found:

$M_{Rd} = 0.8\alpha \cdot (1 - 0.4\alpha) \cdot f_{cd} \cdot b \cdot d^2 + f_{yd} \cdot A'_s \cdot h' = 9654.5$

The compression reinforcement is assumed to yield. This must be verified such that $\varepsilon'_s > \varepsilon_{yd}$:

$\varepsilon'_s = \frac{\alpha d - d'}{\alpha d} \cdot \varepsilon_{cu} - \varepsilon'_{s,free} = 0.00265 - 0.001033 = 0.00162 > 0.00136$

C.C.1.3 Support 9

Inner Beam

$b_w = 800$ mm
$A_s = 32539.4$ mm^2
$d = 1572$ mm
$A'_s = 17684.5$ mm^2
$d' = 145$ mm
$h' = d - d' = 1427$ mm
$\varepsilon_{s,free} = 0.0009597$
$\varepsilon'_{s,free} = 0.0005423$

The compression zone height αd is found by taking equilibrium of the cross section and solving for α.

$\alpha = \frac{f_{yd} A_s - f_{yd} A'_s}{0.8 f_{cd} b d} = 0.353$

Controlling the that the strain in the steel is less than 0.01:

$\varepsilon_s = \frac{\varepsilon_{cu} \cdot (1-\alpha)}{\alpha} + \varepsilon_{s,free} = 0.00642 + 0.0009597 = 0.00738 < 0.01$

Then the moment capacity is found:

$M_{Rd} = 0.8\alpha \cdot (1 - 0.4\alpha) \cdot f_{cd} \cdot b \cdot d^2 + f_{yd} \cdot A'_s \cdot h' = 12302.6$ kNm.

The compression reinforcement is assumed to yield. This must be verified such that $\varepsilon'_s > \varepsilon_{yd}$:

$\varepsilon'_s = \frac{\alpha d - d'}{\alpha d} \cdot \varepsilon_{cu} - \varepsilon'_{s,free} = 0.00258 - 0.0005423 = 0.00204 > 0.00136$

Outer Beam

$b_w = 800$ mm
$A_s = 28645.6$ mm^2
$d = 1589.4$ mm^2

$A'_s = 15273$ mm^2
$d' = 133.4$ mm
$h' = d - d' = 1456$ mm
$\varepsilon_{s,free} = 0.001464$
$\varepsilon'_{s,free} = 0.001040$

The compression zone height αd is found by taking equilibrium of the cross section and solving for α.

$\alpha = \frac{f_{yd}A_s - f_{yd}A'_s}{0.8 f_{cd} b d} = 0.298$

Controlling the that the strain in the steel is less than 0.01:

$\varepsilon_s = \frac{\varepsilon_{cu} \cdot (1-\alpha)}{\alpha} + \varepsilon_{s,free} = 0.00825 + 0.001464 = 0.00971 < 0.01$

Then the moment capacity is found:

$M_{Rd} = 0.8\alpha \cdot (1 - 0.4\alpha) \cdot f_{cd} \cdot b \cdot d^2 + f_{yd} \cdot A'_s \cdot h' = 11140.7$ kNm

The compression reinforcement is assumed to yield. This must be verified such that $\varepsilon'_s > \varepsilon_{yd}$:

$\varepsilon'_s = \frac{\alpha d - d'}{\alpha d} \cdot \varepsilon_{cu} - \varepsilon'_{s,free} = 0.00251 - 0.001040 = 0.00147 > 0.00136$

C.C.2 Field Sections

In the field section, the upper face is in compression and the lower face is in tension.

The neutral axis is assumed to be in the flange and due to a relatively large cross section, the strain in the steel will become significantly large before obtaining the ultimate strain in the concrete. This implies that the strain in the steel will be decisive for the section's capacity. For this case the entire flange is assumed to has uniform compressive stresses. The section is calculated with the effective width, b_{eff} and a resulting compression force working in the middle of the flange. This method is used when the strain obtained in the steel is larger than 10 ‰ for $\varepsilon_c = \varepsilon_{cu}$

In the field sections, there is mainly reinforcement in the tension zone at the lower face. In addition, there are 2ø22 in the upper face to anchor the shear reinforcement. These are taken into account as active reinforcement.

C.C.2.1 Field 1

Inner Beam

$b_{eff} = 3950$ mm
$A_s = 15273$ mm^2
$d = 1576.6$ mm

$A'_s = 759.9$ mm^2
$d' = 84$ mm
$h' = d - d' = 1492.6$ mm
$\varepsilon_{s,free} = 0.0005390$
$\varepsilon'_{s,free} = 0.0009755$

where α is found by equilibrium:

$\alpha = \frac{f_{yd}A_s - f_{yd}A'_s}{0.8 f_{cd} b d} = 0.066$

Controlling the that the strain in the steel is less than 0.01:

$\varepsilon_s = \frac{\varepsilon_{cu} \cdot (1-\alpha)}{\alpha} + \varepsilon_{s,0} = 0.0495 + 0.0005390 > 0.01$

Since the strain in the steel is larger than 0.01 the compression zone is greater than the one found above. The flange can be classified as a thin flange since $t/d = 280/1530 = 0.18 < 0.33$, the compression zone is therefore assumed to be covering the flange thickness with a constant stress distribution.

$M_{Rd} = f_{yd}A_s(d - \frac{t}{2}) + f_{yd}A'_s(\frac{t}{2} - d') = 5979$ kNm

An additional control of the stresses in the flange is necessary, such that $\sigma_c \leq f_{cd}$:

$\sigma_c = \frac{M_{Rd}}{t \cdot b_{eff}(d - t/2)} = 3.76 < f_{cd}$

Outer Beam

$b_{eff} = 3950$ mm
$A_s = 14469$ mm^2
$d = 1581$ mm
$A'_s = 759.9$ mm^2
$d' = 84$ mm
$h' = d - d' = 1497$ mm
$\varepsilon_{s,free} = 0.0005377$
$\varepsilon'_{s,free} = 0.0009755$

α is found by equilibrium:

$\alpha = \frac{f_{yd}A_s - f_{yd}A'_s}{0.8 f_{cd} b d} = 0.0622$

Controlling the that the strain in the steel is less than 0.01:

$\varepsilon_s = \frac{\varepsilon_{cu} \cdot (1-\alpha)}{\alpha} + \varepsilon_{s,free} = 0.0528 + 0.000538 > 0.01$

Since the strain in the steel is larger than 0.01 the compression zone is greater than the one found above. The flange can be classified as a thin flange since $t/d = 280/1581 = 0.18 < 0.33$, the compression zone is therefore assumed to be covering the flange thickness with a constant stress distribution.

$M_{Rd} = f_{yd}A_s(d - \frac{t}{2}) + f_{yd}A'_s(\frac{t}{2} - d') = 5682.7$ kNm

An additional control of the stresses in the flange is necessary, such that $\sigma_c \leq f_{cd}$:

$\sigma_c = \frac{M_{Rd}}{t \cdot b_{eff}(d-t/2)} = 3.57 < f_{cd}$

C.C.2.2 Field 2-8

Inner Beam
$b_{eff} = 3950$ mm
$A_s = 16478$ mm^2
$d = 1565.5$ mm
$A'_s = 759.9$ mm^2
$d' = 84$ mm
$h' = d - d' = 1481.5$ mm
$\varepsilon_{s,free} = 0.0005422$
$\varepsilon'_{s,free} = 0.0009755$

α is found by equilibrium:

$\alpha = \frac{f_{yd}A_s - f_{yd}A'_s}{0.8 f_{cd} bd} = 0.072$

Controlling the that the strain in the steel is less than 0.01:

$\varepsilon_s = \frac{\varepsilon_{cu} \cdot (1-\alpha)}{\alpha} + \varepsilon_{s,free} = 0.0451 + 0.0005422 > 0.01$

Since the strain in the steel is larger than 0.01 the compression zone is greater than the one found above. The flange can be classified as a thin flange since $t/d = 280/1565 = 0.18 < 0.33$, the compression zone is assumed to be covering the flange thickness with a constant stress distribution.

$M_{Rd} = f_{yd}A_s(d - \frac{t}{2}) + f_{yd}A'_s(\frac{t}{2} - d') = 6400$ kNm

An additional control of the stresses in the flange is necessary, such that $\sigma_c \leq f_{cd}$:

$\sigma_c = \frac{M_{Rd}}{t \cdot b_{eff}(d-t/2)} = 4.06 < f_{cd}$

Outer Beam
$b_{eff} = 3950$ mm
$A_s = 14871$ mm^2
$d = 1579$ mm
$A'_s = 759.9$ mm^2
$d' = 84$ mm
$h' = d - d' = 1495$ mm
$\varepsilon_{s,free} = 0.001038$
$\varepsilon'_{s,free} = 0.001475$

α is found by equilibrium:

$\alpha = \frac{f_{yd}A_s - f_{yd}A'_s}{0.8 f_{cd} bd} = 0.0641$

Controlling the that the strain in the steel is less than 0.01:

$\varepsilon_s = \frac{\varepsilon_{cu} \cdot (1-\alpha)}{\alpha} + \varepsilon_{s,free} = 0.051 + 0.001038 > 0.01$

Since the strain in the steel is larger than 0.01 the compression zone is greater than the one found above. The flange can be classified as a thin flange since $t/d = 280/1572 = 0.18 < 0.33$, the compression zone is assumed to be covering the flange thickness with a constant stress distribution.

$M_{Rd} = f_{yd}A_s(d - \frac{t}{2}) + f_{yd}A'_s(\frac{t}{2} - d') = 5832$ kNm.

An additional control of the stresses in the flange is necessary, such that $\sigma_c \leq f_{cd}$:

$\sigma_c = \frac{M_{Rd}}{t \cdot b_{eff}(d - t/2)} = 3.66 < f_{cd}$

C.C.2.3 Field 9

Inner Beam
$b_{eff} = 3950$ mm
$A_s = 24115$ mm^2
$d = 1530$ mm
$A'_s = 759.9$ mm^2
$d' = 84$ mm
$h' = d - d' = 1446.0$ mm
$\varepsilon_{s,free} = 0.0005526$
$\varepsilon'_{s,free} = 0.0009454$

α is found by equilibrium:

$\alpha = \frac{f_{yd}A_s - f_{yd}A'_s}{0.8 f_{cd} bd} = 0.098$

Controlling the that the strain in the steel is less than 0.01:

$\varepsilon_s = \frac{\varepsilon_{cu} \cdot (1-\alpha)}{\alpha} + \varepsilon_{s,free} = 0.032 + 0.0009474 > 0.01$

Since the strain in the steel is larger than 0.01 the compression zone is greater than the one found above. The flange can be classified as a thin flange since $t/d = 280/1530 = 0.18 < 0.33$, the compression zone is assumed to be covering the flange thickness with a constant stress distribution.

$M_{Rd} = f_{yd}A_s(d - \frac{t}{2}) + f_{yd}A'_s(\frac{t}{2} - d') = 9128.8$ kNm

An additional control of the stresses in the flange is necessary, such that $\sigma_c \leq f_{cd}$:

$\sigma_c = \frac{M_{Rd}}{t \cdot b_{eff}(d - t/2)} = 5.94 < f_{cd}$

Outer Beam

$b_{eff} = 3950$ mm
$A_s = 21703.7$ mm^2
$d = 1544$ mm
$A'_s = 759.9$ mm^2
$d' = 84$ mm
$h' = d - d' = 1460$ mm

$\varepsilon_{s,free} = 0.001048$
$\varepsilon'_{s,free} = 0.001475$

α is found by equilibrium:

$\alpha = \frac{f_{yd}A_s - f_{yd}A'_s}{0.8 f_{cd} bd} = 0.0871$

Controlling the that the strain in the steel is less than 0.01:

$\varepsilon_s = \frac{\varepsilon_{cu} \cdot (1-\alpha)}{\alpha} + \varepsilon_{s,free} = 0.0367 + 0.001452 > 0.01$

Since the strain in the steel is larger than 0.01 the compression zone is greater than the one found above. The flange can be classified as a thin flange since $t/d = 280/1544 = 0.18 < 0.33$, the compression zone is assumed to be covering the flange thickness with a constant stress distribution.

$M_{Rd} = f_{yd}A_s(d - \frac{t}{2}) + f_{yd}A'_s(\frac{t}{2} - d') = 8300$ kNm

An additional control of the stresses in the flange is necessary, such that $\sigma_c \leq f_{cd}$:

$\sigma_c = \frac{M_{Rd}}{t \cdot b_{eff}(d - t/2)} = 5.34 < f_{cd}$

C.C.3 Zero Moment Sections

The zero moment section lies in the transition between the field and the support. Ideally, the moment here is zero. Despite this, the reaction from the ASR-load will set the lower part in tension and the upper part in compression.

Looking at the main reinforcement amount in the beam, the most critical section has only 3ø32 in the lower face. In addition, the inclined bars will contribute as explained earlier.

Inner Beam
$b_{eff} = 3950$ mm^2
$A_s = 4099.6$ mm^2
$d = 1483.5$ mm
$A'_s = 3010$ mm^2
$d' = 342.7$ mm
$h' = d - d' = 1140.8$ mm
$\varepsilon_{s,free} = 0.0005661$
$\varepsilon'_{s,free} = 0.0008999$

α is found by equilibrium:

$\alpha = \frac{f_{yd}A_s - f_{yd}A'_s}{0.8 f_{cd} bd} = 0.00526$

Controlling the that the strain in the steel is less than 0.01:

$\varepsilon_s = \frac{\varepsilon_{cu} \cdot (1-\alpha)}{\alpha} + \varepsilon_{s,free} = 0.66 + 0.0005661 > 0.01$

Since the strain in the steel is larger than 0.01 the compression zone is greater than the one found above. The flange can be classified as a thin flange since $t/d = 280/1484 = 0.19 < 0.33$, the compression zone is assumed to be covering the flange thickness with a constant stress distribution.

$M_{Rd} = f_{yd}A_s(d - \frac{t}{2}) + f_{yd}A'_s(\frac{t}{2} - d') = 1332$ kNm

An additional control of the stresses in the flange is necessary, such that $\sigma_c \leq f_{cd}$:

$\sigma_c = \frac{M_{Rd}}{t \cdot b_{eff}(d - t/2)} = 0.897 < f_{cd}$

Outer Beam
$b_{eff} = 3950$ mm^2
$A'_s = 2448$ mm^2
$d = 1483.5$ mm
$A'_s = 2448$ mm^2
$d' = 322.6$ mm
$h' = d - d' = 1160.9$ mm
$\alpha d = 11.85$ mm
$\varepsilon_{s,free} = 0.001066$
$\varepsilon'_{s,free} = 0.001406$

where α is found by equilibrium:

$\alpha = \frac{f_{yd}A_s - f_{yd}A'_s}{0.8 f_{cd} bd} = 0.00799$

Controlling the that the strain in the steel is less than 0.001:

$\varepsilon_s = \frac{\varepsilon_{cu} \cdot (1-\alpha)}{\alpha} + \varepsilon_{s,free} = 0.435 + 0.001066 > 0.01$

Since the strain in the steel is larger than 0.01 the compression zone is greater than the one found above. The flange can be classified as a thin flange since $t/d = 280/1484 = 0.19 < 0.33$, the compression zone is assumed to be covering the flange thickness with a constant stress distribution.

$M_{Rd} = f_{yd}A_s(d - \frac{t}{2}) + f_{yd}A'_s(\frac{t}{2} - d') = 1376.5$ kNm

An additional control of the stresses in the flange is necessary, such that $\sigma_c \leq f_{cd}$:

$\sigma_c = \frac{M_{Rd}}{t \cdot b_{eff}(d - t/2)} = 0.926 < f_{cd}$

h_o	504 mm
h_u	1206 mm
f_{cd}	12 MPa
f_{yd}	272 MPa
ε_{cu}	0.0035
ε_{yd}	0.00137
b_{eff}	3950 mm
b_w	800 mm
t_f	280 mm
$\varepsilon_{c,top,free}$	0.001
$\varepsilon_{c,bottom,free}$	0.0005

C.C.4 Combined Moment and Axial Force capacities

Combined moment and axial force capacity is found by obtaining the equivalent forces of different strain failures. A compression force is defined as positive and a positive moment gives tension at the lower face.

The estimated strain failures are:

1. $\varepsilon_c = \varepsilon_{cu} = 0.0035$ and $\varepsilon_s = \varepsilon_{yd} = 0.00136$

2. $\varepsilon_c = \varepsilon_{cu} = 0.0035$ and $\varepsilon_s = \varepsilon_{su} = 0.01$

3. $\varepsilon_c = 0$ and $\varepsilon_s = \varepsilon_{su} = 0.01$

4. $\varepsilon'_s = \varepsilon'_{yd} = 0.00136$ and $\varepsilon_s = \varepsilon_{su} = 0.01$

The given properties of the cross section are relevant in the following calculations:

The expansion gradient over the cross section is $2.92 \cdot 10^{-7}$ pr mm.

C.C.4.1 Field Sections 2-8

The field sections have tension in the lower part. A_s is the tension reinforcement and A'_s is the compression reinforcement.

A_s	16 478 mm^2
A'_s	159.6 mm^2
d	1566 mm
d'	84 mm
$\varepsilon_{s,free}$	0.0005421
$\varepsilon'_{s,free}$	0.000975

Table C.2: Field sections 2-8

Strain Failure 1

The failure criteria for this point is $\varepsilon_c = \varepsilon_{cu} = 0.0035$ and $\varepsilon_s = \varepsilon_{yd} = 0.00136$

This implies that the total strain in the steel is 0.00136. The initial stain is 0.0005421. The strain obtained in the steel due to external forces is:

$\Delta\varepsilon_s = \varepsilon_s - \varepsilon_{s,free} = 0.0008179$

This strain is used to find αd

$$\alpha d = \frac{\varepsilon_c}{\varepsilon_c + \Delta\varepsilon_s} \cdot d = 1269.4 \text{ mm} \tag{C.3}$$

This is the compression zone in the section. Assuming a uniform stress distribution, the adjusted compression zone is $0.8 \cdot \alpha d$.

The strain in the compression reinforcement must be controlled:

$$\Delta\varepsilon'_s = \frac{\alpha d - d'}{\alpha d} \cdot \varepsilon_{cu} = 0.003268 \text{ in compression} \tag{C.4}$$

Including the initial tension strain, the total strain is obtained:
$\varepsilon'_s = \varepsilon'_{s,free} - \Delta\varepsilon'_s = -0.002293$

The upper reinforcement has a strain in compression above 0.00136 and is yielding.

The compression zone is placed in the web and for simplicity, the compression forces are separated to T_f and T_w working over the flange and web respectively.

$T_f = f_{cd} \cdot b_{eff} \cdot t_f = 13272$ kN
$T_w = (0.8 \cdot \alpha d - t_f) \cdot f_{cd} \cdot b_w = 7060.8$ kN
$T_c = T_f + T_w = 20332.8$ kN

The steel is yielding both in the upper and lower face.

$S = f_{yd} \cdot A_s = 4482$ kN
$S' = f_{yd} \cdot A'_s = 206.6$ kN

Taking equilibrium of the cross section, N_1 and M_1 are obtained.

$$N_1 = T_c + S' - S = 16057 \text{ kN} \tag{C.5}$$

$$M_1 = T_f(h_o - \frac{t_f}{2}) + T_w(h_o - (0.4\alpha d + \frac{t_f}{2})) + S'(h_o - d') + S(d - h_o) = 8662.7 \text{ kNm} \tag{C.6}$$

Strain Failure 2

The failure criteria for this point is $\varepsilon_c = \varepsilon_{cu} = 0.0035$ and $\varepsilon_s = 0.01$

Same procedure is used as for as point 1.

$\Delta\varepsilon_s = \varepsilon_s - \varepsilon_{s,free} = 0.009458$

This strain is used to find αd

$$\alpha d = \frac{\varepsilon_c}{\varepsilon_c + \Delta\varepsilon_s} \cdot d = 422.9mm \tag{C.7}$$

The strain in the compression reinforcement must be controlled:

$$\Delta\varepsilon'_s = \frac{\alpha d - d'}{\alpha d} \cdot \varepsilon_{cu} = 0.002804 \text{ in compression} \tag{C.8}$$

Including the initial tension strain, the total strain is obtained:

$\varepsilon'_s = \varepsilon'_{s,free} - \Delta\varepsilon'_s = -0.001829$

The upper reinforcement has a strain in compression above 0.00136 and is yielding.

$T_f = f_{cd} \cdot b_{eff} \cdot t_f = 13272$ kN
$T_w = (0.8 \cdot \alpha d - t_f) \cdot f_{cd} \cdot b_w = 560.5$ kN
$T_c = T_f + T_w = 13832.5$ kN

The steel is yielding both in the upper and lower face.

$S = f_{yd} \cdot A_s = 4482$ kN
$S' = f_{yd} \cdot A'_s = 206.6$ kN

Taking equilibrium of the cross section, N_2 and M_2 are obtained.

$$N_2 = T_c + S' - S = 9557.1kN \tag{C.9}$$

$$M_2 = T_f(h_o - \frac{t_f}{2}) + T_w(h_o - (0.4\alpha d + \frac{t_f}{2})) + S'(h_o - d') + S(d - h_o) = 9786.8kNm \tag{C.10}$$

Strain Failure 3

The failure criteria for this point is $\varepsilon_c = 0.0$ and $\varepsilon_s = 0.01$

Same procedure is used as for earlier points.

$\Delta\varepsilon_s = \varepsilon_s - \varepsilon_{s,free} = 0.009458$

In this case there is no area in compression and αd is therefore not existing.

The strain in the upper reinforcement must be controlled for yielding. Now, the steel is only subjected to tension.

$$\Delta\varepsilon'_s = \frac{\Delta\varepsilon_s}{d} \cdot d' = 0.0005073 \text{ in tension} \tag{C.11}$$

Including the initial tension strain, the total strain is obtained:

$\varepsilon'_s = \varepsilon'_{s,free} + \Delta\varepsilon'_s = 0.001427$

The upper reinforcement has a strain in tension above 0.00136 and is yielding.

$S = f_{yd} \cdot A_s = 4482$ kN
$S' = f_{yd} \cdot A'_s = 206.6$ kN

Taking equilibrium of the cross section, N_3 and M_3 are obtained.

$$N_3 = -S' - S = -4688.6kN \tag{C.12}$$

$$M_3 = S(d - h_o) - S'(h_o - d') = 4673.1kNm \tag{C.13}$$

Strain Failure 4

The failure criteria for this point is $\varepsilon'_s = \varepsilon_{yd} = 0.00136$ and $\varepsilon_s = 0.01$

Same procedure is used as earlier points.

$\Delta\varepsilon_s = \varepsilon_s - \varepsilon_{s,free} = 0.009458$

In this case there is no area in compression and αd is therefore not existing.

The total strain in the compression reinforcement is now known to be 0.00136 in tension and is yielding.

$S = f_{yd} \cdot A_s = 4482$ kN
$S' = f_{yd} \cdot A'_s = 206.6$ kN

Taking equilibrium of the cross section, N_4 and M_4 are obtained.

$$N_4 = -S' - S = -4688.6kN \tag{C.14}$$

$$M_4 = S(d - h_o) - S'(h_o - d') = 4673.1kNm \tag{C.15}$$

Point 3 and 4 are equal for the field sections, beacause the compression reinforcement is already yielding in point 3. The four points lead to the following M-N diagram:

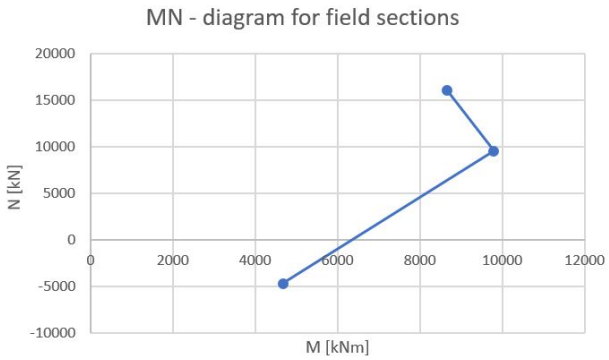

Figure C.15: M-N diagram for field sections

C.C.4.2 Support sections 2-8

The support sections have tension in the upper part. A_s is the tension reinforcement and A'_s is the compression reinforcement.

A_s	25 532.6 mm^2
A'_s	12 057.6 mm^2
d	1587.5 mm
d'	115.2 mm
$\varepsilon_{s,free}$	0.0009642
$\varepsilon'_{s,free}$	0.0005337

Table C.3: Support sections 2-8

Strain Failure 1

The failure criteria for this point is $\varepsilon_c = \varepsilon_{cu} = 0.0035$ and $\varepsilon_s = \varepsilon_{yd} = 0.00136$

This implies that the total strain in the steel is 0.00136. The initial stain is 0.0009642 as the tension reinforcement now lies at the upper face. The strain obtained in the steel due to external forces is:

$\Delta\varepsilon_s = \varepsilon_s - \varepsilon_{s,free} = 0.0003958$

This strain is used to find αd

$$\alpha d = \frac{\varepsilon_c}{\varepsilon_c + \Delta\varepsilon_s} \cdot d = 1426mm \tag{C.16}$$

This is the compression zone in the section. Assuming a uniform stress distribution, the adjusted compression zone is $0.8 \cdot \alpha d$.

The strain in the compression reinforcement at the lower face must be controlled:

$$\Delta\varepsilon'_s = \frac{\alpha d - d'}{\alpha d} \cdot \varepsilon_{cu} = 0.003217 \text{ in compression} \tag{C.17}$$

Including the initial tension strain, the total strain is obtained:
$\varepsilon'_s = \varepsilon'_{s,free} - \Delta\varepsilon'_s = -0.002684$

The upper reinforcement has a strain in compression above 0.00136 and is yielding.

The compression force is found to be:
$T_c = 0.8\alpha d \cdot f_{cd} \cdot b_w = 10953.3$ kN

The steel is yielding both in the upper and lower face.

$S = f_{yd} \cdot A_s = 6944.9$ kN
$S' = f_{yd} \cdot A'_s = 3279.7$ kN

Taking equilibrium of the cross section, N_1 and M_1 are obtained.

$$N_1 = T_c + S' - S = 7288kN \tag{C.18}$$

$$M_1 = -Tc(h_u - 0.4\alpha d) - S'(h_u - d') - S(d - h_o) = -13187.9kNm \tag{C.19}$$

Strain Failure 2

The failure criteria for this point is $\varepsilon_c = \varepsilon_{cu} = 0.0035$ and $\varepsilon_s = 0.01$

Same procedure is used as for as point 1.

$\Delta\varepsilon_s = \varepsilon_s - \varepsilon_{s,free} = 0.009036$

This strain is used to find αd

$$\alpha d = \frac{\varepsilon_c}{\varepsilon_c + \Delta\varepsilon_s} \cdot d = 443.2mm \tag{C.20}$$

The strain in the compression reinforcement must be controlled:

$$\Delta\varepsilon'_s = \frac{\alpha d - d'}{\alpha d} \cdot \varepsilon_{cu} = 0.00259 \text{ in compression} \tag{C.21}$$

Including the initial tension strain, the total strain is obtained:

$\varepsilon'_s = \varepsilon'_{s,free} - \Delta\varepsilon'_s = -0.002057$

The upper reinforcement has a strain in compression above 0.00136 and is yielding.

The compression force in the concrete is found to be:

$T_c = 0.8\alpha d \cdot f_{cd} \cdot b_w = 3404.0$ kN

The steel is yielding both in the upper and lower face.

$S = f_{yd} \cdot A_s = 6944.9$ kN
$S' = f_{yd} \cdot A'_s = 3279.7$ kN

Taking equilibrium of the cross section, N_2 and M_2 are obtained.

$$N_2 = T_c + S' - S = -261.2kN \tag{C.22}$$

$$M_2 = -Tc(h_u - 0.4\alpha d) - S'(h_u - d') - S(d - h_o) = -9728.6kNm \tag{C.23}$$

Strain Failure 3

The failure criteria for this point is $\varepsilon_c = 0.0$ and $\varepsilon_s = 0.01$

Same procedure is used as for earlier points.

$\Delta\varepsilon_s = \varepsilon_s - \varepsilon_{s,free} = 0.009036$

In this case there is no area in compression and αd is therefore not existing.

The strain in the compression reinforcement must be controlled. Now, the reinforcement is only subjected to tension strains.

$$\Delta\varepsilon'_s = \frac{\Delta\varepsilon_s}{d} \cdot d' = 0.0006557 \text{ in tension} \tag{C.24}$$

Including the initial tension strain, the total strain is obtained:

$\varepsilon'_s = \varepsilon'_{s,free} + \Delta\varepsilon'_s = 0.001189$

The lower reinforcement has a strain in tension below 0.00136 and is not yielding.

$S = f_{yd} \cdot A_s = 6944.9$ kN
$S' = \varepsilon'_s \cdot E_s \cdot A'_s = 2868.3$ kN

Taking equilibrium of the cross section, N_3 and M_3 are obtained.

$$N_3 = -S' - S = -9813.1kN \tag{C.25}$$

$$M_3 = -S(d - h_u) + S'(h_u - d') = 479.2kNm \tag{C.26}$$

Strain Failure 4

The failure criteria for this point is $\varepsilon'_s = \varepsilon_{yd} = 0.00136$ and $\varepsilon_s = 0.01$

Same procedure is used as earlier points.

$\Delta\varepsilon_s = \varepsilon_s - \varepsilon_{s,free} = 0.009036$

In this case there is no area in compression and αd is therefore not existing.

The total strain in the compression reinforcement is now known to be 0.00136 in tension and is yielding.

$S = f_{yd} \cdot A_s = 6944.9$ kN
$S' = f_{yd} \cdot A'_s = 3279.7$ kN

Taking equilibrium of the cross section, N_4 and M_4 are obtained.

$$N_4 = -S' - S = -10224.5kN \tag{C.27}$$

$$M_4 = -S(d - h_u) + S'(h_u - d') = 928.0kNm \tag{C.28}$$

This leads to the following M-N diagram for support sections.

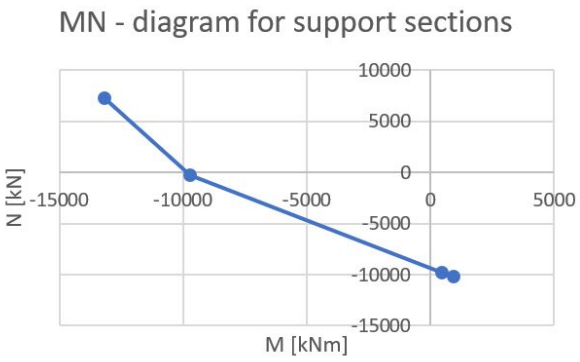

Figure C.16: M-N diagram for support sections

C.C.4.3 Zero Moment Sections

The zero moment sections have tension in the lower part.A_s is the tension reinforcement and A'_s is the compression reinforcement.

A_s	4 101.6 mm^2
A'_s	3 012.2 mm^2
d	1486 mm
d'	338.2 mm
$\varepsilon_{s,free}$	0.0005655
$\varepsilon'_{s,free}$	0.0009011

Table C.4: Zero moment sections 2-8

Strain Failure 1

The failure criteria for this point is $\varepsilon_c = \varepsilon_{cu} = 0.0035$ and $\varepsilon_s = \varepsilon_{yd} = 0.00136$

This implies that the total strain in the steel is 0.00136. The initial stain is 0.0005421. The strain obtained in the steel due to external forces is:

$\Delta\varepsilon_s = \varepsilon_s - \varepsilon_{s,free} = 0.0007945$

This strain is used to find αd

$$\alpha d = \frac{\varepsilon_c}{\varepsilon_c + \Delta\varepsilon_s} \cdot d = 1211.1mm \tag{C.29}$$

This is the compression zone in the section. Assuming a uniform stress distribution, the adjusted compression zone is $0.8 \cdot \alpha d$.

The strain in the compression reinforcement must be controlled:

$$\Delta\varepsilon'_s = \frac{\alpha d - d'}{\alpha d} \cdot \varepsilon_{cu} = 0.002523 \text{ in compression} \tag{C.30}$$

Including the initial tension strain, the total strain is obtained:
$\varepsilon'_s = \varepsilon'_{s,free} - \Delta\varepsilon'_s = -0.001728$

The upper reinforcement has a strain in compression above 0.00136 and is yielding.

The compression zone is placed in the web and for simplicity the compression forces are separated to T_f and T_w working over the flange and web respectively.

$T_f = f_{cd} \cdot b_{eff} \cdot t_f = 13272$ kN
$T_w = (0.8 \cdot \alpha d - t_f) \cdot f_{cd} \cdot b_w = 6613.1$ kN
$T_c = T_f + T_w = 19885.1$ kN

The steel is yielding both in the upper and lower face.

$S = f_{yd} \cdot A_s = 1115.2$ kN
$S' = f_{yd} \cdot A'_s = 818.7$ kN

Taking equilibrium of the cross section, N_1 and M_1 are obtained.

$$N_1 = T_c + S' - S = 19588.6kN \tag{C.31}$$

$$M_1 = T_f(h_o - \frac{t_f}{2}) + T_w(h_o - (0.4\alpha d + \frac{t_f}{2})) + S'(h_o - d') + S(d - h_o) = 5265.4kNm \tag{C.32}$$

Strain Failure 2

The failure criteria for this point is $\varepsilon_c = \varepsilon_{cu} = 0.0035$ and $\varepsilon_s = 0.01$

Same procedure is used as for as point 1.

$\Delta\varepsilon_s = \varepsilon_s - \varepsilon_{s,free} = 0.0094345$

This strain is used to find αd

$$\alpha d = \frac{\varepsilon_c}{\varepsilon_c + \Delta\varepsilon_s} \cdot d = 402.1mm \tag{C.33}$$

The strain in the compression reinforcement must be controlled:

$$\Delta\varepsilon'_s = \frac{\alpha d - d'}{\alpha d} \cdot \varepsilon_{cu} = 0.000556 \text{ in compression} \tag{C.34}$$

Including the initial tension strain, the total strain is obtained:

$\varepsilon'_s = \varepsilon'_{s,free} - \Delta\varepsilon'_s = 0.0003449$

The upper reinforcement has a total strain in tension. So even though the concrete in this area is compressed, the initial tension strain makes the upper reinforcement stand in tension. It is below 0.00136 and therefore not yielding.

$T_f = f_{cd} \cdot b_{eff} \cdot t_f = 13272$ kN
$T_w = (0.8 \cdot \alpha d - t_f) \cdot f_{cd} \cdot b_w = 400.2$ kN
$T_c = T_f + T_w = 13672.2$ kN

The steel is yielding both in the lower part. The upper steel is strained in tension, but not yielding.

$S = f_{yd} \cdot A_s = 1115.2$ kN
$S' = \varepsilon'_s \cdot E_s \cdot A'_s = 207.6$ kN

Taking equilibrium of the cross section, N_2 and M_2 are obtained.

$$N_2 = T_c - S' - S = 12349.1kN \tag{C.35}$$

$$M_2 = T_f(h_o - \frac{t_f}{2}) + T_w(h_o - (0.4\alpha d + \frac{t_f}{2})) - S'(h_o - d') + S(d - h_o) = 5973.0kNm \tag{C.36}$$

Strain Failure 3

The failure criteria for this point is $\varepsilon_c = 0.0$ and $\varepsilon_s = 0.01$

Same procedure is used as for earlier points.

$\Delta\varepsilon_s = \varepsilon_s - \varepsilon_{s,free} = 0.009435$

In this case there is no area in compression and αd is therefore not existing.

The strain in the compression reinforcement must be controlled:

$$\Delta\varepsilon'_s = \frac{\Delta\varepsilon_s}{d} \cdot d' = 0.002147 \text{ in tension} \tag{C.37}$$

Including the initial tension strain, the total strain is obtained:

$\varepsilon'_s = \varepsilon'_{s,free} + \Delta\varepsilon'_s = 0.003048$

The upper reinforcement has a strain in tension above 0.00136 and is yielding.

$S = f_{yd} \cdot A_s = 1115.2$ kN
$S' = f_{yd} \cdot A'_s = 818.7$ kN

Taking equilibrium of the cross section, N_3 and M_3 are obtained.

$$N_3 = -S' - S = -1933kN \tag{C.38}$$

$$M_3 = S(d - h_o) - S'(h_o - d') = 959.4kNm \tag{C.39}$$

Strain Failure 4

The failure criteria for this point is $\varepsilon'_s = \varepsilon_{yd} = 0.00136$ and $\varepsilon_s = 0.01$

Same procedure is used as for earlier points.

$\Delta\varepsilon_s = \varepsilon_s - \varepsilon_{s,free} = 0.009435$

In this case there is no area in compression and αd is therefore not existing.

The total strain in the compression reinforcement is now known to be 0.00136 in tension and is yielding.

$S = f_{yd} \cdot A_s = 1115.2$ kN
$S' = f_{yd} \cdot A'_s = 818.7$ kN

Taking equilibrium of the cross section, N_4 and M_4 are obtained.

$$N_4 = -S' - S = -1933.9kN \tag{C.40}$$

$$M_4 = S(d - h_o) - S'(h_o - d') = 959.4kNm \tag{C.41}$$

Point 3 and 4 are equal for the field sections, because the compression reinforcement is already yielding in point 3. This leads to the following M-N diagram:

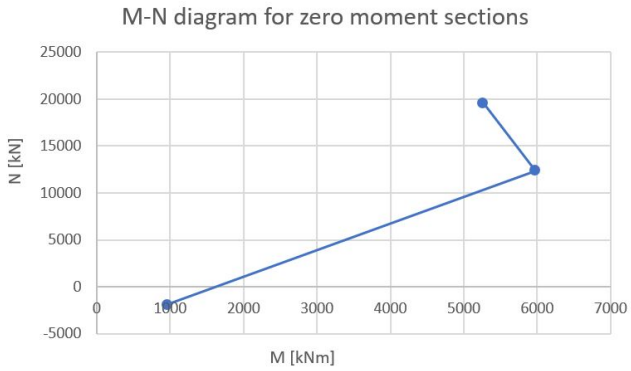

Figure C.17: M-N diagram for sections of zero moment

C.D Shear Capacity in ULS

Shear capacity is calculated by design rules in NS 3473 section 12.3.2 [38]. NS 3473 considers three contributions to the shear-tension capacity in the beam:

- Concrete contribution V_{co}
- Stirrups contribution $V_{sd,s}$
- Contribution from inclined longitudinal reinforcement $V_{sd,i}$

C.D.1 Zero Moment Section

Shear Capacity in ULS without Tensile Forces

In the zero moment section, longitudinal reinforcement is 3ø32 in the tension zone. Inclined bars is defined as bars crossing a fictional shear-tension crack which is 45°, crossing the section at $z = 0.9d$ from the bottom of the beam, see figure ... Following, it is 7ø32 in this section. From the original reinforcement drawing, ø13 stirrups is placed with a distance of 175 mm.

α is angle between the stirrups and the beam's axis. This gives $\alpha = 90$ °.

$A_s = 2411,5$ mm^2
$d = 1626$ mm
$z = 0.9 \cdot d = 1463$ mm
$A_{s,s} = 265$ mm^2
$S_s = 175$ mm
$\frac{A_{s,s}}{S_s} = 1.516$ mm^2/mm
$A_{s,i} = 5627$ mm^2
$\varepsilon_{yd} = 0.00136$

$f_{cd} = 12$ MPa
$f_{td} = 1$ MPa
$\alpha = 90°$
$\gamma_c = 1.4$
$b_w = 800$ mm
$A_c = 2250000$ mm^2

Shear-tension Capacity

Concrete contribution is found by:

$$V_{co} = 0.3 \cdot (f_{td} + \frac{k_A \cdot A_s}{\gamma_c \cdot b_w \cdot d}) b_w \cdot d \leq 0.6 \cdot f_{td} \cdot b_w \cdot d \cdot k_V$$

Where

$k_A = 100$ N/mm^2
$k_V = 1.5 - d/1.0 \geq 1.0 = 1.0$

$V_{co} = 0.3 \cdot (1 + \frac{100 \cdot 2411.5}{1.4 \cdot 800 \cdot 1626}) 800 \cdot 1626 \leq 0.6 \cdot 1 \cdot 800 \cdot 1626 \cdot 1.0 = 441.9$ kN

Contribution from stirrups:

$V_{sd,s} = \frac{f_{yd} \cdot A_{s,s}}{S_s} z(1+\cot\,\alpha)\sin\,\alpha = \frac{272 \cdot 265}{175} \cdot 1463(1+\cot\,90°)\sin\,90° = 603$ kN

Since $\alpha = 90$, the last factors do not contribute. $\cot\,\alpha = 0$ and $\sin\alpha = 1$

Contribution from longitudinal reinforcement with an inclination of 45 :

$V_{sd,i} = \sum f_{yd} \cdot A_{s,i} \cdot \sin\,45° = 272 \cdot 5627 \cdot \sin\,45° = 1082.5$ kN

Such that

$V_{cd} = 2127$ kN

Shear-compression Capacity

$V_{ccd} = 0.3 \cdot 12 \cdot 800 \cdot (1+\cot\,90°) = 2880$ kN $< 0.45 \cdot 12 \cdot 800 \cdot 1463$ kN

Combined Shear and Tension Capacity

It is assumed due to the poor amount of reinforcement in this section that $\varepsilon_s = \varepsilon_{yd}$. It is assumed a axial tension force of 5421 kN, which is obtained from results of the analysis with the solid model in Abaqus/CEA.

$V_{cd,0} = V_{co} \cdot (1 - \frac{N_f}{1.5 \cdot f_{td} \cdot A_c}) = -268.9$ kN≥ 0

Such that $V_{cd,0} = 0$.

The shear-tension capacity including tensile axial force is found by

$V_{cd} = V_{sd,i} + V_{sd,s} = 1685.5$ kN

Appendix D

Equivalent Stiffness

D.A Stage 2 Stiffness

By using known principles it is possible to find the moment of inertia and therefore the bending stiffness of a cracked concrete section. The effective part of the section will change due to the cracks and one must find the new effective parts of both the concrete area and the reinforcement. This is done by following a method provided by S. Sørensen [50]. Since the sections of zero moments are where the largest cracks occur, the equivalent stiffness is found for this section. The activated inclined bars which are set to 70% of the area are included as well as the 2ø22 bars in the plate.

n_{bars}	A_i	Y_i
3ø32	2413	84
0.7·3ø32	1689	424
0.7·4ø32	2252	1286
2ø22	760	1626

Table D.1: Reinforcement in sections of zero moment, inner beam

It is assumed that the compression zone is small and lies within the flange. Therefore the section is assumed to be a rectangular cross-section with the effective flange width. This provides the following tension and compression reinforcement with their respective mass center given from the lower face.

Reinforcement	Area [mm^2]	Placement [mm]]
Lower face, A_s	6534	600.4
Upper face, A'_s	760	1626
Total, $A_{s,tot}$	7114	710.0

Table D.2: Upper and lower reinforcement

The effective arm d for the tension reinforcement is 1109.6 mm from the mass center to the upper face. The effective arm d' for the compression reinforcement

is 84 mm, also measured to the upper face.

The compression zone of the section needs to be obtained. This is done with the same method as for calculating the cross-section's capacity. The concrete section is separated into a contribution from the flange and a contribution from the web. The areas and their respective center of mass is given below.

Part	Area [mm^2]	Mass center [mm]
Flange	1106000	1570
Web	1144000	715
Total	2250000	1135.3

Table D.3: Properties of concrete section with effective flange width

Further, the longterm Young's modulus is 7766 MPa and the steel's Young's modulus is 200 000 MPa. The relationship between the material stiffness is defined as:

$\eta = \frac{E_s}{E_c} = 25.75$

The reinforcement ratios are also defined:

$\rho = \frac{A_s}{b_{eff}d} = 0.00145$
$\rho' = \frac{A'_s}{b_{eff}d} = 0.00173$

Leading to the following properties:

$\eta\rho = 0.03732$
$\eta\mu' = (\eta - 1) \cdot \rho' = 0.00429$
$\eta\mu = (\eta - 1) \cdot \rho = 0.0359$
$f = \frac{tb_f}{bd} = 0$

$f = 0$ since a rectangular cross section is assumed and therefore $b_f = 0$

The height of the compression zone αd is found by solving equation (D.1) for α

$$\alpha^2 + 2A \cdot \alpha - 2 \cdot (A - B) = 0 \tag{D.1}$$

where

$$A = \eta \cdot (\rho + \mu') + f = 0.04162 \tag{D.2}$$

$$B = \eta\mu \cdot (1 - \frac{d'}{d}) + f \cdot (1 - \frac{t}{2d}) = 0.03316 \tag{D.3}$$

Which gives $\alpha = 0.0949$ and $\alpha d = 105.4$ mm.

Then the equivalent moment of inertia is found for a T-cross section with the effective flange width.

$$I_{c,2} = \frac{1}{12}b_{fl}h_{fl}^3+(b_{fl}h_{fl})\cdot(\frac{t_{fl}}{2}-\alpha d)^2+(\eta-1)A_s'(\alpha d-d')2+\eta A_s(d-d)^2 = 1.769\cdot10^{15}\ \text{mm}^4 \tag{D.4}$$

The stage 2 bending stiffness is found to be $EI_{c,2} = 1.374 \cdot 10^{15}$ Nmm^2

This must be compared to the stage 1 stiffness. The area and moment of inertia is found for the same cross section with effective flange width. The whole concrete area is considered as active.

$A_c = 2250000$ mm^2
$\text{I}_c = 6.1323 \cdot 10^{11}$ mm^4

Then the equivalent properties are found.

$A_{eq} = A_c + (\eta - 1) \cdot A_{s,tot} = 2426067$ mm^2
$\text{y}_{eq} = (A_c \cdot y_c + (\eta - 1) \cdot A_{s,tot} \cdot y_s)/A_{eq} = 1104.4$ mm

$I_{eq,c} = I_c + A_c \cdot (y_{eq} - y_c)^2 = 6.154 \cdot 10^{11}$ mm^4
$\sum I_{eq,s,i} = \sum A_{s,i} \cdot (\eta - 1) \cdot (y_{eq} - y_{s,i})^2 = 8.848 \cdot 10^{10}$ mm^2

The total equivalen stiffness is

$$I_{eq,1} = I_c + \sum I_{eq,s,i} = 7.038 \cdot 10^{11}\ \text{mm}^4 \tag{D.5}$$

Which provides a stage 1 bending stiffness of $EI_{c,1} = 5.466 \cdot 10^{15}$ Nmm^2.

The bending stiffness has been reduced by approximately 75%. Implementing this in the Young's modulus the stiffness will go from 7766 MPa to 1941 MPa.

D.B Carbon Fiber Reinforcement

In the frame model the additional strength from the carbon fiber reinforcement is modeled as an increase in stiffness in the strengthened spans. This applies to field 3, field 6 and field 9.

The increase is stiffness is found by using the same principle as for modeling the crack. The bending stiffness is compared between stage 2 concrete without CFRP stage 2 concrete without CFRP. Since the strips cover most parts of the spans, the increase for stage 1 is also found.

The area of the fiber reinforcement perpendicular to the fiber's direction is 672 mm^2. This is placed at the bottom and has a thickness of 1.4 mm. Which means that the mass center is 0.7 mm below the lower face of the concrete. The area is added to the total tension reinforcement and a new d_{sf} is calculated.

$$d_{sf} = \frac{\sum A_{s,i} \cdot y_{s,i} \cdot E_s + A_f \cdot E_f}{A_s \cdot E_s + A_f \cdot E_f} = 1169.7 \text{ mm} \tag{D.6}$$

Reinforcement	Area [mm^2]	Effective arm [mm]
Lower face, A_s	6354	$d_s = 1109.6$
Lower face, A_f	672	$d_f = 1206.7$
Lower face, A_{s_f}	7206	$d_{sf} = 1169.7$
Upper face, A'_s	760	$d'_s = 84$

Table D.4: Upper and lower reinforcement with effective arm

The flexural reinforcement is SIKA M614 has a Young's modulus of $E_f = 210000$ MPa. The material relationship is obtained:

$\eta_f = \frac{E_f}{E_c} = \frac{210000}{7766} = 27.04$

The reinforcement ratios are also defined and combined with the material properties:

$\eta\rho = \frac{\eta_s A_s + \eta_f A_f}{b_{eff} d_{sf}} = 0.0393$

$\eta_s \mu' = (\eta_s - 1) \cdot \rho'_s = (\eta_s - 1) \cdot \frac{A'_s}{b_{eff} d_{sf}} = 0.00407$

$\eta\mu = \frac{(\eta_s - 1) \cdot A_s + (\eta_f) \cdot A_f}{d_{eff} d_{sf}} = 0.0380$

The height of the compression zone

$$\alpha d$$

is found by solving equation (D.7) for α.

$$\alpha^2 + 2A \cdot \alpha - 2 \cdot (A - B) = 0 \tag{D.7}$$

where

$$A = \eta \cdot (\rho + \mu') = 0.0434 \tag{D.8}$$

$$B = \eta\mu \cdot (1 - \frac{d'}{d}) = 0.0352 \tag{D.9}$$

Which gives $\alpha = 0.0916$ and $\alpha d_{sf} = 107.2$ mm.

Then the equivalent moment of inertia is found for a T-cross section with the effective flange width.

$$I_{c,2} = \frac{1}{12} b_{fl} h_{fl}^3 + (b_{fl} h_{fl}) \cdot (\frac{t_{fl}}{2} - \alpha d)^2 + (\eta_s - 1) A_s' (\alpha d - d')^2 + \eta_s A_s (d - \alpha d)^2 + \eta_f A_f (d - \alpha d)^2 \tag{D.10}$$

Which gives
$I_{c,2} = 2.171 \cdot 10^{15}$ mm^4

The stage 2 bending stiffness is found to be $EI_{c,2} = 1.6863 \cdot 10^{15}$ Nmm^2

Compared to the stage 2 bending stiffness without CFRP it has increased with 23%. This implies that the E-module increases from 1941 MPa to 2387 MPa in the cracked sections.

In addition, the rest of the span is investigated which is in stage 1.

The area and moment of inertia is found in section D.A

$A_c = 2250000$ mm^2
$\mathrm{I}_c = 6.1323 \cdot 10^{11}$ mm^4

$A_{eq} = A_c + (\eta_s - 1) A_{s,tot} + (\eta_f) A_f = 2442701$ mm^2
$\mathrm{y}_{eq} = (A_c \cdot y_c + (\eta_s - 1) A_{s,tot} \cdot y_s + \eta_f A_f \cdot y_f) / A_{eq} = 1096.2$ mm

$I_{eq,c} = I_c + A_c \cdot (y_{eq} - y_c)^2 = 6.167 \cdot 10^{11}$ mm^4
$\sum I_{eq,s,i} + I_{eq,f} = \sum A_{s,i} \cdot (\eta - 1) \cdot (y_{eq} - y_{s,i})^2 + A_f \cdot n_f (y_{eq} - y_f)^2 = 1.092 \cdot 10^{11}$ mm^4

The total equivalent stiffness is

$$I_{eq,1} = I_c + \sum I_{eq,s,i} = 7.259 \cdot 10^{11} \text{ mm}^4 \tag{D.11}$$

Which provides a stage 1 bending stiffness of $EI_{c,1} = 5.637 \cdot 10^{15}$ Nmm^2.

This is only a increase of 3.1 %. This is because the concrete being fully active, is contributing to most of the stiffness. The additional stiffness from the CFRP is small in comparison. Still, the Young's modulus is increased from 7766 MPa to 7999 MPa.

Appendix E

Capacity of CFRP in ULS

The capacity of beams including CFRP is found in inner beams in zero moment sections and in the middle of the span. This is because these beams are strengthened and these sections are critical due to the acting forces in the bridge.

Mechanical properties is obtained by product brochures [53], [54] and are presented in table E.1 and E.2.

Table E.1: Mechanical properties of SIKA CarboDur M16

E_f	f_{fk}	ε_{fuk}	γ_f	γ_{BA}
210000 MPa	3000 MPa	1.35%	1.3	1.3

Table E.2: Mechanical properties of SikaWrap 231C

E_f	f_{fk}	ε_{fuk}	γ_f	γ_{BA}
210000 MPa	3850 MPa	1.91 %	1.4	1.3

γ_f and γ_{BA} is obtained from the proposal of the new annex in Eurocode 2 [44]. γ_f is safety factor for tensile strength of the CFRP, while γ_{BA} is safety factor for bond strength.

For calculations, following properties have been used:

Table E.3: Properties of concrete

f_{cd}	12 MPa
f_{ctd}	1 MPa
f_{cm}	28 MPa
E_c	7776 MPa
ε_{cu}	0.0035
$\varepsilon_{c,top,0}$	0.001
$\varepsilon_{c,bottom,0}$	0.0005
h	1710 mm
b_{eff}	3950 mm
b_w	800 mm
t	280 mm
z_c	504.4 mm

Table E.4: Properties of steel reinforcement

f_{yd}	272 MPa
E_s	200000 MPa
ε_{yd}	0.00136
ε_{su}	0.01

E.A Moment capacity

To obtain the moment capacity, multiple situations needs to be verified, which are explained detailed in chapter 6.

To calculate moment capacity, only longitudinal fiber reinforcement is included. This is 8 strips of SIKA CarboDur M16 at the soffit of the beam. Mechanical properties of SIKA CarboDur M16 is listed in E.1. Other properties of the sections are found in tables E.3 and E.4.

Table E.5: Properties of longitudinal fiber reinforcement

f_{fd}	2307 MPa
E_f	210000 MPa
ε_{fud}	0.01038
$\varepsilon_{f,0}$	0.0001
b_f	60 mm
t_f	1.4 mm
n_f	8
A_f	672 mm^2

E.A.1 Bending Moment Capacity of Cross Section

E.A.1.1 Field Section

In the field section, only the reinforcement in the tension zone is included, such that:

$A_s = 16478$ mm^2
$d_s = 1565.5$ mm

Initially, it is assumed that the concrete has reached its ultimate strain, ε_{cu}, such that:

$\varepsilon_c = 0.0035$

k_1 is found by eq. (10.3).

$k_1 = 1 - 2/(3000 * \varepsilon_c) = 0.8095$

The height of the compression zone, x is found by eq. (10.2):

$x = \frac{A_s \cdot f_{yd} + A_f \cdot f_{fd}}{k_1 \cdot f_{cd} \cdot b_{eff}} = 157.2$ mm

It is assumed that the steel and fiber reinforcement has reached its yield limit. This needs to be checked. In addition, a control of strains is necessary to verify that $\varepsilon_s \leq 0.01$ and $\varepsilon_f \leq 0.0135$:

$\varepsilon_f = \varepsilon_c \cdot \frac{h-x}{x} + \varepsilon_{f0} = 0.0347 > 0.0135$
$\varepsilon_s = \varepsilon_c \cdot \frac{d_s - x}{x} = 0.031 > 0.01$

Both fiber and steel reinforcement have exceeded its ultimate strains. This implies that the concrete will not reach its ultimate strain before the capacity is reached. Further, it is assumed that $\varepsilon_c < 0.002$ and we find the compression zone by assuming that $\varepsilon_f = \varepsilon_{fu}$, such that:

$\varepsilon_f = 0.01038$

The strain in the concrete ε_c is found by a linear elastic approach:

$\varepsilon_c = x \cdot \frac{(\varepsilon_f - \varepsilon_0)}{h-x}$

By substitution of this in eq. (10.2) and eq. (10.3), and solving for x, we obtain $x = 220.7$ mm.

Again, the strains in the concrete and steel reinforcement must be verified, such that $\varepsilon_c < 0.002$ and $0.00136 \leq \varepsilon_s \leq 0.01$.

$\varepsilon_c = \frac{x \cdot (\varepsilon_f - \varepsilon_0)}{h-x} = 0.00152 < 0.002$
$\varepsilon_s = \varepsilon_c \cdot \frac{d_s - x}{x} = 0.093 < 0.01$

The precondition of the strain in the fiber reinforcement is valid, and the strains is verified. Following, moment capacity of the zero moment section including CFRP is calculated by eq. (10.4) and eq. (10.1):

$k_2 = \frac{8-1000\varepsilon_c}{4\cdot(6-1000\varepsilon_c)} = 0.0362$

$M_{Rd} = A_s \cdot f_{yd} \cdot (d_s - k_2 \cdot x) + A_f \cdot E_f \cdot \varepsilon_f \cdot (h - k_2 \cdot x) = 9048$ kNm

E.A.1.2 Zero Moment Section

Reinforcement in the web of the beam is assumed to be in the tension zone and compression reinforcement is included, such that:

$A_s = 6350$ mm^2
$d_s = 1110$ mm
$A'_s = 760$ mm^2
$d'_s = 84$ mm
$h' = 1026$ mm

Initially, it is assumed that the concrete has reached its ultimate strain, ε_{cu}, such that:

$\varepsilon_c = 0.0035$

k_1 is found by eq. (10.3).

$k_1 = 1 - 2/(3000 \cdot \varepsilon_c) = 0.8095$

The height of the compression zone, x is found by eq (10.2):

$x = \frac{A_s \cdot f_{yd} + A_f \cdot f_{fd} - f_{yd} \cdot A'_s}{k_1 \cdot f_{cd} \cdot b_{eff}} = 80$ mm

It is assumed that the steel and fiber reinforcement has reached its yield limit. This needs to be checked. In addition, a control of strains is necessary to verify that $\varepsilon_s \leq 0.01$ and $\varepsilon_f \leq 0.0135$:

$\varepsilon_f = \varepsilon_c \cdot \frac{h-x}{x} + \varepsilon_{f0} = 0.0714 > 0.0135$
$\varepsilon_s = \varepsilon_c \cdot \frac{d_s-x}{x} = 0.045 > 0.01$
$\varepsilon'_s = \varepsilon_c \cdot \frac{x-d_s}{x} = -0.00017 < 0.00136$

Both fiber and tension steel reinforcement have exceeded its ultimate strains. This implies that the concrete will not reach its ultimate strain before the capacity is reached. Further, it is assumed that $\varepsilon_c < 0.002$ and we find the compression zone by assuming that $\varepsilon_f = \varepsilon_{fu}$, such that:

$\varepsilon_f = 0.01038$

The strain in the concrete ε_c and compression reinforcement ε'_s is found by a linear elastic approach:

$\varepsilon_c = x \cdot \frac{(\varepsilon_f - \varepsilon_0)}{h-x}$

$\varepsilon'_s = \varepsilon_c \cdot \frac{x-d_s}{x}$

The compression zone, x is found by:

$x = \frac{A_s \cdot f_{yd} + A_f \cdot f_{td} - \varepsilon'_s \cdot E_s \cdot A'_s}{k_1 \cdot f_{cd} \cdot b_{eff}}$

By substitution of the linear elastic equations of ε_c, ε'_s and eq. (10.2) in the previous equation, and solving for x, we obatin $x = 155$ mm.

Again, the strains in the concrete and steel reinforcement must be verified, such that $\varepsilon_c < 0.002$ and $0.00136 \leq \varepsilon_s \leq 0.01$.

$\varepsilon_c = \frac{x \cdot (\varepsilon_f - \varepsilon_0)}{h-x} = 0.001 < 0.002$
$\varepsilon_s = \varepsilon_c \cdot \frac{d_s - x}{x} = 0.0063 < 0.01$ and > 0.00136
$\varepsilon'_s = \varepsilon_c \cdot \frac{x-d_s}{x} = 0.00047 < 0.01$

The precondition of the strain in the fiber reinforcement is valid, and the strains is verified. Following, moment capacity of the zero moment section including CFRP is calculated by eq. (10.4) and (10.1):

$k_2 = \frac{8 - 1000\varepsilon_c}{4 \cdot (6 - 1000\varepsilon_c)} = 0.35$

$M_{Rd} = A_s \cdot f_{yd} \cdot (d_s - k_2 \cdot x) + A_f \cdot E_f \cdot \varepsilon_f \cdot (h - k_2 \cdot x) + \varepsilon'_s \cdot E_s \cdot A'_s = 4323$ kNm

E.A.2 Combined Moment and Axial Force Capacity with CFRP

As the inner beams is subjected to axial tension force, it is essential to find the capacity of both combined. The method is obtained by S.Sørensen section 4.5.2 [50].

The estimated strain failures are:

1. $\varepsilon_c = \varepsilon_{cu} = 0.0035$ and $\varepsilon_s = \varepsilon_{yd} = 0.00136$

2. $\varepsilon_c = \varepsilon_{cu} = 0.0035$ and $\varepsilon_f = \varepsilon_{fu} = 0.01038$

3. $\varepsilon_c = 0$ and $\varepsilon_f = \varepsilon_{fu} = 0.01038$

4. $\varepsilon'_s = \varepsilon'_{yd} = 0.00136$ and $\varepsilon_f = \varepsilon_{fu} = 0.01038$

Properties of the sections is listed in table E.1, E.3, E.4 and E.5.

E.A.2.1 Field Section

As this section is only subjected to a positive moment, only this is evaluated. Reinforcement properties of this section:

$A_s = 16478$ mm^2
$d_s = 1565.5$ mm
$A'_s = 760$ mm^2
$d'_s = 84$ mm

The initial strain of the reinforcement due to ASR expansion is:

$\varepsilon_{s,0} = 0.001 - \frac{0.005}{h} \cdot d_s = 0.000675$
$\varepsilon'_{s,0} = 0.001 - \frac{0.005}{h} \cdot d'_s = 0.000975$

Strain Failure 1

Strain criteria of this failure is:

$\varepsilon_c = \varepsilon_{cu} = 0.0035$
$\varepsilon_s = \varepsilon_{yd} = 0.00136$

$\alpha = \frac{\varepsilon_c}{\varepsilon_c + \varepsilon_s - \varepsilon_{s,0}} = 0.836$

Strain in upper reinforcement:

$\varepsilon'_s = \varepsilon_c \cdot \frac{\alpha \cdot d_s - d'_s}{\alpha \cdot d_s} - \varepsilon'_{s,0} = 0.0023$

Strain in fiber reinforcement:

$\varepsilon_f = \varepsilon_c \cdot \frac{h - \alpha \cdot d_s}{\alpha \cdot d_s} + \varepsilon_{f,0} = 0.00117$

The compression zone αd_s is beneath the flange. Two compression forces is found, one for the flanges and one for the web. It is assumed that it is yielding in the flanges and stresses are reduced in the web. Compression forces in the section is found by:

$T_{c,f} = f_{cd} \cdot t \cdot (b_{eff} - b_w) = 10584$ kN

$T_{c,w} = 0.8 \cdot f_{cd} \cdot \alpha d_s \cdot b_w = 10055$ kN

$T_s = \min(\varepsilon'_s \cdot E_s, f_{yd}) \cdot A'_s = 206.7$ kN

Tension forces in the reinforcements is found by:

$S = \min(\varepsilon_s \cdot E_s), f_{yd}) \cdot A_s = 4482$ kN

$S_f = \varepsilon_f \cdot E_f \cdot A_f = 165.3$ kN

Finally, the axial force N_1 and moment M_1 is obtained by equilibrium:

$N_1 = T_{c,f} + T_{c,s} + T_s - S - S_f = 1620$ kN

$M_1 = T_{c,f}(z_c - t/2) + T_{c,s}(z_c - 0.4 \cdot \alpha d_s) + T_s(z_c - d'_s) + S(d_s - z_c) + S_f(h - z_c)$
$= 8705$ kNm

Strain Failure 2

Strain criteria of this failure is:

$\varepsilon_c = \varepsilon_{cu} = 0.0035$
$\varepsilon_f = \varepsilon_{fu} = 0.01038$

$\alpha = \frac{\varepsilon_c}{\varepsilon_c + \varepsilon_f - \varepsilon_{f,0}} = 0.2539$

Strain in steel reinforcement:

$\varepsilon_s = \varepsilon_c \cdot \frac{\alpha \cdot h - d_s}{\alpha \cdot h} + \varepsilon_{s,0} = 0.0098$

$\varepsilon'_s = \varepsilon_c \cdot \frac{\alpha \cdot h - d'_s}{\alpha \cdot h} - \varepsilon'_{s,0} = 0.00185$

The compression zone αd_s is beneath the flange. Two compression forces is found, one for the flanges and one for the web. It is assumed that it is yielding in the flanges and stresses are reduced in the web. Compression forces in the section is found by:

$T_{c,f} = f_{cd} \cdot t \cdot (b_{eff} - b_w) = 10584$ kN

$T_{c,w} = 0.8 \cdot f_{cd} \cdot \alpha \cdot h \cdot b_w = 3334.5$ kN

$T_s = \min(\varepsilon'_s \cdot E_s, f_{yd}) \cdot A'_s = 206.7$ kN

Tension forces in the reinforcements is found by:

$S = \min(\varepsilon_s \cdot E_s, f_{yd}) \cdot A_s = 4482$ kN

$S_f = \varepsilon_f \cdot E_f \cdot A_f = 1465.5$ kN

Finally, the axial force N_2 and moment M_2 is obtained by equilibrium:

$N_2 = T_{c,f} + T_{c,s} + T_s - S - S_f = 8178$ kN

$M_2 = T_{c,f}(z_c - t/2) + T_{c,s}(z_c - 0.4 \cdot \alpha d_s) + T_s(z_c - d'_s) + S(d_s - z_c) + S_f(h - z_c)$
$= 11569$ kNm

Strain Failure 3

Strain criteria of this failure is:

$\varepsilon_c = 0$
$\varepsilon_f = \varepsilon_{fu} = 0.01038$

Strain in steel reinforcement is found by linear elastic approach:

$$\varepsilon_s = (\varepsilon_f - \varepsilon_{f,0}) \cdot \frac{d_s}{h} + \varepsilon_{s,0} = 0.010$$

$$\varepsilon'_s = (\varepsilon_f - \varepsilon_{f,0}) \cdot \frac{d'_s}{h} + \varepsilon'_{s,0} = 0.00148$$

The upper reinforcement is in tension strain, ergo this will give tension. There is no compression in the concrete at this strain failure. Forces is found by:

$$T_s = \min(\varepsilon'_s \cdot E_s, f_{yd}) \cdot A'_s = 206.7 \text{ kN}$$

$$S = \min(\varepsilon_s \cdot E_s, f_{yd}) \cdot A_s = 4482 \text{ kN}$$

$$S_f = \varepsilon_f \cdot E_f \cdot A_f = 1465.5 \text{ kN}$$

Finally, the axial force N_3 and moment M_3 is obtained by equilibrium:

$$N_3 = -T_s - S - S_f = -6154 \text{ kN}$$

$$M_3 = T_s(d'_s - z_c) + S(d_s - z_c) + S_f(h - z_c) = 6436 \text{ kNm}$$

Strain Failure 4

Strain criteria of this failure is:

$\varepsilon'_s = \varepsilon_{yd} = 0.00136$
$\varepsilon_f = \varepsilon_{fu} = 0.01038$

Strain in steel reinforcement is found by linear elastic approach:

$$\varepsilon_s = (\varepsilon'_s - \varepsilon'_{s,0}) + [(\varepsilon_f - \varepsilon_{f,0}) - (\varepsilon'_s - \varepsilon'_{s,0})] \cdot \frac{d_s - d'_s}{h - d'_s} + \varepsilon_{s,0} = 0.010$$

The upper reinforcement is in tension strain, ergo this will give tension. There is no compression in the concrete at this strain failure. Forces is found by:

$$T_s = \min(\varepsilon'_s \cdot E_s), f_{yd}) \cdot A'_s = 206.7 \text{ kN}$$

$$S = \min(\varepsilon_s \cdot E_s, f_{yd}) \cdot A_s = 4482 \text{ kN}$$

$$S_f = \varepsilon_f \cdot E_f \cdot A_f = 1465.5 \text{ kN}$$

Finally, the axial force N_4 and moment M_4 is obtained by equilibrium:

$$N_4 = -T_s - S - S_f = -6154 \text{ kN}$$

$$M_4 = T_s(d'_s - z_c) + S(d_s - z_c) + S_f(h - z_c) = 6436 \text{ kNm}$$

These values gives the following M-N diagram for field sections:

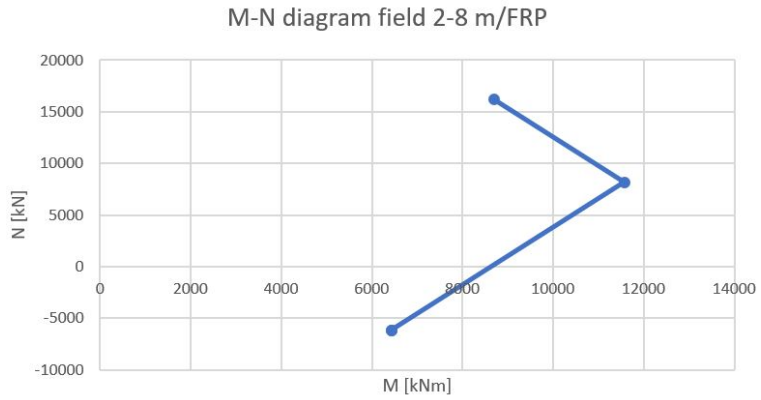

Figure E.1: M-N diagram for field sections with CFRP

E.A.2.2 Zero Moment Section

As this section is only subjected to a positive moment with tension at the bottom of the beam, only this is evaluated. Reinforcement properties of this section:

$A_s = 4099 \text{ mm}^2$
$d_s = 1483.5 \text{ mm}$
$A'_s = 3010 \text{ mm}^2$
$d'_s = 342.7 \text{ mm}$

The initial strain of the reinforcement due to ASR expansion is:

$\varepsilon_{s,0} = 0.001 - \frac{0.005}{h} \cdot d_s = 0.000566$
$\varepsilon'_{s,0} = 0.001 - \frac{0.005}{h} \cdot d'_s = 0.0008998$

Strain Failure 1

Strain criteria of this failure is:

$\varepsilon_c = \varepsilon_{cu} = 0.0035$
$\varepsilon_s = \varepsilon_{yd} = 0.00136$

$\alpha = \frac{\varepsilon_c}{\varepsilon_c + \varepsilon_s - \varepsilon_{s,0}} = 0.815$

Strain in upper reinforcement:

$\varepsilon'_s = \varepsilon_c \cdot \frac{\alpha \cdot d_s - d'_s}{\alpha \cdot d_s} - \varepsilon'_{s,0} = 0.0016$

Strain in fiber reinforcement:

$\varepsilon_f = \varepsilon_c \cdot \frac{h-\alpha \cdot d_s}{\alpha \cdot d_s} + \varepsilon_{f,0} = 0.00155$

The compression zone αd_s is beneath the flange. Two compression forces is found, one for the flanges and one for the web. It is assumed that it is yielding in the flanges and stresses are reduced in the web. Compression forces in the section is found by:

$T_{c,f} = f_{cd} \cdot t \cdot (b_{eff} - b_w) = 10584$ kN

$T_{c,w} = 0.8 \cdot f_{cd} \cdot \alpha d_s \cdot b_w = 9287$ kN

$T_s = \min(\varepsilon'_s \cdot E_s, f_{yd}) \cdot A'_s = 818.7$ kN

Tension forces in the reinforcements is found by:

$S = \min(\varepsilon_s \cdot E_s), f_{yd}) \cdot A_s = 1115$ kN

$S_f = \varepsilon_f \cdot E_f \cdot A_f = 218.6$ kN

Finally, the axial force N_1 and moment M_1 is obtained by equilibrium:

$N_1 = T_{c,f} + T_{c,s} + T_s - S - S_f = 1935.6$ kN

$M_1 = T_{c,f}(z_c - t/2) + T_{c,s}(z_c - 0.4 \cdot \alpha d_s) + T_s(z_c - d'_s) + S(d_s - z_c) + S_f(h - z_c)$ $= 5537$ kNm

Strain Failure 2

Strain criteria of this failure is:

$\varepsilon_c = \varepsilon_{cu} = 0.0035$
$\varepsilon_f = \varepsilon_{fu} = 0.01038$

$\alpha = \frac{\varepsilon_c}{\varepsilon_c + \varepsilon_f - \varepsilon_{f,0}} = 0.2539$

Strain in steel reinforcement:

$\varepsilon_s = \varepsilon_c \cdot \frac{\alpha \cdot h - d_s}{\alpha \cdot h} + \varepsilon_{s,0} = 0.00902$

$\varepsilon'_s = \varepsilon_c \cdot \frac{\alpha \cdot h - d'_s}{\alpha \cdot h} - \varepsilon'_{s,0} = -0.00016$

The compression zone αd_s is beneath the flange. Two compression forces is found, one for the flanges and one for the web. It is assumed that it is yielding in the flanges and stresses are reduced in the web. Compression forces in the section is found by:

$T_{c,f} = f_{cd} \cdot t \cdot (b_{eff} - b_w) = 10584$ kN

$T_{c,w} = 0.8 \cdot f_{cd} \cdot \alpha \cdot h \cdot b_w = 3334.5$ kN

$T_s = \min(\varepsilon'_s \cdot E_s, f_{yd}) \cdot A'_s = -97.7$ kN

As the strain in the upper reinforcement is in tension due to the initial strain, it will give a tension force, hereby a negative force.

Tension forces in the reinforcements is found by:

$S = \min(\varepsilon_s \cdot E_s, f_{yd}) \cdot A_s = 1115$ kN

$S_f = \varepsilon_f \cdot E_f \cdot A_f = 1465.5$ kN

Finally, the axial force N_2 and moment M_2 is obtained by equilibrium:

$N_2 = T_{c,f} + T_{c,s} + T_s - S - S_f = 1124$ kN

$M_2 = T_{c,f}(z_c - t/2) + T_{c,s}(z_c - 0.4 \cdot \alpha d_s) + T_s(z_c - d'_s) + S(d_s - z_c) + S_f(h - z_c)$
$= 7802$ kNm

Strain Failure 3

Strain criteria of this failure is:

$\varepsilon_c = 0$
$\varepsilon_f = \varepsilon_{fu} = 0.01038$

Strain in steel reinforcement is found by linear elastic approach:

$\varepsilon_s = (\varepsilon_f - \varepsilon_{f,0}) \cdot \frac{d_s}{h} + \varepsilon_{s,0} = 0.00949$

$\varepsilon'_s = (\varepsilon_f - \varepsilon_{f,0}) \cdot \frac{d'_s}{h} + \varepsilon'_{s,0} = 0.00296$

The upper reinforcement is in tension strain, ergo this will give tension. There is no compression in the concrete at this strain failure. Forces is found by:

$T_s = \min(\varepsilon'_s \cdot E_s, f_{yd}) \cdot A'_s = 818.7$ kN

$S = \min(\varepsilon_s \cdot E_s, f_{yd}) \cdot A_s = 1115$ kN

$S_f = \varepsilon_f \cdot E_f \cdot A_f = 1465.5$ kN

Finally, the axial force N_3 and moment M_3 is obtained by equilibrium:

$N_3 = -T_s - S - S_f = -3399$ kN

$M_3 = T_s(d'_s - z_c) + S(d_s - z_c) + S_f(h - z_c) = 2726$ kNm

Strain Failure 4

Strain criteria of this failure is:

$\varepsilon'_s = \varepsilon_{yd} = 0.00136$
$\varepsilon_f = \varepsilon_{fu} = 0.01038$

Strain in steel reinforcement is found by linear elastic approach:

$$\varepsilon_s = (\varepsilon'_s - \varepsilon'_{s,0}) + [(\varepsilon_f - \varepsilon_{f,0}) - (\varepsilon'_s - \varepsilon'_{s,0})] \cdot \frac{d_s - d'_s}{h - d'_s} + \varepsilon_{s,0} = 0.0096$$

The upper reinforcement is in tension strain, ergo this will give tension. There is no compression in the concrete at this strain failure. Forces is found by:

$$T_s = \min(\varepsilon'_s \cdot E_s), f_{yd}) \cdot A'_s = 818.7 \text{ kN}$$

$$S = \min(\varepsilon_s \cdot E_s, f_{yd}) \cdot A_s = 1115 \text{ kN}$$

$$S_f = \varepsilon_f \cdot E_f \cdot A_f = 1465.5 \text{ kN}$$

Finally, the axial force N_4 and moment M_4 is obtained by equilibrium:

$$N_4 = -T_s - S - S_f = -3399 \text{ kN}$$

$$M_4 = T_s(d'_s - z_c) + S(d_s - z_c) + S_f(h - z_c) = 2726 \text{ kNm}$$

This leads to the following M-N diagram for the sections of zero moments:

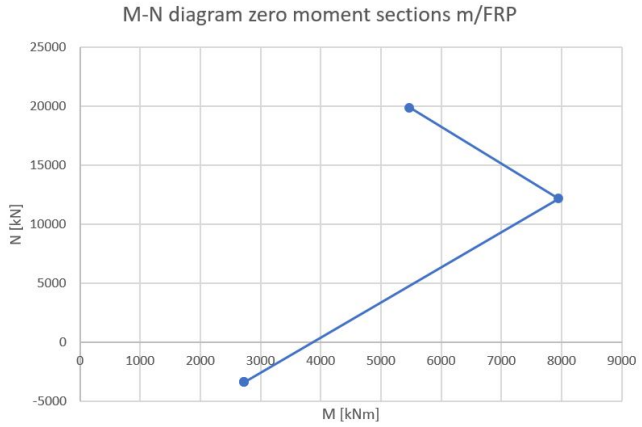

Figure E.2: M-N diagram for field sections with CFRP

E.A.2.3 Intermediate Crack Debonding

Capacity for intermediate crack debonding is calculated as detailed in 6.2.1.

Intermediate Crack Debonding is evaluated at an area between zero moment section and field sections. This area is assumed to have the same properties as the field section.

Properties of field section:

$A_s = 16478$ mm^2
$d_s = 1565.5$ mm
$n_{\emptyset 32} = 20$
$n_{\emptyset 16} = 2$

Properties of concrete, steel reinforcement and fiber reinforcement in found in table E.3, E.4 and E.5, respectively.
The crack spacing, s_r, is found by $s_r = 1.5 \cdot l_{e,0}$. $l_{e,0}$ is calculated as in formula (6.16).

The cracking moment M_{cr} given by (6.17) is found by calculating the section modulus $W_{c,0}$ for the uncracked T-cross section, whereas $I_y = 6.1326 \cdot 10^(11)$.

$$W_{c,0} = \frac{I_y}{h - z_c} = 5.083 \cdot 10^8 \text{mm}^3$$

$\kappa_{fl} = (1.6 - h/1000) < 1$ leading to $\kappa_{fl} = 1$

$$\text{M}_{cr} = \kappa_{fl} \cdot W_{c,0} \cdot f_{ctm} = 1118 \text{ kNm}$$

The bond force per length between the steel reinforcement and the concrete F_{bsm} depends on the steel properties as given in (6.18). The mean bond stress is determined as followed:

$$f_{bsm} = \begin{cases} 0.43 \cdot \kappa_{vb1} \cdot f_{cm}^{2/3} \text{ for ribbed bars} \\ 0.28 \cdot \kappa_{vb2} \cdot \sqrt{f_{cm}} \text{ for smooth bars} \end{cases} \tag{E.1}$$

Where $\kappa_{vb1} = \kappa_{vb2} = 1$ for good bond conditions, $\kappa_{vb1} = 0.7$ and $\kappa_{vb2} = 0.5$ for medium bond conditions.

It is assumed to be smooth bars and good bond conditions because the reinforcement is at the bottom of the beam, such that $\kappa_{vb2} = 1$, resulting in:

$$f_{bsm} = 0.28 \cdot \kappa_{vb2} \cdot \sqrt{f_c m} = 1.482 \text{ MPa}$$

$$F_{bsm} = f_{bsm} \cdot \pi \cdot (n_{\emptyset 32} \cdot \phi_{32} + n_{16} \cdot \phi_{16}) = 3128 \text{ N/mm}$$

Such that:

$$l_{e,0} = \frac{M_{cr}}{0.85 \cdot d_s \cdot F_{bsm}} = 246 \text{ mm}$$

$s_r = 1.5 \cdot l_{e,0} = 369$ mm which is larger than 400 mm, leading to $s_r = 400$ mm.

With known crack spacing, the bond resistance transmission to the FRP between the cracks is calculated with equation (6.20).

$$k_b = \sqrt{\frac{2 - n_f \cdot \frac{b_f}{b}}{1 + n_f \cdot \frac{b_f}{b}}} \geq 1 = 1$$

τ_{b1d} and τ_{bFd} is obtained by:

$\tau_{b1k} = 0.23 \cdot k_b^2 \cdot f_{cm}^{2/3} = 2.121$ MPa

Such that $\tau_{b1d} = \frac{\tau_{b1k}}{\gamma_{BA}} = 1.63$ MPa

$\tau_{bFk} = 10.8 \cdot \alpha_{cc} \cdot f_{cm}^{-0.89} = 0.556$ MPa whereas $\alpha_{cc} = 0.8$

Such that $\tau_{bFd} = \frac{\tau_{bFk}}{\gamma_{BA}} = 0.428$ MPa

Which is leading to the following contributions:

$\Delta F_{fd,B} = 2.3 \cdot \tau_{b1d} \sqrt{s_r} \cdot b_f \cdot n_f = 36$ kN

$\Delta F_{fd,F} = 0.1 \cdot \tau_{bFd} \cdot s_r^{4/3} \cdot b_f \cdot n_f = 60.56$ kN

$\Delta F_{fd,C} = \frac{\kappa_h}{h} \cdot s_r^{1/3} \cdot b_f \cdot n_f = 4.14$ kN as $\kappa_h = 2000$

Summarizing all of the contributions, the resistance of change in tensile forces at each element becomes:

$\Delta F_{fRd} = 100.7$ kN

E.A.3 Shear Capacity

E.A.3.1 Insufficient Shear Capacity

The following properties are used for calculating the additional shear capacity due to the CFRP.

$b_f = 300mm$
$t_0 = 0.128$
$t_f = 0.503mm$
$A_{fw} = 301.6mm^2$
$f_{fk} = 3850MPa$
$E_f = 210000MPa$
$s_f = 424.4$
$h_f = 1309.7mm$
$\alpha = 45°$
$\theta = 21.8°$
$a_t = 0.8$
$f_{cm} = 28MPa$
$\gamma_{fb} = 1.3$

The material properties are found in table E.2. The other properties are estimated using Eurocode 2 and Fib Bulletin 90.

A full area bond have been assumed and since the strips are aligned continuously, the spacing measured along the beams axis is given by $s_f = b_f/sin\alpha$.

The design rules from the new Eurocode 2 annex is using b_f as the fiber width perpendicular to the fibers direction and an effective thickness when calculating the area. The effective thickness is reduced due to the amount of layers. Since the number of layers are above 4, the reduction is given as:

$$t_f = n^{0.85} \cdot t_0 \tag{E.2}$$

which gives an effective thickness of $5^{0.85} \cdot 0.128 = 0.503mm$

To find the height of the crack, and adjustment of the effective arm of the steel must be modified. The effective depth of the steel in the zero moment section is 1483.5 mm. The crack is assumed to only occur in the web which has a height of 1430 mm. With respect to the web, the steel has an effective height $d = 1203.5$ mm. Due to the full-depth application, $h_f = h_w - 0.1d_s = 1309.7$ mm.

The capacity of a closed application must be compared to the the bond strength and the smallest value is decisive:

$$f_{fwd} = min(f_{fbwd}, f_{fwd,c}) \tag{E.3}$$

Where f_{fwdc} is found by using equation (6.26).

The factor k_r taking into account non-uniform stress distribution and fibres around corner is found based on the corner's radius R.

$$k_r = \begin{cases} 0.5\frac{R}{50} \cdot (2 - \frac{R}{50}) & \text{R} < 50 \text{ mm} \\ 0.5 & \text{R} \geq 50 \text{ mm} \end{cases} \tag{E.4}$$

It is assumed that the edges of the web has been rounded of before placing the CFRP, but there is no documented value of R. Therefore it is assumed that R is greater than 50 mm. k_r is set to 0.5.

This gives:

$f_{fwdc} = 0.5 \cdot 0.8\frac{3850}{1.3}\text{MPa} = 1185 \text{ MPa}$

To assume a full bond strength, the effective length must be larger than the bond length. First, the effective bond length l_e is found. Recalling equation (6.6):

$$l_e = 1.5 \cdot \frac{\pi}{k_b} \cdot \sqrt{\frac{E_f \cdot t_f}{8 \cdot f_{cm}^{2/3}}} \tag{E.5}$$

The characteristic value of k is used, $k_k = 0.017$. k_b is calculated by (6.4). Since the shear-reinforcement is laid continuously, $b = b_f$, and $k_b = 0.707$. Then l_e is found to be:

$l_e = 1.5 \cdot \frac{\pi}{0.707} \cdot \sqrt{\frac{210000 \cdot 0.503}{8 \cdot 28^{2/3}}} = 252 \text{ mm}$

To verify that the bond length is greater than the effective length, the following conditions must be controlled:

$h_f/sin\alpha > l_e$ and $l_e < \frac{s_f}{(cot\theta + cot\alpha) \cdot sin\alpha} < h_f/sin\alpha$.

$h_f/sin\alpha = 1852$ and $\frac{s_f}{(cot\theta + cot\alpha) \cdot sin\alpha} = 285$. This verifies that all the bond lengths of the strips covering the crack are larger than the effective bond length. This also gives a $\beta_1 = 1$ from equation (6.9). The characteristic bond strength is obtained by using equation (6.11)

$$f_{fbk} = 0.17 \cdot 0.707 \cdot 1\sqrt{\frac{2 \cdot 210000}{0.128} \cdot 28^{(2/3)}} = 661\text{MPa} \tag{E.6}$$

Which gives $f_{fbwd} = \frac{f_{fbk}}{\gamma_{fb}} = 508.5$ MPa. This is lower than f_{fwdc} and the bond strength will be the decisive strength of the fibre reinforcement.

Finally the shear capacity is found by using equation (6.25).

$$V_{rdf} = \frac{301.6}{424.3} \cdot 1309.7 \cdot 508.5 \cdot (1+1) \cdot 0.707 = 669.7\text{kN} \tag{E.7}$$

The shear capacity $V_{rdf} = 669.7$ kN is found for a fictitious shear crack with a 45° inclination which is the worst possible inclination concerning shear tension capacity.

Existing Crack
Regarding the existing crack, it is assumed that all of the steel reinforcement is ineffective. The same control for $l_e > l_b$ is done and this indicates that some strips may have an effective length smaller than the bond length. The bond strength is therefore reduced. In addition, the crack extends over the entire height of the web, $h_f = 1430$. The reduced bond strength can be found by using equation (6.29):

$$f_{fbwd} = (1 - \frac{1}{3}\frac{252}{1430/sin45}) \cdot \frac{661}{1.3} \tag{E.8}$$

This equation is derived for the case with full area bond and $h_f/sin\alpha \geq l_e$. This gives $f_{fbwd} = 487.4$ MPa.

The shear force sustained in one strip is:

$S_{wd} = A_{fw} \cdot f_{fbwd} \cdot sin\alpha = 301.6 \text{ mm}^2 \cdot 487.4 \text{ MPa} \cdot 0.707 = 125.1 \text{ kN}$

The total shear capacity of all four strips is $V_{rdf,crack} = 500.4$ kN

E.A.3.2 Shear Strengthening due to Flexural Debonding

Two controls are preformed in regards to shear strengthening due to flexural debonding:

- Detachment of concrete
- Shear induced intermediate debonding

This is performed in accordance with 6.3.3.

Investigating the possibility of concrete cover separation, the modified shear strength is found by using equation (6.32) with the following properties:

$a_f = 200\text{mm}$
$\rho_s = \frac{24442.6}{800 \cdot 1605} = 1.90 \cdot 10^{-2}$

a_f is found from the drawings of the fiber applications made by Aas-Jakobsen. This shows that the fiber is placed 600 mm from the center of the column. The column has a radius of 400 mm which gives a distance of $a_f = 200$ mm form the edge of the column.

ρ_s is taken from a section near the support, where A_s is the tension reinforcemnt.

V_{Rdc} is the design value for the shear resistance in members not requiring shear reinforcement found in NS EN 1992-1-1. Though, for this calculation, NS 3437 is used. In NS 4347 the capacity in ULS is set equal to $V_{co} = 441.9$ kN found in C.D.1

This gives a modified shear resistance of:

$$V_{Rs,c,fe} = 0,75[1 + 19.6\frac{(100 \cdot 1.90 \cdot 10^{-2})^{0.15}}{200}]441.9 \text{ kN} = 367.2 \text{ kN} \qquad \text{(E.9)}$$

The control for shear induced intermediate crack debonding is a control regarding the whole memeber. To simplify the control, an average d for the sections is set to 1570 mm.
$z = 0.9d = 0.9 \cdot 1570 = 1413$ mm

A limit based on the steel's stress is determined and given in eq. (6.34)

As the stirrups are assumed smooth, the limit of 25 MPa is used. The maximum shear compression resistance is found in appendix C.D.1. Eq. (6.35) is substituted for σ_{sw} and the equation is solved for V_{Ed} obtaining the maximum value:

$$V_{Ed,max} = \sqrt{25 \cdot \frac{A_{sw}}{s} \cdot z \cdot \ \cot\theta \cdot V_{Rd,max} \cdot (cot\theta + cot\alpha)sin\alpha} \qquad \text{(E.10)}$$

$$V_{Ed,max} = \sqrt{25 \cdot \frac{265}{175} \cdot 1413 \cdot 1 \cdot 2880000 \cdot (1+1) \cdot 0.707} = 466 \text{ kN} \qquad \text{(E.11)}$$

$V_{Rd,max}$ is the same shear compression strength, V_{ccd} found in section C.D.

The designing shear force due to shear induced intermediate debonding is $V_{Ed,max} =$ 468 kN.

Appendix F

Design Forces Intermediate Crack Debonding

The design forces to impose intermediate crack debonding is the shift of tensile forces at each element between cracks.

To evaluate the shift of tensile forces, the moment distribution must be found. Live loads q_Q and self weight q_G is distributed loads. For a beam fixed at both ends, the moment distribution is:

$$M_G(x) = -\frac{q_G x^2}{2} + \frac{q_G L \cdot x}{12} - \frac{q_G L^2}{12}$$

$$M_Q(x) = -\frac{q_Q x^2}{2} + \frac{q_Q L \cdot x}{12} - \frac{q_Q L^2}{12}$$

The maximum load combination gives $M_G = 1740$ kNm and $M_Q = 4476$ kNm at field section. Inserting $x = L/2$ in the equations above, q_G and q_Q is obtained:

$$g_G = \frac{M_G(L/2)}{L^2} \cdot 24 = 82.5 \text{ kN/m}$$

$$g_G = \frac{M_Q(L/2)}{L^2} \cdot 24 = 212 \text{ kN/m}$$

The moment distribution of ASR is assumed to be linear between the axis and field section. With a moment of about 2450 kNm at axis 8 and 3913 kNm at field 8, we obtain the ASR moment distribution:

$$M_{ASR}(x) = 2450 \text{ kNm} + 130 \text{ kN} \cdot x$$

Calculations is done according to 6.2.1 and fib bulletin [18]. Properties are found in Appendix C.C. F_{fEd} depends on the tension of the steel reinforcement, which is found by eq. (**??**) and (**??**), repeated below:

$$\sigma_s(x) = \sigma_{s,0}(x) + \frac{\Delta M_{Ed}(x)}{z_m} \cdot \frac{d_s \cdot E_s}{E_f A_f + E_s A_s}$$

Where

$\sigma_{s,0}(x) = \frac{M_{Ed,0}(x)}{0.85 \cdot d_s \cdot A_s}$

$\Delta M_{Ed}(x)$ is additional bending moment after strengthening, in this case live load $M_Q(x)$. $M_{Ed,0}(x)$ is the initial bending moment before strengthening, in this case $M_{ASR}(x)$ and $M_G(x)$. The weighted level arm z_m is found by:

$z_m \approx 0.8 \cdot \frac{d_f E_f A_f + d_s E_s A_s}{E_f A_f + E_s A_s} = 1257.15$ mm

A MATLAB code is used to calculate the shift in tension force in the CFRP. The tension force is found by eq. (6.19) and the shift in tension force is found by eq. (6.15). $S_r = 400$ mm is calculated in E.A.2.3.

Due to uncertainties about the ASR imposed moment, a code without $M_{ASR}(x)$ is submitted.

Appendix G

MATLAB Codes

```
clear all

q_Q = 212; %kN/m
q_G=82.5; %kN/m
sr=0.4; %m
zm=1257.15; %mm
zs=1453; %mm
As=16478; %mm^2
ds=1565.5; %mm
Es=200000; %MPa
h=1710; %mm
Af=672; %mm^2
Ef=210000; %MPa
fyd=272; %MPa
L=22.5; %m
sigma_0 = [];

Ffed=[];


i=1;

for x=4.25:sr:11.05

    M_nytte=-(q_Q*L^2)/12 - (q_Q*x^2)/2 + (q_Q*L*x)/2;
    M_asr= 2450 + 130*x;
    M_g=-(q_G*L^2)/12 - (q_G*x^2)/2 + (q_G*L*x)/2;

    sigma_0
(i)=(M_asr+M_g)*10^6/(zs*As)+M_nytte*10^6*ds*Es/(zm*(h*Ef*Af+ds*Es*As));

    if sigma_0 < fyd;

        Ffed(i)=M_nytte*10^6*Af*h*Ef/(zm*(h*Ef*Af+ds*Es*As));
    else
      Ffed(i)=((M_asr+M_g+M_nytte)*10^6/zm)-As*fyd;
   end
    i=i+1;
end

DeltaFfed=[];

for j=1:17;

    DeltaFfed(j)=Ffed(j+1)-Ffed(j);
end

disp(Ffed)
disp(DeltaFfed)

x = 4.25:0.4:11.05;

figure()
plot (x,Ffed/10^3)
```

```
figure()
plot (DeltaFfed/10^3)
```

Elise Sophie Christensen and Sigrid Freihow Sande

Evaluation of Externally Reinforced Bridge Exposed to Alkali-Silica Reactions

NTNU
Norwegian University of Science and Technology